BEILSTEIN JOURNAL OF NANOTECHNOLOGY

# Advanced atomic force microscopy techniques V

Edited by Philipp Rahe, Ilko Bald, Nadine Hauptmann, Regina Hoffmann-Vogel, Harry Mönig, Michael Reichling

# Imprint

Beilstein Journal of Nanotechnology
www.bjnano.org
ISSN 2190-4286
Email: journals-support@beilstein-institut.de

The *Beilstein Journal of Nanotechnology* is published by the Beilstein-Institut zur Förderung der Chemischen Wissenschaften.

Beilstein-Institut zur Förderung der Chemischen Wissenschaften
Trakehner Straße 7–9
60487 Frankfurt am Main
Germany
www.beilstein-institut.de

BEILSTEIN JOURNAL OF NANOTECHNOLOGY

# Advanced atomic force microscopy techniques V

Philipp Rahe*[1], Ilko Bald[2], Nadine Hauptmann[3], Regina Hoffmann-Vogel[4], Harry Mönig[5] and Michael Reichling[1]

Editorial

Open Access

Address:
[1]Institut für Physik, Universität Osnabrück, Barbarastraße 7, 49076 Osnabrück, Germany, [2]Institute of Chemistry, Hybrid Nanostructures, University of Potsdam, Karl-Liebknecht-Straße 24–25, 14476 Potsdam, Germany, [3]Institute for Molecules and Materials, Radboud University, 6525 AJ Nijmegen, The Netherlands, [4]Institute of Physics and Astronomy, University of Potsdam, Karl-Liebknecht-Str. 24–25, 14476 Potsdam, Germany and [5]Physikalisches Institut, Universität Münster, Wilhelm-Klemm-Str. 10, 48149 Münster, Germany

Email:
Philipp Rahe* - prahe@uni-osnabrueck.de

* Corresponding author

Keywords:
AFM; atomic force microscopy; conductivity; drift correction; force spectroscopy; NC-AFM; non-contact atomic force microscopy; resistivity; tip–surface interaction

*Beilstein J. Nanotechnol.* **2025,** *16,* 54–56.
https://doi.org/10.3762/bjnano.16.6

Received: 15 December 2024
Accepted: 07 January 2025
Published: 21 January 2025

This article is part of the thematic issue "Advanced atomic force microscopy techniques V".

Editor-in-Chief: G. Wilde



With the restrictions on travelling and social distancing lifted, we were delighted to continue two series of meetings on atomic force microscopy (AFM), the 23rd International Conference on Non-Contact Atomic Force Microscopy (NC-AFM) held in Nijmegen (Netherlands) and the 6th International Workshop on Advanced Atomic Force Microscopy Techniques held in Potsdam (Germany). The strong advance in the field and the high quality of the presentations motivated us to establish this thematic issue in the *Beilstein Journal of Nanotechnology* for compiling the latest results on developments and applications of atomic force microscopy techniques.

Atomic force microscopy, a technique soon celebrating its 40th anniversary, is nowadays a well-established tool for the investigation of nanoscale phenomena. The technique is steadily developed to increase accuracy, precision, and versatility; some of these developments are presented in contributions to this thematic issue.

Along these lines, Dickbreder et al. address the precision of scanning probe microscopy experiments by introducing a software for lateral drift correction [1]. Post-data acquisition drift correction for longer series of consecutively recorded image sets can be cumbersome and extremely time consuming. Here, the authors develop an easy-to-use and robust software tool (”unDrift”), which allows reliable and fast drift correction. Dickbreder et al. demonstrate the robust performance of the software tool by AFM data recorded under varying conditions (vacuum or liquid environment) on calcite surfaces with recording times up to several hours.

The work by Nony et al. addresses the significantly increased precision of force spectroscopy measurements when performed with a quartz cantilever allowing to reduce the oscillation amplitude to values in the low picometer regime [2]. As the conversion of frequency-shift to force data critically depends on the accurate knowledge of the quartz cantilever stiffness,

the authors develop a method to quantify the stiffness based on thermal noise measurements and numerical simulation.

Calibrated measurements of conductivity and resistivity are the focus of the contribution by Piquemal et al. [3]. A particular challenge in precision measurements of local electrical parameters lies on possible contributions of environmental factors as well as on unknown electrical properties of the scanning tip. The work by Piquemal et al. tackles these challenges by introducing a reference sample suitable for calibrating the microscope over a wide current range. A central zone of the sample offers several contact pads, each addressable by the tip of a conductive atomic force microscopy probe, and each connected to a different calibrated resistor. Thus, calibrated current measurements over a large current range become possible.

Khachartryan et al. highlight the strength of cantilever displacement detection with a Michelson-type fibre interferometer and provide a model for interferometric signal generation [4]. The interferometer response is slightly nonlinear under typical NC-AFM working conditions, while a large cantilever oscillation amplitude yields a signal with a complex temporal structure. This is due to the interferometer signal being limited in amplitude by the spatial periodicity of the cavity light field. By the fit of a model function to the measured time-domain interferometer signal, all displacement signal parameters can precisely be determined regardless of the oscillation amplitude. As the periodicity of the cavity light field scales with the length standard given by the laser light wavelength, this specifically facilitates a calibration of the oscillation amplitude with unprecedented accuracy and precision not involving any tip–surface interaction.

The measurement of electrostatic properties at the nanoscale emerged as a most relevant subfield of atomic force microscopy, especially driven by electrostatic force microscopy (EFM), Kelvin probe force microscopy (KPFM), and closely related techniques.

Grévin et al. further push the boundaries of the detection by implementing an open-loop variant of KPFM which accesses the spectrum of a time-periodic surface potential [5]. By exploiting a double heterodyne frequency mixing effect, they can selectively transfer each harmonic component to the second cantilever eigenmode, which is particularly relevant when generating the time-periodic potential by optical or electrical pumping. With this development, the authors could present the detection of modulated components that are below the detection limit of other KPFM measurement modes.

Da Lisca et al. investigate the cross-sectional potential distribution across a III-V multilayer stack [6]. With a spatial resolution down to 20 nm at ambient conditions, they identified the presence of several space charge regions along the stack. The authors further conclude on future requirements on electrical contacts to carry out a more detailed characterization of the optoelectronic properties.

Rothhardt et al. map the local work function on graphene nanoribbons [7]. They experimentally investigate the charge transfer between a gold substrate and graphene nanoribbons and compare that to DFT calculations. Indeed, the doping of the graphene nanoribbons is reflected by the local work function. They also measure and calculate the local work function as a function of tip–sample distance and compare results to those of simple electrostatic models of a graphene nanoribbon, validating the overall approach of measurement and calculations.

Eftekari et al. measure the local surface photovoltage generated in a silicon photodiode integrated with a piezoelectric membrane [8]. The design of such a device allows for the laterally resolved simultaneous quantification of the photovoltage generated by the photodiode as well as the mechanical oscillation of the piezoelectric membrane with highest resolution in real time.

In addition to the measurement of surface potentials or photovoltages, Navarro-Rodriguez et al. investigate the dynamics of surface charges and how they couple to the detection system [9]. They describe in detail how Joule dissipation leads to energy dissipation of the cantilever oscillation and a reduction in amplitude for constant excitation. They focus on two-dimensional materials and discuss how the reduction in amplitude resulting from energy dissipation influences the height measurement. In addition to the inaccuracy caused by electrostatic or capillary forces, this is an additional mechanism having an impact on AFM height measurements.

Closely related is the measurement of conductivity. Skolaut et al. investigate conductivity in dependence on the roughness of the substrate using alkanethiol self-assembled monolayers (SAMs) and conducting AFM [10]. The authors find that rougher surfaces lead to stronger variations in conductivity, and it is suggested that a correlation of topography and conductivity maps is carried out to identify suitable areas for a representative averaging of conductivity values.

Müller et al. present the application of AFM-based infrared nanospectroscopy to coated polymer surfaces [11]. The authors prepare thin films of $SiO_x$ on polypropylene surfaces by plasma-enhanced chemical vapor deposition (PE-CVD), which is commonly done to improve gas barrier properties of

polypropylene. They characterize $SiO_x$ films as thin as 5 nm by the so-called surface-sensitive mode, in contrast to the established contact mode, which provides much less surface sensitivity.

A particular strength for the study of materials is the combination of different measurement modes. Rothe et al. extend the characterization of defects in a single layer of graphene on iridium that were induced by rare-gas ion bombardment by using combined scanning tunnelling microscopy (STM) measurements and NC-AFM [12]. The authors reveal that presumed monoatomic vacancies, as deduced from STM measurements alone, have rather different origins. The authors assign one type of defects to a possible defect in the Ir surface. The other type is identified as four missing carbon atoms corroborated by a higher reactivity with the tip.

We thank all authors who contributed to this thematic issue and we are grateful to all reviewers for their input which was most helpful. It has been our greatest pleasure to work with the team at the *Beilstein Journal of Nanotechnology* and we appreciate their continuous support.

Philipp Rahe, Ilko Bald, Nadine Hauptmann, Regina Hoffmann-Vogel, Harry Mönig and Michael Reichling

Osnabrück, Potsdam, Nijmegen, and Münster, December 2024

## Author Contributions

Philipp Rahe: writing – review & editing. Ilko Bald: writing – review & editing. Nadine Hauptmann: writing – review & editing. Regina Hoffmann-Vogel: writing – review & editing. Harry Mönig: writing – review & editing. Michael Reichling: writing – review & editing.

## ORCID® iDs

Philipp Rahe - https://orcid.org/0000-0002-2768-8381
Ilko Bald - https://orcid.org/0000-0002-6683-5065
Nadine Hauptmann - https://orcid.org/0000-0003-4264-2493
Regina Hoffmann-Vogel - https://orcid.org/0000-0002-5771-7956
Harry Mönig - https://orcid.org/0000-0003-2639-9198
Michael Reichling - https://orcid.org/0000-0003-3186-9000

## Data Availability Statement

Data sharing is not applicable as no new data was generated or analyzed in this study.

## References

1. Dickbreder, T.; Sabath, F.; Höltkemeier, L.; Bechstein, R.; Kühnle, A. *Beilstein J. Nanotechnol.* **2023,** *14,* 1225–1237. doi:10.3762/bjnano.14.101
2. Nony, L.; Clair, S.; Uehli, D.; Herrero, A.; Themlin, J.-M.; Campos, A.; Para, F.; Pioda, A.; Loppacher, C. *Beilstein J. Nanotechnol.* **2024,** *15,* 580–602. doi:10.3762/bjnano.15.50
3. Piquemal, F.; Kaja, K.; Chrétien, P.; Morán-Meza, J.; Houzé, F.; Ulysse, C.; Harouri, A. *Beilstein J. Nanotechnol.* **2023,** *14,* 1141–1148. doi:10.3762/bjnano.14.94
4. Khachatryan, K.; Anter, S.; Reichling, M.; von Schmidsfeld, A. *Beilstein J. Nanotechnol.* **2024,** *15,* 1070–1076. doi:10.3762/bjnano.15.87
5. Grévin, B.; Husainy, F.; Aldakov, D.; Aumaître, C. *Beilstein J. Nanotechnol.* **2023,** *14,* 1068–1084. doi:10.3762/bjnano.14.88
6. da Lisca, M.; Alvarez, J.; Connolly, J. P.; Vaissiere, N.; Mekhazni, K.; Decobert, J.; Kleider, J.-P. *Beilstein J. Nanotechnol.* **2023,** *14,* 725–737. doi:10.3762/bjnano.14.59
7. Rothhardt, D.; Kimouche, A.; Klamroth, T.; Hoffmann-Vogel, R. *Beilstein J. Nanotechnol.* **2024,** *15,* 1125–1131. doi:10.3762/bjnano.15.91
8. Eftekhari, Z.; Rezaei, N.; Stokkel, H.; Zheng, J.-Y.; Cerreta, A.; Hermes, I.; Nguyen, M.; Rijnders, G.; Saive, R. *Beilstein J. Nanotechnol.* **2023,** *14,* 1059–1067. doi:10.3762/bjnano.14.87
9. Navarro-Rodriguez, M.; Somoza, A. M.; Palacios-Lidon, E. *Beilstein J. Nanotechnol.* **2024,** *15,* 767–780. doi:10.3762/bjnano.15.64
10. Skolaut, J.; Tepper, J.; Galli, F.; Wulfhekel, W.; van Ruitenbeek, J. M. *Beilstein J. Nanotechnol.* **2023,** *14,* 1169–1177. doi:10.3762/bjnano.14.97
11. Müller, H.; Stadler, H.; de los Arcos, T.; Keller, A.; Grundmeier, G. *Beilstein J. Nanotechnol.* **2024,** *15,* 603–611. doi:10.3762/bjnano.15.51
12. Rothe, K.; Néel, N.; Kröger, J. *Beilstein J. Nanotechnol.* **2024,** *15,* 416–425. doi:10.3762/bjnano.15.37

## License and Terms

BEILSTEIN JOURNAL OF NANOTECHNOLOGY

# Cross-sectional Kelvin probe force microscopy on III–V epitaxial multilayer stacks: challenges and perspectives

Mattia da Lisca*[1,2,3], José Alvarez[1,2,3], James P. Connolly[1,2,3], Nicolas Vaissiere[4], Karim Mekhazni[4], Jean Decobert[4] and Jean-Paul Kleider[1,2,3]

Full Research Paper

Open Access

Address:
[1]Institut Photovoltaïque d'Ile de France, 30 Route Départementale 128, 91120, Palaiseau, France, [2]Université Paris-Saclay, CentraleSupélec, CNRS, Laboratoire de Génie Electrique et Electronique de Paris, 91192, Gif-sur-Yvette, France, [3]Sorbonne Université CNRS, Laboratoire de Génie Electrique et Electronique de Paris, 75252, Paris, France and [4]III-V Lab, 1 Avenue Augustin Fresnel, 97167 Palaiseau, France

Email:
Mattia da Lisca* - mattia.dalisca1@gmail.com

* Corresponding author

Keywords:
FM-KPFM; frequency-modulated Kelvin probe force microscopy; III–V multilayer stack; Kelvin probe modelling; KP modelling; SPV; surface photovoltage

*Beilstein J. Nanotechnol.* **2023,** *14,* 725–737.
https://doi.org/10.3762/bjnano.14.59

Received: 28 October 2022
Accepted: 19 May 2023
Published: 14 June 2023

This article is part of the thematic issue "Advanced atomic force microscopy techniques V".

Guest Editor: P. Rahe



## Abstract

Multilayer III–V-based solar cells are complex devices consisting of many layers and interfaces. The study and the comprehension of the mechanisms that take place at the interfaces is crucial for efficiency improvement. In this work, we apply frequency-modulated Kelvin probe force microscopy under ambient conditions to investigate the capability of this technique for the analysis of an InP/GaInAs(P) multilayer stack. KPFM reveals a strong dependence on the local doping concentration, allowing for the detection of the surface potential of layers with a resolution as low as 20 nm. The analysis of the surface potential allowed for the identification of space charge regions and, thus, the presence of several junctions along the stack. Furthermore, a contrast enhancement in the surface potential image was observed when KPFM was performed under illumination, which is analysed in terms of the reduction of surface band bending induced by surface defects by photogenerated carrier distributions. The analysis of the KPFM data was assisted by means of theoretical modelling simulating the energy bands profile and KPFM measurements.

## Introduction

The development of photovoltaic (PV) technologies has progressed significantly over the past twenty years as a result of considerable advancements in solar cell device engineering and material science. As a consequence, solar cells have turned into complex structures containing numerous layers and interfaces [1]. The capability to conduct local investigations at the nano-

scale level that provide information on the electrical properties of materials and along physical interfaces is becoming crucial for solar photovoltaic device efficiency improvement [2].

Electrical measurements based on scanning probe microscopy (SPM) allow for the analysis of two-dimensional (2D) features at the surface and along a physical cross section of nanoscale semiconductor structures. Among the wide variety of SPM techniques available [3], Kelvin probe force microscopy (KPFM) is an application of the atomic force microscope (AFM) for the evaluation of the surface potential with nanometric resolution. KPFM is a valuable investigative approach for the study of work functions via the measurement of the contact potential difference $V_{CPD}$, that is, the difference between the electrostatic potential at the surface of the investigated structure and that of the KPFM probe [4].

KPFM has been extensively used in the PV field [5-7]; more specifically, by the analysis of interfaces in a solar device [8,9], it can reveal the presence of unintentional potential barriers or pn junctions, which hinder the extraction of the photogenerated charges. III–V-based solar devices belong to the PV technology of thin and ultrathin films in which layers with widths of the order of a few nanometres are often integrated for an optimal surface passivation or for better carrier extraction, considerably enhancing device efficiency [10,11]. Consequently, the experimental demonstration of the sensitivity of KPFM to the narrower layers can be crucial for the investigation and comprehension of local surface properties and charge transport mechanisms at interfaces [12].

Within this context, this work presents a study about the capability of cross-sectional KPFM for the study of a III–V multilayer stack under ambient conditions. In particular, we have investigated an InP/GaInAs(P) multilayer structure with layers of different widths and doping concentrations.

The first objective of this analysis is the evaluation of the spatial resolution of our KPFM setup under ambient conditions. The second objective is a full understanding of the $V_{CPD}$ results combined with a description of the principal factors that affect KPFM measurements with the application of Kelvin probe (KP) numerical modelling. This enables the interpretation of the KPFM data, specifically to investigate the effect of space charge regions, surface defects, and illumination on $V_{CPD}$ [13].

# Experimental

## Sample preparation

The structure of the studied sample is summarized in Table 1. This multilayer stack structure was epitaxially grown using a MOVPE process in an AIXTRON "Close Coupled Showerhead" reactor (6″ × 2″) at three different surface temperatures (580/600/640 °C). The n-type AXT substrate doping was typically in the range of $3 \times 10^{18}$ to $5 \times 10^{18}$ $cm^{-3}$ with a thickness of 500 µm. Trimethylindium (TMIn), trimethylgallium (TMGa), phosphine ($PH_3$), and arsine ($AsH_3$) were the source materials, with hydrogen ($H_2$) as a carrier gas. Diethylzinc (DEZn) was used as a source of Zn for p-type doping the InP:Zn and the phosphorus-based quaternary (GaInAsP:Zn) and GaInAs:Zn layers. The precursor flow was varied to cover a doping level range from $1 \times 10^{18}$ $cm^{-3}$ to $2.5 \times 10^{19}$ $cm^{-3}$. The first part of the structure was used to measure the growth rate of the non-intentionally doped InP layers (InP:nid) at surface temperatures of 600 and 640 °C. The reflectance signal, monitored with an in situ Laytec EpiCurve TT tool, did not show any difference between the growth rates at the two surface temperatures, which were around 2.13 µm·$h^{-1}$. The second part of the structure corresponds to the Zn calibration stack used for the p-type clad-

**Table 1:** Full structure of the investigated multilayer stack sample.

| Layer | Material | Doping concentration ($cm^{-3}$) | Thickness (nm) |
|---|---|---|---|
| substrate | InP:S | (3–5) × $10^{18}$ | 500 µm |
| buffer | InP | nid | 100 |
| interlayer | GaInAs | nid | 5 |
| buffer | InP | nid | 300 |
| interlayer | GaInAs | nid | 5 |
| buffer | InP | nid | 250 |
| cladding | InP:Zn | 2 × $10^{18}$ | 500 |
| cladding | InP:Zn | 1.50 × $10^{18}$ | 750 |
| cladding | InP:Zn | 1 × $10^{18}$ | 500 |
| transition | GaInAsP:Zn | 6 × $10^{18}$ | 20 |
| contact | GaInAs:Zn | 2.50 × $10^{19}$ | 200 |

ding of the multiple quantum well-based structure. The doping concentration of the InP:Zn layers was varied from $2 \times 10^{18}$ to $1 \times 10^{18}$ cm$^{-3}$. The three Zn doping levels of InP layers were purposely inverted along the growth direction to facilitate electrochemical capacitance–voltage (ECV) characterization due to the strong Zn diffusion. The InP:Zn and the GaInAsP:Zn layers were epitaxially grown at a surface temperature of 600 °C. Note that the GaInAsP:Zn layer is an intermediate layer with a doping concentration of $6 \times 10^{18}$ cm$^{-3}$ with the purpose to smooth the InP:Zn/GaInAs:Zn transition bandgap and to reduce contact resistances. Finally, a GaInAs:Zn contact layer was made at a lower temperature of 580 °C in order to reach a higher doping level around $2.5 \times 10^{19}$ cm$^{-3}$.

Before starting the KPFM analysis, the sample was cleaved, and a surface cleaning was carried out to expose a clean cross section. We performed a chemical treatment based on sequential ultrasonic baths of acetone, ethanol, and deionized water. The sample was then placed in 1% HF solution for 30 s to etch the top oxide layer. This step was followed by a rinsing with deionized water and drying in air. This procedure was necessary for an optimal KPFM analysis since the presence of a native oxide surface layer on top can lead to the measurement of a misleading $V_{CPD}$ value [14].

## Kelvin probe force microscopy

The following KPFM experimental procedures closely follow those described in [12]. KPFM evaluates the contact potential difference ($V_{CPD}$) between the surface of metallic and semiconductive samples and a conductive AFM tip, which at equilibrium can be related to the work functions as:

$$qV_{CPD} = \phi_{tip} - \phi_{sample}, \quad (1)$$

where $\phi_{sample}$ and $\phi_{tip}$ are the work functions of the sample and of the tip, respectively [4]. The $V_{CPD}$ value is acquired by evaluating the DC voltage required to compensate for the electrostatic force generated between the tip and the sample, which, in turn, defines the KPFM signal [15]. KPFM was performed using a scanning probe microscopy system from AIST-NT (TRIOS platform) under ambient conditions and operated in the frequency-modulated KPFM (FM-KPFM) mode using a two-pass scanning mode, where the second pass was performed at a constant distance of 10 nm from the sample surface. Topographical data were collected on the first pass, whereas $V_{CPD}$ was measured during the second one. The schematic of our KPFM setup is depicted in Figure 1.

The FM-KPFM mode was chosen over the amplitude-modulation mode (AM-KPFM) since it is well known that it provides better spatial resolution. In particular, in AM-KPFM the electrical force between the tip and the sample is directly evaluated, whereas in FM-KPFM the gradient of the force is analysed. As a result, FM-KPFM is more sensitive to local tip apex–sample surface interactions; therefore, long-range electrostatic interactions of the cantilever are reduced, as well as the effect of parasitic capacitances [16]. Additionally, in FM-KPFM, surface potential measurements are less dependent on the lift-height tip–sample distance than in AM-KPFM since this mode is less sensitive to static offsets induced by capacitive coupling or crosstalk [17].

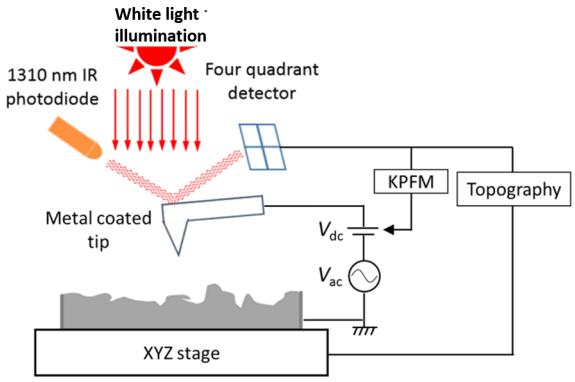


**Figure 1:** Schematic diagram of the KPFM system employed in this analysis. While an ac + dc potential is applied, the KPFM tip scans across a surface. The ac signal is sinusoidal with a frequency that equals the mechanical resonance of the cantilever. The four-quadrant detector gives feedback in order to minimize cantilever oscillation modifying the dc signal providing the sample surface potential relative to that of the tip. Figure 1 was reproduced from [13] (© 2019 C. Marchat et al., published by EDP Sciences, distributed under the terms of the Creative Commons Attribution 4.0 International License, https://creativecommons.org/licenses/by/4.0).

The laser beam deflection system in our AFM employs a laser wavelength of 1310 nm, which is well below the bandgap of our sample; therefore, the parasitic laser absorption, which may interfere with the KPFM measurement, is reduced to negligible levels [13]. Highly doped n$^+$-Si ARROW EFM tips (radius < 25 nm) with a conductive Pt/Ir coating at a resonance frequency of 75 kHz were used.

During KPFM measurements under ambient conditions, tip contamination is likely to occur because of pollutants that may be present on the sample surface causing a variation of $\phi_{tip}$ [18]. Hence, $\phi_{tip}$ was evaluated periodically in the course of the analysis using Equation 1 by measuring the $V_{CPD}$ value of a freshly exfoliated surface of highly ordered pyrolytic graphite (HOPG) with $\phi_{sample}$ being equal to 4.6 eV [19]. The successively measured $\phi_{tip}$ values showed only small variations with values ranging between 5.65 and 5.75 eV.

KPFM measurements were performed under dark conditions and under illumination on the cross section of the sample. The acquisition of $V_{CPD/light}$ enables the evaluation of the surface photovoltage (SPV), which is defined as the light-induced change of the contact potential difference at the surface of a photoactive material [20]. Since the surface potential of the tip is assumed to be unaffected by illumination, the difference between $V_{CPD/light}$ and $V_{CPD/dark}$ is equal to the change in surface potential of the sample between illumination and dark, which defines the surface photovoltage:

$$\mathrm{SPV} = V_{\mathrm{CPD(light)}} - V_{\mathrm{CPD(dark)}}. \quad (2)$$

It is important to mention that although KPFM is primarily a surface technique, the SPV can be sensitive to the presence of buried interfaces and/or deep charge trap states that may be present far from the surface in the bulk of semiconductors. Therefore, in our study the white light coming from the camera connected to the microscope was used. The white-light wavelength range is 400 to 700 nm, and for these wavelengths the penetration depth in GaInAs ranges between 10 and 100 nm. This makes our measurements mainly sensitive to the surface states and surface band bending. Additionally, a uniform illumination of the surface cross section was achieved thanks to the wide light spot.

Finally, the power density was 750 $\mathrm{W{\cdot}m^{-2}}$ as measured by a thermal power sensor S401C from Thorlabs, which has a flat spectral response in the white-light range of wavelengths. This relatively low power density allows one to minimize the Dember effect since its contribution becomes significant only under high-injection conditions [20].

## KP modelling

In order to analyse the experimental characterization, scanning KP simulation was performed using the ATLAS software from Silvaco Inc. [21], controlled by the in-house software KELSCAN [13], which evaluates the contact potential and surface photovoltage as a function of the position.

The Silvaco ATLAS model solves the Poisson equation self-consistently coupled to carrier continuity and transport equations in the well-known drift diffusion model, which is given detail in [22] and not repeated here for brevity. The solution presented in this work assumes ohmic contacts and, therefore, Dirichlet boundary conditions fixing potential and carrier concentrations at the boundaries, as reported in section 3.5 of the SILVACO ATLAS manual. The ATLAS module solves semiconductor transport and continuity equations numerically in two dimensions and includes flexible descriptions of bulk and surface defect distributions. KELSCAN simulates the experimental setup by sequentially moving the AFM tip across the surface of the sample, statically solving the semiconductor equations at each position, and then evaluating the contact potential at each position from the field distribution calculated by ATLAS and exported to KELSCAN.

In order to replicate the experimental conditions, the radius of the tip is set at 25 nm, the distance between the tip and the sample cross section is set at 10 nm, and the $\phi_{tip}$ value is set at 5.7 eV, that is, the value measured on our tip as reported above. Note that KELSCAN allows one to simulate $V_{CPD}$ measurements either under dark conditions or under illumination. In the case of "under illumination" simulations, the power density described in the above section was used.

KPFM is a surface technique; therefore, KPFM measurements are strongly influenced by the presence of surface defects. In order to provide a quantitative analysis of the experimental results, KELSCAN allows for the introduction of defects in a surface layer of arbitrary depth. The model of defects extending into the volume is physically more appropriate than a simpler two-dimensional surface distribution [23]. The introduced defect volume density of states (DOS), $N(E)$ ($\mathrm{eV^{-1}{\cdot}cm^{-3}}$), is assumed to be homogeneous throughout the thickness of the defective layer, $t_{DL}$, which we took equal to 1 nm. This can be translated into a surface density of states $N_{ss}(E)$ ($\mathrm{eV^{-1}{\cdot}cm^{-2}}$): $N_{ss}(E) = N(E) \times t_{DL}$, with $t_{DL} = 1 \times 10^{-7}$ cm. In addition, the DOS consists of the sum of two distributions of monovalent donor and acceptor states, $N_D(E)$ and $N_A(E)$, respectively: $N(E) = N_D(E) + N_A(E)$. These determine the charge neutrality level (CNL) of the surface defects. That is, when the Fermi level ($E_F$) at the surface coincides with the CNL, there is no net charge coming from the surface defects. In contrast, when $E_F$ is above (below) the CNL, surface defects are overall negatively (positively) charged. Here, to illustrate the effect of the defects on the band bending and on the measured surface potential profile, we introduced a simple constant DOS for both donor and acceptor states. The CNL is thus easily deduced from the ratio of the constant donor and acceptor DOSs. If they are chosen equal, the CNL is set at mid-gap, whereas it is moved towards the valence (conduction) band if the ratio of acceptor to donor DOS is larger (smaller) than 1 [24].

# Results

## KPFM cross-sectional investigation under dark conditions

The cross section of the sample was first investigated by KPFM under dark conditions, immediately after the chemical cleaning step. The topography and the associated $V_{CPD}$ image are reported in Figure 2a and Figure 2b, respectively.

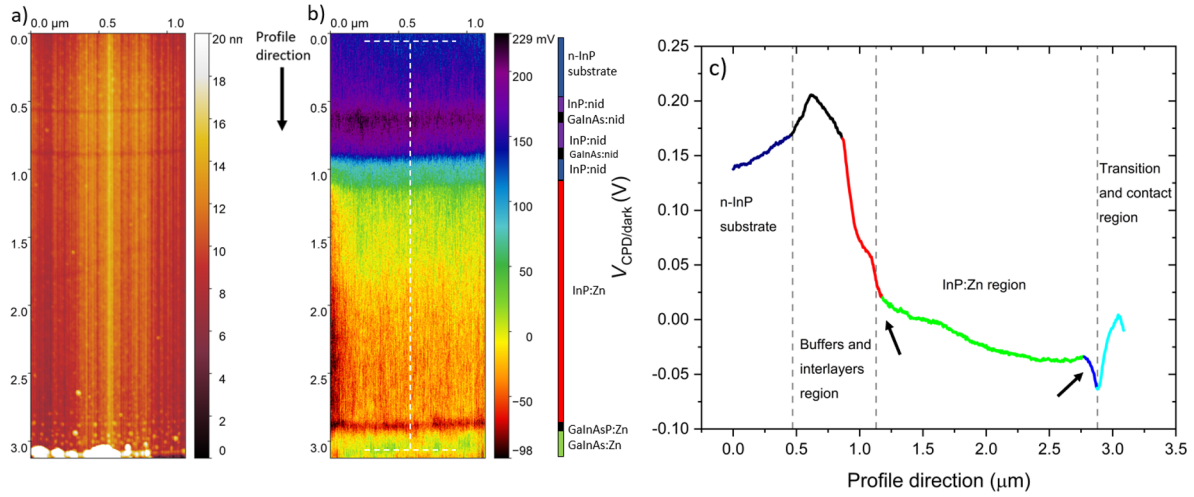


**Figure 2:** KPFM measurement under ambient conditions on the surface cross section of the sample under dark conditions: (a) topography and (b) $V_{CPD}$ image. A vertical coloured bar is included to ease the identification of the different layers. The profile in (c) corresponds to the region identified by the dotted white segments in (b), each point of the profile (vertical) direction being an average of 207 points over a width of 0.7 μm along the *x* axis. Several regions along the structure have been highlighted using different colours (see text). Two black arrows indicate the space charge regions at the interfaces of the InP:Zn region.

Note that the origin (0;0) is identified as a point in the InP substrate. Moving along the positive direction of the *y* axis, one will reach the end of the sample, that is, the surface of the 2D wafer (e.g., around 3.09 μm in Figure 2). In order to achieve a successful KPFM analysis, a low surface roughness is essential to obtain high-quality images since surface inhomogeneities can cause a topographical image imprint on the surface potential image. With sufficiently low surface roughness, the topographic influence on the measurement is minor, and the observed contrast of the $V_{CPD}$ map is dominated by the surface potential such that topographic artefacts can be neglected.

A first look at the $V_{CPD}$ image and the extrapolated profile (Figure 2c) allows for a qualitative analysis. KPFM successfully detects the n-InP substrate (from 0 to 0.46 μm), the InP:nid/GaInAs:nid region (from 0.46 to 1.12 μm), the InP:Zn region (from 1.12 to 2.87 μm), and the GaInAsP:Zn/GaInAs:Zn region (from 2.87 to 3.09 μm).

KPFM demonstrated a strong sensitivity on the local doping concentration as reported in a number of publications [12,25]. However, a clear identification of the 5 nm GaInAs:nid interlayers among the InP:nid buffer layers is not achieved in the $V_{CPD}$ image. Nevertheless, their presence was still detected and represented in the $V_{CPD}$ image by the dark and blue lines at 0.61 and 0.91 μm, respectively. The low resolution of the interlayers can be attributed either to their narrowness or to the experimental conditions since the two GaInAs:nid layers are well resolved in the topography image. Certainly, the width of these layers is narrower than the radius of the tip (<25 nm), and the operating conditions, namely the tip–surface distance and ambient measurements, negatively affect the resolution of KPFM measurements [26]. In particular, KPFM under ambient conditions is affected by the tip-averaging effect due to the long-range nature of the electrostatic force. The tip can sense multiple layers with different properties simultaneously, resulting in the detection of an averaged $V_{CPD}$ at the interfaces [27].

During KPFM measurements, the tip scans the cross section from the n-InP substrate to the end of the sample; consequently, it will sense the surface potential variation along the structure. The progression of the $V_{CPD}$ profile shows that four different slopes are present considering the region from the last InP:nid buffer layer to the GaInAs:Zn contact layer (from 0.86 to 3.09 μm). In particular, the first is located between the last InP:nid buffer layer and the first InP:Zn layer (from 0.86 to 1.17 μm), the second in the InP:Zn region (from 1.17 to 2.76 μm), the third between the last InP:Zn layer and the GaInAsP:Zn transition layer (from 2.76 to 2.87 μm), and the fourth between the GaInAsP:Zn transition layer and the GaInAs:Zn contact layer (from 2.87 to 3.09 μm). These regions have been identified with the colours red, green, blue, and light blue in the $V_{CPD}$ profile, respectively.

The green profile represents the InP:Zn region; because of the comparable doping concentration of the three InP:Zn layers, a

small variation of $V_{CPD}$ of the order of 20 mV is expected to be measured along this region. However, the experimental $V_{CPD}$ profile presents a $V_{CPD}$ variation of the order of 50 mV along the InP:Zn region (from 1.13 to 2.87 µm). Several factors can influence KPFM measurements leading to this experimental evidence, namely the sample preparation, the experimental conditions, and the presence of surface defects. All these aspects have an impact on the surface potential, as we will see in the Discussion section ("KPFM experimental conditions and sample preparation").

Regarding the other slopes pointed out above, their detection is attributable to the formation of space charge regions among the different layers along the structure [28]. Specifically, the $V_{CPD}$ progression reflects the band bending present in the presence of depletion and accumulation regions. In particular, undoped InP crystals always contain different unintentional impurities due to the growth processes. The InP:nid layers fabricated at III–V Lab usually present an intrinsic n-type doping of the order of $10^{15}$ cm$^{-3}$, which results in shallow donor energy levels within the energy gap. Since the intentional Zn p-type doping concentration is much greater than this residual n-type doping present in the InP:nid buffer, the space charge region is expected to be located almost exclusively in the buffer layer.

Similarly, two Zn doping concentration gradients are present from the last InP:Zn layer to the GaInAsP:Zn transition layer (from $1 \times 10^{18}$ to $6 \times 10^{18}$ cm$^{-3}$) and from the GaInAsP:Zn transition layer to the GaInAs:Zn contact layer (from $6 \times 10^{18}$ to $2 \times 10^{19}$ cm$^{-3}$). This results in two space charge regions situated almost completely in the InP:Zn layer and in the GaInAsP:Zn transition layer, respectively.

It is worth to mention that the band bending induced by the different space charge regions along the structure depends on the doping concentration (e.g., number of involved charge carriers) and on the width of the layers. Consequently, the corresponding $V_{CPD}$ variation will depend on the same parameters [12].

In order to investigate the effect of the space charge on the measured $V_{CPD}$, we have implemented theoretical modelling to this work. As a first step, we have simulated through ATLAS/Silvaco software [21] the energy bands profile of the analysed structure in the ideal case in which no surface defects are considered, qualitatively reproducing the expected energy bands profile in our sample. The widths and doping concentrations of the layers were chosen as reported in Table 1, whereas the other physical parameters (e.g., energy gaps) are present in the Silvaco database [21]. Note that in order to simulate the InP:Zn region, we have specified just one Zn doping concentration of $1.5 \times 10^{18}$ cm$^{-3}$. Furthermore, in order to replicate the experiment, we have included a metal layer on the left of the n-type InP substrate. Under these conditions, the metal layer represents the contact between the sample holder and the n-type InP substrate. Finally, the work function of the metal was set to be equal to that of the substrate to guarantee an ohmic contact. The simulated energy bands profile confirmed our hypothesis showing the induced band bending along three space charge regions at the InP:nid/InP:Zn, the InP:Zn/GaInAsP:Zn, and the GaInAsP:Zn/GaInAs:Zn interfaces, as shown in Figure 3a.

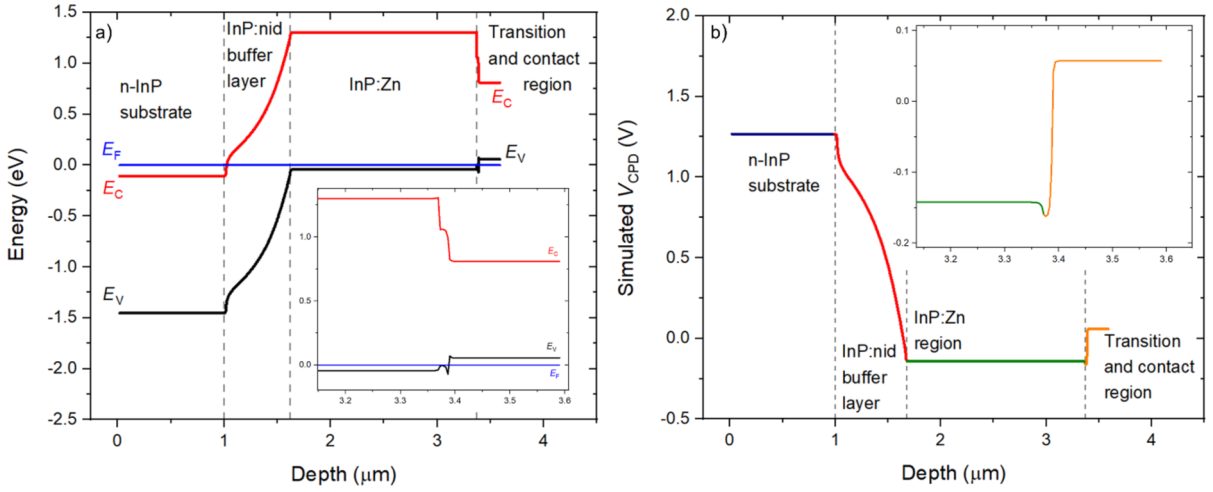


**Figure 3:** (a) Cross-sectional profile at equilibrium of the surface band energies (black: valence band maximum, $E_V$, and red: conduction band minimum, $E_C$) along the structure assumed free of any surface defects. The constant Fermi level, $E_F$, is taken as the energy reference (blue horizontal line). (b) $V_{CPD}$ evolution along the same simulated structure obtained by KP modelling. Note that both figures present an inset detailing the InP:Zn/GaInAsP:Zn/GaInAs:Zn interfaces close to the external surface of the sample.

In particular, because of the low doping concentration of the InP:nid layer compared to the adjacent n-InP substrate and the InP:Zn region, a space charge extends over its complete width. The $V_{CPD}$ profile across the InP:Zn/GaInAsP:Zn/GaInAs:Zn interfaces results from the different work functions. The work function of GaInAsP:Zn is slightly larger (by 0.04 eV) than that of InP:Zn, and it is substantially larger (by 0.22 eV) than that of the GaInAs:Zn contact layer, which leads to a decrease and an increase of potential, respectively. It is important to note that due to the narrowness of the GaInAsP:Zn transition layer (20 nm), the space charges at the two neighbouring heterojunctions overlap in this layer, leading to an asymmetric U-shape of the $V_{CPD}$ profile. The asymmetric U-shape is also present in the experimental profile in Figure 2c (dark blue and light blue parts emphasizing the decrease and increase in potential, respectively). The mismatch of the conduction and valence bands between these materials then leads to the peculiar band energy diagram. Insets have been added to Figure 3a and Figure 3b to zoom in this region. Additionally, KP modelling [13] was used to simulate the $V_{CPD}$ profile along the same structure assumed to be free of any surface defects for a quantitative evaluation of the effect of space charge on the surface potential (Figure 3b). $V_{CPD}$ is proportional to the difference between the vacuum level and $E_F$; therefore, the changes in the energy bands profile will be reflected in the simulated $V_{CPD}$ profile.

The simulated $V_{CPD}$ profile shows the same qualitative progression as the experimental profile reported in Figure 2c. However, several important differences can be noted by the comparison between the experimental and simulated $V_{CPD}$. In particular, the experimental $V_{CPD}$ profile (Figure 2c) seems to show that a part of the first space charge extends into the first InP:Zn layer (from 1.12 to 1.20 µm); similarly, the second space charge seems to extend more into the last InP:Zn layer than the modelling predicts (from 2.76 to 2.87 µm). These two regions are indicated by the two black arrows in Figure 2c. Additionally, the simulated $V_{CPD}$ shows a flat profile a few nanometres inside the GaInAs:Zn contact layer, whereas a flat surface potential is not obtained experimentally. In other words, experimental surface potential variations occur over distances larger than one may expect solely from the extrinsic Debye lengths calculated from the nominal doping densities, which are only a few nanometres [29]. As a consequence, the lack of a sharp transition among the interfaces can cause difficulties in the identification of the position of the metallurgical junctions in the $V_{CPD}$ image [28]. In particular, one reason can be found in the aforementioned tip-averaging effect: The tip still senses parts of the space charge in the InP:nid buffer layer and in the GaInAsP:Zn transition layer although being already on the first InP:Zn layer and on the GaInAs:Zn contact layer, respectively. Similarly, the tip starts to sense prematurely parts of the space charge inside the last InP:Zn layer. Furthermore, non-ideal abrupt junctions may contribute to this effect, for instance, because of dopant interdiffusion, as will be described in the following section.

Finally, the simulated $V_{CPD}$ progression predicts an overall surface potential change of the order of around 1.34 V from the n-type InP substrate to the InP:Zn region. Conversely, this $V_{CPD}$ variation in our experimental results is of the order of around 0.18 V. This is a first indication that the experimental surface potential is modified by the presence of surface states induced by surface defects since we know that KPFM is a surface technique and that the simulated $V_{CPD}$ variation at this stage is based solely on bulk material properties and is not affected by any surface defects. Therefore, the experimental surface potential results to be less pronounced than in the "gedanken profile" that occurs far from the surface. This will be fully addressed in the Discussion section ("KPFM experimental conditions and sample preparation").

## KPFM cross-sectional investigation under illumination

In order to study the effect of the illumination on the sample cross section, we have performed KPFM measurements under white-light illumination. The topography and the associated $V_{CPD}$ image are reported in Figure 4a and Figure 4b, respectively. The $V_{CPD/light}$ image of Figure 4b shows a significant contrast enhancement due to the interaction with the light compared to $V_{CPD/dark}$ of Figure 2b. As a consequence, $V_{CPD/light}$ results to be more homogenous all along the cross section than $V_{CPD/dark}$, as shown in the corresponding $V_{CPD/light}$ profile reported in Figure 4c. Moreover, the improvement of contrast also facilitates the identification of the narrower interlayers and of the position of the metallurgical junctions at the InP:nid/InP:Zn and the InP:Zn/GaInAsP:Zn interfaces, which were more undefined in the previous $V_{CPD/dark}$ image.

Overall, the $V_{CPD/light}$ profile follows the same evolution as the profile of $V_{CPD/dark}$; also in this case, four different $V_{CPD}$ slopes are present in the profile. In particular, the first is located between the last InP:nid buffer layer and the first InP:Zn layer (from 0.83 to 1.25 µm), the second in the InP:Zn region (from 1.25 to 2.78 µm), the third between the last InP:Zn layer and the GaInAsP:Zn transition layer (from 2.78 to 2.85 µm), and the fourth between the GaInAsP:Zn transition layer and the GaInAs:Zn contact layer (from 2.85 to 3.07 µm). These regions have again been identified with the colours red, green, blue, and light blue in the $V_{CPD}$ profile, respectively.

Notably, the $V_{CPD/light}$ profile along the InP:Zn region between 1.25 and 2.78 µm is flatter compared to that of $V_{CPD/dark}$. This $V_{CPD/light}$ profile is more consistent with what the modelling

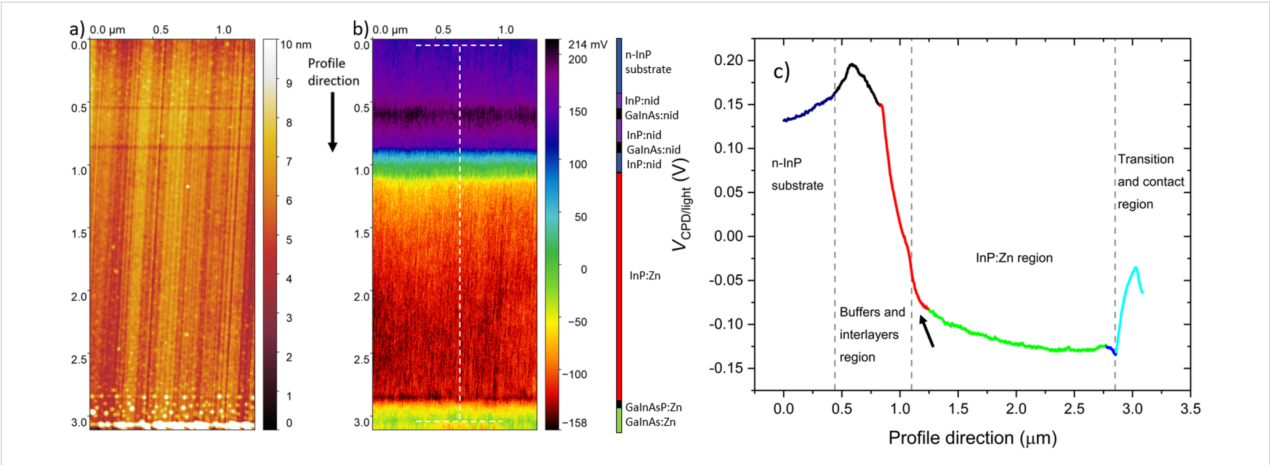


**Figure 4:** KPFM measurement under ambient conditions on the surface cross section of the sample under illumination: (a) topography and (b) $V_{CPD}$ image. A vertical coloured bar is included to ease the identification of the different layers. The profile in (c) corresponds to the region identified by the dotted white segments in (b), each point of the profile (vertical) direction being an average of 207 points over a width of 0.7 μm along the *x* axis. Several regions along the structure have been highlighted using different colours (see text). The black arrow indicates the space charge region at the InP:nid/InP:Zn interface.

predicts for such small variations in the Zn doping concentration along the InP:Zn region. Conversely, at the beginning of the InP:Zn layer, from 1.10 to 1.25 μm (indicated by the black arrow), the $V_{CPD}$ profile presents a steeper slope suggesting that the tip is still sensing the band bending induced by the space charge between the last InP:nid and the first InP:Zn layer. However, the tip-averaging effect alone cannot explain the detection of a space charge that extends for around 0.16 μm inside the first InP:Zn region. As a matter of fact, the diffusion of Zn impurities is likely to occur due to the high temperatures required for the growth of the material and the high diffusion coefficient of Zn in InP [30]. Therefore, the true spatial extent of the space charge region is not trivial to determine and may differ from what would be expected given the nominal structure of the sample. Conversely, the width of space charge region between the last InP:Zn layer and the GaInAsP:Zn transition layer is reduced and closer to the modelled one. Additionally, the detected surface potential change related to the space charge region at the GaInAsP:Zn/GaInAs:Zn interface is higher and closer to the simulation.

As described in the Experimental section ("Kelvin probe force microscopy"), the SPV can be calculated by applying Equation 2 to the experimental values of $V_{CPD/light}$ and $V_{CPD/dark}$. The SPV along the structure is reported in Figure 5.

The SPV progression along the structure shows an overall negative SPV. For highly doped semiconductors in the absence of surface states (or for surface state densities small enough so that they cannot introduce significant surface band bending) a SPV signal close to zero is expected to be measured [20]. We therefore expect a vanishing SPV signal in the highly doped n-type InP substrate, which is degenerately doped at $5 \times 10^{18}$ cm$^{-3}$ with respect to the InP effective conduction band density of states ($5.7 \times 10^{17}$ cm$^{-3}$ [31]). Experimentally the uncertainty on extracted SPV values can be evaluated at ±20 mV. Hence, the obtained value of around −10 mV in the highly doped n-type InP substrate is in good agreement with the theoretical expectation of vanishing SPV.

Furthermore, a negative SPV of around −95 mV is estimated for the InP:Zn region, which is consistent with the fact that a negative SPV is expected for a p-type semiconductor because of surface band bending due to surface states produced by surface

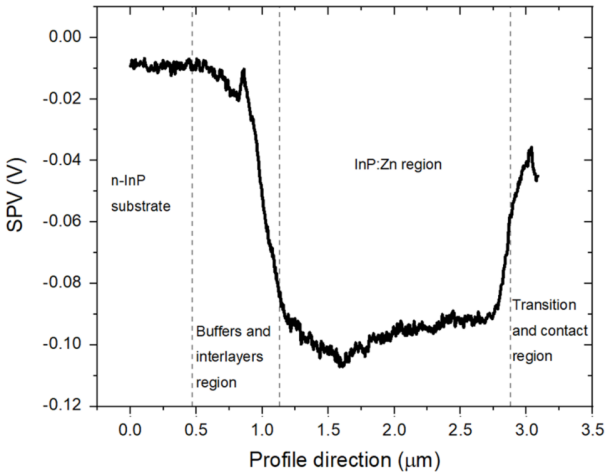


**Figure 5:** SPV profile along the structure calculated from the values of $V_{CPD/dark}$ and $V_{CPD/light}$ shown in the profiles of Figure 2c and Figure 4c, respectively, applying Equation 2.

defects. In particular, the detection of a negative SPV implies that a downward band bending is present in the vicinity of the surface [32]; this aspect will be fully addressed in the Discussion section ("Effect of the illumination on the VCPD"). Finally, it is worth mentioning that after illumination the initial conditions are restored, which excludes the presence of long-lived charge accumulation along the different junctions.

## Discussion

In this section the principal factors that affect KPFM measurements will be addressed in order to develop a methodology of analysis and apply it to experimental results.

### KPFM experimental conditions and sample preparation

Several factors can influence KPFM measurements, namely the experimental conditions and the status of sample surface and AFM tip. Additionally, as pointed out in the Results section ("KPFM cross-sectional investigation under dark conditions"), the presence of surface non-idealities (e.g., surface defects) has an effect on the surface potential and, thus, on the measured $V_{CPD}$. All these aspects can lead to surface inhomogeneities, which result in $V_{CPD}$ variations compared to an otherwise constant measurement on bulk material.

KPFM analysis was carried out under ambient conditions, which result in surface oxidation and in the adsorption of water molecules on the sample surface due to the humidity present in air [18]. Furthermore, a non-optimal deoxidation procedure may result in an inhomogeneous removal of the surface oxide. Additionally, the condition of the tip during the numerous scans along the sample cross section must also be considered. In particular, contamination of the tip is likely to occur due to pollutants (e.g., nano- and/or micrometre-size dust grains), which may be present on the sample surface leading to a variation of the tip surface potential.

The tip-averaging effect represents an important aspect of KPFM under ambient conditions, as revealed in the Results section ("KPFM cross-sectional investigation under dark conditions"). Even at extremely short tip–sample distances (5 nm), the tip-averaging effect can lower the lateral resolution as well as the measured KPFM signal [25]. This is especially evident in KPFM under ambient conditions, where typical tip–surface distances are of the order of tens of nanometres because of the vibrating tip amplitude necessary to achieve an acceptable signal-to-noise ratio.

Finally, it is well documented in the literature [20] that the cleavage procedure produces surface defects, which strongly impact the $V_{CPD}$. In order to study the effects of surface defects on the $V_{CPD}$, we have extended the energy band simulations to a non-ideal case in which constant distributions of acceptor-like and donor-like defects have been introduced at the surface, as described in the Experimental section ("KP modelling"). In order to clarify the analysis and focus on essentials, we have simulated a simpler structure with respect to the analysed multilayer sample, in which we did not include the 5 nm InGaAs:nid interlayers and the final InGaAs(P):Zn transition and contact layers. Specifically, we have compared the ideal structure free of surface defects to three different cases in which identical acceptor-like and donor-like surface defects densities of $1 \times 10^{12}$, $1 \times 10^{13}$, and $5 \times 10^{13}$ $eV^{-1}{\cdot}cm^{-2}$ (taken to be constant throughout the bandgap) were introduced at the surface. The results are reported in Figure 6. In this specific case, the charge neutrality level of surface defects is set at mid-gap. Thus, increasing the surface defect densities will produce a pinning of the Fermi level at the neutrality level of the surface states and the energy of valence and conduction bands will appear symmetric with respect to mid-gap position [24]. In particular, it is possible to observe this trend even at relatively low surface defects densities ($2 \times 10^{12}$ $eV^{-1}{\cdot}cm^{-2}$, see Figure 6b) in the InP:nid layer because of the low doping concentration ($1 \times 10^{15}$ $cm^{-3}$) compared to the other two layers. Conversely, in the n-InP substrate and in the InP:Zn layer, this trend is only well evidenced when high surface defects densities (above $10^{13}$ $eV^{-1}{\cdot}cm^{-2}$) are introduced at the sample surface; the trend is already visible for $2 \times 10^{13}$ $eV^{-1}{\cdot}cm^{-2}$ and really clear for $1 \times 10^{14}$ $eV^{-1}{\cdot}cm^{-2}$ in Figure 6c and Figure 6d, respectively.

Increasing the surface defect densities leads to an increase of the valence and conduction band energies within the n-InP substrate and to a decrease in the InP:Zn layer, so that the overall potential drop across the junctions is significantly reduced, from 1.42 V in Figure 6a to 0.15 V in Figure 6d. Specifically, to an increase of energy corresponds a decrease of surface potential, which reflects the upward band bending induced by the presence of surface defects. Conversely, a decrease of energy corresponds to an increase of surface potential, which reflects the downward band bending induced by the presence of surface defects.

We conclude that the presence of surface defects can explain the overall experimental $V_{CPD}$ variation along the structure that is less pronounced than in the simulated ideal case of a defect-free surface, as described in the Results section ("KPFM cross-sectional investigation under dark conditions"). This conclusion on the overall mitigation of the $V_{CPD}$ variation is not changed if we choose other surface defect density distributions (not constant vs energy) that produce different charge neutrality levels in the energy gap (which is not presented here for brevity).

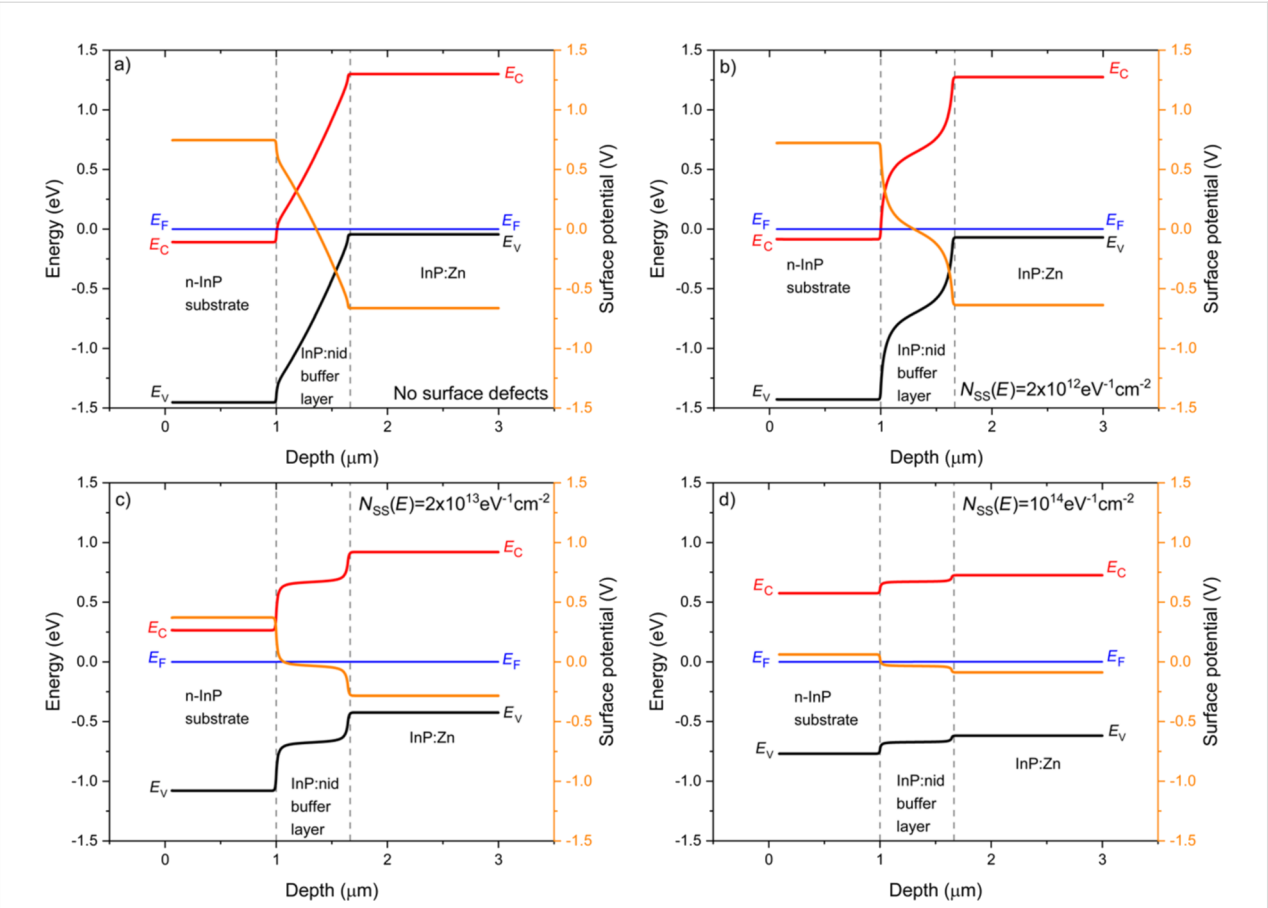


**Figure 6:** Cross-sectional profile at equilibrium of the surface band energies (black: valence band maximum, $E_V$, and red: conduction band minimum, $E_C$) along a simulated n-InP/InP:nid/InP:Zn structure considering surface defects densities made of the sum of constant and identical acceptor-like and donor-like defect distributions (in $eV^{-1}{\cdot}cm^{-2}$): (a) 0, (b) $2 \times 10^{12}$, (c) $2 \times 10^{13}$, and (d) $1 \times 10^{14}$. The energy reference is taken at the constant Fermi level, $E_F$ (blue horizontal line). The profile of the surface potential is also shown in orange (right *y* axis of the graphs).

However, large surface defect densities not only mitigate the overall change in $V_{CPD}$, but they are also responsible for strong changes in the shape of the surface potential. For instance, in Figure 6d the surface potential appears flat along the simulated structure with the exception of very narrow transition regions at the two layer interfaces. In other words, large surface defect densities also decrease the effective screening lengths compared to the ones calculated exclusively from the nominal doping densities, due to the extra charges directly provided by the surface states. The essentially constant flat profile in the InP:nid buffer layer strongly departs from the progressively decreasing profile observed experimentally in Figure 2c. In order to provide an explanation for the observed experimental profile that is both mitigated and progressively decreased in this buffer layer, it is necessary to decrease the surface defect density in the buffer layer, while keeping a very large value in the external n-InP substrate and p-InP:Zn layer. Therefore, the n-InP substrate and the p-InP:Zn layer require a high value of $N_{SS} = 1 \times 10^{14}$ $eV^{-1}{\cdot}cm^{-2}$, whereas the InP:nid layer requires a lower value of $N_{SS} = 2 \times 10^{12}$ $eV^{-1}{\cdot}cm^{-2}$. Furthermore, in order to provide a more quantitative explanation of the experimental profile of Figure 2c, the GaInAsP:Zn transition and GaInAs:Zn contact layers have been included again in the simulated structure ($N_{SS} = 1 \times 10^{14}$ $eV^{-1}{\cdot}cm^{-2}$). The energy bands and surface potential profiles simulated with these parameters are shown in Figure 7.

The surface potential shown in Figure 7 is in good agreement with the experimental profile of Figure 2c. In particular, the potential drop from the n-InP substrate to the InP:Zn layer is comparable to the 0.18 V obtained experimentally. Additionally, the shape of the surface potential in the InP:nid layer shows a progressive change extending all over the InP:nid buffer layer. Finally, the GaInAsP:Zn transition and GaInAs:Zn contact layers are again consistent with the higher value of $N_{SS} = 1 \times 10^{14}$ $eV^{-1}{\cdot}cm^{-2}$. In particular, the potential difference between the InP:Zn and the GaInAs:Zn contact layers is also attenuated with respect to the ideal case shown in Figure 3b as

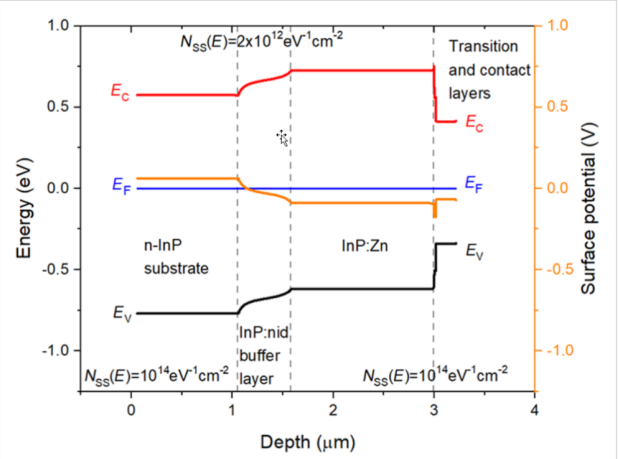


**Figure 7:** Cross-sectional profile at equilibrium of the surface band energies (black: valence band maximum, $E_V$, and red: conduction band minimum, $E_C$) along a simulated n-InP/InP:nid/InP:Zn/GaInAsP:Zn/GaInAs:Zn structure considering different surface defect densities in the various layers. For the n-InP substrate and the InP:Zn, GaInAsP:Zn, and GaInAs:Zn layers a total surface defect density (made of the sum of constant and identical acceptor-like and donor-like defect distributions) of 1 × $10^{14}$ $eV^{-1}·cm^{-2}$ was considered, whereas for the InP:nid layer a total surface defect density of 2 × $10^{12}$ $eV^{-1}·cm^{-2}$ was introduced. The energy reference is taken at the constant Fermi level, $E_F$ (blue line). The profile of the surface potential is also shown in orange (right *y* axis).

in the experimental $V_{CPD}$ profile of Figure 2c. Overall, this approach demonstrates that the surface defect density variations provide good agreement with the experimental surface potential profile of Figure 2c.

In conclusion, a quantitative description of the accurate surface defects distributions that characterize the surface of semiconductors materials is a complex task as it is not always certain that surface defects are homogeneously distributed across the entire cross section. This is particularly true in our case since the several layers present different physical properties because of varying doping types and concentrations [33].

In order to overcome these challenges related to the operating conditions and to the cleaving process presented in this paragraph, KPFM measurements can be performed in ultrahigh vacuum (UHV) at an optimal surface–tip distance of the order of a few nanometres [34] with particular attention to the sample preparation either in the deoxidation and cleaving process.

## Effect of the illumination on the $V_{CPD}$

In the Results section ("KPFM cross-sectional investigation under illumination"), we have pointed out the enhancement of contrast in the $V_{CPD}$ image under white-light illumination of the sample cross section. In particular, since the bulk lattice periodicity is interrupted at the surface of a cleaved semiconductor, surface reconstruction and formation of dangling bonds of surface atoms may occur, creating surface states within the energy bandgap. For instance, these surface states can pin the Fermi level and cause downward (upward) band bending from the bulk to the surface in a p-type (n-type) semiconductor in the case of the formation of a depletion (or inversion) space charge layer imposed by the charge neutrality condition [32,35].

By illuminating the sample, a SPV is generated by the drift and diffusion of photogenerated carriers towards the surface, which counteracts the defect-induced band bending energy variations [20]. As illustrated in Figure 8, in the case of downward surface band bending in an p-type semiconductor, photogenerated holes are repelled from the surface, while photogenerated electrons flow in the direction of the surface, balancing the positive charges corresponding to empty donor-type surface states. This results in a reduction of surface band bending and a decrease of surface potential, that is, a negative SPV.

Conversely, in the case of upward surface band bending in an n-type semiconductor, photogenerated electrons are repelled from the surface, while photogenerated holes flow towards the surface, balancing the negative charges corresponding to ionized occupied acceptor-type surface states, that is, a positive SPV.

As shown in Figure 5, an overall negative SPV was calculated along the structure, and a SPV of −95 mV was obtained in the InP:Zn region, which seems in good agreement with the expected trend in a p-type layer with surface defects. However, in case of pn junctions, the SPV can also include the contribution of the open-circuit voltage ($V_{OC}$) of the pn junction due to the splitting of the quasi-Fermi levels of electrons and holes and the related charge separation at the junction. In our case, because

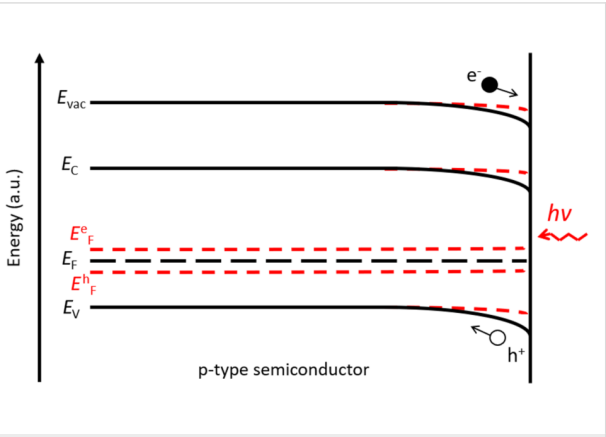


**Figure 8:** Representation of the energy band profile in a p-type semiconductor under dark conditions and under illumination depicted by black solid lines and red dashed lines, respectively. $E^e_F$ and $E^h_F$ represent possible profiles for the quasi-Fermi levels for electrons and holes, respectively.

the n-type side of the junction (substrate) is grounded, we expect a positive SPV contribution from the $V_{OC}$ of the pn junction at the surface of the p layer outside the space charge region of the pn junction. Therefore, the SPV measured in the InP:Zn region should be a trade-off between the negative contribution due to the flattening of surface defect-related band bending and the positive contribution of $V_{OC}$. As a consequence, the slightly negative SPV value of −95 mV measured in the InP:Zn region indicates a weaker contribution of the pn junction ($V_{OC}$) compared to the change in surface band bending related to surface defects.

In order to provide a quantitative analysis of this experimental evidence, we have calculated the conduction and valence band energy shift induced by the illumination simulating two simple structures. The first one is metal/n-InP/air, the n-type InP simulates our n-type substrate with a doping concentration of $5 \times 10^{18}$ cm$^{-3}$, and the second one is metal/InP:Zn/air, with InP:Zn having a p-type doping concentration of $1.5 \times 10^{18}$ cm$^{-3}$, similarly to the p-doped layer in our sample. In these simulations, the back metal/InP contact was assumed to be ohmic in both structures. We introduced unequal donor-like and acceptor-like surface defect densities. Specifically, the donor-like defect density was chosen equal to $1 \times 10^{13}$ eV$^{-1}$·cm$^{-2}$, and the acceptor-like was 20 times lower, $5 \times 10^{11}$ eV$^{-1}$·cm$^{-2}$, resulting in a charge neutrality level very close to the conduction band of InP.

Under these conditions, a SPV close to zero and a negative SPV are expected for the n-type InP substrate and for the InP:Zn layer, respectively. The simulated results gave a SPV close to zero (very slightly positive) and a negative SPV of −356 mV for the n-type InP substrate and for the InP:Zn layer, respectively.

In this specific case, a $V_{OC}$ of 261 mV would have been produced across the pn junction considering the experimental SPV result of −95 mV. This surprisingly low $V_{OC}$ value could be explained either by a poor material quality of the sample, in which a high density of bulk defects is responsible for reducing the carrier lifetime, or by the lack of a true ohmic contact between the sample holder and the n-type InP substrate during the KPFM measurement. In the second case, a potential barrier would be present at the metal contact/n-InP substrate interface, which could reduce the overall $V_{OC}$. Nevertheless, these considerations need further investigations and further support from modelling.

## Conclusion

In this contribution, it is shown that KPFM under ambient conditions is a valuable tool to investigate III–V multilayer stacks with high spatial resolution of down to 20 nm. The verified sensitivity of our KPFM setup to the narrower layers will be crucial for the study of the cross sections of operating solar device in future works.

The analysis of the surface potential profile identified the presence of space charge regions and, thus, the formation of several junctions along the stack. The complexity of the analysed structure combined with the ambient operating conditions caused challenges in the identification of the real position of the junctions in the $V_{CPD}$ image.

KPFM measurements are significantly affected by surface defects and other surface inhomogeneities. In particular, numerical modelling and analysis indicated that surface defects are responsible for a significant departure of the magnitude of the surface potential from the value in the bulk material. Also, we showed that the observed potential profile along the cleaved surface of the n-InP/InP:nid/p-InP:Zn heterojunction stack can be explained by large surface defect densities in the highly doped n-InP and p-InP:Zn layers, with a much lower defect density in the InP:nid buffer layer.

With further characterization and analysis, we have shown that white-light illumination reduces the surface band bending induced by surface defects, providing an enhancement of the contrast in the $V_{CPD}$ image. The analysis of the SPV variation along the structure cross section further suggests that either bulk defects or a non-ohmic contact between the metallic sample holder and the n-type InP substrate may exist. For future work, it will be necessary to assure a good ohmic contact between the sample holder and the sample and to carry out complementary characterization of the optoelectronic properties of the layers to refine the analysis of the results.

## ORCID® iDs

Mattia da Lisca - https://orcid.org/0000-0002-1549-319X
Nicolas Vaissiere - https://orcid.org/0000-0003-3568-1670
Jean-Paul Kleider - https://orcid.org/0000-0003-4388-6326

## References

1. Green, M. A.; Dunlop, E. D.; Hohl-Ebinger, J.; Yoshita, M.; Kopidakis, N.; Bothe, K.; Hinken, D.; Rauer, M.; Hao, X. *Prog. Photovoltaics* **2022,** *30,* 687–701. doi:10.1002/pip.3595
2. Narchi, P.; Alvarez, J.; Chrétien, P.; Picardi, G.; Cariou, R.; Foldyna, M.; Prod'homme, P.; Kleider, J.-P.; i Cabarrocas, P. R. *Nanoscale Res. Lett.* **2016,** *11,* 55. doi:10.1186/s11671-016-1268-1
3. Bian, K.; Gerber, C.; Heinrich, A. J.; Müller, D. J.; Scheuring, S.; Jiang, Y. *Nat. Rev. Methods Primers* **2021,** *1,* 36. doi:10.1038/s43586-021-00033-2
4. Melitz, W.; Shen, J.; Kummel, A. C.; Lee, S. *Surf. Sci. Rep.* **2011,** *66,* 1–27. doi:10.1016/j.surfrep.2010.10.001

5. Takihara, M.; Igarashi, T.; Ujihara, T.; Takahashi, T. *Jpn. J. Appl. Phys., Part 1* **2007,** *46,* 5548. doi:10.1143/jjap.46.5548
6. Lanzoni, E. M.; Gallet, T.; Spindler, C.; Ramírez, O.; Boumenou, C. K.; Siebentritt, S.; Redinger, A. *Nano Energy* **2021,** *88,* 106270. doi:10.1016/j.nanoen.2021.106270
7. Kang, Z.; Si, H.; Shi, M.; Xu, C.; Fan, W.; Ma, S.; Kausar, A.; Liao, Q.; Zhang, Z.; Zhang, Y. *Sci. China Mater.* **2019,** *62,* 776–789. doi:10.1007/s40843-018-9395-y
8. Weber, S. A. L.; Hermes, I. M.; Turren-Cruz, S.-H.; Gort, C.; Bergmann, V. W.; Gilson, L.; Hagfeldt, A.; Graetzel, M.; Tress, W.; Berger, R. *Energy Environ. Sci.* **2018,** *11,* 2404–2413. doi:10.1039/c8ee01447g
9. Tseberlidis, G.; Trifiletti, V.; Vitiello, E.; Husien, A. H.; Frioni, L.; Da Lisca, M.; Alvarez, J.; Acciarri, M.; Binetti, S. O. *ACS Omega* **2022,** *7,* 23445–23456. doi:10.1021/acsomega.2c01786
10. Li, J.; Aierken, A.; Liu, Y.; Zhuang, Y.; Yang, X.; Mo, J. H.; Fan, R. K.; Chen, Q. Y.; Zhang, S. Y.; Huang, Y. M.; Zhang, Q. *Front. Phys.* **2021,** *8,* 631925. doi:10.3389/fphy.2020.631925
11. Soresi, S.; da Lisca, M.; Besancon, C.; Vaissière, N.; Larrue, A.; Calò, C.; Álvarez, J. C.; Longeaud, C.; Largeau, L.; Garcia Linares, P.; Tournié, E.; Kleider, J.-P.; Decobert, J. *EPJ Photovoltaics* **2023,** *14,* 1. doi:10.1051/epjpv/2022027
12. da Lisca, M.; Connolly, J. P.; Alvarez, J.; Mekhazni, K.; Vaissiere, N.; Decobert, J.; Kleider, J.-P. *EPJ Photovoltaics* **2022,** *13,* 19. doi:10.1051/epjpv/2022017
13. Marchat, C.; Connolly, J. P.; Kleider, J.-P.; Alvarez, J.; Koduvelikulathu, L. J.; Puel, J. B. *EPJ Photovoltaics* **2019,** *10,* 3. doi:10.1051/epjpv/2019002
14. Glatzel, T.; Sadewasser, S.; Shikler, R.; Rosenwaks, Y.; Lux-Steiner, M. C. *Mater. Sci. Eng., B* **2003,** *102,* 138–142. doi:10.1016/s0921-5107(03)00020-5
15. Glatzel, T.; Lux-Steiner, M. C.; Strassburg, E.; Boag, A.; Rosenwaks, Y. Principles of Kelvin Probe Force Microscopy. In *Scanning Probe Microscopy;* Kalinin, S.; Gruverman, A., Eds.; Springer, 2007; pp 113–131. doi:10.1007/978-0-387-28668-6_5
16. Axt, A.; Hermes, I. M.; Bergmann, V. W.; Tausendpfund, N.; Weber, S. A. L. *Beilstein J. Nanotechnol.* **2018,** *9,* 1809–1819. doi:10.3762/bjnano.9.172
17. Ziegler, D.; Stemmer, A. *Nanotechnology* **2011,** *22,* 075501. doi:10.1088/0957-4484/22/7/075501
18. Narchi, P. Investigation of Crystalline Silicon Solar Cells at the Nano-Scale Using Scanning Probe Microscopy Techniques. Ph.D. Thesis, Université Paris-Saclay, Paris, France, 2016.
19. Fernández Garrillo, P. A.; Grévin, B.; Chevalier, N.; Borowik, Ł. *Rev. Sci. Instrum.* **2018,** *89,* 043702. doi:10.1063/1.5007619
20. Kronik, L.; Shapira, Y. *Surf. Sci. Rep.* **1999,** *37,* 1–206. doi:10.1016/s0167-5729(99)00002-3
21. SILVACO® ATLAS™ User's Manual, 2016.
22. Huang, Y.; Gheno, A.; Rolland, A.; Pedesseau, L.; Vedraine, S.; Durand, O.; Bouclé, J.; Connolly, J. P.; Etgar, L.; Even, J. *Opt. Quantum Electron.* **2018,** *50,* 41. doi:10.1007/s11082-017-1305-z
23. Rosenwaks, Y.; Shikler, R.; Glatzel, T.; Sadewasser, S. *Phys. Rev. B* **2004,** *70,* 085320. doi:10.1103/physrevb.70.085320
24. Tersoff, J.; Harrison, W. A. *Phys. Rev. Lett.* **1987,** *58,* 2367–2370. doi:10.1103/physrevlett.58.2367
25. Gysin, U.; Meyer, E.; Glatzel, T.; Günzburger, G.; Rossmann, H. R.; Jung, T. A.; Reshanov, S.; Schöner, A.; Bartolf, H. *Microelectron. Eng.* **2016,** *160,* 18–21. doi:10.1016/j.mee.2016.02.056
26. Li, G.; Mao, B.; Lan, F.; Liu, L. *Rev. Sci. Instrum.* **2012,** *83,* 113701. doi:10.1063/1.4761922
27. Baier, R.; Leendertz, C.; Lux-Steiner, M. C.; Sadewasser, S. *Phys. Rev. B* **2012,** *85,* 165436. doi:10.1103/physrevb.85.165436
28. Baumgart, C.; Helm, M.; Schmidt, H. *Phys. Rev. B* **2009,** *80,* 085305. doi:10.1103/physrevb.80.085305
29. Shohet, J. L. Plasma Science and Engineering. In *Encyclopedia of Physical Science and Technology,* 3rd ed.; Meyers, R. A., Ed.; Academic Press, 2003; pp 401–423. doi:10.1016/b0-12-227410-5/00584-6
30. Schubert, E. F.; Pinzone, C. J.; Geva, M. *Appl. Phys. Lett.* **1995,** *67,* 700–702. doi:10.1063/1.115279
31. Levinshtein, M. E.; Rumyantsev, S. L. Silicon (Si). In *Handbook Series on Semiconductor Parameters;* Levinshtein, M.; Rumyantsev, S.; Shur, M., Eds.; World Scientific, 1996; Vol. 1, pp 1–32. doi:10.1142/9789812832078_0001
32. Sun, X.; Wang, X.; Wang, P.; Sheng, B.; Li, M.; Su, J.; Zhang, J.; Liu, F.; Rong, X.; Xu, F.; Yang, X.; Qin, Z.; Ge, W.; Shen, B. *Opt. Mater. Express* **2017,** *7,* 904–912. doi:10.1364/ome.7.000904
33. Dadras, J.; Park, J. H.; Ratsch, C. *Phys. Rev. B* **2019,** *99,* 245406. doi:10.1103/physrevb.99.245406
34. Sadewasser, S.; Glatzel, T.; Shikler, R.; Rosenwaks, Y.; Lux-Steiner, M. C. *Appl. Surf. Sci.* **2003,** *210,* 32–36. doi:10.1016/s0169-4332(02)01475-7
35. Lüth, H. *Solid Surfaces, Interfaces and Thin Films;* Springer, 2010. doi:10.1007/978-3-642-13592-7


## License and Terms

BEILSTEIN JOURNAL OF NANOTECHNOLOGY

# Spatial mapping of photovoltage and light-induced displacement of on-chip coupled piezo/photodiodes by Kelvin probe force microscopy under modulated illumination

Zeinab Eftekhari*[1], Nasim Rezaei[1], Hidde Stokkel[1], Jian-Yao Zheng[1], Andrea Cerreta[2], Ilka Hermes[2], Minh Nguyen[1], Guus Rijnders[1] and Rebecca Saive[1]

Full Research Paper

Open Access

Address:
[1]Inorganic Materials Science, MESA+, University of Twente, Enschede, 7522NB, the Netherlands and [2]Park Systems Europe GmbH, 68199 Mannheim, Germany

Email:
Zeinab Eftekhari* - z.eftekhari@utwente.nl

* Corresponding author

Keywords:
Kelvin probe force microscopy (KPFM); light-driven micro/nano systems; piezoelectric membrane; surface photovoltage (SPV); time-dependent AFM

*Beilstein J. Nanotechnol.* **2023,** *14,* 1059–1067.
https://doi.org/10.3762/bjnano.14.87

Received: 21 February 2023
Accepted: 16 October 2023
Published: 06 November 2023

This article is part of the thematic issue "Advanced atomic force microscopy techniques V".

Guest Editor: M. Reichling



## Abstract

In this work, a silicon photodiode integrated with a piezoelectric membrane is studied by Kelvin probe force microscopy (KPFM) under modulated illumination. Time-dependent KPFM enables simultaneous quantification of the surface photovoltage generated by the photodiode as well as the resulting mechanical oscillation of the piezoelectric membrane with vertical atomic resolution in real-time. This technique offers the opportunity to measure concurrently the optoelectronic and mechanical response of the device at the nanoscale. Furthermore, time-dependent atomic force microscopy (AFM) was employed to spatially map voltage-induced oscillation of various sizes of piezoelectric membranes without the photodiode to investigate their position- and size-dependent displacement.

## Introduction

Light has been recognized as a versatile external energy source to actuate micro/nanorobots with outstanding merits of wireless, remote, and precise controllability [1-4]. Light-driven micro/nanorobots convert light into mechanical motion and are able to perform precise motion with high resolution. This offers promising possibilities for biomedical, environmental, and micro/nanoengineering applications [5,6]. Various types of design and actuation mechanisms have been developed in recent years [7,8]. A primary requirement to unlock the better performance of these micro/nano devices is to scrutinize their structure and the interaction between their different components. This can be done by high-resolution characterization techniques that simultaneously probe dynamic properties of different parts of the device. This enables the decoupling of the roles

of each function of the components on the overall motion behavior.

A variety of characterization techniques, such as white light interferometry, laser Doppler vibrometry (LDV), and double-beam laser interferometry (DBLI) have been used to determine the displacement of piezoelectric membranes [9,10]. However, the working principle of these techniques is based on optical interferometry mapping which can be challenging for light-sensitive devices. Furthermore, it can be advantageous to employ a method that also allows for mechanical contact and manipulation. Atomic force microscopy (AFM) [11-14] is a powerful and versatile technique to study fundamental and functional characteristics of materials and devices at the nanoscale, with application in physics, materials science, engineering, and biology. It can operate in either static (contact mode) or dynamic (tapping and noncontact mode) modes with atomic vertical resolution. In several studies, AFM has been used to determine photo-induced height/topography variation in organic–inorganic lead halide perovskites [15], nanosheets [16], and photosensitive polymers [17].

Kelvin probe force microscopy (KPFM), an electrostatic variant of AFM, can be used to measure contact potential difference (CPD) between the tip and the sample [18-20]. In particular, time-dependent KPFM [21-23] allows us to determine temporal changes of CPD and understand the dynamic behavior of functional devices at the nanoscale. Kelvin probe force microscopy in combination with illumination has been used to investigate photo-generated charge carriers of photovoltaic materials and devices. This is done by determining the CPD shift under illumination known as surface photovoltage (SPV) by calculating $SPV = CPD_{light} - CPD_{dark}$, whereas $CPD_{dark}$ is the CPD in the dark and $CPD_{light}$ is the CPD under illumination in that same location [24-27]. In some studies, KPFM has been employed for simultaneous study of structural and optoelectronic properties of materials and functional devices [28-30]. For example, the topography and SPV of illuminated photostrictive materials have simultaneously been examined through KPFM to determine the generated photovoltage and the following lattice change of the material [31].

Here, we present a KPFM study involving modulated illumination to investigate local height changes (vertical displacement) and the correlative SPV of the light-driven piezo/photodiode device over time. Employing modulated illumination enabled us to quantify precisely the device displacement due to improved signal-to-noise ratio, which could not be achieved by continuous illumination. The configuration of the hybrid piezo/photodiode device has previously been developed and reported by our group [32].

In further investigations, we used time-dependent AFM to determine the voltage-induced displacement of solely piezoelectric membranes without the photodiode. This experiment was performed to probe the local electromechanical properties of the piezoelectric membrane as a reference sample, which can reveal its contribution to the piezo/photodiode device.

# Methodology

## Sample fabrication

The device type-I employed in this study is a piezo/photodiode device, fabricated following a previously reported procedure [32], where the piezoelectric material, lead zirconate titanate (PZT), was integrated onto a silicon photodiode. The PZT layer was sandwiched between two lanthanum nickelate (LNO) electrodes and ultimately the backside of the silicon substate was etched to enhance the motion of the membrane. More detailed information on the fabrication and cross-sectional scanning electron microscopy images can be found in [32]. The top view of the piezo/photodiode device is given in Figure 1a, where the inset represents the cross section of the device stack. Owing to the integration of PZT with silicon processing and operation at low voltages, this device can be actuated by either modulated illumination or electrical bias.

The device type-II used in this study had the same configuration as the device type-I only without the photodiode. A series of devices with different sizes were fabricated in which the active device dimensions were (7.6 × 7.6), (5.2 × 5.2), (2.8 × 2.8) and (1.4 × 1.2) $mm^2$ labeled as A, B, C, and D, respectively. In the process of fabrication, a 100 nm thick layer of LNO as the bottom electrode was first deposited, using pulsed laser deposition (PLD) technique, on a single crystal silicon wafer. Then, an 850 nm lead barium zirconia titanate (PBZT) and a 150 nm LNO as the top electrode were deposited. The wafer was patterned by a standard photolithographic process, starting with the application and patterning of the photoresist mask for defining the device areas. Subsequently, the excess PBZT and LNO were removed by a wet etching process with a diluted $BHF:HNO_3:H_2O$ solution and a HCl solution, respectively. To avoid shunting of the device, a $SiO_2$ insulating layer was deposited. Patterned aluminum (Al) contacts which connect to the top and bottom electrodes of the PBZT were fabricated through a lift-off process. The fabrication was finalized by etching circular holes from the backside of the wafer to obtain thin membranes. The sizes of these holes were defined by applying and patterning a photoresist on the backside of the wafer, which was then anisotropically etched by deep reactive ion etching (DRIE) using $SF_6$, $O_2$, and $C_4F_8$ gases. This final step was carried out to minimize the clamping effect of the actuator on the silicon substrate, thus enhancing the movement of the membrane.

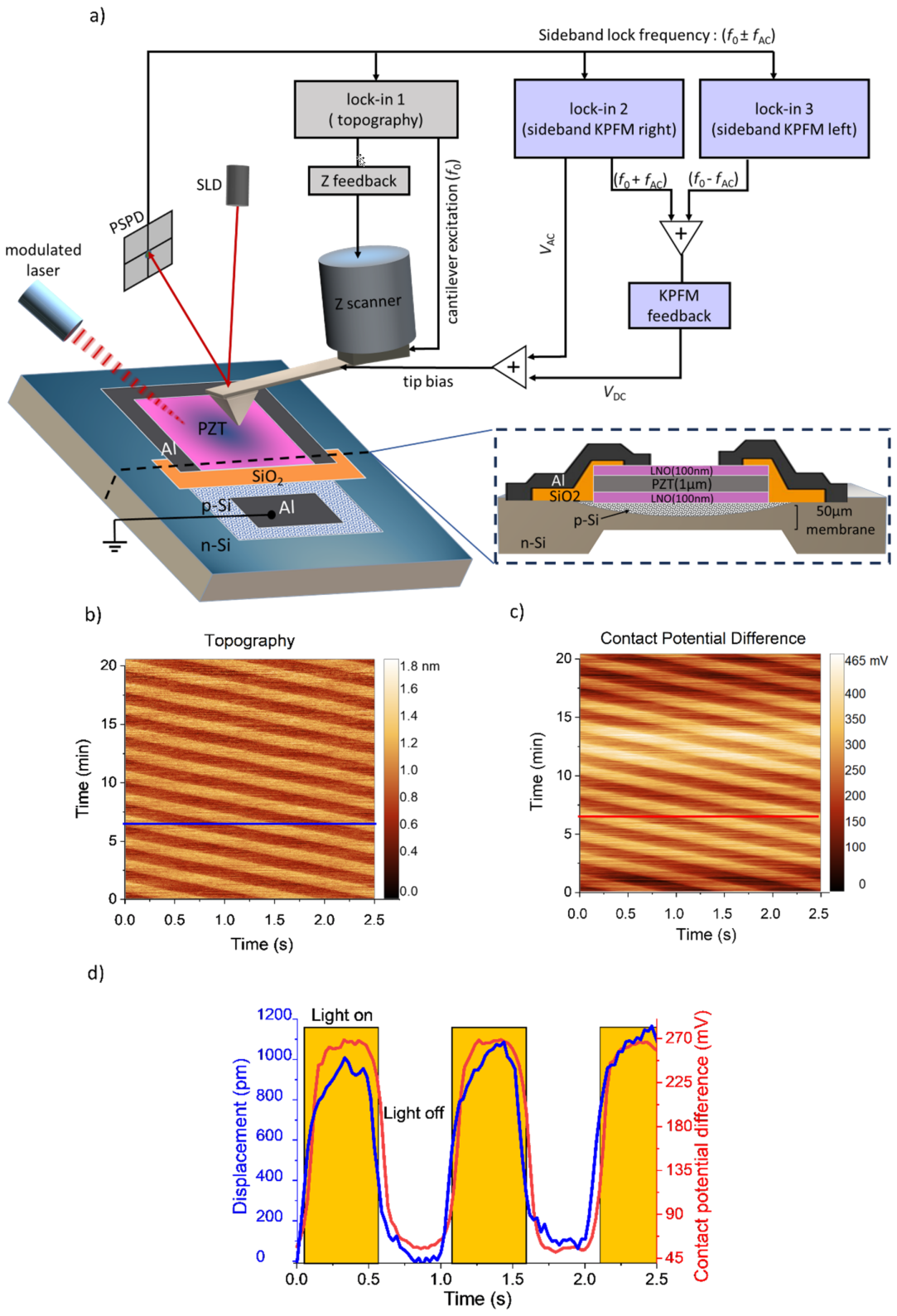


**Figure 1:** (a) Schematic illustrating the connection diagram of sideband KPFM measuring the piezo/photodiode device under modulated illumination. The top view of the device is shown where the inset represents the cross section of the device stack. (b) Time-dependent topography scan showing height variation under alternating illumination, and (c) corresponding time-dependent CPD under alternating illumination. (d) Temporal behavior of displacement and CPD obtained from averaging multiple linear profiles selected from b and c.

## Kelvin probe force microscopy under modulated illumination

In this experiment, we used KPFM with modulated illumination to study device type-I, namely the piezo/photodiode device. The device was illuminated from the top surface using a laser diode at a wavelength of 628 nm. The light source was installed inside the AFM chamber, and the light beam was aligned towards the active area of the device. The illumination source was modulated by a square waveform voltage at an adjustable frequency, operated through a function generator (GWInstek, SFG-1013). Here, the selected modulation frequency was 1 Hz. It should be noted that the active area of the device stack of piezoelectric layer (PZT) and LNO electrodes is transparent and thus the incoming light from the top reached the Si p–n junction and generated electron–hole pairs, building a potential difference across the junction. The generated photovoltage was applied to the piezoelectric capacitor through the photolithographically defined contacts and induced mechanical displacement in the piezoelectric stack. Kelvin probe force microscopy was employed to measure the photoinduced voltage simultaneously with the displacement at the surface of the top LNO electrode as the bottom electrode was grounded. These measurements were performed with a Park Systems NX10 AFM microscope equipped with Pt/Ir-coated silicon probes (ARROW-EFM from nanoworld). Topographical measurements were performed in amplitude-modulated (AM) AFM. The KPFM measurements were carried out in single-pass sideband mode [33], which is a technique that detects electrostatic force gradients. The connection diagram of the sideband KPFM shown in Figure 1a illustrates multiple lock-in amplifiers employed to excite the cantilever both mechanically and electrically at the same time, and to retrieve simultaneously the amplitude and phase of the movement of the cantilever at different frequencies. The cantilever is excited at its mechanical resonance frequency ($f_0$) executed by the lock-in amplifier 1 and the generated topography signal is controlled by the Z feedback. A sinusoidal AC bias ($V_{AC}$) with drive of 1 V and frequency ($f_{AC}$) of 5 kHz is applied to the tip through lock-in 2, generating a signal with a frequency of $f_0 \pm f_{AC}$ near the cantilever resonance. Modulating the tip with $V_{AC}$ while the cantilever is oscillating near its resonance frequency leads to frequency mixing and intermodulation of the two frequencies ($f_0 \pm f_{AC}$) [34]. The lock-in amplifiers 2 and 3 are fed with the vertical deflection signal of the cantilever to measure the sideband signals at $f_0 + f_{AC}$ and $f_0 - f_{AC}$. Then, their average is used for the KPFM feedback to adjust the DC bias. If $f_{AC}$ is chosen to be small enough, such that the sideband peaks are close to $f_0$, the amplitude of these peaks will be enhanced by the mechanical resonance of the cantilever leading to a better signal-to-noise ratio. The feedback applies a DC bias ($V_{DC}$) matching the potential difference between the tip and the sample, which compensates for the electrostatic force. Therefore, the sidebands disappear. The value of $V_{DC}$ corresponds to the contact potential difference.

Measurements of modulated topography and CPD were conducted at the center of the membrane, where the AFM tip was positioned at a single point (zero scan size) to avoid any effect of the topography on the results. In conventional AFM images, each pixel represents the value of a specific signal relative to its position within a defined surface region. Herein, the acquired topography and CPD images shown in Figure 1b and Figure 1c were represented in the time domain. Therefore, the horizontal scale of the images indicates the time at which a given pixel has been acquired in one line, while the vertical scale indicates the temporal evolution of this timeline throughout the measurement process. These scans indicate the reproducibility of acquired displacement and photovoltage under modulated illumination at a single point. To analyze them, we extracted 10 line profiles depicted in blue and red for topography and CPD as a function of time, respectively. The average value of the peak-to-peak amplitude was calculated over the collectively selected profiles. The extracted profiles in Figure 1d were fit using a sinusoidal function in which their peak-to-peak amplitude represents the displacement and the photovoltage. The CPD profile in Figure 1d shows a 50 mV baseline in the dark, which can be attributed to the generation of charge carriers due to the stray light from the super luminescent diode (SLD) of the AFM. The wavelength of the SLD beam employed in the measurements is 830 nm, which can be absorbed by the Si photodiode and lead to a nonzero baseline. However, it does not affect the photovoltage as the peak-to-peak potential was calculated. Comparative measurements over a micrometric area of the sample were performed (see Supporting Information File 1). The CPD of a 1 $\mu m^2$ area at the center of the sample was measured in the dark, under continuous and modulated illumination, respectively. The obtained results indicate that the difference between CPD in the dark and under continuous illumination is similar to that under alternating illumination. It is important to note that the acquired photovoltage for the micrometric measurement is comparable to the locally measured photovoltage. However, we were not able to quantify precisely the displacement of the membrane by conventional imaging since a temperature-induced drift occurs under illumination. Therefore, we modified the method in the point scan mode.

The basic principle of our method lies in the acquisition of light-modulated CPD and vertical displacement at a single point on a two-dimensional grid to unveil the 3D motion of the membrane and the corresponding SPV map. To facilitate light alignment on the sample during measurements, we divided the active area of the device ($5.6 \times 5.6$ $mm^2$) into four quadrants. Initially,

one of the quadrants was subdivided into a grid consisting of 25 points with steps of 0.7 mm in both $x$ and $y$ directions, where the displacement and SPV of each point were recorded one after another. To ensure that the cantilever or the AFM head does not block the light from reaching the sample, the sample was manually rotated, and the measurement was performed on the second quarter of the device using the same procedure. As all four quadrants of the sample surface were mapped, the points located at the quadrant boundaries were measured twice during each rotation. Therefore, we took the average of the readout signals for each quadrant boundary. Lastly, all the acquired data for displacement and photovoltage of the four quadrants were stitched together and presented in color maps.

## Time-dependent AFM to measure voltage-driven properties

In this experiment, we studied type-II devices (which do not include the photodiode), and the piezoelectric membrane was excited by an external bias. Time-dependent AFM was employed to determine the voltage-induced displacement of the piezoelectric layer. The AFM measurements were carried out in tapping mode, where the tip was located at a single point of the membrane. The external bias with an amplitude of 2.5 V and frequency of 2 Hz in a square waveform provided by the function generator was applied to the top and bottom Al contacts of the piezoelectric device. The height change of a specific point at the center of the membrane was recorded over time for the utilized voltage and frequency. We selected 10 line profiles from the modulated topography image, took the average over the selected lines similarly to the previous case, and fitted these with a sinusoidal function. The peak-to-peak value of the averaged and fitted data represented the displacement of the membrane for a given point. The cantilever was lifted and moved to the next point and the same measurement was performed. By this approach, spatial mapping of the active area was conducted for four piezoelectric actuators of varying sizes, namely A, B, C, and D. Only one-quarter of the devices were mapped, considering their symmetry. The experiment focused on studying the size-dependent displacement of these devices.

## Simulations

We used COMSOL Multiphysics for the finite element method (FEM) simulations of our devices. Solid mechanics and electrostatics modules were coupled to facilitate the piezoelectricity calculations. As shown in Figure 2, the symmetry condition is used to reduce the computation cost of the simulations. Analogous to our AFM and KPFM experiments, the sample edges are fixed. Additionally, the effect of gravity on the displacement is taken into account. The voltage excitation signal is introduced to the LNO terminals as shown in the inset of Figure 2.

The material properties of PZT and LNO thin films were derived from the literature and are summarized in Table 1. The strain-charge form is employed for the piezoelectric material.

# Results and Discussion

The optoelectronic and mechanical responses of the piezo/photodiode device (device type-I) measured by the KPFM technique are presented in Figure 3. As expected, the maximum displacement is obtained at points positioned at the center of the

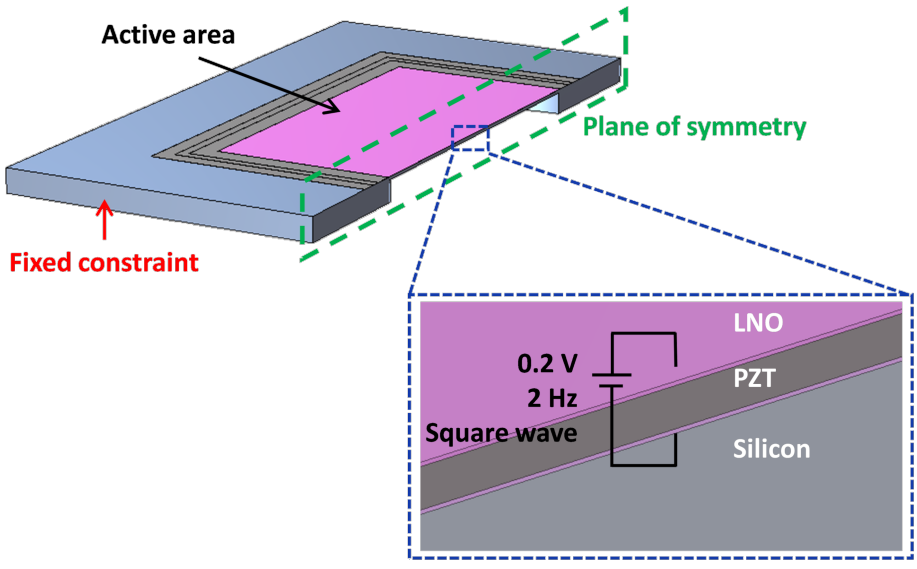


**Figure 2:** Unit cell of the piezo/photodiode device as simulated in COMSOL.

**Table 1:** Properties of PZT [35,36] and LNO films [37]. Compliance matrix elements (elastic compliance constants, $S_{ij}$) and coupling matrix elements (piezoelectric coefficients, $d_{ij}$) have the units of $\frac{1}{\mathrm{TPa}}$ and $\frac{\mathrm{pm}}{\mathrm{V}}$, respectively.

| Material | Relative permittivity | Poisson's ratio | Elastic compliance constants | | | | Piezoelectric coefficients | | |
|---|---|---|---|---|---|---|---|---|---|
| | | | $S_{11}$ | $S_{12}$ | $S_{13}$ | $S_{33}$ | $d_{15}$ | $d_{31}$ | $d_{33}$ |
| PZT | 600 | 0.32 | 13.8 | −4.07 | −5.8 | 20.7 | 494 | −93.5 | 223 |
| LNO | −∞ | 0.27 | | | | | | | |

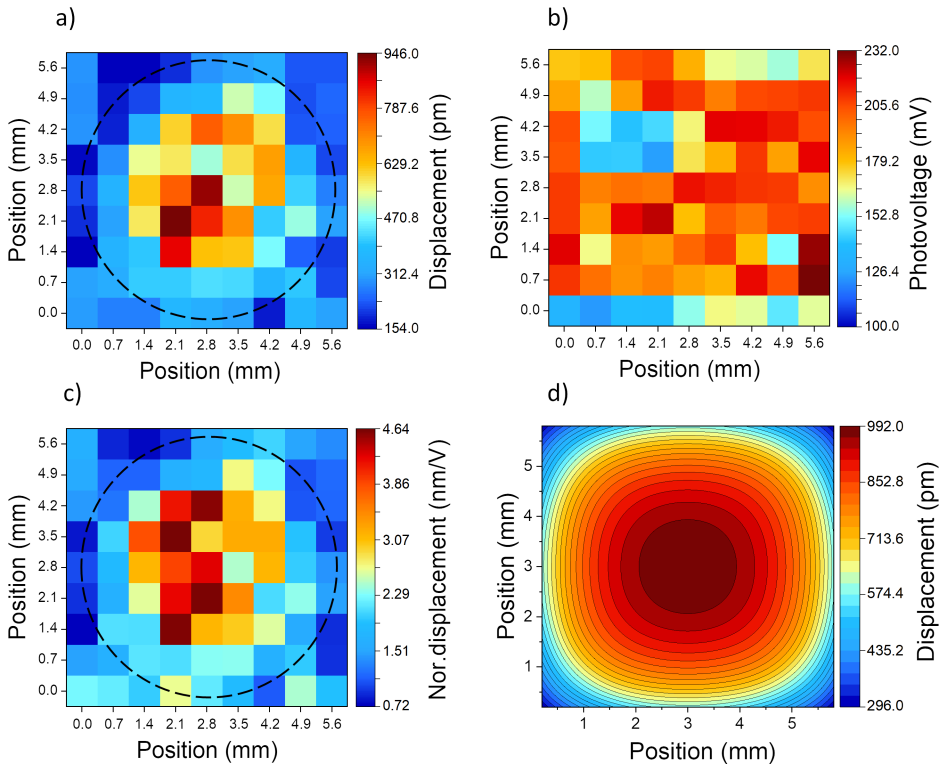


**Figure 3:** Device type-I corresponding color map of (a) light-induced displacement determined at each point of a predefined grid over the surface of the device. A total of 81 points on the surface active area of 5.6 × 5.6 mm$^2$ are mapped. The dashed black circle marks the hole etched on the back-side of the silicon substrate. (b) The surface photovoltage of each measured point. (c) Displacement normalized to the corresponding photovoltage at each point. (d) Simulation results of the same sample.

membrane with a maximum of 946 pm, while decreasing to a few picometers at the side edges. The decay of displacement from the center to the edge is expected from the clamping effect at the edges, where the Si substrate is thicker [38]. The measured CPD shift in Figure 3b indicates that the photovoltage stays nearly constant regardless of the scanned position, and is comparable with the open-circuit voltage ($V_{OC}$) of the photodiode (270 mV, measured by a multimeter). By inspecting the displacement and photovoltage color maps it is possible to confirm that the drum-like displacement of the device is due to the flexible center of the membrane and clamped edges, and it is not attributed to the variation of induced photovoltage. The simulation results of the same device (Figure 3d) confirm the shape and range of displacement mapping over the active area. It is instructive to note that ideally the measured photovoltage over the LNO contacts is equal to the $V_{OC}$ of the photodiode. However, as can be seen in Figure 3b, this value varies between 100 and 232 mV. This can be attributed to multiple factors, including i) the resistance of the contacts, ii) damages to various points on the top LNO layer from previous measurements or the etching process and hence its lower conductivity, and iii) other factors such as improper light alignment or SPV underestimation by KPFM.

Figure 3c presents the mechanical displacement of the membrane normalized to the photovoltage. These values were ob-

tained by dividing the displacement values for each point in Figure 3a by the corresponding photovoltage in Figure 3b. This analysis confirms that despite fluctuations in the photovoltage, the membrane deformation follows the trend that is expected from simulations. It demonstrates that the maximal displacement that occurred at the center is around 3 to 4.6 nm/V, showing notable performance of the piezo-photodiode device under low photovoltage.

The strength of our approach lies in its capability to decouple the contributions of different aspects of our hybrid system effectively, as the optoelectronic and mechanical properties are simultaneously determined. One of the shortcomings of the implemented KPFM method in our previous work [32] was its operation in dual-pass mode, in which topography measurements were done in the first pass and the CPD in the second pass. Such a measurement can give rise to a phase shift between these two signals.

Figure 4a–d exhibits the spatial mappings of one-quarter of the voltage-driven piezoelectric actuators (device type-II) with different dimensions from large to small sizes, respectively. The backside etching of the silicon substrate is marked by the dashed line. The measured displacement for each point is normalized to its corresponding applied voltage, shown in picometer per volt (pm/V). It should be noted that the upper limit of the color bars varies according to the maximal displacement value of each device. The maximal displacement is expected at the center of the device, which is the bottom-right corner of each color map. The expected bulging shape is observed for samples B and C shown in Figure 4b and c, respectively. The smallest sample (D) nonetheless shows a relatively uniform displacement, which can arise from the increased stiffness of the membrane as a result of its minuscule dimension (see Figure 4d). Based on the simulations [39], at an excitation voltage of 0.2 V, for active area values larger than ≃6 × 6 mm$^2$, the gravitational force dominates the piezoelectric force, causing the membrane to "cave in" in the middle part. This is consistent with the observations in Figure 4. It can also be related to the backside etching of the substrate with poor selectivity, which can form undercuts, causing thinner edges than the central part of the membrane and restricting the movement of the membrane on top.

From the simulations, we expected that the maximum displacement increases with the sample size. However, the experimental results are inconclusive since it can be seen that sample C shows larger displacement than samples A and B despite its

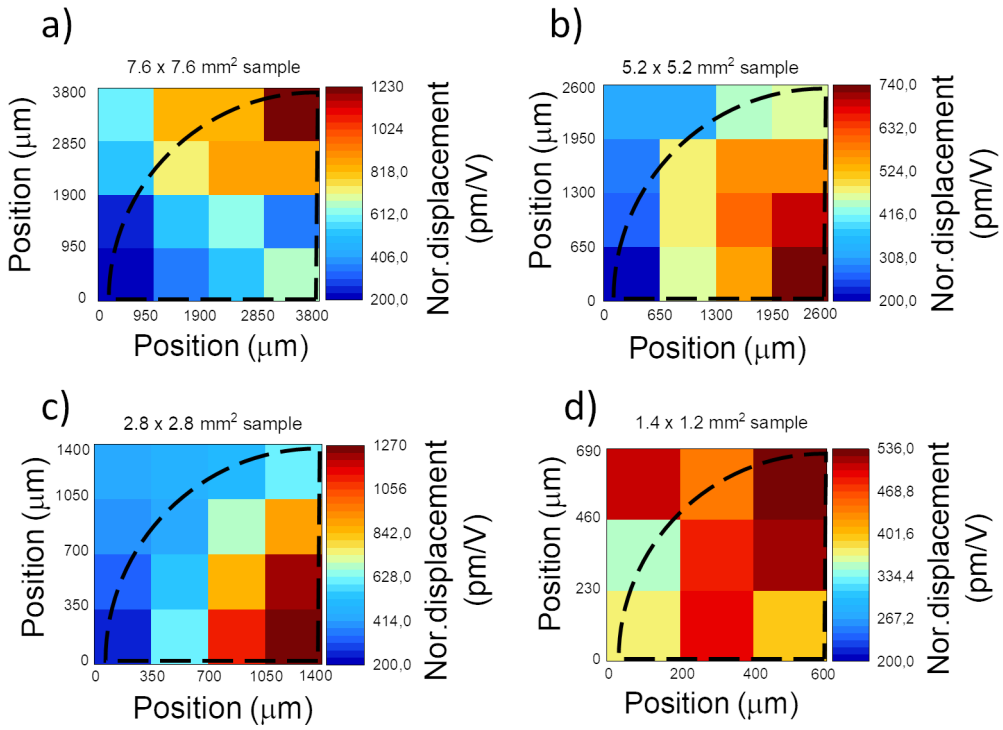


**Figure 4:** Color map of the quarters of the surface area of device type-II, (a) A with dimensions of (7.6 × 7.6) mm$^2$, (b) B with dimensions of (5.2 × 5.2) mm$^2$, (c) C with dimensions of (2.8 × 2.8) mm$^2$, and (d) D with dimensions of (1.4 × 1.2) mm$^2$, where voltage-induced displacement is measured by AFM. The displacement is normalized to the corresponding voltage applied to each point.

smaller size. This may be due to the nonuniform etching of the backside of the sample and thickness variations. While with the presented characterization technique, we cannot fully conclude the reason for the deviation from the expected behavior, the results stress the importance of employing advanced, time-dependent spatial mapping characterization techniques for the development of novel nano/micro-actuators.

## Conclusion

In this study, we demonstrated position-dependent, light-induced measurements of the displacement and photovoltage of a piezo/photodiode device. Kelvin probe force microscopy was employed to record topography and CPD concurrently which allows to distinguish optoelectronic and mechanical responses at the nanoscale. The measured displacements of the light-driven membrane are in good agreement with the simulation results. Moreover, time-dependent AFM was used to investigate position-dependent and size-dependent displacement of piezoelectric actuators driven by an electrical bias. Deviations from the expected membrane behavior stress the importance of advanced characterization methods for the design of novel nano/micro-actuators. The method presented here can offer remarkable opportunities to investigate the properties of devices driven with alternating light or bias voltage, properties of nanoscale mechanical systems, and combinations thereof. As one example, the time-dependent AFM technique in contact mode can be implemented to measure energy conversion efficiency by pressing the AFM tip with a defined counter force against the motion of the system. This allows us to calculate the work that the system is performing against the counter force and with knowledge of the input energy (e.g., absorbed light) the energy conversion efficiency can be determined.

## Supporting Information

### Supporting Information File 1

Additional figures.
[https://www.beilstein-journals.org/bjnano/content/supplementary/2190-4286-14-87-S1.pdf]

## Acknowledgements

The authors thank Kai Sotthewes from the University of Twente for his advice.

## Funding

This publication is part of the project Piezo-photomotion: light-driven nano piezo-propulsion and agitation with project number VI.Vidi.193.020 of the research programs Vidi and Aspasia, which is financed by the Dutch Research Council (NWO).

## ORCID® iDs

Zeinab Eftekhari - https://orcid.org/0000-0002-2669-5600
Nasim Rezaei - https://orcid.org/0000-0003-1244-3717
Hidde Stokkel - https://orcid.org/0000-0003-1515-9359
Jian-Yao Zheng - https://orcid.org/0000-0002-2731-4072
Andrea Cerreta - https://orcid.org/0000-0003-3694-7645
Rebecca Saive - https://orcid.org/0000-0001-7420-9155

## References

1. Zeng, H.; Wasylczyk, P.; Parmeggiani, C.; Martella, D.; Burresi, M.; Wiersma, D. S. *Adv. Mater. (Weinheim, Ger.)* **2015,** *27,* 3883–3887. doi:10.1002/adma.201501446
2. Wang, J.; Xiong, Z.; Zhan, X.; Dai, B.; Zheng, J.; Liu, J.; Tang, J. *Adv. Mater. (Weinheim, Ger.)* **2017,** *29,* 1701451. doi:10.1002/adma.201701451
3. Dai, B.; Wang, J.; Xiong, Z.; Zhan, X.; Dai, W.; Li, C.-C.; Feng, S.-P.; Tang, J. *Nat. Nanotechnol.* **2016,** *11,* 1087–1092. doi:10.1038/nnano.2016.187
4. Zeng, H.; Wasylczyk, P.; Wiersma, D. S.; Priimagi, A. *Adv. Mater. (Weinheim, Ger.)* **2018,** *30,* 1703554. doi:10.1002/adma.201703554
5. Bunea, A.-I.; Martella, D.; Nocentini, S.; Parmeggiani, C.; Taboryski, R.; Wiersma, D. S. *Adv. Intell. Syst.* **2021,** *3,* 2000256. doi:10.1002/aisy.202000256
6. Li, J.; Zhou, X.; Liu, Z.; Li, J.; Zhou, X.; Liu, Z. *Adv. Opt. Mater.* **2020,** *8,* 2000886. doi:10.1002/adom.202000886
7. Zhan, Z.; Wei, F.; Zheng, J.; Yang, W.; Luo, J.; Yao, L. *Nanotechnol. Rev.* **2018,** *7,* 555–581. doi:10.1515/ntrev-2018-0106
8. Chen, H.; Zhao, Q.; Du, X. *Micromachines* **2018,** *9,* 41. doi:10.3390/mi9020041
9. Nguyen, M. D.; Nazeer, H.; Karakaya, K.; Pham, S. V.; Steenwelle, R.; Dekkers, M.; Abelmann, L.; Blank, D. H. A.; Rijnders, G. *J. Micromech. Microeng.* **2010,** *20,* 085022. doi:10.1088/0960-1317/20/8/085022
10. Nguyen, M. D.; Vu, H. N.; Blank, D. H. A.; Rijnders, G. *Adv. Nat. Sci.: Nanosci. Nanotechnol.* **2011,** *2,* 015005. doi:10.1088/2043-6262/2/1/015005
11. Binnig, G.; Quate, C. F.; Gerber, C. *Phys. Rev. Lett.* **1986,** *56,* 930–933. doi:10.1103/physrevlett.56.930
12. García, R.; Pérez, R. *Surf. Sci. Rep.* **2002,** *47,* 197–301. doi:10.1016/s0167-5729(02)00077-8
13. Giessibl, F. J. *Rev. Mod. Phys.* **2003,** *75,* 949–983. doi:10.1103/revmodphys.75.949
14. Giessibl, F. J.; Quate, C. F. *Phys. Today* **2006,** *59* (12), 44–50. doi:10.1063/1.2435681
15. Zhou, Y.; You, L.; Wang, S.; Ku, Z.; Fan, H.; Schmidt, D.; Rusydi, A.; Chang, L.; Wang, L.; Ren, P.; Chen, L.; Yuan, G.; Chen, L.; Wang, J. *Nat. Commun.* **2016,** *7,* 11193. doi:10.1038/ncomms11193
16. Zhang, Z.; Remsing, R. C.; Chakraborty, H.; Gao, W.; Yuan, G.; Klein, M. L.; Ren, S. *Proc. Natl. Acad. Sci. U. S. A.* **2018,** *115,* 3776–3781. doi:10.1073/pnas.1800234115
17. Kopyshev, A.; Galvin, C. J.; Patil, R. R.; Genzer, J.; Lomadze, N.; Feldmann, D.; Zakrevski, J.; Santer, S. *ACS Appl. Mater. Interfaces* **2016,** *8,* 19175–19184. doi:10.1021/acsami.6b06881
18. Nonnenmacher, M.; O'Boyle, M. P.; Wickramasinghe, H. K. *Appl. Phys. Lett.* **1991,** *58,* 2921–2923. doi:10.1063/1.105227

19. Weaver, J. M. R.; Abraham, D. W. *J. Vac. Sci. Technol., B: Microelectron. Nanometer Struct.–Process., Meas., Phenom.* **1991,** *9,* 1559–1561. doi:10.1116/1.585423
20. Zerweck, U.; Loppacher, C.; Otto, T.; Grafström, S.; Eng, L. M. *Phys. Rev. B: Condens. Matter Mater. Phys.* **2005,** *71,* 125424. doi:10.1103/physrevb.71.125424
21. Mascaro, A.; Miyahara, Y.; Enright, T.; Dagdeviren, O. E.; Grütter, P. *Beilstein J. Nanotechnol.* **2019,** *10,* 617–633. doi:10.3762/bjnano.10.62
22. Grévin, B.; Bardagot, O.; Demadrille, R. *Beilstein J. Nanotechnol.* **2020,** *11,* 323–337. doi:10.3762/bjnano.11.24
23. Bergmann, V. W.; Guo, Y.; Tanaka, H.; Hermes, I. M.; Li, D.; Klasen, A.; Bretschneider, S. A.; Nakamura, E.; Berger, R.; Weber, S. A. L. *ACS Appl. Mater. Interfaces* **2016,** *8,* 19402–19409. doi:10.1021/acsami.6b04104
24. Weber, S. A. L.; Hermes, I. M.; Turren-Cruz, S.-H.; Gort, C.; Bergmann, V. W.; Gilson, L.; Hagfeldt, A.; Graetzel, M.; Tress, W.; Berger, R. *Energy Environ. Sci.* **2018,** *11,* 2404–2413. doi:10.1039/c8ee01447g
25. Miyazaki, M.; Sugawara, Y.; Li, Y. J. *Beilstein J. Nanotechnol.* **2022,** *13,* 712–720. doi:10.3762/bjnano.13.63
26. Saive, R.; Scherer, M.; Mueller, C.; Daume, D.; Schinke, J.; Kroeger, M.; Kowalsky, W. *Adv. Funct. Mater.* **2013,** *23,* 5854–5860. doi:10.1002/adfm.201301315
27. Garrett, J. L.; Tennyson, E. M.; Hu, M.; Huang, J.; Munday, J. N.; Leite, M. S. *Nano Lett.* **2017,** *17,* 2554–2560. doi:10.1021/acs.nanolett.7b00289
28. Yun, J. S.; Ho-Baillie, A.; Huang, S.; Woo, S. H.; Heo, Y.; Seidel, J.; Huang, F.; Cheng, Y.-B.; Green, M. A. *J. Phys. Chem. Lett.* **2015,** *6,* 875–880. doi:10.1021/acs.jpclett.5b00182
29. Jakob, D. S.; Wang, H.; Xu, X. G. *ACS Nano* **2020,** *14,* 4839–4848. doi:10.1021/acsnano.0c00767
30. Fuchs, F.; Caffy, F.; Demadrille, R.; Mélin, T.; Grévin, B. *ACS Nano* **2016,** *10,* 739–746. doi:10.1021/acsnano.5b05810
31. Palacio, M. L. B.; Bhushan, B. *Crit. Rev. Solid State Mater. Sci.* **2010,** *35,* 73–104. doi:10.1080/10408430903546691
32. Luiten, W. M.; van der Werf, V. M.; Raza, N.; Saive, R. *AIP Adv.* **2020,** *10,* 105121. doi:10.1063/5.0028481
33. Axt, A.; Hermes, I. M.; Bergmann, V. W.; Tausendpfund, N.; Weber, S. A. L. *Beilstein J. Nanotechnol.* **2018,** *9,* 1809–1819. doi:10.3762/bjnano.9.172
34. Borgani, R.; Forchheimer, D.; Bergqvist, J.; Thorén, P.-A.; Inganäs, O.; Haviland, D. B. *Appl. Phys. Lett.* **2014,** *105,* 143113. doi:10.1063/1.4897966
35. Serhatlioglu, M.; Ayas, S.; Biyikli, N.; Dana, A.; Solmaz, M. E. *Opt. Lett.* **2016,** *41,* 1724. doi:10.1364/ol.41.001724
36. Lian, L.; Sottos, N. R. *J. Appl. Phys.* **2000,** *87,* 3941–3949. doi:10.1063/1.372439
37. Masys, Š.; Jonauskas, V. *Comput. Mater. Sci.* **2015,** *108,* 153–159. doi:10.1016/j.commatsci.2015.06.034
38. Kim, D. M.; Eom, C. B.; Nagarajan, V.; Ouyang, J.; Ramesh, R.; Vaithyanathan, V.; Schlom, D. G. *Appl. Phys. Lett.* **2006,** *88,* 142904. doi:10.1063/1.2185614
39. Rezaei, N.; Eftekhari, Z.; Zheng, J.-Y.; Saive, R. *Sens. Actuators, A* **2023,** *363,* 114690. doi:10.1016/j.sna.2023.114690

## License and Terms

BEILSTEIN JOURNAL OF NANOTECHNOLOGY

# Dual-heterodyne Kelvin probe force microscopy

Benjamin Grévin*, Fatima Husainy, Dmitry Aldakov and Cyril Aumaître

Full Research Paper

Open Access

Address:
Univ. Grenoble Alpes, CNRS, CEA, IRIG-SyMMES, 38000 Grenoble, France

Email:
Benjamin Grévin* - benjamin.grevin@cnrs.fr

* Corresponding author

Keywords:
heterodyne; intermodulation; KPFM; nc-AFM; surface photovoltage; time-resolved measurements

*Beilstein J. Nanotechnol.* **2023,** *14,* 1068–1084.
https://doi.org/10.3762/bjnano.14.88

Received: 03 July 2023
Accepted: 17 October 2023
Published: 07 November 2023

This article is part of the thematic issue "Advanced atomic force microscopy techniques V".

Guest Editor: P. Rahe



## Abstract

We present a new open-loop implementation of Kelvin probe force microscopy (KPFM) that provides access to the Fourier spectrum of the time-periodic surface electrostatic potential generated under optical (or electrical) pumping with an atomic force microscope. The modulus and phase coefficients are probed by exploiting a double heterodyne frequency mixing effect between the mechanical oscillation of the cantilever, modulated components of the time-periodic electrostatic potential at harmonic frequencies of the pump, and an ac bias modulation signal. Each harmonic can be selectively transferred to the second cantilever eigenmode. We show how phase coherent sideband generation and signal demodulation at the second eigenmode can be achieved by using two numerical lock-in amplifiers configured in cascade. Dual-heterodyne KPFM (DHe-KPFM) can be used to map any harmonic (amplitude/phase) of the time-periodic surface potential at a standard scanning speed. The Fourier spectrum (series of harmonics) can also be recorded in spectroscopic mode (DHe-KPFM spectroscopy), and 2D dynamic images can be acquired in data cube mode. The capabilities of DHe-KPFM in terms of time-resolved measurements, surface photovoltage (SPV) imaging, and detection of weak SPV signals are demonstrated through a series of experiments on difference surfaces: a reference substrate, a bulk organic photovoltaic heterojunction thin film, and an optoelectronic interface obtained by depositing caesium lead bromide perovskite nanosheets on a graphite surface. The conclusion provides perspectives for future improvements and applications.

## Introduction

Kelvin probe force microscopy (KPFM) is a well-known variant of AFM that allows probing at the nanoscale the electrostatic landscape on the surface of a sample by measuring the so-called contact potential difference (CPD). If one considers a simple junction formed by a metallic AFM tip and a metallic sample, the CPD originates from the tip–sample work function difference. More generally, the CPD stems from the existence of electric charges and/or dipoles in the system under consideration. As a result, the applications of KPFM are extremely broad. It is now used by physicists, chemists, and biologists to charac-

terize the nanoscale electronic/electrostatic properties of an ever-expanding range of materials, interfaces, and devices, in ambient conditions, under ultrahigh vacuum, or at the liquid–substrate interface.

Since the early 90's, a variety of approaches have been implemented to improve KPFM performances in terms of spatial, potentiometric, and temporal resolution. Several research teams continue to work in this direction and KPFM is still an evolving technique in many aspects. In particular, the development of KPFM-based approaches specifically designed to investigate photogeneration mechanisms and charge dynamics at the nanoscale in photovoltaic and optoelectronic materials is an active research area.

In photoassisted KPFM, the idea is to probe the surface photovoltage (SPV), which is the illumination-induced change in the surface electrostatic potential (i.e., the opposite of the CPD shift under illumination). To map the SPV, the most basic approach consists in performing a dual-pass experiment. Two CPD maps are recorded, the first in the "dark state" and the second under continuous wave (cw) illumination. An SPV image can eventually be recalculated as the difference between both sets of data [1]. The inherent drawback of this dual-pass method is that the source images used for the SPV calculation may feature misalignments, which is especially unavoidable at room temperature (RT) due to thermal drift [2,3]. Another issue is that some of the SPV components – related to dynamical processes – can remain hidden to this "conventional" SPV imaging [4].

To mitigate the effects of thermal drift, a first alternative consists in performing a data cube acquisition of CPD curves synchronously recorded with the application of a light pulse (i.e., a curve is recorded at each point of the surface along a 2D grid). Again, a differential SPV image can be reconstructed from the matrix of spectroscopic curves [5]. However, this approach is not free from artefacts, in particular the cantilever photothermal bending can significantly modify (depending on the optical power) the tip–surface distance during the spectroscopic measurement (which has to be performed in open z-loop).

Whenever possible, it is preferable to investigate the photoresponse of the sample under modulated or pulsed illumination. Provided that the modulation frequency of the light source is set high enough, it becomes possible to "stabilize" the static bending in a steady state, and photothermal cantilever excitation can be avoided (by setting the optical modulation at a frequency that differs from the cantilever resonance eigenmodes).

Working under modulated illumination also allows direct SPV measurements using special modulation/demodulation schemes, such as the one recently proposed by Miyazaki and co-workers for ac-bias KPFM [6]. In addition, most time-resolved KPFM modes developed so far rely on the use of a pulsed/modulated illumination chain. This is for instance the case of intensity-modulated KPFM [7-9], pump-probe KPFM [4,10,11], or G-mode KPFM [12], to name a few (we refer the readers to review articles for a more comprehensive introduction to AFM-based time-resolved potentiometric and electrostatic modes [13,14]).

Each of these approaches have advantages and disadvantages. Intensity-modulated KPFM implementation is straightforward, since it simply consists in analysing the frequency response of the time-average CPD under modulated illumination. Nevertheless, it is prone to capacitive artefacts [15]. Accurate quantitative measurements can be performed by pump-probe KPFM (pp-KPFM), with a time-resolution down to the sub-nanosecond scale [10]. However, pp-KPFM features a severely limited bandwidth. In the case of our last implementation of pp-KPFM [4], several tens of seconds (to minutes) are needed to record a single spectroscopic curve, and tens of hours to several days are needed to map a 2D matrix of data. Last, G-mode KPFM requires analysis of large datasets acquired with high-speed data capture [12].

A few years ago, Borgani and Haviland presented an interesting alternative for time-resolved SPV measurements [16], which consists in analysing the intermodulation products between the mechanical oscillation of the cantilever and the photogenerated surface potential. In short, intermodulation spectroscopy allows working in the frequency domain (instead of the time domain) by extracting, during a single measurement, quantities that are directly proportional to the Fourier coefficients of the time-periodic surface photovoltage. Unfortunately, the translation of this promising technique from ambient conditions – where it has proven its worth – to ultra-high vacuum poses significant challenges. This is mainly due to the enhanced quality factors under vacuum, which severely limits the frequency window available to increase the amplitude of the intermodulation products (for a more detailed discussion, see [14]).

In this work, we propose to approach the measurement of intermodulation products with non-contact AFM under ultra-high vacuum in a slightly different way. We demonstrate that the Fourier spectrum (modulus and phase coefficients) of the time-periodic electrostatic surface potential generated under optical (or electrical) pumping can be probed, by exploiting a double heterodyne frequency mixing effect between the cantilever mechanical oscillation, the surface photovoltage harmonics, and an ac bias modulation signal. The frequency of the modulated bias

can be set so that any given spectral component of the surface potential (or intermodulation product) can be "transferred" to the second cantilever eigenmode. This transfer or rejection (i.e., a measurement of a Fourier harmonic at the pump frequency through a demodulation at the second eigenmode frequency) is achieved by using two numerical lock-in amplifiers in cascade, which allows the generation of proper phase-coherent combination of reference signals.

Dual-heterodyne KPFM (DHe-KPFM) dramatically enhances the sensitivity to "weak" (i.e., a few mV) surface photovoltage signals, thanks to the amplification by the second resonance mode. Time-resolved measurements can be performed in datacube mode, by recording spectra of the SPV Fourier components (modulus and phase) onto a 2D grid. The validity of DHe-KPFM implementation is first demonstrated by carrying out measurements on a conducting reference substrate under electrical pumping. The results confirm that – thanks to the constant transfer function over the entire spectrum provided by the signal demodulation at the second cantilever eigenmode – a quantitative measurement of the Fourier spectrum can be performed. In the case of the amplitude spectrum, that measurement is done within a scalar factor related to the capacitance gradient. Furthermore, 2D images of time constant that characterize the surface photovoltage dynamics are acquired on a photovoltaic organic bulk-heterojunction (BHJ) thin film. The time-constant values are shown to be fully consistent with the results of pump-probe KPFM. Last, the ability of DHe-KPFM to detect weak SPV signals is illustrated by investigating optoelectronic interfaces formed between caesium lead bromide perovskite nanosheets and highly oriented pyrolytic graphite.

## Kelvin Probe Force Microscopy Background, Amplitude-Modulated Heterodyne KPFM

Many KPFM modes rely on the detection of a modulated component of the electrostatic force proportional to the CPD, using a lock-in amplifier. The attractive electrostatic force between the tip and the surface can be expressed as:

$$F_{\mathrm{el}} = \frac{1}{2} C'_{\mathrm{z}} \left(V_{\mathrm{bias}} \pm V_{\mathrm{CPD}}\right)^2 . \quad (1)$$

In the above equation, $C'_{\mathrm{z}}$ stands for the tip–sample capacitive gradient. $V_{\mathrm{bias}}$ represents the external bias voltage applied to the system (including both a dc and an ac component, see hereafter). The plus or minus sign applies if $V_{\mathrm{bias}}$ is applied to the tip (+ sign) or to the sample (− sign), respectively.

The lock-in output provides a modulated ac bias voltage ($V_{\mathrm{ac}}$, amplitude $U_{\mathrm{ac}}$, and angular frequency $\omega_{\mathrm{ac}}$) that is added to the static dc voltage applied to the tip (or sample), $V_{\mathrm{bias}} = V_{\mathrm{ac}} + V_{\mathrm{dc}}$. The electrostatic force displays modulated components, and some are directly proportional to the dc electrostatic potential term (i.e., $V_{\mathrm{dc}} \pm V_{\mathrm{CPD}}$). The idea is to demodulate such a component, and feed it into a loop which controls the dc bias. The KPFM controller (with a zero set point), will eventually adjusts the dc bias to minimize its input, yielding a measurement of the CPD ($V_{\mathrm{dc}} = \pm V_{\mathrm{CPD}}$ depending on the setup geometry). In the following, the dc compensation bias provided to the tip by the KPFM controller (in our setup $V_{\mathrm{dc}} = -\mathrm{CPD}$) will be referred to as either $V_{\mathrm{dc}}$ or KPFM potential. To avoid repetition, this quantity is sometimes also referred to as "surface potential". This is obviously a misuse of language, as KPFM gives a relative measurement of the surface electrostatic potential with respect to that of the tip. However, it is partly justified because in our setup the compensation bias is applied to the tip. Then, provided that the effective work function of the tip remains constant during the measurement, any change in the KPFM compensation potential will strictly follow the change in the surface electrostatic potential without sign inversion (a local positive surface charging corresponds to a positive $V_{\mathrm{dc}}$ change).

Actually, there are many ways to perform the signal demodulation. Amplitude heterodyne KPFM, introduced in 2012 by Sugawara et al. [17], is a very elegant approach. It combines the advantages of frequency-modulated KPFM (FM-KPFM) and amplitude-modulated KPFM (in terms of lateral resolution and sensitivity, respectively). This mode takes advantage of heterodyning effects (frequency mixing) between the electrical bias modulation and the cantilever mechanical oscillation (usually performed at the first eigenmode, angular frequency $\omega_0$). These effects result in the existence of additional modulated component of the electrostatic force (or sidebands) at frequencies $\omega_0 \pm \omega_{\mathrm{ac}}$. They stem from higher harmonic components in the capacitance term [16,18]:

$$C'_{\mathrm{z}} = K_0 + \sum_{n=1}^{+\infty} K_n \cos\left(n\omega_0 t\right) = K_0 + K_1 \cos\left(\omega_0 t\right) + \ldots \quad (2)$$

If we restrict ourselves to the first harmonic ($n = 1$), electrostatic force components emerge (we just describe the first set of sidebands, other exist at $\omega_0 \pm 2\omega_{\mathrm{ac}}$) which are:

$$F_{\omega_0 \pm \omega_{\mathrm{ac}}} = 1/2\, K_1 U_{\mathrm{ac}} \left(V_{\mathrm{dc}} \pm V_{\mathrm{CPD}}\right) \cdot \begin{bmatrix} \cos\left(\left(\omega_0 - \omega_{\mathrm{ac}}\right)t\right) \\ +\cos\left(\left(\omega_0 + \omega_{\mathrm{ac}}\right)t\right) \end{bmatrix} . \quad (3)$$

It can be shown [18], that the Fourier coefficient at $n = 1$ is proportional to the second z-derivative of the capacitance ($K_1 \equiv C''_z$). Consequently, demodulating the amplitude of the sidebands gives access at a term that is proportional to the dc potential difference, and one works (like in frequency-modulation KPFM) on a signal that is proportional to the electrostatic force gradient (through $C''_z$). For that reason, this "side-band" KPFM is often referred to as a variant of FM-KPFM.

Amplitude-modulated heterodyne KPFM [17] further improves this approach. The idea is to set the modulated bias angular frequency so that the first right sideband ($\omega_0 + \omega_{ac}$) is "rejected" at the second mechanical resonance eigenmode (frequency $\omega_1$) of the cantilever. Implementing this modulation/demodulation scheme is nowadays greatly facilitated by the flexibility offered by last-generation digital lock-in amplifiers, which allow generating (and demodulating) phase-coherent combinations of multiple oscillators (i.e., an excitation at $\omega_{ac} = \omega_1 - \omega_0$ and a demodulation at $\omega_1$).

Here, it is mandatory to stress a very important point. In all strictness, in the above, we should have written that $\omega_{ac} = \omega_1 - (\omega_0 + \Delta\omega_0)$, where $\Delta\omega_0$ stands for the cantilever frequency shift due to the tip–surface interaction. In heterodyne KPFM, the reference sideband that drives the modulated bias is indeed generated as follows. The frequency of the first source signal (or lock-in internal oscillator) is set to $\omega_1$, ultimately it will be used for signal demodulation. The second source signal is obtained by tracking the cantilever resonance frequency at its first eigenmode ($\omega_0 + \Delta\omega_0$) with a second oscillator configured as a phase-locked loop (PLL). This tracking is necessary because the first mode is used by the main AFM controller for topographic control (in frequency modulation mode in the case of non-contact AFM under UHV). In other words, it is the AFM controller which generates the source signal at $\omega_0 + \Delta\omega_0$ which "excites" the mechanical oscillation of the cantilever. The frequency mixing effect will effectively generate a modulated electrostatic component at $\omega_1$ – phase-coherent with the demodulation chain – only and if only the frequency shift that the cantilever (at its first resonance mode) experiences in the tip–surface interaction is taken into account. In FM-AFM, it is impossible to perform a heterodyne-KPFM measurement by setting a "fixed" value for $\omega_0$.

## Dual-Heterodyne Kelvin Probe Force Microscopy: Principle

To understand how dual-heterodyne KPFM works, consider the case of a sample subjected to a time-periodic pump that generates a (time-)periodic electrostatic potential. Within the framework of investigations on photoactive materials, of course, the pump will consist of light pulses (in which case one generates a periodic SPV), but DHe KPFM experiments (as shown below) can also be performed under electrical pumping (by applying bias pulses directly to the sample with an arbitrary waveform generator).

The time-periodic electrostatic potential $V_{mod}$ (or photopotential) generated at the sample under modulated illumination can be described by a Fourier series:

$$V_{mod} = V_0 + \sum_{n=1}^{+\infty} V_n \cos\left(n\omega_{mod}t + \phi_n\right) \tag{4}$$

As in other KPFM modes, a combination of dc ($V_{dc}$) and ac ($V_{ac}$) bias is applied to the AFM tip. The total electrostatic force between the tip and the sample is now:

$$F_{el} = \frac{1}{2}C'_z\left[\left(V_{dc} + V_{CPD}\right) + V_{ac} - V_{mod}\right]^2 \quad \text{with } V_{ac} = U_{ac}\cos\left(\omega_{ac}t\right) \tag{5}$$

Note that in the above, we assumed that the dc potential is applied to the tip (this actually corresponds to the configuration of our setup). $V_{CPD}$ encompasses the "in-dark" electrostatic potential difference between the tip and the sample. The additional time-averaged shift due to the SPV is accounted for by the first term in the Fourier series ($V_0$). The harmonic terms ($n \geq 1$ in Equation 4) contain all the information about the time dependence of the SPV. To prevent misunderstanding, it is important to stress that the amplitude spectrum (i.e., the $V_n$ terms) should not be confused with the amplitude of the time-periodic SPV. Strictly speaking, the $V_n$ terms correspond to the modulus of complex Fourier coefficients (see Supporting Information File 1). The reader is asked to keep this fact in mind when the $V_n$ series will be referred to as the amplitude (modulus) spectrum in the following. Obviously, by linearity of the Fourier transform, each component of the "amplitude spectrum" (including the static term) is proportional to the amplitude (or magnitude) of the SPV. We will see later on how static (SPV magnitude) and dynamic (SPV decay time constant) images can be mapped by appropriately fitting the amplitude spectrum.

As with AM-heterodyne KPFM, there is a frequency mixing effect due to the capacitance term, and we restrict ourselves to the first harmonic to describe the time response of the capacitance gradient ($K_1$, Equation 2). Moreover, under periodic pumping, an additional frequency mixing process occurs due to the simultaneous existence of modulated potentials at $\omega = \omega_{ac}$ and $\omega = n\omega_{mod}$. In our case, the terms of interest are those resulting from the multiplication of $V_{ac}$ by $V_{mod}$ in Equation 5 (in

the following we will omit the other terms, bearing in mind that they exist):

$$2U_{\mathrm{ac}}\cos\left(\omega_{\mathrm{ac}}t\right)\times\sum_{n=1}^{+\infty}V_n\cos\left(n\omega_{\mathrm{mod}}t+\phi_n\right). \tag{6}$$

This can be rewritten as:

$$U_{\mathrm{ac}}\sum_{n=1}^{+\infty}\begin{array}{l}V_n\cdot\cos\left(\left(n\omega_{\mathrm{mod}}+\omega_{\mathrm{ac}}\right)t+\phi_n\right)\\+V_n\cdot\cos\left(\left(n\omega_{\mathrm{mod}}-\omega_{\mathrm{ac}}\right)t+\phi_n\right)\end{array}. \tag{7}$$

Finally, the other frequency mixing process (multiplication by the capacitive term, first harmonic) results in the appearance of additional spectral components in the oscillating electrostatic force, but this time there are $4\times n$ of them (instead of two sidebands for conventional AM-heterodyne KPFM):

$$\frac{1}{4}K_1U_{\mathrm{ac}}\sum_{n=1}^{+\infty}\begin{array}{r}V_n\cdot\cos\left(\left(\omega_0+n\omega_{\mathrm{mod}}+\omega_{\mathrm{ac}}\right)t+\phi_n\right)\\+V_n\cdot\cos\left(\left(\omega_0-n\omega_{\mathrm{mod}}-\omega_{\mathrm{ac}}\right)t-\phi_n\right)\\+V_n\cdot\cos\left(\left(\omega_0+n\omega_{\mathrm{mod}}-\omega_{\mathrm{ac}}\right)t+\phi_n\right)\\+V_n\cdot\cos\left(\left(\omega_0-n\omega_{\mathrm{mod}}+\omega_{\mathrm{ac}}\right)t-\phi_n\right)\end{array}. \tag{8}$$

To avoid any confusion, in the following, the sidebands will be labelled as follow:

$$\text{Side band n\_1:}\frac{1}{4}K_1U_{\mathrm{ac}}V_n\cos\left(\left(\omega_0+n\omega_{\mathrm{mod}}+\omega_{\mathrm{ac}}\right)t+\phi_n\right), \tag{9}$$

$$\text{Side band n\_2:}\frac{1}{4}K_1U_{\mathrm{ac}}V_n\cos\left(\left(\omega_0-n\omega_{\mathrm{mod}}-\omega_{\mathrm{ac}}\right)t-\phi_n\right), \tag{10}$$

$$\text{Side band n\_3:}\frac{1}{4}K_1U_{\mathrm{ac}}V_n\cos\left(\left(\omega_0+n\omega_{\mathrm{mod}}-\omega_{\mathrm{ac}}\right)t+\phi_n\right), \tag{11}$$

$$\text{Side band n\_4:}\frac{1}{4}K_1U_{\mathrm{ac}}V_n\cos\left(\left(\omega_0-n\omega_{\mathrm{mod}}+\omega_{\mathrm{ac}}\right)t-\phi_n\right). \tag{12}$$

As with conventional AM-heterodyne KPFM, the idea is to use the second mechanical resonance eigenmode of the cantilever to "boost" a selected sideband. For example, the ac value can be adjusted so that the n_4 sideband frequency is rejected at the second eigenmode (i.e., $\omega_{\mathrm{ac}}=\omega_1-\omega_0+n\omega_{\mathrm{mod}}$). Note that depending on the frequency range of the harmonics, other bands can be used for rejection (such as the n_1 one, with $\omega_{\mathrm{ac}}=\omega_1-\omega_0-n\omega_{\mathrm{mod}}$).

Before going further, we would like to note that the same result (i.e., Equation 8 and Equations 9–12) would have been obtained by first considering a frequency mixing effect between the mechanical oscillation at $\omega_0$ and the modulated components at $n\omega_{\mathrm{mod}}$, and then a second heterodyning process with the ac bias modulation. This may sound trivial, but considering things in this order may provide a useful way to visualise how harmonics can be "transferred" by properly setting the ac bias modulation frequency at the second eigenmode, as shown in Supporting Information File 1, Figure S4.

Demodulating the amplitude of the second eigenmode (at $\omega_1$) gives thus a direct access to the Fourier coefficients characterizing the $n$-th harmonic component of the time-periodic electrostatic potential of interest. It is important to understand that, in practice, such demodulation can only be carried out if phase (time) coherence is maintained between all the signals throughout the modulation/demodulation chain. This requires the use of two numerical lock-in amplifiers in cascade, as shown in Figure 1.

As with AM-heterodyne KPFM, the first lock-in unit performs a combination of two signals to generate a reference at the frequency $\omega_{\mathrm{ref}}=\omega_1-(\omega_0+\Delta\omega_0)$. The frequency of the first source signal (or internal oscillator) is set to $\omega_1$, ultimately it will be used for signal demodulation. The second source signal is obtained by tracking the cantilever resonance frequency at its first eigenmode ($\omega_0+\Delta\omega_0$) with a second oscillator configured in a PLL configuration.

In conventional AM-heterodyne KPFM, the reference signal at $\omega_1-(\omega_0+\Delta\omega_0)$ is used to perform the electrical excitation. In dual-heterodyne KPFM, it is instead used as an "intermediate" reference signal. It is subsequently fed to the external input of a second digital lock-in, which tracks it with a dedicated PLL. A second internal PLL is used to track a second reference signal generated by an arbitrary waveform generator at $n\omega_{\mathrm{mod}}$. Actually, this AWG unit generates two in-phase coherent signals. The first channel generates a square-waved modulation (period $2\pi/\omega_{\mathrm{mod}}$, duty ratio fixed at the user convenience), which is used to pump the sample (via a digital modulated laser source, or a direct electrical connection to the sample for tests under electrical pumping). The second channel generates a sinusoidal reference signal at $n\omega_{\mathrm{mod}}$. The modulated bias voltage $V_{\mathrm{ac}}$ can then be generated by the second digital lock-in by performing a phase-coherent combination of the two reference signals at $\omega_1-(\omega_0+\Delta\omega_0)$ and $n\omega_{\mathrm{mod}}$. Finally, the amplitude and phase of the second eigenmode are demodulated at $\omega_1$ by the first lock-in unit. The schematic diagram in Figure 1 shows how the modulation/demodulation chain is set up.

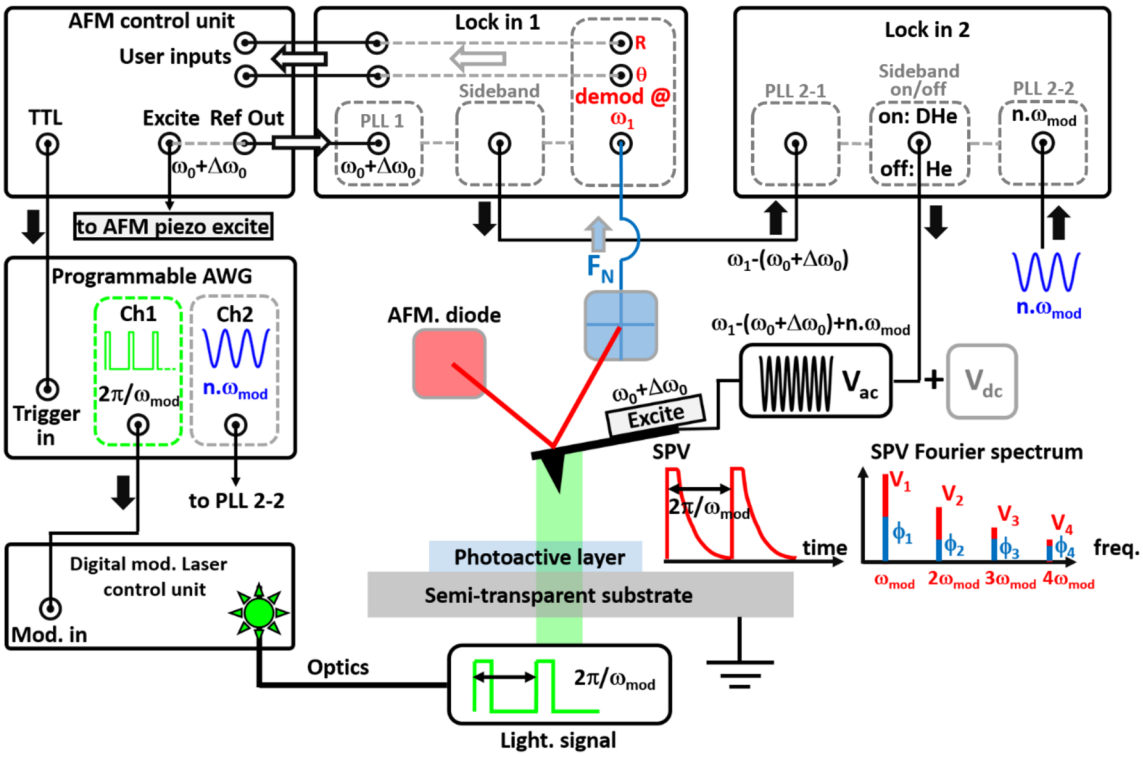


**Figure 1:** The implementation of DHe-KPFM. The real geometry of the sample stage (backside or front side illumination depending on the nature of the substrate) and the external optics differ from that of the simplified scheme. The cantilever is mechanically excited by the AFM control unit at its first eigenmode resonance frequency $\omega_0$, shifted by $\Delta\omega_0$ in the tip-surface interaction. The first lock-in unit performs a combination (or sideband generation) to generate a reference sine at $\omega_1 - (\omega_0 + \Delta\omega_0)$. The "intermediate" reference signal at $\omega_1 - (\omega_0 + \Delta\omega_0)$ is subsequently fed to the external input of a second digital lock-in. The second lock-in combines it with another reference sine signal generated by the arbitrary waveform generator (AWG, channel 2) at $n\omega_{mod}$. Then, a modulated bias $V_{ac}$ with an angular frequency $\omega_{ac} = \omega_1 - (\omega_0 + \Delta\omega_0) + n\omega_{mod}$ is generated at the lock-in output and applied to the AFM cantilever. NB: the configuration can be switched (software-controlled toggle of the modulation unit) between DHe-KPFM (DHe) and standard AM-heterodyne-KPFM (He). The AWG also generates the pump source signal (channel 1, i.e.; a square-waved modulation with period $2\pi/\omega_{mod}$, duty ratio fixed at the user convenience). The time-periodic SPV displays multispectral components at the frequencies $n\omega_{mod}$ which stem from the dynamics of photoexcited states. Demodulating the normal force at $\omega_1$ yields access to the SPV $n$-th Fourier coefficients (amplitude and phase). Curves of the SPV Fourier spectrum are acquired by sequentially sweeping the output signal from the second channel of the AWG (i.e., $n\omega_{mod}$ with $n = 1$, $n = 2$, $n = 3$, etc.). This is achieved by playing a pre-programmed list of waveforms, triggered by TTL pulses generated by the AFM controller.

To sum up, DHe-KPFM allows a selective demodulation of the Fourier coefficients $(V_n,\Phi_n)$ of the periodic electrostatic potential generated at the sample surface under a modulated pump.

The first and most straightforward application consists in mapping a selected component (such as the first harmonic $n = 1$) to obtain a set of images (amplitude/phase) directly related to the SPV generated under modulated/pulsed illumination. Series of images can be acquired for different pump parameters (period and duty ratio), providing a first approach to check the nature of the SPV dynamics. Compared to previous "modulated" SPV imaging techniques, dual-heterodyne KPFM provides an enhanced sensitivity (as demonstrated in the following), thanks to the amplification of the intermodulation products by the second resonance eigenmode.

In addition, alike intermodulation spectroscopy [16], time-resolved measurements can be performed by DHe-KPFM by recording several harmonics of the SPV signal. To that end, we implemented (as detailed hereafter in the "DHe-KPFM implementation" section) a spectroscopic variant which allows recording onto 2D grid curves of the Fourier coefficients $(V_n,\Phi_n)$ as a function of the harmonic number.

As far as the phase is concerned, two points should be stressed. The first is trivial: depending on the sideband used for rejection, a + or − sign must be applied after demodulating the signal (intermodulation products have a phase of $\pm\Phi_n$, see Equation 8). More importantly, the phase measurement is relative, since the demodulation chain introduces an arbitrary phase shift with respect to the "zero" phase of the average component of the

modulated SPV ($V_0$ in Equation 4). To solve that issue, we added a refinement which consists in "switching" (during a selected time window of the spectroscopic sequence) the sideband generation to the standard AM-heterodyne KPFM scheme (i.e., $\omega_{ac} = \omega_1 - (\omega_0 + \Delta\omega_0)$ instead of $\omega_{ac} = \omega_1 - (\omega_0 + \Delta\omega_0) + n\omega_{mod}$ when working with the $4n$-th sidebands). In this configuration, the demodulated component yield access to the "dc" Fourier coefficient $V_0$ and to the reference phase shift $\Phi_0$.

Compared to intermodulation spectroscopy [16], our approach has the disadvantage of being "sequential" in the sense that the Fourier components are measured one after the other and not during the same acquisition time window. However, it offers interesting advantages. First, the sideband rejection at the second eigenmode ensures that the transfer function remains exactly the same regardless of the measured harmonic. This allows a quantitative measurement of the Fourier components without the need for cantilever transfer function calibration. More importantly, there is virtually no limit to the number of harmonics that can be probed and the time resolution, other than that imposed by the maximum modulation/demodulation frequencies allowed by the lock-in units and the AWG. Last but not least, DHe-KPFM can be implemented on a non-contact AFM operating under ultra-high vacuum, where the high resonance quality factors should now become an advantage and provide greater sensitivity. In the next section, we will provide some details on the technical implementation of DHe-KPFM on an nc-AFM. We will then demonstrate its ability to detect weak SPV signals and perform time-resolved measurements.

Before ending this section, two final remarks should be made. DHe-KPFM is an "open loop" variant of KPFM. It does not rely on the application of an "active" compensation bias to probe the electrostatic potential of the sample. It yields a measurement of the Fourier spectrum of the time-periodic surface potential, which may be in principle used to reconstruct the signal in the time domain. However, in the current version of our implementation, this retro-conversion process from the frequency domain will only provide data that are proportional to the surface potential (or photopotential). This stems from the fact that the tip–sample capacitance second derivative $C''_z$ ($K_1$ term in Equation 8 and Equations 9–12) remains unknown. In principle, alike in the case of dual-harmonic KPFM [19], it should be possible to perform a quantitative measurement of $C''_z$ by employing a complementary demodulation scheme. For that purpose, one would need to reject at the second eigenmode another set of sidebands ($\omega_0 \pm 2\omega_{ac}$). This point – beyond the scope of the current study – will be the subject of a forthcoming work. In the remainder of this article, for the sake of brevity, we will omit to systematically recall that the measurement of the amplitude coefficients is performed within a multiplication by the factor $K_1$. We will write $V_n$ instead of $K_1 \times V_n$. The amplitude spectrum data will be given in mV (instead of arbitrary units), as they correspond to the demodulated amplitudes at the output of the locking device. However, once again, a confusion should not be made between these amplitudes (modulus) values and the SPV amplitude itself.

The second comment is also related to the fact that DHe-KPFM is an open variant of KPFM. It cannot be used for an active electrostatic compensation. However, as in the case of pump-probe KPFM [4,10], it is possible to use a second additional FM-KPFM loop which cancels the "time-averaged" dc part of the potential. This feature will not be used in this work, but its implementation has been validated. In the schematic (Figure 1), the dc bias applied to the tip represents the compensation bias of this second loop (it also has its own modulated bias, which is not shown in the schematic). As with pump-probe KPFM, there is no crosstalk between the two modulation/demodulation units because their operating frequency ranges are far apart. In FM-KPFM, the bias is modulated at a few kHz, while in the double-heterodyne scheme, much higher frequencies are used for electrical excitation. This spectral range difference also holds true for signal demodulation, which is performed at a few kHz for the FM-KPFM loop and hundreds of kHz (demodulation at the second eigenmode) for its heterodyne counterpart.

## Dual-Heterodyne Kelvin Probe Force Microscopy: Implementation

Non-contact AFM (nc-AFM) and KPFM experiments are performed with a VT-beam AFM system (Scienta-Omicron) at room temperature (RT) under ultra-high vacuum (UHV), driven by a Mimea scanning probe microscope (SPM) controller (SPECS-Nanonis). Topographic imaging is performed in FM mode (FM-AFM) in the attractive regime, with negative frequency shifts of a few Hz and vibration amplitudes of a few tens of nm. All experiments were performed with Pt/Ir coated silicon cantilevers (PPP-EFM, Nanosensors, resonance frequency in the range 45–115 kHz), annealed in situ to remove atmospheric contaminants.

The dual-heterodyne KPFM mode was implemented by combining the SPM unit with two digital lock-ins from Zurich Instruments (lock-in 1: MFLI, lock-in 2: HF2LI). Both are equipped with multiple oscillators, control loops, PLLs, and modulation modules (2 for the HF2LI). The MFLI modulation module is used to generate the intermediate reference signal with an angular frequency of $\omega_1 - (\omega_0 + \Delta\omega_0)$. The reference sidebands for the electrical excitation ($V_{ac}$, $\omega_{ac}$) are generated by the HF2LI modulation module. As aforementioned, different series of sidebands can be used to probe the signal Fourier spectrum. In this regard, it should be noted that a 180 phase

shift is added by the HF2LI to its output ($V_{ac}$) if one uses the left sideband (with respect to the carrier, as defined in the HF2LI modulation module) instead of the right one. In our case, this additional 180 phase shift is taken into account when the n_1 sidebands are used instead of the n_4 ones.

The pump (modulated square wave with an adjustable duty ratio and period $2\pi/\omega_{mod}$) and the harmonic reference (sine, angular freq. $n \times \omega_{mod}$) are generated by a Keysight 33600 A arbitrary waveform generator. The maximum frequency for the sine signal is 120 MHz, 50 MHz for a square wave with a duty ratio of 25%. On its part, the HF2LI unit can handle signals up to 50 MHz. In principle, these combined features allow up to approximately 10 harmonics to be sampled with a base pump period as small as 200 ns ($10 \times \omega_{mod}/2\pi \sim 50$ MHz). It should be noted, however, that other factors may limit measurements at high frequencies (e.g., attenuation of the ac signals transmitted to the cantilever).

Time-resolved measurements are performed by recording curves of the demodulated Fourier components of the time-periodic surface potential ($V_n$,$\Phi_n$) as a function of the harmonic number ($n$). This is done by sequentially sweeping the output signal from the second channel of the AWG (i.e., $n\omega_{mod}$ with $n = 1$, $n = 2$, $n = 3$, etc.). To that end, a pre-programmed list of waveforms is played, and the triggering is done by TTL pulses generated by the AFM controller. The AWG waveform playlist is programmed by using the Keysight benchlink pro software, and the TTL pulses are generated during the course of the spectroscopic ramp by using a user-available high speed digital output of the Mimea unit.

To measure the "dc" components of the Fourier spectrum ($V_0$ and the reference phase $\Phi_0$), the sideband generation is switched during a dedicated time window within the spectroscopic ramps (i.e., from DHe-KPFM to standard AM-heterodyne KPFM configuration). To do so, a Python routine is used to toggle the output configuration of the HF2LI modulation module (see Supporting Information File 1), as a function of a trigger signal sent by the Mimea unit. The full phase spectrum ($\Phi_n$) is eventually reconstructed by shifting the data set from $\Phi_0$ (n_4 sidebands) or $\Phi_0 + 180°$ (n_1 sidebands).

An external fibre-coupled laser source (Omicron Laserage, PhoxX+ at 515 nm) was used for sample illumination through an optical viewport of the UHV AFM chamber. Samples can be illuminated either from the front or from the back using sample holders with on-board mirrors [3]. The latter configuration is used in the case of organic BHJ thin films (processed on transparent substrates, i.e., glass coated with indium thin oxide). The light intensity is adjusted using the laser power control and optical density filters. In the following, for each measurement, the optical power $P_{opt}$ (maximum pulse intensity in the case of experiments under modulated illumination) is given in the corresponding figure caption. The $P_{opt}$ value is roughly defined per unit area, taking into account the diameter of the laser beam (approximately 1 mm) and the angle of the optical beam with respect to the plane of the substrate.

# Results and Discussion

## Dual-heterodyne Kelvin probe force microscopy under electrical pumping: benchmarking

Similar to the case of pp-KPFM [11], we tested this new implementation by performing DHe-KPFM measurements under electrical pumping on a highly oriented pyrolytic graphite substrate (HOPG). For these tests, the sample was electrically connected to the AWG (channel 1 in Figure 1) by mounting the HOPG substrate onto a sample holder designed with in situ electrical contacts [11]. The results of four measurements with different pump signals are shown in Figure 2. In all cases the pump period was fixed at 100 µs, and the pump shape illustrates a textbook case in the field of Fourier transforms (the Fourier coefficients for all waveforms are derived in Supporting Information File 1).

The results of the first two measurements alone would be sufficient to demonstrate the ability of DHe-KPFM to probe the Fourier spectrum of the time-periodic electrostatic surface potential. The pumps consisted of a square wave with a 50% duty ratio (Figure 2a) and a saw-tooth (Figure 2b). In either case, the amplitude and phase spectra almost perfectly match those expected from a simple Fourier transform of the pump.

In short, the square-wave spectrum has only odd harmonics, while the saw-tooth has all of them. In both cases, the amplitude is inversely proportional to the harmonic number, and the phase shows almost perfect quadrature with respect to the dc reference. This last point already demonstrates the validity of the proposed procedure for an absolute determination of the phase signal.

This conclusion is reinforced by the second test results (Figure 2c and Figure 2d), which have been both carried out with a square wave pump, for which the duty ratio was reduced to 10%. The only difference here is that the second measurement (Figure 2d) has been performed by rejecting the n_1 sidebands at the second eigenmode, instead of the n_4 ones (Figure 2c). Both spectra are identical, but – as expected (Equations 9–12) – the phases are inverted (i.e., $-\Phi_n$ instead of $+\Phi_n$) with respect to the pump Fourier transform in the case of a

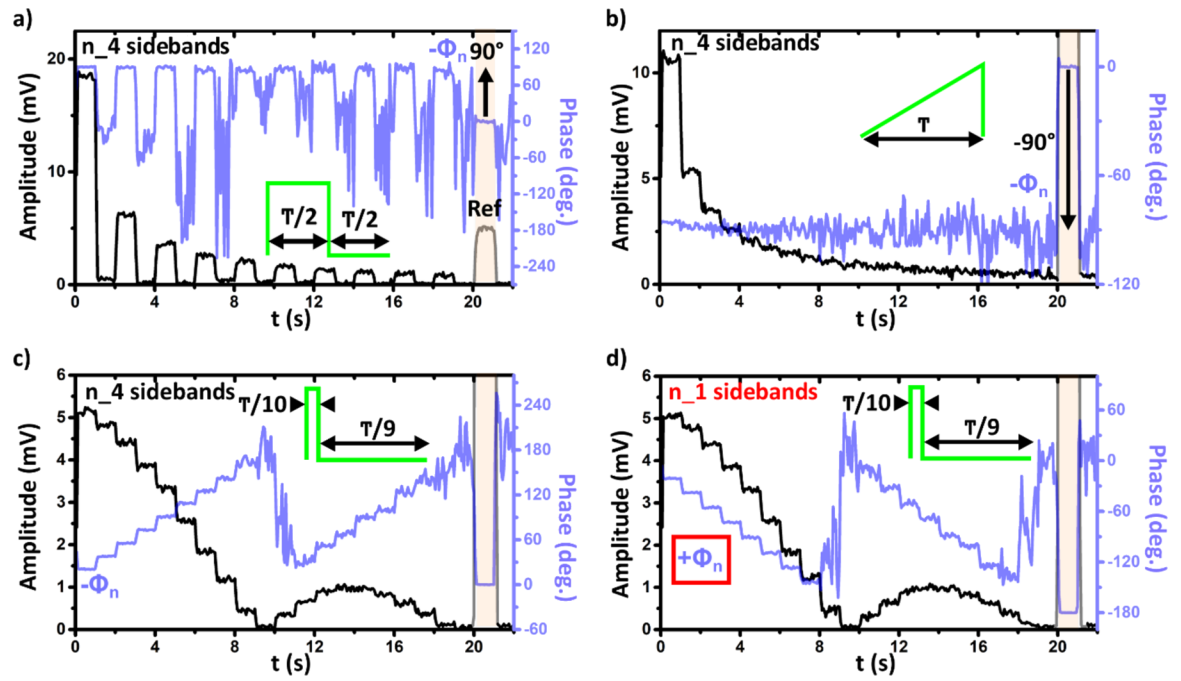


**Figure 2:** Benchmarking of DHe-KPFM under electrical pumping. Plots of the demodulated amplitude and phase (lock-in outputs) at the second cantilever eigenmode as a function of time, recorded on an HOPG sample under electrical pumping (pump period $T$ = 100 µs and peak-to-peak amplitude of 1 V for all spectra). $\omega_0/2\pi \approx 83.3$ kHz, $\omega_1/2\pi \approx 519.3$ kHz, $\Delta\omega_0/2\pi = -25$ Hz, $\omega_{mod}/2\pi = 10$ kHz, $U_{ac} = 0.5$ V. The first 20 harmonics have been recorded ($n$ = 1 to 20, 1 s per harmonic). a) Square-wave pump with a 50% duty ratio. b) Saw-tooth ramp. c,d) Square-wave pump with a 10% duty ratio. a,b,c) Rejection at $\omega_1$ of the n_4 sidebands, $\omega_{ac} = \omega_1 - (\omega_0 + \Delta\omega_0) + n\omega_{mod}$. d) Rejection at $\omega_1$ of the n_1 sidebands, $(\omega_{ac} = \omega_1 - (\omega_0 + \Delta\omega_0) - n\omega_{mod})$. The controller configuration is switched in standard AM-heterodyne KPFM ($\omega_{ac} = \omega_1 - (\omega_0 + \Delta\omega_0)$) during the 20 s < $t$ < 21 s time window (highlighted by a semi-transparent pink area). This allows setting a reference phase level (zero or 180° depending on the set of sidebands used to probe the intermodulation products, see main text).

signal demodulation based on the n_4 sidebands. At the exception of the harmonics directly neighbouring the null component ($n$ = 10 in the case of a 10% duty ratio pump waveform), the measured phase values match fairly well the ones expected from the pump Fourier transform. For their part, the amplitude spectra are identical, they display the typical cardinal sine (sinc) shape (see Supporting Information File 1) and perfectly match the calculated ones. A figure where all set of data (experimental and calculated) are gathered is provided in Supporting Information File 1 (Supporting Information File 1, Figure S5).

## Dual-heterodyne Kelvin probe force microscopy under optical pumping on an organic solar cell

To further validate the DHe-KPFM implementation, a second set of measurements was performed under optical pumping on an organic photovoltaic donor–acceptor blend. As in our previous works, we used the $PTB_7$:$PC_{71}BM$ tandem. We refer the reader to our former reports [4,11] and review articles for a detailed introduction to KPFM on organic heterojunctions [20], and to the specificities of the PTB7:$PC_{71}BM$ blend.

We limit ourselves here to recall that in these organic blends, charge photogeneration can be understood, in a first approach, as the result of exciton dissociation into Coulomb bound charge transfer (CT) states at the donor–acceptor interfaces. This event is finally followed by the dissociation of the CT states into delocalized carriers of opposite sign on both sides of the D–A interface.

In the context of this work, it is also worth recalling that KPFM investigations are carried out in an "open circuit voltage" configuration. In such a geometry, the surface photovoltage probed under continuous-wave illumination results from a balance between the processes of photogeneration and carrier annihilation (by electron–hole recombination). In addition, from the venture of time-resolved KPFM under pulsed illumination, the SPV dynamics are mainly governed by the effective carrier mobility and trapping mechanisms. The main factor limiting the photocharging dynamics is indeed the effective mobility of holes and electrons (under the effect of drift diffusion) in the donor and acceptor networks. After the application of a light pulse – and during the duration of the pulse – the charge

mobility limits the rate at which an electrostatic equilibrium can be reached in the sample. Clearly, this parameter also has an impact on the SPV decay dynamics. However, in the latter case, the slower trap release processes are actually the limiting factor. In particular, in the case of the PTB7:$PC_{71}BM$ system, it is now well-established that isolated $PC_{71}BM$ clusters act as electron trapping centres. The blend morphology, phase composition and concentration gradients of the donor and acceptor species (through the film thickness) can therefore have a dramatic impact on the SPV decay dynamics probed by KPFM.

The sample investigated in this work has been specifically processed to display finely intermixed networks of the donor and acceptor species at the scale of a few tens of nanometres. This was achieved by using diiodooctane as a solvent additive [21], following an identical processing protocol than the one described in our former report [11]. The topographic nc-AFM images (Figure 3a, and numeric zoom in Supporting Information File 1, Figure S6) indicate that the thin-film processing was performed as expected. They display a uniform contrast at the hundred-nanometre scale, indicating that a fine intermixing of donor and acceptor species has been obtained. On a smaller scale (see Supporting Information File 1, Figure S6), nanoscale features appear in the form of small topographic elevations.

The contrasts obtained by imaging the first harmonic components of the time-periodic SPV under modulated/pulsed illumination (amplitude in Figure 3b and phase in Figure 3c) clearly

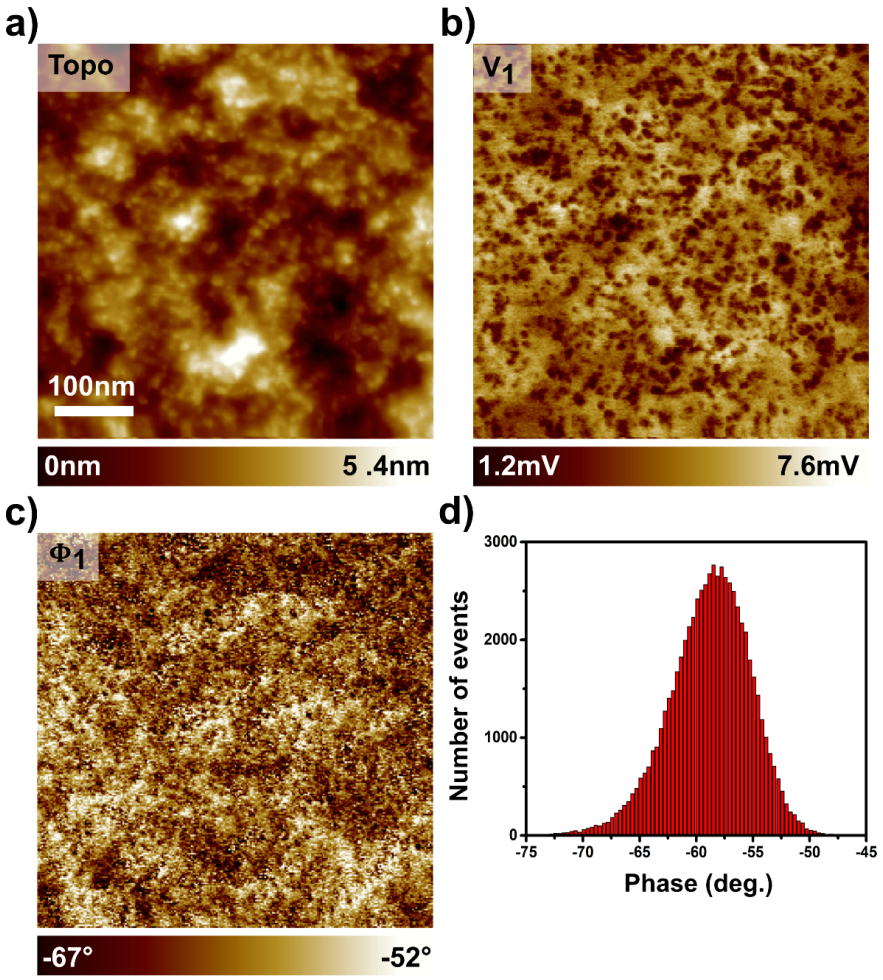


**Figure 3:** The SPV imaging of an organic solar cell by DHe-KPFM. Topographic (a) and DHe-KPFM (b,c) images (500 × 500 nm, 256 × 256 pixels) of a $PTB_7$:$PC_{71}BM$ blend acquired under pulsed illumination (λ = 515 nm, $P_{opt}$ = 300 mW·cm$^{-2}$, illumination in backside geometry). $\omega_0/2\pi \approx 83.3$ kHz, $\omega_1/2\pi \approx 519.3$ kHz, $\Delta\omega_0/2\pi = -30$ Hz, $U_{ac} = 1$ V. $\omega_{ac} = \omega_1 - (\omega_0 + \Delta\omega_0) + n\omega_{mod}$ with $n = 1$. The optical pump consists in a square-shaped signal with a base period of 5 ms ($\omega_{mod}/2\pi = 200$ Hz) and a duty ratio of 20 percent (optical pulse duration: 1 ms). The DHe-KPFM data have been acquired by demodulating (n_4 sideband) the amplitude $V_1$ (b) and the phase $\Phi_1$ (c) of the first ($n = 1$) harmonic of the time-periodic SPV. The scan rate was set to 5 s/line. d) Histogram of the phase values.

confirm that the phases are segregated at the 10 nm scale. In addition, it is clear that the local topographic protrusions correlate with local minima in the amplitude channel (compare Supporting Information File 1, Figures S6a and S6b).

In all likelihood, the observed contrasts originate from the nanoscale phase segregated donor-acceptor networks. However, it is not possible to perform a phase identification on the sole basis of the harmonic amplitude signal (Figure 3b). Taken alone, that channel gives indeed no information about the polarity of the SPV signal.

In principle, one could use the phase signal for that purpose. Unfortunately, contrary to the case of measurements performed in data-cube spectroscopy (shown hereafter), it is here not possible to determine the phase reference level ($\Phi_0$). It is still possible, however, to draw a partial conclusion from the examination of the phase data. Their values are indeed distributed in a relatively narrow band, as shown by the histogram in Figure 3d. This indicates that regardless of the area of the sample being scanned, the SPV – or more specifically, its first harmonic component – keeps a constant polarity (otherwise, 180 phase reversals should be observed). As shown hereafter, this assumption is confirmed by spectroscopic DHe-KPFM measurements. It is moreover consistent with the results of complementary AM-heterodyne KPFM measurements of the “static” SPV performed by using a differential spectroscopic protocol. These additional data, presented in Supporting Information File 1 (Figure S7), reveal that the SPV is positive over the entire surface, with values ranging from ca. 40 mV to ca. 170 mV (for 95% of the data according to the SPV histogram, see Supporting Information File 1, Figure S7).

Consequently, the local minima in the DHe-KPFM amplitude image (appearing as dark spots in Figure 3b and Supporting Information File 1, Figure S6b) correspond to areas of the sample where the SPV is "less positive". Thus, from an electrostatic point of view, the most reasonable hypothesis is that these contrasts (and the correlated topographic protrusions) reveal the location of the electron-acceptor ($PC_{71}BM$) sub-network.

These first series of DHe-KPFM measurements has been performed under an optical pump signal featuring a relatively long time-period (5 ms), and 1 ms wide light pulses. This choice of parameters was made according to the results of our previous pp-KPFM measurements on $PTB_7$:$PC_{71}BM$ blends [4,11], which showed that the SPV decay time constant can vary from tens of µs to several hundreds of µs, depending on the morphology and phase composition. Doing so, we maximized our chances to generate a time-dependent SPV (which first harmonic could be mapped by DHe-KPFM) by choosing a pump time-period higher than a few ms (i.e., the order of magnitude of the longest decay time constants that we observed so far in this system [4]). Naturally, at this stage, the contrasts observed do not allow us to conclude as to the nature of the SPV dynamics (i.e., decay time-constant). In turn, this experiment confirms that DHe-KPFM allows an ac-demodulated imaging of the SPV (to within the $K_1$ scalar constant) with a very high spatial resolution (a lateral resolution of a few nanometres has been achieved according to image cross-sections, not shown), and at a standard scanning speed (here 5 s/line).

It is now time to test the ability of DHe-KPFM to probe the SPV dynamics. Therefore, the 10 first harmonic components (amplitude/phase) were recorded in a data cube spectroscopy experiment under an optical pump, this time operated at a tenfold smaller time scale (100 µs light pulses repeated over a 500 µs period). Figure 4a presents one set of spectra (demodulated amplitude and phase at the second eigenmode as a function of the harmonic number) acquired during this 2D data-cube acquisition. Both the phase and amplitude spectra can be adjusted using fit functions, which are obtained from an analytical calculation of the Fourier components for a time-periodic SPV, whose decay dynamics between light pulses follows an exponential time dependence (with a time constant $\tau_d$). An initial approach to the problem consists in neglecting the photocharging dynamics (i.e., making the approximation of an instantaneous sample photocharging as soon as a light pulse is applied). The calculation of these functions and of the Fourier coefficients is given in a dedicated section of Supporting Information File 1.

The results of this data-cube DHe-KPFM experiment and of the post-data acquisition data treatment (automated adjustment of the matrix of spectroscopic curves by batch processing with OriginPro software) are presented in Figure 4, along with the topographic image recorded simultaneously pixel by pixel with the spectroscopic curves. Note that the spectroscopic images displayed in this figure have been treated by applying a Gaussian smooth filter. The raw data are shown in Supporting Information File 1, Figure S8, they display the same features, but with a higher noise level. Remember also that the reference phase ($\Phi_0$) is now measured for each pixel. Accordingly, a post-acquisition correction is applied to the phase data, resulting in absolute values that can be adjusted with the above-mentioned mathematical function (derived from Equation S18 in Supporting Information File 1).

A first sight, both the amplitude and phase data agree reasonably with the calculated Fourier coefficients. The spectroscopic curves (Figure 4b) can be fairly well adjusted, yielding similar

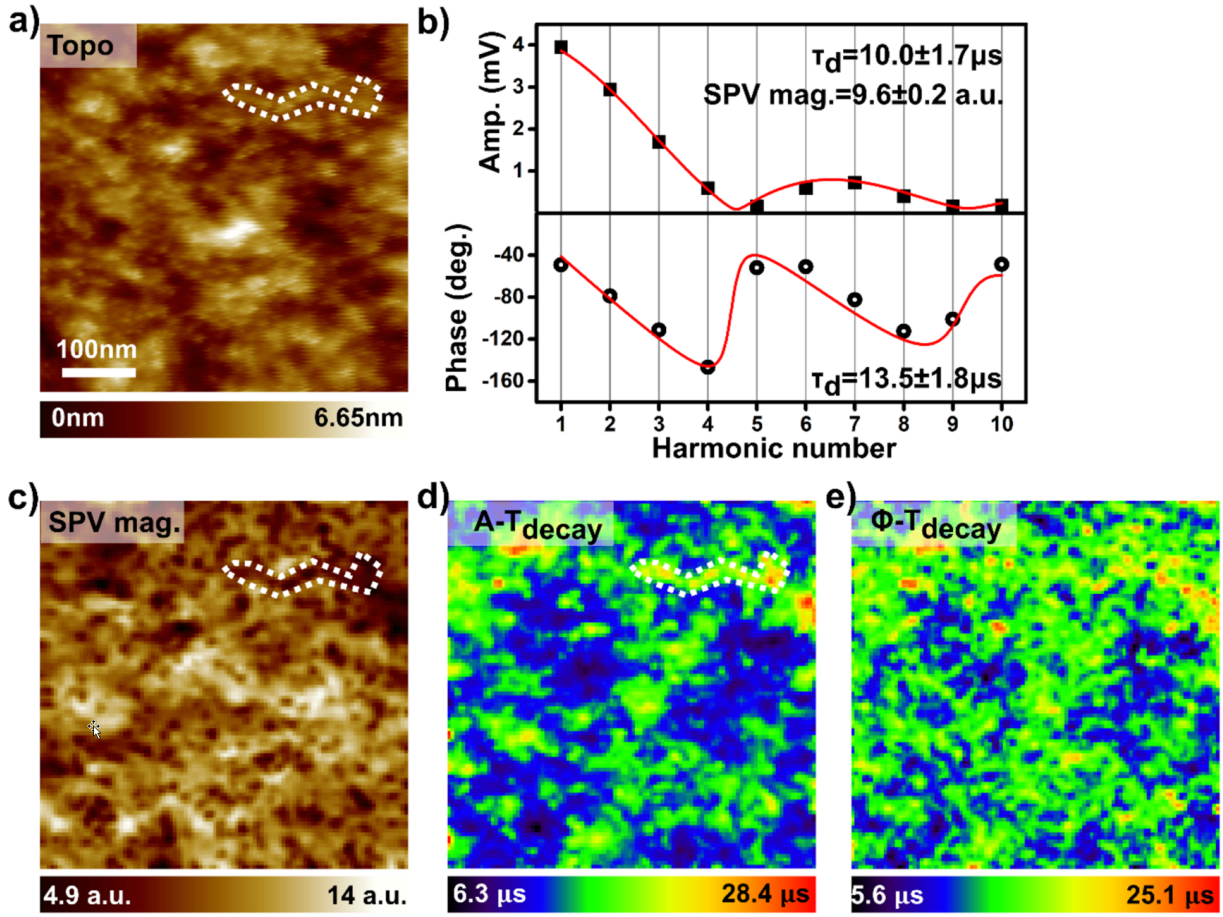


**Figure 4:** Data-cube DHe-KPFM spectroscopy. Topographic (a) and spectroscopic (b,c,d,e) data acquired onto a 2D grid (102 × 102 pixels) during a data-cube DHe-KPFM measurement on the $PTB_7$:$PC_{71}BM$ blend. $\omega_0/2\pi \approx 83.3$ kHz, $\omega_1/2\pi \approx 519.3$ kHz, $\Delta\omega_0/2\pi = -30$ Hz, $\omega_{ac} = \omega_1 - (\omega_0 + \Delta\omega_0) + n\omega_{mod}$, $U_{ac} = 1$ V. The optical pump consists in a square-shaped signal with a base period of 500 μs ($\omega_{mod}/2\pi = 2$ kHz) and a duty ratio of 20 percent (optical pulse duration: 100 μs). λ = 515 nm, $P_{opt} = 300$ mW·cm$^{-2}$, illumination in backside geometry. a) Sample topography (500 × 500 nm) acquired simultaneously with the spectroscopic data. b) Couple of Fourier spectra (top: demodulated amplitude, bottom: demodulated phase, shifted with respect to the reference $\Phi_0$, see text) acquired during the data-cube measurement. The curves show the result of adjustments performed by using mathematical functions that are described in the supplementary information (Supporting Information File 1, Equations S18). $\tau_d$ is a time constant that characterizes the SPV decay dynamics between the light pulses. c,d) Images of the SPV magnitude c) and decay time constant $\tau_d$ d) recalculated by performing an automated adjustment of the 2D matrix of Fourier amplitude spectra. e) "$\tau_d$ image" recalculated from the adjustment of the phase data.

SPV time-constant decay values, ranging from a few μs to a few tens of μs (depending on the sample area). In addition to the SPV decay time constant, a second variable parameter – the SPV magnitude (or amplitude in absolute value) – is required to adjust the amplitude (or modulus) coefficients. Following what precedes, the output of that adjustment is given in arbitrary units (since the amplitude coefficients are all probed to within a multiplication by the same unknown factor, $K_1$).

The calculated SPV magnitude image (Figure 4c) displays contrasts, which definitely confirm our former assumptions. It displays indeed local minima that are correlated with the topographic protrusions. At the same time, the full set of phase data confirms that the SPV polarity remains constant over the entire sample area. Whatever the harmonic, the phase values are indeed distributed in ranges that are incompatible with local polarity inversion (phase images for each harmonic are presented in Supporting Information File 1, Figure S9).

On average, higher decay time constants are observed over the areas associated with the $PC_{71}BM$ subnetwork. There are clear correlations between the magnitude minima (Figure 4c) and the decay time constant maxima (Figure 4d and Figure 4e) in several parts of the surface. One of these areas is highlighted by dashed contours in Figure 4c and Figure 4d. This observation is consistent with a well-known fact for fullerene derivative-based heterojunctions: $PC_{71}BM$ aggregates act as charge trapping

centres. The trap release processes become the limiting factor determining the SPV decay dynamics.

It is also important to note that although both sets of data (amplitude/phase) show good agreement, a better data fit was obtained in the case of the amplitude. In fact, although the relative error ($\Delta\tau_d/\tau_d$) is on average slightly smaller for the constants fitted from the phase data (17% instead of 25% for the constants calculated from the amplitude), the fit failed (phase only) for a small fraction of the data (see the images of relative errors and time constant histograms in Supporting Information File 1, Figure S8).

At this stage of our investigations, we have not been able to definitively establish the origin of these differences. A hint can be found by considering the fact that the phase signal obviously shows a higher noise level for the harmonics with the smallest magnitude (e.g., $n = 5$, see the phase image in Supporting Information File 1, Figure S9). The question also arises as to whether a better adjustment could be achieved, by taking into account the photocharging dynamics in the mathematical model used to describe the SPV dynamics.

A first approach consists in checking what the dynamics of the SPV are from the perspective of another technique. To that end, we performed a series of complementary spectroscopic measurements (single data points at selected locations on the surface) by switching the configuration of the setup to perform pump-probe KPFM measurements. We will merely remind that now, the SPV time-measurement proceeds by recording the KPFM compensation potential as a function of a time-delay between the optical pump and the probe. The probe is obtained by restricting the application of the modulation bias to a restricted time window. We refer the reader to our former report [4] for more details; the measurements discussed herein have been realized using exactly the same setup configuration. The pp-KPFM spectra (Figure S10 in Supporting Information File 1) reveal that the SPV decay can be relatively well accounted by a single exponential law, with time-constant values fully consistent with the ones calculated from DHe-KPFM spectra. In addition, the pp-KPFM data show that only a few hundreds of nanoseconds are needed to reach an electrostatic equilibrium once a light pulse has been applied to the sample. This supports the idea that, even if we cannot rule out the possibility of a better fit, neglecting in a first step the photocharging dynamics remains (in the current case) a reasonable approximation. Last, we also note that the pp-KPFM data once again confirm the (positive) SPV polarity.

To conclude this part of the work, it is important to check whether the data obtained for this PTB7:$PC_{71}BM$ sample are consistent with the results of our previous investigations on BHJ thin films based on the same donor–acceptor tandem. Considering only the SPV decay dynamics, the current result seems to contradict those of previous investigations on other PTB7:$PC_{71}BM$ nanophase-segregated blends. Indeed, previous pp-KPFM studies yielded decay time constant values in the order of hundreds of µs to ms for similar PTB7:$PC_{71}BM$ blends processed with diiodooctane additive [4,11]. However, it is important to note that, in contrast to the present case, these earlier series of samples exhibited an overall negative SPV. This shows that although all of these samples are “nanophase segregated”, the morphology of the donor and acceptor subnetworks can show significant variation from batch to batch. In fact, the decay time constant dynamics we observed here are reminiscent of the SPV dynamics we previously observed in PTB7-enriched regions of blends processed without solvent additive [4]. The comparison seems even more pertinent when one considers that these PTB7-enriched areas also showed a positive SPV [4]. Although the following model remains tentative, the picture that seems to emerge is that the BHJs investigated in this work feature nanophase-segregated networks with a higher concentration of the electron-donor polymer (accounting for the positive SPV), and/or a lower density of non-percolating $PC_{71}BM$ clusters (delaying the SPV decay less).

## Imaging weak surface photovoltage signals: $CsPbBr_3$ nanosheets on HOPG

We have just seen that images of SPV magnitude and dynamics can be obtained with high spatial resolution. In this final section, we will show that DHe-KPFM, thanks to the signal enhancement provided by the second eigenmode, can image weak SPV signals that would otherwise be barely detectable.

To illustrate the capabilities of DHe-KPFM in terms of high sensitivity, we have chosen as a model system an optoelectronic interface that can be obtained by depositing caesium lead halide perovskite nanosheets (NSs) on a highly oriented pyrolytic graphite (HOPG) substrate. Lead halide perovskites have emerged recently as materials with unique optical and electronic properties, such as high absorption coefficients, high defect tolerance, and charge mobility. Due to this, they are very promising for the use in many applications, such as LEDs, solar cells, and photodetectors. Reducing their size down to the nanoscale by synthesizing colloidal nanocrystals in solution can allow high control over the perovskite crystallinity and access to various morphologies. Thus, cubic lead halide perovskite nanocrystals have been widely studied and used for various optoelectronic applications [22,23]. More recently, ultra-thin nanoplatelets or nanosheets (several nm thick and hundreds nm large) with very appealing properties were reported [24]. Due to

the 2D quantum confinement in the vertical direction and their smooth surfaces with atomic thickness control, very precise control over the optical gap and exciton energy of NSs can be achieved through chemical synthesis, making them very interesting objects for various studies.

As in previous works [25], the $CsPbBr_3$ nanosheets (NSs) synthesized for our investigations display an orthorhombic phase (confirmed by X-ray diffraction characterizations, not shown), a thickness of a few unit cells, and lateral dimensions of a few hundreds of nanometres (the synthesis protocol is described in the Supporting Information File 1). Complementary characterizations were carried out by photoluminescence spectroscopy (Supporting Information File 1, Figure S11), scanning electron microscopy (SEM, Supporting Information File 1, Figure S12), and AFM in ambient conditions (Supporting Information File 1, Figure S13), on a series of samples obtained by depositing the NSs (by spin coating the hexane solution where they are dispersed) on silicon and HOPG substrates (for SEM and AFM). Note that prior to SEM and AFM investigations, the excess of ligands was removed by immersing the substrates in an anhydrous ethyl acetate solution.

Sometimes we observe by AFM sample areas where a non-negligible fraction of the surface is covered by NSs monolayers (about 4.5 nm according to the topographic cross section profiles, see Supporting Information File 1, Figure S13). In most cases, however, the NSs form stacks on the surface that are tens to hundreds of nanometres high. This is due to the fact that these objects have a natural tendency to aggregate in solution over time. It is on one of these areas of a HOPG substrate that the DHe-KPFM experiments were performed, the results of which are shown in Figure 5, along with preliminary measurements performed by “differential” SPV imaging (panels a,b,c, and f in Figure 5).

This differential imaging proceeds by recording a 2D matrix of curves of the KPFM potential as a function of time (setup configured in standard AM-heterodyne KPFM, and spectroscopic acquisition performed with an open z-loop). During the spectroscopic ramp, the illumination (continuous wave) is turned on during a pre-determined time window. The difference between the KPFM compensation potential values at the end of the light pulse and just before the light is turned on can be calculated for each pixel.

These differential images (Figure 5b) reveal that a negative SPV develops in the NSs stacks under illumination, with an amplitude exceeding several tens of mV in many places. In a first approach, this negative photocharging may be explained by the existence of a built-in electric field at the interface between the graphite substrate and the $CsPbBr_3$ stacks. The KPFM images taken in the "dark state" (Supporting Information File 1, Figure S14) show that the surface potential is in average more positive by ca. 720 mV over the NSs, compared to the bare substrate. A reasonable hypothesis, although not yet definitely confirmed, is that this built-in electric field results from a negative charge transfer mechanism from the $CsPbBr_3$ stacks to the substrate. Consequently, the extra charge carriers generated under illumination undergo a drift process, resulting in a spatial separation of electron and hole populations across the space charge region. In other words, the negative SPV that we observe is consistent with a downward band bending at the graphite/$CsPbBr_3$ interface. This situation is shown in Supporting Information File 1, Figure S14, together with the "in-dark" KPFM image. While this model seems most plausible, we note that other mechanisms could be invoked to explain the observed SPV (such as illumination-induced band flattening at the top of the stacks, as a result of Fermi level pinning by surface states).

Trapping processes are also clearly involved, as shown by the time course of the KPFM potential (Figure 5c). After each illumination, it takes several seconds for the KPFM potential to return to its initial state (note that an additional 500 ms delay was added between each spectroscopic acquisition, which accounts for the observed difference between the signals at $t = 0$ and $t = 5$ s). Compared to the case of the organic BHJ, the trap release processes now take place on time scales that are several orders of magnitude higher.

A closer examination of the entire set of spectroscopic curves reveals that, in some areas of the sample, a certain fraction of the negative charges may be released more rapidly than in other areas. In fact, some curves exhibit a sharp rise just after the light pulse stops, while others show only a smooth slope increase. Two curves showing this different behaviour, labelled 1 and 2 (corresponding to the locations where they were recorded, as indicated by the markers in Figure 5a and Figure 5b), are shown in Figure 5c.

It turns out that when using DHe-KPFM to map the sample photoresponse under modulated illumination, these specific sample areas become clearly visible. The results of that second data acquisition in DHe-KPFM are presented in Figure 5e (along with the topography in Figure 5d), which displays the amplitude of the first Fourier harmonic ($V_1$) recorded under a 10 ms periodic square-wave modulated illumination (i.e., a 50% duty ratio). The demodulated signal peaks at exactly the same location (highlighted by an arrow in Figure 5e) where the spectroscopic KPFM($t$) curves indicate that part of the photopotential is decaying at a faster rate. Again, it is not possible to

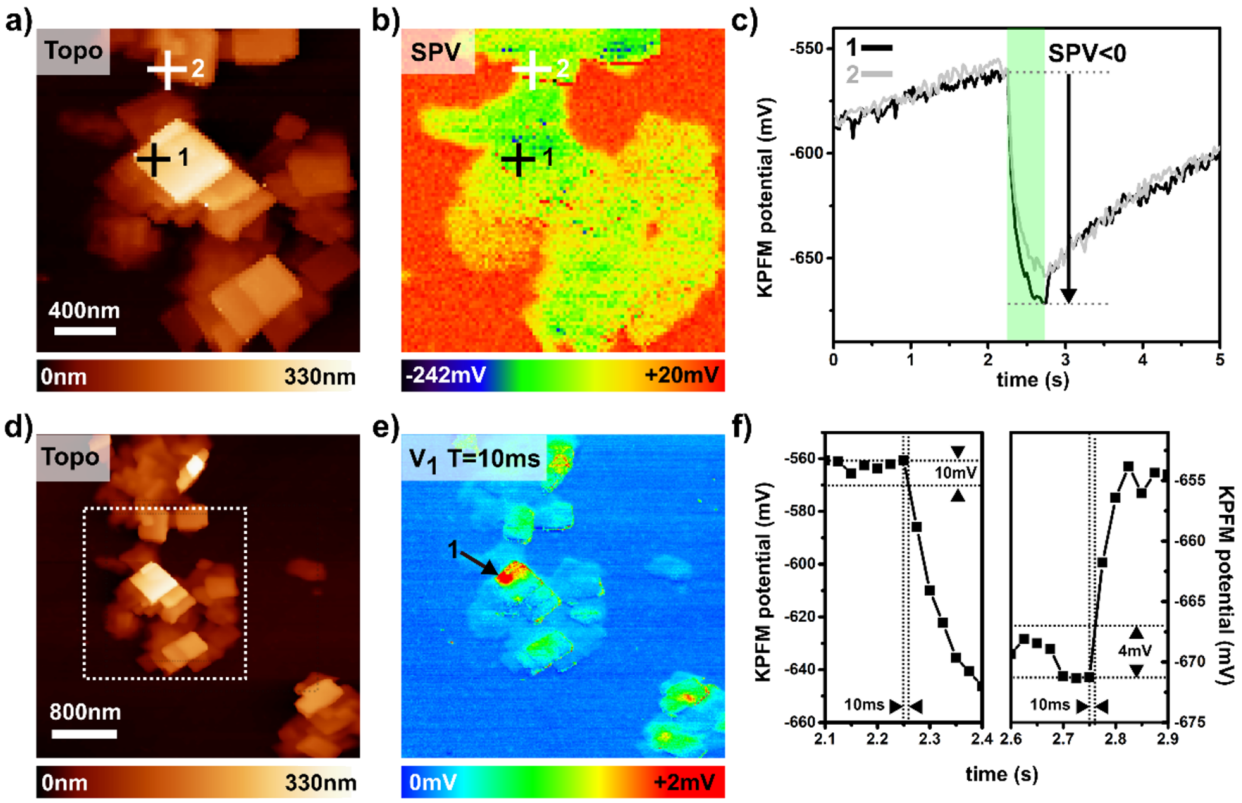


**Figure 5:** Imaging the photoresponse of a $CsPbBr_3$:HOPG interface. (a,b,c,f) Data acquired by differential SPV imaging with the setup configured for AM-heterodyne KPFM ($\omega_{ac} = \omega_1 - (\omega_0 + \Delta\omega_0)$). (d,e) DHe-KPFM measurements ($\omega_{ac} = \omega_1 - (\omega_0 + \Delta\omega_0) + n\omega_{mod}$ with $n = 1$). For all measurements, $\lambda = 515$ nm, $P_{opt} = 1.5$ mW·cm$^{-2}$. $\omega_0/2\pi \approx 63.6$ kHz. $\omega_1/2\pi \approx 401.7$ kHz. a,b) Topography a) and SPV b) images (2.1 µm × 2.1 µm). For this measurement, $\Delta\omega_0/2\pi = -4$ Hz, $\omega_{ac} = \omega_1 - (\omega_0 + \Delta\omega_0)$, $U_{ac} = 0.5$ V. The SPV map is reconstructed from the 2D matrix (96 × 96 pixels) of KPFM($t$) curves (see text). c) Two curves of the KPFM compensation potential as a function of time (200 pixels), recorded on the locations indicated by markers (labelled 1 and 2) in the topographic and SPV images. For each spectroscopic acquisition, a single 500 ms long light pulse (equivalent to a continuous wave illumination) is applied during the 2.25 s < $t$ ≤ 2.75 s time window. Note that an extra 500 ms delay is set between each spectroscopic measurement (i.e., from one image pixel to the next). d,e) Images of the topography d) and amplitude of the first Fourier harmonic e) mapped by DHe-KPFM (256 × 256 pixels, 4 µm × 4 µm). For this measurement, $\Delta\omega_0/2\pi = -12$ Hz, $\omega_{ac} = \omega_1 - (\omega_0 + \Delta\omega_0) + n\omega_{mod}$ with $n = 1$, $U_{ac} = 1$ V. The optical pump consists in a square-shaped signal with a base period of 10 ms ($\omega_{mod}/2\pi = 100$ Hz) and a duty ratio of 50 percent (optical pulse duration: 5 ms). The dotted contours in d) delimit approximately the area investigated by differential SPV imaging. The arrow in e) pinpoints the location corresponding to the KPFM($t$) curve labelled 1 in c). f) Zooms on the KPFM($t$) curve labelled 1. The aim is to highlight what happens immediately after the light pulse is applied, and after its extinction. Extrapolating the photoresponse to the DHe-KPFM case (modulated illumination with a 10 ms time-period) shows that the modulated SPV magnitude (i.e., $V_1$, panel e) cannot exceed a few mV.

provide a truly quantitative measurement of the harmonic amplitude $V_1$ (since the measurement is performed within the multiplicative factor $K_1$). However, since both series of images were acquired at the same location, a direct comparison can be made between the DHe-KPFM data and the KPFM curves recorded in the time domain.

For that purpose, let us zoom in on the parts of the KPFM($t$) curves that correspond to the start and end of the "long" light pulses applied for the differential SPV imaging (Figure 5f). These zooms show that, depending on whether one is interested in the SPV growth or decay regime, the electrostatic potential cannot be changed by more than 10 mV or 4–5 mV in a 10 ms time-lapse. Thus, under modulated illumination, the "modulated SPV" magnitude is limited by the slower decay dynamics, and cannot exceed a few mV. The 4–5 mV value appears really as a maximum, since instead of a 10 ms timescale, it would be more rigorous to consider only the 5 ms periods corresponding to the interval between the light pulses used for the DHe-KPFM experiment.

The very high sensitivity of DHe-KPFM is fully demonstrated by the simple fact that clear contrasts are also observed even on sample areas where the magnitude of the modulated SPV is smaller. According to the comparison with the time domain spectroscopic data corresponding to the sample location labelled 2, a resolution at the mV limit may have been achieved. Further investigations would be needed to precisely quantify the

magnitude of the modulated SPV component. At the very least, complementary measurements performed under electrical pumping (see Supporting Information File 1, Figure S15) confirm that modulated components as small as a few mV can be detected.

## Conclusion

We have introduced DHe-KPFM as a new approach to measure the Fourier spectrum (or intermodulation products) of a time-periodic surface potential with an atomic force microscope. It has been specially designed for experiments with an nc-AFM under UHV conditions, where the high resonance quality factors of the cantilever are an obstacle to the application of a direct intermodulation scheme [16]. Through a series of experiments on model systems, we have demonstrated the ability of DHe-KPFM not only to probe the Fourier harmonics under optical or electrical pumping, but also to detect modulated components within the resolution limit of other reported KPFM methods. This was made possible by exploiting the amplification of the signal by the second eigenmode of the cantilever. In this sense, DHe-KPFM is the first step towards an open-loop generalization of the AM-heterodyne KPFM method. The only drawback – at this stage – is that the measurement of the amplitude spectrum is achieved within a multiplication by a scalar constant. We have good reason to believe that this issue will soon be solved. Preliminary tests have indeed shown that it is also possible to demodulate other series of sidebands through the second eigenmode, which yields access to the capacitance gradient harmonics. In the short term, it will thus be possible to apply a fully automated retro-conversion process to reconstruct truly quantitative (photo)-potential data in the time domain. This will also provide a simple path for dual-harmonic open-loop KPFM measurements [19], without the need to calibrate the transfer function of the system (keeping in mind that whatever the sideband is, the signal is detected at the fixed second eigenmode frequency).

To conclude this work, we would like to emphasize that beyond time-resolved measurements, perhaps the greatest contributions of DHe-KPFM will come from its ability to detect very weak photomodulated signals. In some cases, this may make it possible to reveal phenomena that would otherwise remain inaccessible to other KPFM-based SPV imaging modes. This applies to any type of system where the net density of spatially separated photogenerated charges is insufficient to generate an electrostatic potential difference greater than a few mV. This situation may for instance occur in some cases in hybrid perovskite thin films when the internal electric fields at the interfaces (with the substrate or the vacuum) are too weak. This could also be the case for molecular heterojunctions in the single layer limit.

## Supporting Information

Fourier coefficient calculation and derivation of the formulas used to fit the spectroscopic DHe-KPFM data acquired under optical pumping on the organic BHJ solar cell (text and Figures S1, S2 and S3). Schematic illustration of the dual frequency mixing effect (Figure S4). Python routine for switching the demodulation configuration. Comparison between the data acquired under electrical pumping with n_4 sidebands, n_1 sidebands, and calculated Fourier coefficients (Figure S5). Numeric zooms from the images acquired by DHe-KPFM on the PTB7:$PC_{71}BM$ blend (Figure S6). Complementary measurements on the PTB7:$PC_{71}BM$ blend by differential SPV spectroscopy (Figure S7). DHe-KPFM data-cube spectroscopy on the PTB7:$PC_{71}BM$ blend: unfiltered (raw-data) images and error images (Figure S8). Images of the first ten harmonic phase signals recorded on the PTB7:$PC_{71}BM$ blend (Figure S9). Complementary measurements on the PTB7:$PC_{71}BM$ blend by pump-probe KPFM (Figure S10). $CsPbBr_3$ nanosheets: synthesis protocol (text); $CsPbBr_3$ nanosheets: photoluminescence spectroscopy (Figure S11). $CsPbBr_3$ nanosheets: complementary characterization by SEM imaging (Figure S12). $CsPbBr_3$ nanosheets: complementary characterization, by “tapping-mode” AFM imaging (Figure S13). $CsPbBr_3$ nanosheets on HOPG: in dark KPFM data and built-in interface electric field model (Figure S14); detecting weak modulated components: complementary DHe-KPFM measurements under electrical pump (Figure S15).

### Supporting Information File 1

Supporting information.
[https://www.beilstein-journals.org/bjnano/content/supplementary/2190-4286-14-88-S1.pdf]

## Funding

The HF2LI numeric lock-in has been acquired thanks to a fund by the French National Research Agency (ANR), under the project TRAPPER (ANR19-CE05-0040). Research on $CsPbBr_3$/HOPG interfaces have been carried out in the frame of the Matra2D project (ANR20-CE24-0017).

## Author Contributions

BG implemented the DHe-KPFM setup, carried out the nc-AFM/(DHe)-KPFM experiments, processed the data, and proposed physical interpretations accounting for the results. CA processed the PTB7:$PC_{71}BM$ blend. FH synthesized and processed the $CsPbBr_3$ NSs under the supervision of DA, and carried out complementary characteriza-

tions under the supervision of DA (photoluminescence, SEM imaging) and BG (tapping mode AFM). BG wrote the manuscript, with contributions from FH and DA for the section on NSs (NSs background and description of the synthesis protocol).

## ORCID® iDs

Benjamin Grévin - https://orcid.org/0000-0002-6494-8138
Dmitry Aldakov - https://orcid.org/0000-0002-4581-2462
Cyril Aumaître - https://orcid.org/0000-0003-4640-4193

## References

1. Hoppe, H.; Glatzel, T.; Niggemann, M.; Hinsch, A.; Lux-Steiner, M. C.; Sariciftci, N. S. *Nano Lett.* **2005,** *5,* 269–274. doi:10.1021/nl048176c
2. Fuchs, F.; Caffy, F.; Demadrille, R.; Mélin, T.; Grévin, B. *ACS Nano* **2016,** *10,* 739–746. doi:10.1021/acsnano.5b05810
3. Grévin, B.; Schwartz, P.-O.; Biniek, L.; Brinkmann, M.; Leclerc, N.; Zaborova, E.; Méry, S. *Beilstein J. Nanotechnol.* **2016,** *7,* 799–808. doi:10.3762/bjnano.7.71
4. Aubriet, V.; Courouble, K.; Bardagot, O.; Demadrille, R.; Borowik, Ł.; Grévin, B. *Nanotechnology* **2022,** *33,* 225401. doi:10.1088/1361-6528/ac5542
5. Almadori, Y.; Bendiab, N.; Grévin, B. *ACS Appl. Mater. Interfaces* **2018,** *10,* 1363–1373. doi:10.1021/acsami.7b14616
6. Miyazaki, M.; Sugawara, Y.; Li, Y. J. *Beilstein J. Nanotechnol.* **2022,** *13,* 712–720. doi:10.3762/bjnano.13.63
7. Takihara, M.; Takahashi, T.; Ujihara, T. *Appl. Phys. Lett.* **2008,** *93,* 021902. doi:10.1063/1.2957468
8. Shao, G.; Glaz, M. S.; Ma, F.; Ju, H.; Ginger, D. S. *ACS Nano* **2014,** *8,* 10799–10807. doi:10.1021/nn5045867
9. Fernández Garrillo, P. A.; Borowik, Ł.; Caffy, F.; Demadrille, R.; Grévin, B. *ACS Appl. Mater. Interfaces* **2016,** *8,* 31460–31468. doi:10.1021/acsami.6b11423
10. Murawski, J.; Graupner, T.; Milde, P.; Raupach, R.; Zerweck-Trogisch, U.; Eng, L. M. *J. Appl. Phys.* **2015,** *118,* 154302. doi:10.1063/1.4933289
11. Grévin, B.; Bardagot, O.; Demadrille, R. *Beilstein J. Nanotechnol.* **2020,** *11,* 323–337. doi:10.3762/bjnano.11.24
12. Collins, L.; Ahmadi, M.; Qin, J.; Liu, Y.; Ovchinnikova, O. S.; Hu, B.; Jesse, S.; Kalinin, S. V. *Nanotechnology* **2018,** *29,* 445703. doi:10.1088/1361-6528/aad873
13. Sadewasser, S.; Nicoara, N. *Time-Resolved Electrostatic and Kelvin Probe Force Microscopy*. In *Kelvin Probe Force Microscopy;* Sadewasser, S.; Glatzel, T., Eds.; Springer Series in Surface Sciences, Vol. 65; Springer: Cham, 2018. doi:10.1007/978-3-319-75687-5_5
14. Mascaro, A.; Miyahara, Y.; Enright, T.; Dagdeviren, O. E.; Grütter, P. *Beilstein J. Nanotechnol.* **2019,** *10,* 617–633. doi:10.3762/bjnano.10.62
15. Schumacher, Z.; Miyahara, Y.; Spielhofer, A.; Grutter, P. *Phys. Rev. Appl.* **2016,** *5,* 044018. doi:10.1103/physrevapplied.5.044018
16. Borgani, R.; Haviland, D. B. *Rev. Sci. Instrum.* **2019,** *90,* 013705. doi:10.1063/1.5060727
17. Sugawara, Y.; Kou, L.; Ma, Z.; Kamijo, T.; Naitoh, Y.; Li, Y. J. *Appl. Phys. Lett.* **2012,** *100,* 223104. doi:10.1063/1.4723697
18. Axt, A.; Hermes, I. M.; Bergmann, V. W.; Tausendpfund, N.; Weber, S. A. L. *Beilstein J. Nanotechnol.* **2018,** *9,* 1809–1819. doi:10.3762/bjnano.9.172
19. Collins, L.; Kilpatrick, J. I.; Weber, S. A. L.; Tselev, A.; Vlassiouk, I. V.; Ivanov, I. N.; Jesse, S.; Kalinin, S. V.; Rodriguez, B. J. *Nanotechnology* **2013,** *24,* 475702. doi:10.1088/0957-4484/24/47/475702
20. Grévin, B. *Kelvin Probe Force Microscopy Characterization of Organic and Hybrid Perovskite Solar Cells*. In *Kelvin Probe Force Microscopy;* Sadewasser, S.; Glatzel, T., Eds.; Springer Series in Surface Sciences, Vol. 65; Springer: Cham, 2018. doi:10.1007/978-3-319-75687-5_11
21. Kim, W.; Kim, J. K.; Kim, E.; Ahn, T. K.; Wang, D. H.; Park, J. H. *J. Phys. Chem. C* **2015,** *119,* 5954–5961. doi:10.1021/jp510996w
22. Aldakov, D.; Reiss, P. *J. Phys. Chem. C* **2019,** *123,* 12527–12541. doi:10.1021/acs.jpcc.8b12228
23. Dey, A.; Ye, J.; De, A.; Debroye, E.; Ha, S. K.; Bladt, E.; Kshirsagar, A. S.; Wang, Z.; Yin, J.; Wang, Y.; Quan, L. N.; Yan, F.; Gao, M.; Li, X.; Shamsi, J.; Debnath, T.; Cao, M.; Scheel, M. A.; Kumar, S.; Steele, J. A.; Gerhard, M.; Chouhan, L.; Xu, K.; Wu, X.-g.; Li, Y.; Zhang, Y.; Dutta, A.; Han, C.; Vincon, I.; Rogach, A. L.; Nag, A.; Samanta, A.; Korgel, B. A.; Shih, C.-J.; Gamelin, D. R.; Son, D. H.; Zeng, H.; Zhong, H.; Sun, H.; Demir, H. V.; Scheblykin, I. G.; Mora-Seró, I.; Stolarczyk, J. K.; Zhang, J. Z.; Feldmann, J.; Hofkens, J.; Luther, J. M.; Pérez-Prieto, J.; Li, L.; Manna, L.; Bodnarchuk, M. I.; Kovalenko, M. V.; Roeffaers, M. B. J.; Pradhan, N.; Mohammed, O. F.; Bakr, O. M.; Yang, P.; Müller-Buschbaum, P.; Kamat, P. V.; Bao, Q.; Zhang, Q.; Krahne, R.; Galian, R. E.; Stranks, S. D.; Bals, S.; Biju, V.; Tisdale, W. A.; Yan, Y.; Hoye, R. L. Z.; Polavarapu, L. *ACS Nano* **2021,** *15,* 10775–10981. doi:10.1021/acsnano.0c08903
24. OteroMartínez, C.; Ye, J.; Sung, J.; PastorizaSantos, I.; PérezJuste, J.; Xia, Z.; Rao, A.; Hoye, R. L. Z.; Polavarapu, L. *Adv. Mater. (Weinheim, Ger.)* **2022,** *34,* 2107105. doi:10.1002/adma.202107105
25. Shamsi, J.; Dang, Z.; Bianchini, P.; Canale, C.; Di Stasio, F.; Brescia, R.; Prato, M.; Manna, L. *J. Am. Chem. Soc.* **2016,** *138,* 7240–7243. doi:10.1021/jacs.6b03166

## License and Terms

BEILSTEIN JOURNAL OF NANOTECHNOLOGY

# A multi-resistance wide-range calibration sample for conductive probe atomic force microscopy measurements

François Piquemal[*1], Khaled Kaja[1], Pascal Chrétien[2,3], José Morán-Meza[1], Frédéric Houzé[2,3], Christian Ulysse[4] and Abdelmounaim Harouri[4]

Full Research Paper

Open Access

Address:
[1]Laboratoire national de métrologie et d'essais - LNE, Trappes, 78197 Cedex, France, [2]Université Paris-Saclay, CentraleSupélec, CNRS, Laboratoire de Génie Électrique et Électronique de Paris, 91192, Gif-sur-Yvette, France, [3]Sorbonne Université, CNRS, Laboratoire de Génie Électrique et Électronique de Paris, 75250, Paris, France and [4]Centre de Nanosciences et de Nanotechnologies - C2N, Université Paris-Saclay, CNRS, UMR 9001, Palaiseau, 91120, France

Email:
François Piquemal[*] - francois.piquemal@lne.fr

* Corresponding author

Keywords:
calibration; conductive probe atomic force microscopy; measurement protocol; nanoscale; resistance reference

*Beilstein J. Nanotechnol.* **2023,** *14,* 1141–1148.
https://doi.org/10.3762/bjnano.14.94

Received: 13 June 2023
Accepted: 09 November 2023
Published: 22 November 2023

This article is part of the thematic issue "Advanced atomic force microscopy techniques V".

Guest Editor: P. Rahe



## Abstract

Measuring resistances at the nanoscale has attracted recent attention for developing microelectronic components, memory devices, molecular electronics, and two-dimensional materials. Despite the decisive contribution of scanning probe microscopy in imaging resistance and current variations, measurements have remained restricted to qualitative comparisons. Reference resistance calibration samples are key to advancing the research-to-manufacturing process of nanoscale devices and materials through calibrated, reliable, and comparable measurements. No such calibration reference samples have been proposed so far. In this work, we demonstrate the development of a multi-resistance reference sample for calibrating resistance measurements in conductive probe atomic force microscopy (C-AFM) covering the range from 100 Ω to 100 GΩ. We present a comprehensive protocol for in situ calibration of the whole measurement circuit encompassing the tip, the current sensing device, and the system controller. Furthermore, we show that our developed resistance reference enables the calibration of C-AFM with a combined relative uncertainty (given at one standard deviation) lower than 2.5% over an extended range from 10 kΩ to 100 GΩ and lower than 1% for a reduced range from 1 MΩ to 50 GΩ. Our findings break through the long-standing bottleneck in C-AFM measurements, providing a universal means for adopting calibrated resistance measurements at the nanoscale in the industrial and academic research and development sectors.

## Introduction

Since its introduction thirty years ago by Murrell et al. [1], conductive probe atomic force microscopy (C-AFM) has evolved into a unique and powerful technique for measuring local electrical quantities (i.e., current and resistance) at the nanoscale. In C-AFM, a micro-machined conductive probe with a sharp nanometer-sized tip acts as a top electrode brought into contact with the surface of a sample while applying a potential difference relative to a back electrode. The small currents flowing through the system are measured using a current amplifier, typically ranging from 100 fA to 10 μA for most commercially available microscopes [2,3]. By sweeping the potential difference while the tip is fixed in contact with the sample, current versus voltage (*I*–*V*) curves are acquired. *I*–*V* curves are essentially used to extract resistance values or to characterize the electric behavior of components and devices [4]. Alternatively, current variation maps are acquired at a given applied voltage by scanning the AFM tip in contact mode across a defined sample surface area [5]. Owing to its versatility and high resolution in probing the local conductivity of materials, C-AFM has been extensively used in studying semiconductors [6,7], two-dimensional materials [8-10], memristive devices [11-15], photoelectric systems [16-18], dielectric films [19-23], molecular electronics [24-29], organic and biological systems [30-34], and quantum devices [35-37]. Various technical methods have been developed in C-AFM to cope with the diversity of its applications, including advanced sensors and low-noise preamplifiers [2,38-40]. Nevertheless, quantifying the measured currents and resistances remains a bottleneck issue in C-AFM, inhibiting an effective comparison of results to comprehend experimental processes.

C-AFM measurements are prone to environmental and experimental factors that heavily affect their stability, reproducibility, repeatability, and exactness [41,42]. The formation of a humidity-induced water meniscus at the tip–sample interface, the presence of surface contamination, and thermal drifts induce significant instabilities in C-AFM measurements [42,43]. Moreover, local overheating and anodic oxidation phenomena are commonly observed in C-AFM because of highly localized electric fields at the tip apex leading to structural damage considerably affecting the measurement reliability. These effects are further amplified during scanning in contact mode due to shear forces and strong mechanical stress imposed on the tip apex [44]. Therefore, it is common to measure sudden alterations in local currents and resistances in C-AFM unrelated to the sample's physical properties [43]. The combination of the effects above makes it difficult to quantify and reproduce the measured values in C-AFM experiments, which degrades the method's efficiency in advancing the understanding of many processes in materials sciences and industrial developments. Despite the widely experienced difficulties, no universal solution to ensure the calibration and traceability of C-AFM measurements has been proposed in the literature. So far, only personalized custom approaches have been adopted that are restricted to specific setups or experiments [20,45].

In this paper, we propose a multi-resistance reference sample covering a wide range of values from 100 Ω to 100 GΩ, enabling a universal calibration approach to quantitative measurements in C-AFM applicable to all systems and setups.

## Results and Discussion

Our approach consists of three main steps performed in a one-month timeframe. First, we calibrate the resistors employed in the fabrication of the reference sample using probe station measurements. Second, we use C-AFM imaging to obtain resistance maps and identify the error sources associated with the imaging-mode measurements. Finally, we apply spectroscopic C-AFM measurements to extract current versus voltage (*I*–*V*) curves for each resistance value on the sample. We undertake a comprehensive analysis to compare resistance values obtained by C-AFM imaging and *I*–*V* curves measurement to define the conditions for calibrated measurements.

### Calibration sample design and fabrication

The sample developed in this work consisted of a square fused silica substrate (11 mm wide, 2 mm thick), on which gold connection lines and pads were fabricated by standard photolithography, using a mask aligner (MA6, Karl Suss, Germany), and conventional deposition techniques. Following a resist (about 1 μm thick) development process, a 2 inch diameter wafer was placed in a vacuum chamber for electron beam deposition of a 200 nm thick titanium/gold layer. Subsequently, a lift-off process in acetone was employed to reveal the gold pattern. Finally, square samples were cut to match the dimensions of the measurement setup. We hand-soldered thick-film surface-mounted-device (SMD) resistors onto the connection gold pads on the surface using small soldering paste droplets (F42240, lead-free solder paste – class 5, CIF, France). The fused silica substrate was placed on a heating plate set to 270 °C, which required around 3 min to reach the melting temperature of the solder droplets (217 °C), as observed under an optical microscope. Upon cooling, 16 SMD resistors were fixed on the sample surface, creating a set of 15 resistance values, as shown in Figure 1a. The substrate was fixed onto a circular metallic plate (15 mm diameter), which acts as a back electrode connected to all resistances using a peripheral gold line and dashes of silver paste deposited on the sample edges. Each resistance was connected to an intermediate gold pad (300 μm × 470 μm) designed for microcontacting using a probe

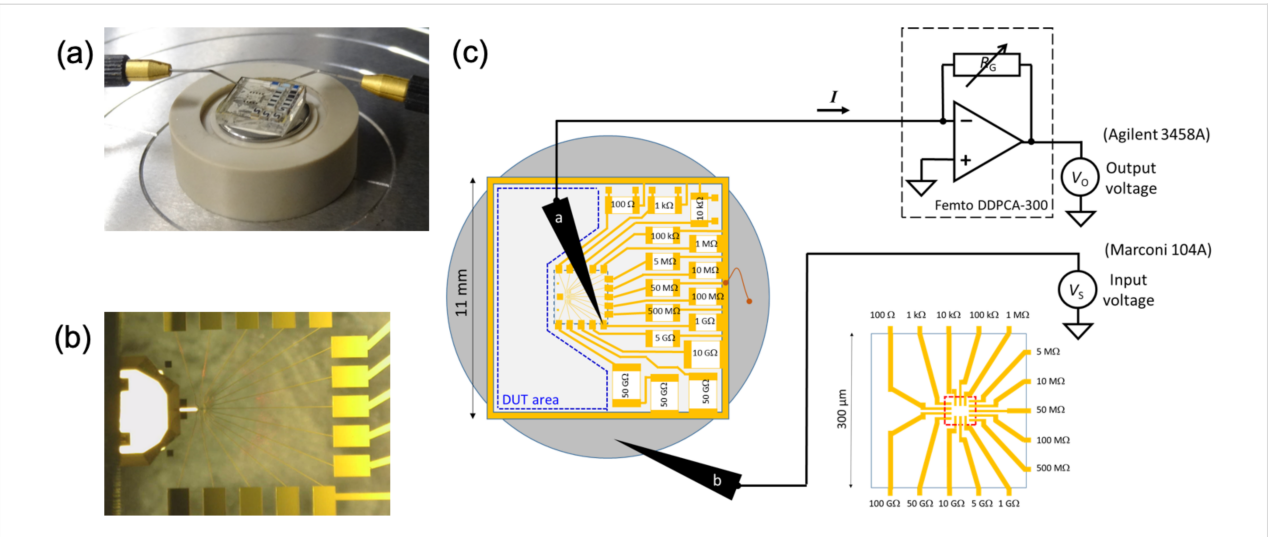


**Figure 1:** (a) Picture of the resistance reference sample connected to the probe station. (b) Top view of the sample underneath the AFM tip. (c) Schematics of the resistance measurement circuit involving two microprobes, an ultra-low current amplifier, and a digital nanovoltmeter. The first drawing shows the sample with the 15 resistive arms and a free area of around 35 $mm^2$ (delimited by blue dotted lines) designed to place a device under test (DUT) with a possible connection to the peripheral gold line. The second drawing shows the central zone (delimited by a red dotted line) of the sample designed for local imaging and spectroscopic measurements in C-AFM.

station setup, as shown in Figure 1a,b. Furthermore, the contacts were extended to the central area (60 µm × 60 µm) of the sample, forming a set of 15 small (i.e., 5 µm wide) electrode arms designed for local C-AFM imaging and spectroscopic measurements. The gold lines' dimensions were characterized for calculating their intrinsic resistances using the gold resistivity value.

## Calibration of SMD resistors and gold lines

Before conducting C-AFM measurements, the resistance values of the SMD resistors and the gold connection lines should be determined using calibrated equipment. To this end, the intermediate gold pads were used as terminals to calibrate the corresponding resistance values relative to the back electrode. We used a probe station (Cascade Microtech MPS150) coupled to a programmable voltage source (Marconi 104A) and a high-precision ammeter to measure the resistance values of the SMD devices in an electromagnetically shielded environment under stabilized air temperature (22.9 ± 0.1) °C and relative humidity (40.7 ± 0.3)%. Two different calibrated ammeters were used depending on the range of the expected resistance values. As shown in Figure 1, a digital voltage multimeter (DVM) (Keysight 3458A) was used for the resistance range between 100 Ω and 1 GΩ, while a very low noise (fA/$Hz^{1/2}$) current amplifier (Femto DDPCA-300) was associated with the same DVM for the upper resistance range between 1 GΩ and 100 GΩ. The DVM and the current amplifier were calibrated at the French National Metrology Institute (LNE) following the highest standards in metrology (see Supporting Information File 1, section S1).

Table 1 compares the nominal resistance values with those measured for each resistor, $R_{i,meas}$, at the rectangular pads using probe station measurements with the combined uncertainties. All uncertainties in the paper are given at one standard deviation corresponding to a 68% confidence level in the case of a normal distribution [46]. All measured values were in excellent agreement with the nominal ones within the tolerance limit indicated by the manufacturer, except for the first three pads. Owing to their low values, these three resistances ($R_{1,meas}$, $R_{2,meas}$, and $R_{3,meas}$) were corrected by accounting for the resistances of the connection line segments, $R_{i,seg}$, in the central zone of the sample, and the resistance of the wiring, $R_{wire}$, between the two probes and the DVM. Considering the dimensions of the line segments and the measured resistivity of the deposited gold lines ($\rho = (31.4 \pm 0.4) \times 10^{-9}$ Ω·m), we calculated three correction resistances $R_{1,seg} = 21.2$ Ω, $R_{2,seg} = 20.1$ Ω, and $R_{3,seg} = 22.4$ Ω for the first three pads, respectively. The measured value of the supplementary resistance due to the wiring (including the resistance of the two probes and the cable resistances) was determined at $R_{wire} = 1.8$ Ω (see Supporting Information File 1, section S2).

The combined uncertainty values in Table 1 were calculated using the root-sum-square method (RSS) from uncertainties related to the sample, the environmental conditions, the measurement circuit, and the measurement repeatability. The uncertainties were estimated using the reference evaluation methods [46]. The major uncertainty components originated from the sample temperature and voltage effects, ranging from 1.1 parts in $10^3$ to 1 part in $10^4$ with decreasing resistance values. The

**Table 1:** Nominal ($R_{i,nom}$) and measured ($R_{i,meas}$) values for the 15 pads and combined uncertainties $u_i$ in relative values (%). The uncertainties are given at one standard deviation. The tolerance on the values of the mounted resistors and the measurement date are given.

| *i* (pad index) | $R_{i,nom}$ (Ω) (resistor) | Tolerance (%) | $R_{i,meas}$ (Ω) (pad) | $u_i$ (%) |
|---|---|---|---|---|
| 1 | $1 \times 10^2$ | 0.5 | $1.672 \times 10^2$ | 0.03 |
| 2 | $1 \times 10^3$ | 1 | $1.068 \times 10^3$ | 0.03 |
| 3 | $1 \times 10^4$ | 0.05 | $1.007 \times 10^4$ | 0.03 |
| 4 | $1 \times 10^5$ | 0.1 | $1.000 \times 10^5$ | 0.03 |
| 5 | $1 \times 10^6$ | 1 | $1.000 \times 10^6$ | 0.03 |
| 6 | $5 \times 10^6$ | 1 | $5.011 \times 10^6$ | 0.03 |
| 7 | $1 \times 10^7$ | 1 | $0.998 \times 10^7$ | 0.03 |
| 8 | $5 \times 10^7$ | 1 | $4.975 \times 10^7$ | 0.03 |
| 9 | $1 \times 10^8$ | 1 | $0.998 \times 10^8$ | 0.03 |
| 10 | $5 \times 10^8$ | 5 | $5.043 \times 10^8$ | 0.06 |
| 11 | $1 \times 10^9$ | 10 | $1.000 \times 10^9$ | 0.09 |
| 12 | $5 \times 10^9$ | 10 | $4.610 \times 10^9$ | 0.13 |
| 13 | $1 \times 10^{10}$ | 30 | $0.972 \times 10^{10}$ | 0.13 |
| 14 | $5 \times 10^{10}$ | 30 | $3.611 \times 10^{10}$ | 0.17 |
| 15 | $1 \times 10^{11}$ | 30 | $0.784 \times 10^{11}$ | 0.17 |

other main uncertainties did not exceed 4 parts in $10^4$, which were related to the calibrations of the measurement instruments (particularly the current amplifier gain), the leakage resistances, and the measurement noise (see Supporting Information File 1, sections S3 and S4).

## Resistance values in C-AFM imaging mode

Following the calibration of the SMD resistors, C-AFM imaging measurements were conducted by scanning the central zone of the sample. Experiments were performed using a Multimode 8 AFM system with a Nanoscope V controller (Bruker, USA) operated in contact mode with CDT-FMR diamond-coated probes (Nanosensors, USA). Resistance maps (512 × 512 pixels) were recorded using a recently developed custom-built external wide-range current measuring device (WCMD), connected to the AFM system operating under ambient environmental conditions (no shielding and no air conditioning system). The WCMD device consists of a current amplifier with an automatic gain regulation. It allows for, under usual AFM scanning conditions, current and resistance mapping as well as *I*–*V* spectroscopy over a wide range of current measurement (from 100 µA to less than 100 fA) (see Supporting Information File 1, section S1). Previous experiments have shown diamond-coated tips to be most suitable for imaging gold surfaces in ambient air. A DC bias voltage of 1 V was applied to the sample, while the scanning speed was set to 12 µm·s$^{-1}$ and the scan orientation was parallel to the cantilever's central axis.

The resistance map in Figure 2 was acquired over the central zone of the sample, showing 15 electrode arms corresponding to the end of the gold connection lines linked to the intermediate gold pads previously measured in Table 1. The imaging result shows a distinguishable resistance contrast for the values expected between 10 kΩ and 100 GΩ, which validates the applicability of the developed sample for the calibration of C-AFM measurements in scanning mode. To extract quantitative values comparable to those listed in Table 1, the surface of each electrode was individually imaged at different locations using the same operating parameters, that is, scan speed, scan orientation, applied force, and bias voltage. A histogram was extracted for each resistance map, and the data were fitted to Gaussian distributions. The results showed that the mean value of measured resistances deviates significantly from the expected value in Table 1 by more than 100% for the first three electrode arms

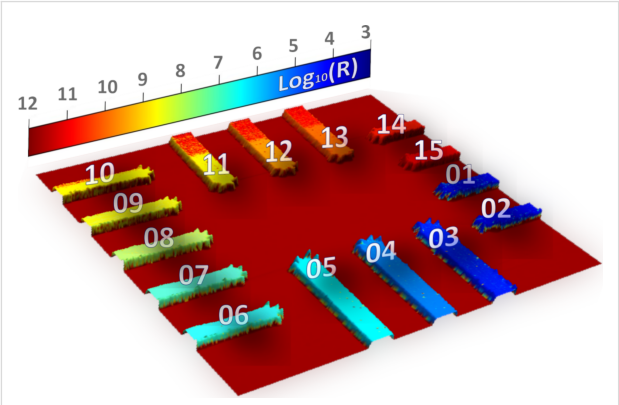


**Figure 2:** Resistance map of the sample's central zone (60 µm × 60 µm) imaged by C-AFM. Numbers refer to the index *i* of the resistance arms. The color rendering refers to the measured resistance values given in decimal logarithm scale.

$i$ = 1 to $i$ = 3 (i.e., 100 Ω, 1 kΩ, and 10 kΩ). In this case, the significant deviation was attributed to the high resistance of the AFM tip (ca. 10 kΩ, nominal value from the manufacturer), which prevents a correct measurement of small resistance values. For the remaining electrode arms $i$ = 4 to $i$ = 15 (i.e., 100 kΩ to 100 GΩ), the measured values from the resistance maps deviated by 20% to 28% compared to those determined in Table 1. This error was partly related to an erroneous reading from the AFM controller unit, which systematically added an offset to the measured values, as identified by injecting external test DC voltage signals to the controller. Thus, further measurements were conducted by shortcutting the AFM controller and recording resistance values measured directly by the WCMD device. Nonetheless, a remaining deviation of the resistance values obtained in C-AFM imaging mode relative to the values in Table 1 was still observed of the order of 8%.

## Resistance values from C-AFM *I–V* curves

To comprehend the origin of this remaining error, we proceeded into removing any possible contamination of the tip apex by repeatedly scanning over a fixed line (typically a few tens of nanometers) on the sample surface (i.e., by disabling the slow-scan axis). The effective contamination removal was associated with a stable measurement of a minimal resistance value. Then, we positioned the tip at a fixed location in contact with the electrode's surface with an applied force of 900 nN to extract *I–V* curves by sweeping the applied voltage between −1 V and +1 V. This approach mitigates the difficulties related to surface contamination on the gold electrodes during scanning. Resistance values for each electrode arm were determined from the slopes of the *I–V* straights using a regression model. For each value, the coefficient of determination ($R^2$) was equal to 1 (see Supporting Information File 1, section S5 and Figure S1). The results were globally found within a 2.5% deviation relative to the resistance values in Table 1.

In comparison, an excellent agreement (within 1%) was obtained for the specific range of 1 MΩ and 50 GΩ, as shown in Figure 3. The resistance values for the electrode arms $i$ = 3, 4, and 5 (i.e., 10 kΩ, 100 kΩ, and 1 MΩ, respectively) were corrected by accounting for the tip resistance, which was measured on a copper film at $R_{tip}$ = 6591 Ω with a relative

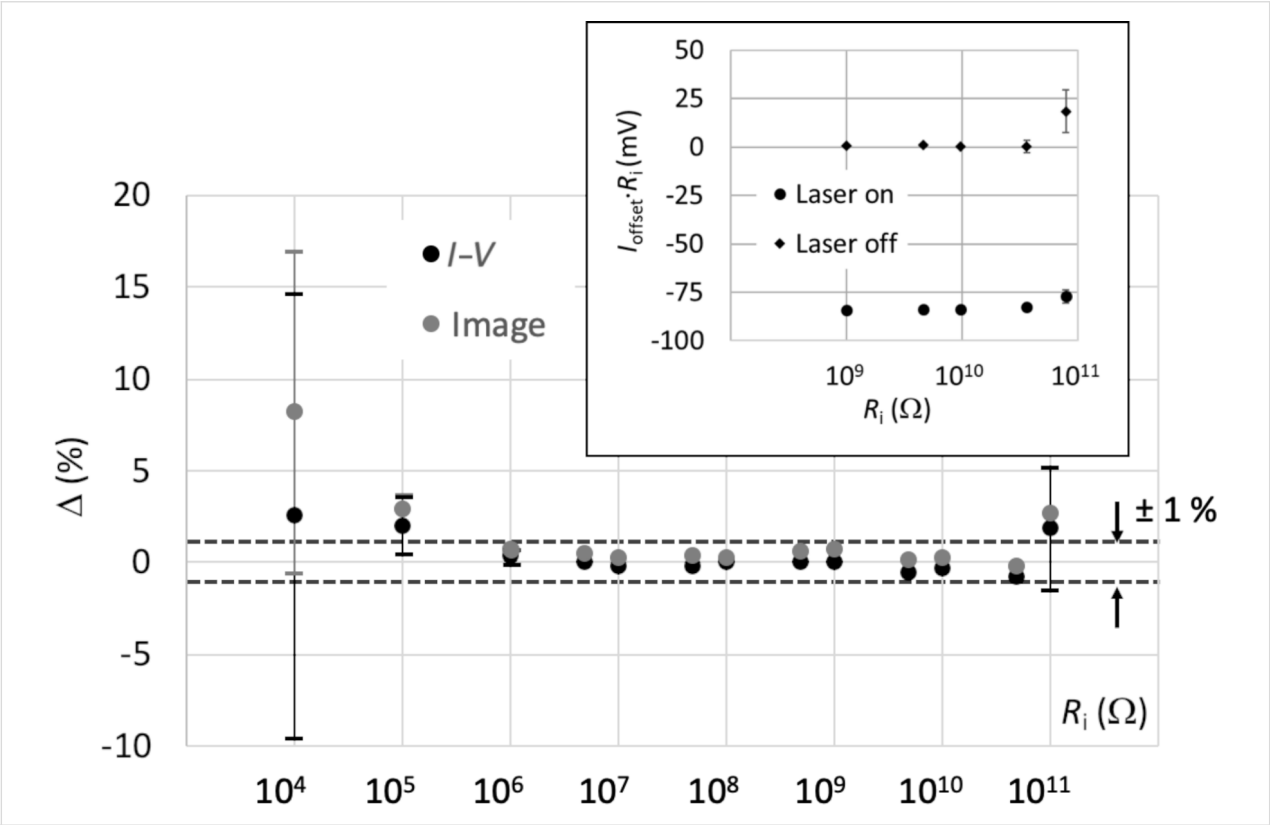


**Figure 3:** Relative deviations $\Delta = (R_{i,AFM} - R_{i,cal})/R_{i,cal}$ in percent from imaging (full grey circles) and from *I–V* curves (full black circles). Values for 10 kΩ, 100 kΩ, and 1 MΩ were corrected to take into account the measured tip resistance (6591 Ω). The error bars denote the uncertainties calculated from the RSS method from the total uncertainties due to the resistance reference (reported in Table 1) and the measurement repeatability. In the insert, the products $I_{offset}$·$R_i$ are given in millivolts, where $I_{offset}$ denotes the current offset observed at zero bias voltage on the *I–V* curves, when the AFM laser is turned on (full circles) and off (full diamonds), for the highest resistances. The error bar (only visible for $10^{11}$ Ω) refers to the standard deviation of data (repeatability).

uncertainty of 1% (conservative value). It is worth noting that, for higher resistance values up to 100 GΩ, the correction accounting for the tip resistance value becomes largely insignificant. Despite the reduced uncertainty for the resistance values determined from the *I*–*V* curves, those obtained from the imaging results still showed a non-negligible deviation. In addition, we noticed that all *I*–*V* straights did not pass through zero, which introduced a shift in the measured currents leading to an increase in the resistance values by a constant amount of (+8 ± 1)%, which agrees very well with the deviations observed from the image values (taken at a bias voltage of +1 V).

The origin of *I*–*V* curves not going through zero is commonly associated with photovoltaic effects, which was indeed validated by the disappearance of this observation when the laser of the AFM setup was switched off. Although, a photovoltaic effect might be intriguing in current measurements on gold pads, this observation was systematically made for the *I*–*V* curves measured on all gold electrode arms. Through further investigations, we were able to associate this observation with the use of worn AFM diamond tips, especially formed by a p-type diamond coating on a highly doped n-type Si core. Thus, the photovoltage effect observed in our paper is solely related to the tip apex and does not depend on the measured sample. We were able to confirm this aspect by running *I*–*V* curves using new probes with intact apexes, which showed no shift around zero even with the AFM laser on. This effect is currently under thorough investigations for a future publication. Accordingly, a new set of images was acquired for the electrodes $i = 3$ to $i = 15$ at two bias voltages of +1 V and −1 V, and the corresponding resistance value was determined by their mean value. For each electrode, this imaging protocol was repeated at three to five zones to enhance statistical values. The final resistance of an electrode corresponded to the average value of the three to five measurements. Figure 3 shows an excellent agreement between the resistance values obtained from C-AFM images and those from *I*–*V* curves with a maximum global deviation of 1%. However, the electrode arm $10^4$ Ω ($i = 3$) showed 5.7% deviation, which is well within the corresponding uncertainty.

Our findings show that the multi-resistance reference sample developed in this work enables a universal calibration of C-AFM measurements in both imaging and spectroscopic (i.e., *I*–*V* curves) modes with a 1% achievable relative uncertainty level in the range between $10^6$ Ω and $5 \times 10^{10}$ Ω. The protocols adopted in this study highlight several routes for further improvements. Using platinum as metallic material instead of gold for the small electrode arms would help reduce surface contamination-related issues. Consequently, measuring the lowest resistance values would become accessible using low-resistance metallic probes (e.g., Pt-coated or full bulk Pt probes). However, using such probes will require limiting the current (typically 100 μA) to avoid excessive Joule heating within the nanocontact.

## Conclusion

We have designed a multi-resistance wide-range reference for calibrating the complete C-AFM measurement circuit over a resistance range from 100 Ω to 100 GΩ. A set of operating protocols have been demonstrated for measuring resistance in C-AFM within the range from 10 kΩ to 100 GΩ with deviations lower than 2.5% relative to values calibrated at the macroscale using probe station measurements. The design of the proposed calibration sample features access to a wide range of resistance values (nine decades) within a single AFM scan, calibration of these resistances at the macroscale using a probe station, compatibility with any commercially available AFM system, and the possibility of positioning a device under test (DUT) on the reference sample. Further efforts are underway to develop another sample version featuring easier access to C-AFM measurements of the lowest resistances (from 100 Ω to 10 kΩ) and an expanded resistance range up to 1 TΩ. The outcome of the present work is expected to promote the applicability of C-AFM for the local measurements of DC resistances and currents at the nanoscale, which constitutes an essential requirement for coping with the ever-increasing shrinkage of technological devices. It is worth noting that the authors are closely working with the International Electrotechnical Commission (IEC-TC113) for the creation of documentary standards regarding resistance measurements in C-AFM.

## Supporting Information

### Supporting Information File 1

Additional experimental information.
[https://www.beilstein-journals.org/bjnano/content/supplementary/2190-4286-14-94-S1.pdf]

## Acknowledgements

Part of this work was done at the C2N micro nanotechnologies platforms and was partly supported by the RENATECH network and the General Council of Essonne. The authors are grateful to José Alvarez for fruitful discussions, Emmanuel Patois for calibration assistance, and Djamel Ziane for software assistance.

## Funding

This research work was carried out in the framework of the ELENA project (EMPIR 20IND12), which is supported by the European Metrology Programme for Innovation and Research

(EMPIR). The EMPIR initiative is co-funded by the European Horizon 2020 research and innovation program and the EMPIR Participating States.

## Competing Interests

The authors declare no competing interests.

## ORCID® iDs

François Piquemal - https://orcid.org/0000-0002-7950-0475
Khaled Kaja - https://orcid.org/0000-0002-2394-4595
Pascal Chrétien - https://orcid.org/0009-0005-5177-1360
José Morán-Meza - https://orcid.org/0000-0001-6352-6040
Frédéric Houzé - https://orcid.org/0000-0001-8054-3184
Christian Ulysse - https://orcid.org/0000-0001-9814-0535
Abdelmounaim Harouri - https://orcid.org/0000-0003-1813-6347

## Preprint

A non-peer-reviewed version of this article has been previously published as a preprint: https://doi.org/10.3762/bxiv.2023.24.v1

## References

1. Murrell, M. P.; Welland, M. E.; O'Shea, S. J.; Wong, T. M. H.; Barnes, J. R.; McKinnon, A. W.; Heyns, M.; Verhaverbeke, S. *Appl. Phys. Lett.* **1993,** *62,* 786–788. doi:10.1063/1.108579
2. Lanza, M., Ed. *Conductive Atomic Force Microscopy: Applications in Nanomaterials;* Wiley-VCH: Weinheim, Germany, 2017. doi:10.1002/9783527699773
3. Kalinin, S. V.; Gruverman, A. Introduction scanning probe microscopy techniques for electrical and electromechanical characterization. *Scanning Probe Microscopy;* Springer: New York, NY, USA, 2007; Vol. 1, pp 1–8. doi:10.1007/978-0-387-28668-6_1
4. Mikulik, D.; Ricci, M.; Tutuncuoglu, G.; Matteini, F.; Vukajlovic, J.; Vulic, N.; Alarcon-Llado, E.; Fontcuberta i Morral, A. *Nano Energy* **2017,** *41,* 566–572. doi:10.1016/j.nanoen.2017.10.016
5. Rodenbücher, C.; Bihlmayer, G.; Speier, W.; Kubacki, J.; Wojtyniak, M.; Rogala, M.; Wrana, D.; Krok, F.; Szot, K. *Nanoscale* **2018,** *10,* 11498–11505. doi:10.1039/c8nr02562b
6. Fernando, P. S.; Mativetsky, J. M. *J. Phys. Chem. C* **2023,** *127,* 9903–9910. doi:10.1021/acs.jpcc.3c01651
7. Greco, G.; Fiorenza, P.; Schilirò, E.; Bongiorno, C.; Di Franco, S.; Coulon, P.-M.; Frayssinet, E.; Bartoli, F.; Giannazzo, F.; Alquier, D.; Cordier, Y.; Roccaforte, F. *Microelectron. Eng.* **2023,** *276,* 112009. doi:10.1016/j.mee.2023.112009
8. Hussain, S.; Xu, K.; Ye, S.; Lei, L.; Liu, X.; Xu, R.; Xie, L.; Cheng, Z. *Front. Phys.* **2019,** *14,* 33401. doi:10.1007/s11467-018-0879-7
9. Giannazzo, F.; Schilirò, E.; Greco, G.; Roccaforte, F. *Nanomaterials* **2020,** *10,* 803. doi:10.3390/nano10040803
10. Daher Mansour, M.; Oswald, J.; Beretta, D.; Stiefel, M.; Furrer, R.; Calame, M.; Vuillaume, D. *Nanoscale* **2023,** *15,* 9203–9213. doi:10.1039/d2nr06682c
11. Thomas, S. *Nat. Electron.* **2023,** *6,* 264. doi:10.1038/s41928-023-00963-7
12. Wei, T.; Lu, Y.; Zhang, F.; Tang, J.; Gao, B.; Yu, P.; Qian, H.; Wu, H. *Adv. Mater. (Weinheim, Ger.)* **2023,** *35,* 2209925. doi:10.1002/adma.202209925
13. Liang, Z. W.; Wu, P.; Wang, L. C.; Shen, B. G.; Wang, Z.-H. *Chin. Phys. B* **2023,** *32,* 047303. doi:10.1088/1674-1056/acb421
14. Roldán, J. B.; Miranda, E.; Maldonado, D.; Mikhaylov, A. N.; Agudov, N. V.; Dubkov, A. A.; Koryazhkina, M. N.; González, M. B.; Villena, M. A.; Poblador, S.; Saludes-Tapia, M.; Picos, R.; Jiménez-Molinos, F.; Stavrinides, S. G.; Salvador, E.; Alonso, F. J.; Campabadal, F.; Spagnolo, B.; Lanza, M.; Chua, L. O. *Adv. Intell. Syst.* **2023,** 2200338. doi:10.1002/aisy.202200338
15. Roldán, J. B.; Maldonado, D.; Cantudo, A.; Shen, Y.; Zheng, W.; Lanza, M. *Appl. Phys. Lett.* **2023,** *122,* 203502. doi:10.1063/5.0147403
16. Kutes, Y.; Aguirre, B. A.; Bosse, J. L.; Cruz-Campa, J. L.; Zubia, D.; Huey, B. D. *Prog. Photovoltaics* **2016,** *24,* 315–325. doi:10.1002/pip.2698
17. Lee, A.-T.; Tan, C.-S.; Huang, M. H. *ACS Cent. Sci.* **2021,** *7,* 1929–1937. doi:10.1021/acscentsci.1c01067
18. Si, H.; Zhang, S.; Ma, S.; Xiong, Z.; Kausar, A.; Liao, Q.; Zhang, Z.; Sattar, A.; Kang, Z.; Zhang, Y. *Adv. Energy Mater.* **2020,** *10,* 1903922. doi:10.1002/aenm.201903922
19. Chang, M. N.; Chen, C. Y.; Yang, M. J.; Chien, C. H. *Appl. Phys. Lett.* **2006,** *89,* 133109. doi:10.1063/1.2357873
20. Frammelsberger, W.; Benstetter, G.; Kiely, J.; Stamp, R. *Appl. Surf. Sci.* **2007,** *253,* 3615–3626. doi:10.1016/j.apsusc.2006.07.070
21. Yang, H.; Shin, T. J.; Ling, M.-M.; Cho, K.; Ryu, C. Y.; Bao, Z. *J. Am. Chem. Soc.* **2005,** *127,* 11542–11543. doi:10.1021/ja052478e
22. Iglesias, V.; Porti, M.; Nafría, M.; Aymerich, X.; Dudek, P.; Bersuker, G. *J. Vac. Sci. Technol., B: Nanotechnol. Microelectron.: Mater., Process., Meas., Phenom.* **2011,** *29,* 01AB02. doi:10.1116/1.3532945
23. Ganesan, K.; Ilango, S.; Mariyappan, S.; Baroughi, M. F.; Kamruddin, M.; Tyagi, A. K. *Appl. Phys. Lett.* **2011,** *98,* 092902. doi:10.1063/1.3560307
24. Sakaguchi, H.; Hirai, A.; Iwata, F.; Sasaki, A.; Nagamura, T.; Kawata, E.; Nakabayashi, S. *Appl. Phys. Lett.* **2001,** *79,* 3708–3710. doi:10.1063/1.1421233
25. Duong, D. T.; Phan, H.; Hanifi, D.; Jo, P. S.; Nguyen, T.-Q.; Salleo, A. *Adv. Mater. (Weinheim, Ger.)* **2014,** *26,* 6069–6073. doi:10.1002/adma.201402015
26. Pingree, L. S. C.; Reid, O. G.; Ginger, D. S. *Adv. Mater. (Weinheim, Ger.)* **2009,** *21,* 19–28. doi:10.1002/adma.200801466
27. Rawlett, A. M.; Hopson, T. J.; Nagahara, L. A.; Tsui, R. K.; Ramachandran, G. K.; Lindsay, S. M. *Appl. Phys. Lett.* **2002,** *81,* 3043–3045. doi:10.1063/1.1512815
28. Kelley, T. W.; Granstrom, E.; Frisbie, C. D. *Adv. Mater. (Weinheim, Ger.)* **1999,** *11,* 261–264. doi:10.1002/(sici)1521-4095(199903)11:3<261::aid-adma261>3.0.co;2-b
29. Mativetsky, J. M.; Loo, Y.-L.; Samorì, P. *J. Mater. Chem. C* **2014,** *2,* 3118–3128. doi:10.1039/c3tc32050b
30. Muzyka, K.; Rico, F.; Xu, G.; Casuso, I. *J. Electroanal. Chem.* **2023,** *938,* 117448. doi:10.1016/j.jelechem.2023.117448
31. Wang, Y.; Xie, Y.; Gao, M.; Zhang, W.; Liu, L.; Qu, Y.; Wang, J.; Hu, C.; Song, Z.; Wang, Z. *Nanotechnology* **2022,** *33,* 055301. doi:10.1088/1361-6528/ac0be6
32. Zhao, J.; Davis, J. J. *Nanotechnology* **2003,** *14,* 1023–1028. doi:10.1088/0957-4484/14/9/317
33. Zhao, L.; Du, X.; Fang, B.; Liu, Q.; Yang, H.; Li, F.; Sheng, Y.; Zeng, X.; Zhong, H.; Zhao, W. *Ultramicroscopy* **2022,** *237,* 113531. doi:10.1016/j.ultramic.2022.113531

34. Zhao, W.; Cheong, L.-Z.; Xu, S.; Cui, W.; Song, S.; Rourk, C. J.; Shen, C. J. *J. Microsc. (Oxford, U. K.)* **2020,** *277,* 49–57. doi:10.1111/jmi.12861
35. Sato, T.; Kasai, S.; Hasegawa, H. *Jpn. J. Appl. Phys., Part 1* **2001,** *40,* 2021. doi:10.1143/jjap.40.2021
36. Ranjan, A.; Raghavan, N.; Molina, J.; O'Shea, S. J.; Shubhakar, K.; Pey, K. L. *Microelectron. Reliab.* **2016,** *64,* 172–178. doi:10.1016/j.microrel.2016.07.112
37. Tejedor, P.; García-Tabarés, E.; Galiana, B.; Vázquez, L.; García, B. J. *Appl. Surf. Sci.* **2023,** *616,* 156518. doi:10.1016/j.apsusc.2023.156518
38. Vandervorst, W.; Meuris, M. Method for resistance measurements on a semiconductor element with controlled probe pressure. U.S. Patent US5369372A, Nov 29, 1994.
39. Schneegans, O.; Chrétien, P.; Houzé, F. Apparatus for measuring the local electrical resistance of a surface. WO Pat. Appl. WO2011138738A1, Oct 11, 2011.
40. Schneegans, O.; Chrétien, P.; Houzé, F. Apparatus for measuring the local electrical resistance of a surface. Eur. Pat. Appl. EP2567245A1, March 13, 2013.
41. Sumaiya, S. A.; Martini, A.; Baykara, M. Z. *Nano Express* **2020,** *1,* 030023. doi:10.1088/2632-959x/abcae0
42. Vazirisereshk, M. R.; Sumaiya, S. A.; Chen, R.; Baykara, M. Z.; Martini, A. *Tribol. Lett.* **2021,** *69,* 50. doi:10.1007/s11249-021-01420-2
43. Jiang, L.; Weber, J.; Puglisi, F. M.; Pavan, P.; Larcher, L.; Frammelsberger, W.; Benstetter, G.; Lanza, M. *Materials* **2019,** *12,* 459. doi:10.3390/ma12030459
44. Weber, J.; Yuan, Y.; Kühnel, F.; Metzke, C.; Schätz, J.; Frammelsberger, W.; Benstetter, G.; Lanza, M. *ACS Appl. Mater. Interfaces* **2023,** *15,* 21602–21608. doi:10.1021/acsami.3c01102
45. Lanza, M. *Materials* **2014,** *7,* 2155–2182. doi:10.3390/ma7032155
46. Joint Committee for Guides in Metrology - JCGM. Evaluation of Measurement Data – Guide to the Expression of Uncertainty in Measurement. JCGM 100 2008. https://www.bipm.org/en/publications/guides/gum.html.

## License and Terms

BEILSTEIN JOURNAL OF NANOTECHNOLOGY

# Spatial variations of conductivity of self-assembled monolayers of dodecanethiol on Au/mica and Au/Si substrates

Julian Skolaut*[1], Jędrzej Tepper[2], Federica Galli[2], Wulf Wulfhekel[1,3] and Jan M. van Ruitenbeek[2]

Full Research Paper

Open Access

Address:
[1]Institute for Quantum Materials and Technology, Karlsruhe Institute of Technology, Hermann-von-Helmholtz-Platz 1, 76344 Eggenstein-Leopoldshafen, Germany, [2]Huygens-Kamerlingh Onnes Laboratorium, Leiden University, Niels Bohrweg 2, 2333 CA Leiden, Netherlands and [3]Physikalisches Institut, Karlsruhe Institute of Technology, Wolfgang-Gaede-Straße 1, 76131, Karlsruhe, Germany

Email:
Julian Skolaut* - jskolaut@uni-mainz.de

* Corresponding author

Keywords:
Au/mica; Au/Si; conductive atomic force microscopy; dodecanethiol; self-assembled monolayers

*Beilstein J. Nanotechnol.* **2023,** *14,* 1169–1177.
https://doi.org/10.3762/bjnano.14.97

Received: 23 June 2023
Accepted: 08 November 2023
Published: 05 December 2023

This article is part of the thematic issue "Advanced atomic force microscopy techniques V".

Associate Editor: T. Glatzel



## Abstract

Determining the conductivity of molecular layers is a crucial step in advancing towards applications in molecular electronics. A common test bed for fundamental investigations on how to acquire this conductivity are alkanethiol layers on gold substrates. A widely used approach in measuring the conductivity of a molecular layer is conductive atomic force microscopy. Using this method, we investigate the influence of a rougher and a flatter gold substrate on the lateral variation of the conductivity. We find that the roughness of the substrate crucially defines this variation. We conclude that it is paramount to adequately choose a gold substrate for investigations on molecular layer conductivity.

## Introduction

For decades, the need for miniaturization of electronics has pushed the research field into the direction of bottom-up, rather than top-down, approaches. In this research field, molecular electronics [1-3] has always held a central role, as the flexibility and control over the structure of molecules is unmatched. One of the fundamental parts of devices employing a bottom-up approach combined with molecular electronics is comprised of metal electrodes and molecular layers deposited onto them.

For the use in applications, the properties of such layers of molecules and the interface they form with the metal substrate have to be investigated carefully and systematically. In order to achieve comparability between different types of molecules, ordered layers are favorable, which makes self-assembled monolayers (SAMs) a perfect test bed for studies on molecular layers.

With the idea of molecular electronics in mind, most studies have been aimed at studying the conductivity of SAMs. In previous studies, the contacting of SAMs has been achieved in various ways [4]. We focus here on the contacting of molecular layers between a metal surface and a locally probing electrode. In early studies using this approach, the layers were contacted by a mercury droplet at the end of an electrode, which was then placed on top of the SAM [5-7]. Applying a voltage and, therefore, a current to the substrate and the mercury electrode yields the conductivity of the SAM, averaged over the contact area of the mercury droplet. In such studies, one of the crucial problems was mercury filling out defects in the SAMs, which leads to short circuits and unreliable currents running through the microcontact.

This was avoided in later experiments by using eutectic GaIn (eGaIn) droplets [8-11]. These are much more viscous, to the point that they are almost solid. This reduces the amount of leak currents significantly and makes studies on the conductivity of SAMs much more reliable. A more widely applied method uses conductive atomic force microscopy (CAFM). In this technique, a conductive probe is used in an AFM, which allows for imaging the surface topography (and other characteristics such as adhesion and stiffness) with lateral resolution while simultaneously being able to measure current characteristics. Moreover, the probes used in CAFM are significantly sharper compared to, for example, mercury droplets or eGaIn, which makes it possible to avoid short circuits to the metallic surface relatively easily.

In previous studies, CAFM has been used to investigate the conductivity of surfaces and SAMs, including many studies performed recently on SAMs of helical oligopeptides studying chiral-induced spin-selectivity [12-15]. Here, we re-examine the information that is obtained from CAFM, and we demonstrate that the nature of the metallic substrate is of critical importance. The lateral variation of current characteristics strongly depends on the substrate chosen to deposit the SAM onto. For this study, we employ alkane thiols, which are allowed to form a SAM on different types of Au substrates. We have chosen dodecanethiol (DDT) molecules and study them on commercially available Au substrates consisting of thin Au layers of different surface roughness. We compare granular Au films deposited on Si wafers with epitaxial (flat) Au films on mica.

## Experimental

Before the experimental results are presented, this section focuses on the preparation of the samples under study and the setup used to carry out the measurements. As mentioned above, two types of Au substrates were used, that is, Au-coated Si (Au/Si) and epitaxially grown Au on mica (Au/mica), bought from Sigma-Aldrich and Phasis, respectively. The Au thicknesses are 200 nm for Au/mica and 100 nm for Au/Si substrates. The Au/mica substrates were used directly out of the box without any further cleaning steps. Au/Si was additionally cleaned by boiling in acetone followed by ethanol for 20 min under a fume hood. It was then dried in a glovebox in $N_2$ atmosphere, exposed to ozone to remove organic contaminants, and finally rinsed with warm ethanol.

DDT SAMs were deposited onto these substrates by immersing them in a 10 mM solution of DDT in ethanol with subsequent incubation for 24 h. After transfer into a glovebox, the samples were rinsed with ethanol and dried. To improve the order of the SAMs, they were again immersed in 10 mM DDT/ethanol solution and heated to ≈80 °C for 1 h. After gradual cooldown, the samples were again rinsed and dried in $N_2$ atmosphere in the glovebox.

The obtained samples were studied using a commercially available JPK NanoWizard® 3 AFM setup. The setup has been upgraded by a CAFM tip holder with an integrated preamplifier, whose feedback resistor of 1 GΩ fixes the maximum measurable current to 12 nA, sets the amplification to $10^9$ V/A, and allows one to measure currents down to few tens of picoamperes.

In the studies presented here, two types of CAFM-probes were used. For the studies on DDT SAMs on Au/mica, Bruker MESP-V2 (CoCr-coated Si) probes were used, whereas, for the remaining measurements, Rocky Mountain Nanotechnology RMN-25PT300B probes with solid Pt wire as tips were used. The latter have the advantage that they do not oxidize easily and remain conductive, as there is no fragile metal coating on a non-conductive probe in contrast to the CoCr-coated Si probes. This is at the cost of lateral resolution due to the larger radius of the probe apex.

All measurements presented here were carried out in the Quantitative Imaging (QI™) mode by JPK. A sketch of the procedure is shown in Figure 1. In this mode of CAFM operation, a force–distance curve is measured at every pixel of the image. The tip is approached until a certain bend of the cantilever is

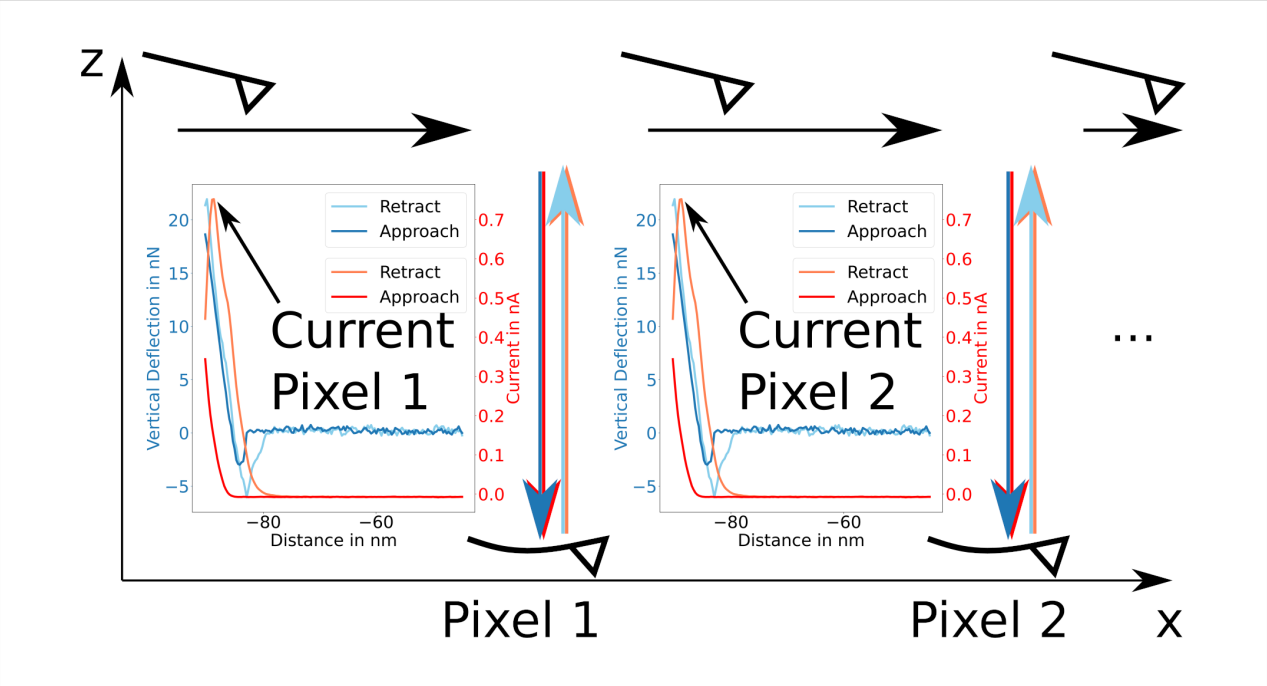


**Figure 1:** In QI™ mode, the probe measures force and conductance curves at a raster of points on the surface, shown here for a row along the *x* direction. The probe is moved from pixel to pixel in a retracted position far away from the surface. At each point, a force–distance curve is measured while simultaneously acquiring the current. Current maps show the currents extracted as the extremal value of each current curve.

reached, corresponding to the force setpoint $F_{\text{setpoint}}$. Plotting the $z$ position at which the force setpoint is reached provides the topographic information, which we represent here as a yellow–blue color map. During the whole measurement, a bias voltage $U_{\text{bias}}$ is applied between tip and sample. Simultaneously to the force–distance curve, the current is acquired. As it can be seen from the example curves in Figure 1, the extremal current is usually found close to the force setpoint, and both are correlated. The small shift of the position of the extremal current towards larger $z$ distance can be explained by the bandwidth of the preamplifier (specified as 2 kHz). The relatively high rate of 40 approach/retraction cycles per second was chosen as a compromise between bandwidth distortion and total measurement time.

Plotting the extremal current yields the current maps shown here in gray scale and provides a measure to compare the conductive properties in different areas of the surface. Using the QI mode is particularly advantageous in our study, since it measures topography and current simultaneously and reduces wear effects on the tips.

## Results and Discussion

We divided the results obtained with the methods described above into two main sections. These are studies on (i) the bare substrates and on (ii) the DDT SAMs on these substrates. The bare substrates were investigated as a reference for the measurements thereafter. They show topographies and current maps characteristic for Au/Si and Au/mica. Subsequently, it was observed how these characteristics change with SAMs deposited onto the surface. A strong resemblance between bare and SAM-covered surfaces was observed. This bears important consequences for the choice of substrates for studies on molecular SAMs; flat substrates are advantageous for such studies.

### Bare Au/Si and Au/mica substrates

As mentioned above, two types of Au substrates were investigated, namely Au/Si and Au/mica. The measurements on bare substrates presented here serve as a reference for the studies on the lateral variation of the conductivity of DDT SAMs on said substrates. The reference helps in identifying how much of the SAM's lateral variation of conductivity stems from the substrate.

Figure 2a and Figure 2b show the topography and the current map, respectively, for a Au/mica substrate. The 300 × 300 nm$^2$ topography map shows that the Au/mica substrate has large flat areas on which the height does not change significantly. The overall change in height throughout the image is approximately 4 nm, and the most significant changes in height occur at the boundaries between different flat areas.

The corresponding current map (Figure 2b) shows a nearly homogeneous distribution of the current throughout the whole

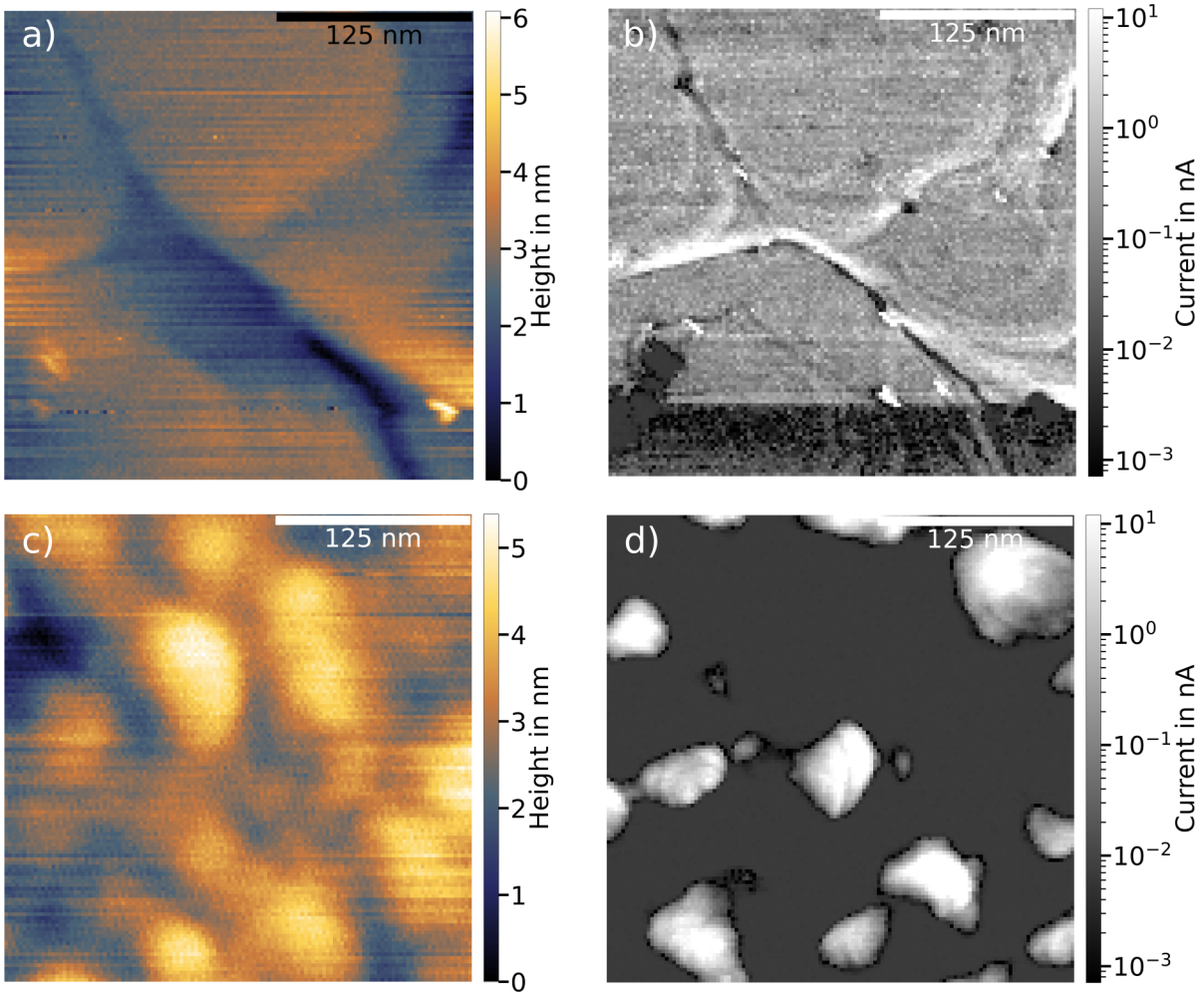


**Figure 2:** (a, b) Topography and current map, respectively, of the bare Au/mica substrate. The large flat areas provide a homogeneous current distribution throughout large parts of the image. The sudden change in current in the lower part of the image can be attributed to a tip change. (c, d) The same data for a Au/Si substrate. The topography shows more substructures, which is reflected in more extreme current values in the current map ($F_{setpoint}$ = 50 nN, $U_{bias}$ = 100 mV, RMN probe).

image, where the current takes on well-measurable values distributed around 200 pA. Only the edges between the flat areas show significant variation from the homogeneous current distribution, making the terrace edges clearly visible. However, as these edge regions are small compared to the flat areas, the overall current distribution is narrow (see Supporting Information File 1, Figure S2a).

In contrast to the Au/mica surface, the Au/Si substrate exhibits a rougher surface, as seen in Figure 2c, in agreement with the difference in growth mode of Au films on the two substrates. For mica, epitaxial growth is obtained [16,17], while Au on $Si/SiO_2$ forms a granular film [18]. Although the overall height variation is not very different from that observed for the Au/mica substrate (approximately 5 nm), the Au/Si surface shows much more substructures and no flat terraces. Compared to the flat terraces of Au/mica, Au/Si has more peaks and valleys, which is also reflected in the current map in Figure 2d. Here, most of the current map is either at the lower limit of the measurable current (few tens of picoamperes) or at the top end of the current range (high-nanoampere regime) (see Supporting Information File 1, Figure S2b). The transition from low to high currents takes place on rather small length scales of tens of nanometers.

The areas of high current appear to coincide with areas of lower topography, slightly skewed to the bottom right of areas with higher topography. This happens all over the image and indicates an effect of the probe influencing the occurrence of high-current areas. The higher currents found in the valleys likely

result from varying surface-normal load forces. They are smaller if the probe contacts the surface on a flat area and larger if the contact is on a slope in the topography. As the load force only controls the force component normal to the sample plane, this leads to larger variations in the local normal force when the tip lands on a slope. Therefore, the rougher topography is likely influencing the occurrence of high- and low-current areas. More specifically, this means that the conductance can appear higher on slopes and rough surfaces, as the tip contacts the surface laterally.

This rationalizes the large systematic difference between the two substrates regarding their topography and lateral current variation. The Au/mica substrate shows a flatter topography accompanied by a more homogeneous current distribution. Generally, this is favorable for current measurements on SAMs, as it provides larger areas of comparable current to study the conductive properties of molecular SAMs and their lateral variation. With the lateral variation of the current of the bare substrates being known, a well-founded description of the changes after SAM deposition can be made.

Overall, five areas were investigated on Au/mica and three for Au/Si, which all showed consistent images.

## Dodecanethiol SAMs on Au/mica

Figure 3 shows images of the DDT-covered Au/mica surface obtained after the deposition procedure described above. In

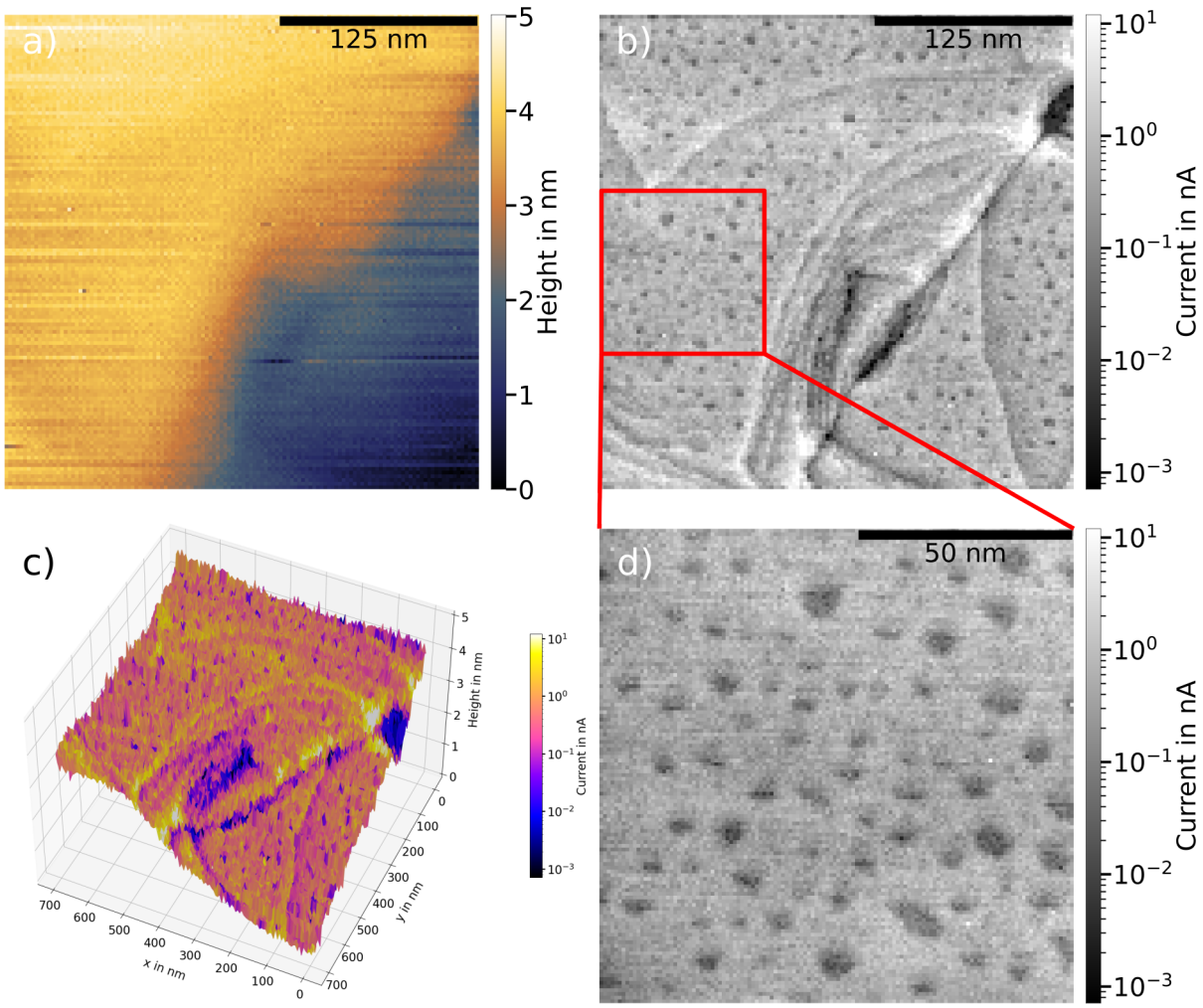


**Figure 3:** (a, b) Topography and current map, respectively, for a DDT SAM on Au/mica, obtained simultaneously on the same area. The current map reveals additional features of the substrate such as shallow terraces and etch pits. The closeup in (d) shows that the etch pit size matches the expected value of a few nanometers. (c) 3D view of the surface, in which the color coding indicates the measured current at each point, clarifying the connection between topography and current. The point of view is adjusted for best visibility ($F_{setpoint}$ = 80 nN, $U_{bias}$ = 1 V, MESP probe).

total, four different areas on two DDT/Au/mica samples were investigated, yielding consistent results. In Figure 3a, the topography is similar to that obtained for the bare Au/mica surface, that is, relatively large flat areas, only small height differences throughout the image, and small roughness of the surface. By means of topography alone, the surface cannot be distinguished from that of the bare Au/mica surface.

Also, upon looking at the current distribution, many features are similar to those of the bare Au/mica surface, including its homogeneous current distribution, for this specific case (Figure 3) around 800 pA. It is sensible that the average current is higher compared to the measurements on the bare Au/mica substrate (Figure 2b), as force setpoint and bias voltage are higher. The average current value of 800 pA is again well measurable and allows for a rough estimation of the resistance of each molecule. Such an estimation can be done without consideration of the resistance of the bare Au substrate, as its resistance is much lower than the SAM's resistance. Assuming that approximately 1000 molecules are contacted [4] and all contacted molecules are connected in parallel, the total resistance of $R_{tot} = U_{bias}/I = 1.25 \times 10^3$ MΩ results in a resistance for one molecule of $R_{mol} = 1.25 \times 10^6$ MΩ. Comparing this value to the literature value ranging between $10^6$ and $10^7$ MΩ per molecule, as presented in [4], shows reasonable agreement.

In addition to the features observed for the bare substrate, including its homogeneous distribution around well-measurable current values, more features are visible in the current map (Figure 3b). First, finer topographic details, namely shallower terraces and boundaries between flat areas of the topography, possibly step edges between single atomic steps of the Au surface, become clearly observable. Second, dark spots on the terraces of the current map appear, which can be seen clearly in the expanded-scale image in Figure 3d. These can be attributed to so-called etch pits that arise from the growth of sulfur-bound SAMs on Au surfaces [19,20]. These etch pits are monatomically deep holes in the Au surface. They are produced in the process of SAM formation by sulfur–gold bonds, which result in removing Au atoms from the top layer. This leaves the surface with Au atom vacancies that arrange into small islands of a few nanometers in size. This size matches the darker areas observed in the current maps after DDT SAM formation. The presence of a well-ordered SAM on the surface was confirmed by scanning tunneling microscopy (STM) images on alkanethiol-covered Au surfaces prepared in the same way, in which the individual molecules can be resolved, shown in Figure S4 in Supporting Information File 1. The etch pits serve as evidence that the SAMs form in an ordered fashion. The abovementioned features can also be seen clearly in the 3D view of the surface in Figure 3c, where the color coding indicates the measured current at each point. The 3D view also underlines the direct correspondence between features in the current map and the topography.

A further indication that the SAM has formed correctly is the observation that it can be thinned by imaging smaller areas with high load forces. As shown in Figure S5 in Supporting Information File 1, after three consecutive imaging runs performed on the same area, the center square of the image appears lower in topography compared to the sides when the scanning area is widened. Also, the measured current increases from image to image, while the etch pits remain intact, indicating that the Au surface structure remains unaffected. We attribute lower topography and increased current to a thinning of the SAM by pushing aside molecules with the probe. Another effect contributing to the thinning of the SAM is molecules being picked up by the probe during the measurement. The effect we observe here is most likely a combination of both processes.

All these indications lead to the conclusion that ordered DDT SAMs form on the surface with the chosen deposition technique. More importantly, the current maps in Figure 3 show that substrate and measurement technique are suitable for obtaining information on the conductivity of a molecular SAM, as the measured currents show a homogeneous distribution and large areas without change in the topography, allowing for comparison between the currents measured on these areas. For quantitative information, it is also important to reduce the load force as suggested by the observed removal of part of the SAM by the tip during imaging. Studies of the extent and type presented here can be used as the basis for well-founded statements concerning electronic properties such as the current–voltage characteristics of the molecular SAM. To this purpose, the characteristics should only be averaged over comparable areas, excluding terrace boundaries and other edges. As the Au/mica substrates provide large areas of this kind, they are favored for the use in studies of the conductive properties of SAMs.

## Dodecanethiol SAMs on Au/Si

The SAM formation technique used for the Au/mica substrates was also used for the Au/Si substrates. As it seems to be suitable for Au/mica substrates, it should also yield densely packed molecular SAMs on Au/Si substrates, allowing for the evaluation of the influence of the substrate on the lateral variation of the conductive properties of SAMs.

For comparison, Figure 4 presents measurements of DDT SAMs on a Au/Si substrate. Comparing topography (Figure 4a) and current map (Figure 4b) to the ones of the bare Au/Si substrate, close similarities can be seen. After coverage of the surface by the SAM, the surface retains the same roughness with

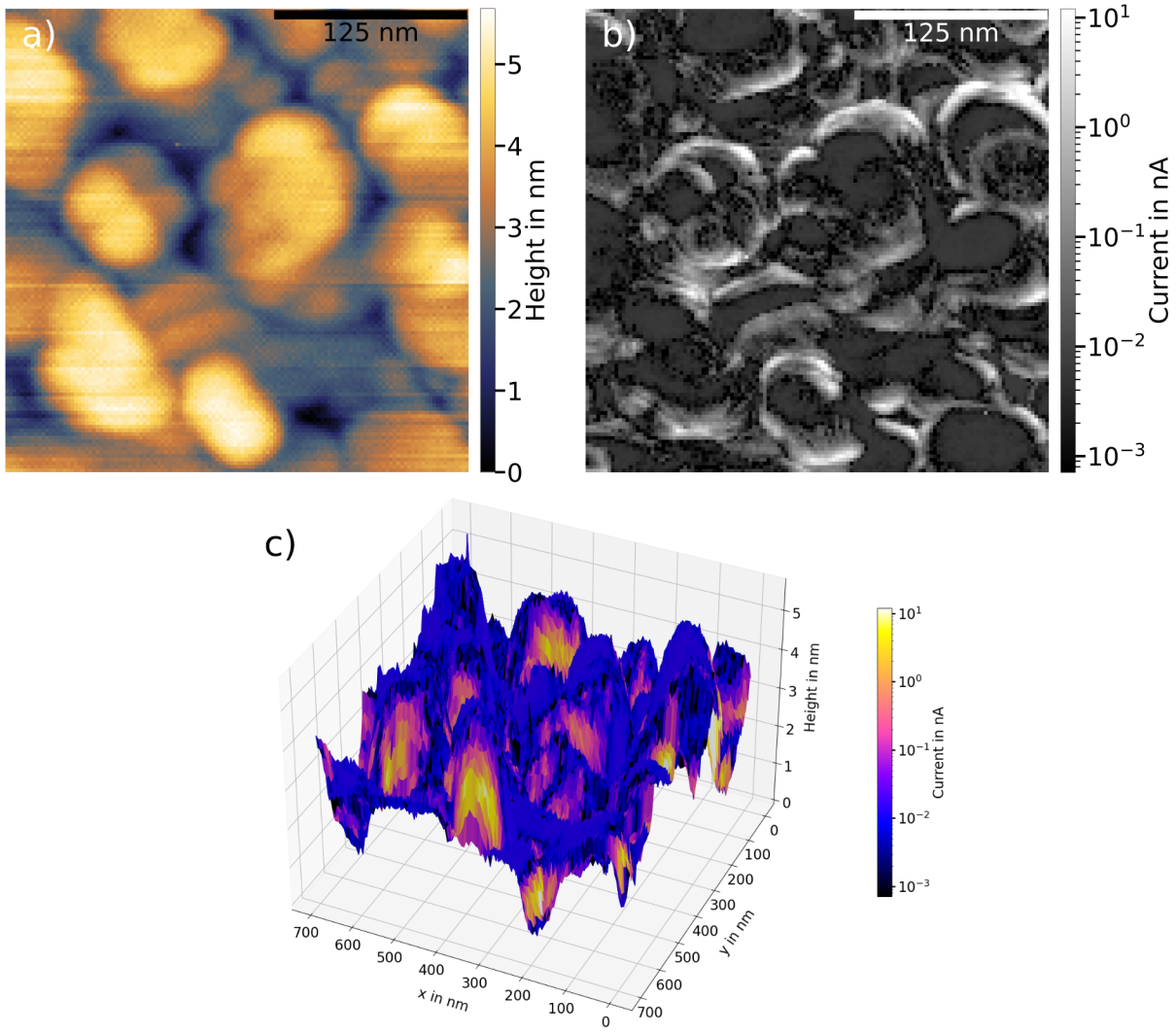


**Figure 4:** (a, b) Topography and current map, respectively, of a DDT SAM on a Au/Si substrate. The rougher surface seen for the bare substrate is also found here together with its influence on the current map. Very small currents dominate the map, changing to high currents rather abruptly. This yields only small areas with measurable currents, which is unfavorable for the averaging of conductive properties of the surface. The 3D view in (c) emphasizes the correlation between the rougher surface structure and the high currents on the slopes of the grains. The point of view is adjusted for best visibility ($F_{setpoint}$ = 20 nN, $U_{bias}$ = 1 V, RMN probe).

only small flat areas. Although in Figure 4 this is slightly distorted by a probe effect duplicating features, the systematic difference in surface structure between Au/Si and Au/mica, already observed in the bare substrates, is reproduced.

Just as for the bare Au/Si, the substructures of the substrate lead to strong variations in the corresponding current map. There are large areas with very small currents on the flatter areas of the topography. The current rather abruptly increases at the slopes of the topography. The 3D view of the surface in Figure 4c, represented in the same way as in Figure 3c, shows clearly that large currents can only be observed at the slopes of the topography as is also the case for bare Au/Si. The flatter areas, however, show very low current values, close to the lower limit of observability. The 3D view also emphasizes the higher roughness of the surface of the DDT SAM on Au/Si compared to the Au/mica substrate.

Additional measurements on SAMs of sulfur-bound oligopeptides (SH–$(CH_2)_2$NH–(Ala-Aib)$_5$–COOH) [12] on Au/mica substrates yielded no measurable currents and are therefore omitted in this report.

Our observations show that, when studying the conductive properties of DDT SAMs on Au/Si, the variation in the current is governed by the structure of the substrate, which remains

qualitatively unchanged by the deposition of the SAM. For the Au/Si substrate, the rough topography yields only small areas on the surface on which comparable conductive properties can be expected. Without information on the surface topography, the conductance obtained from averaging over random points on the surface [12,21-24] is prone to incorrect averaging. The lateral variation of the conductive properties limits strongly the amount of lateral probe positions over which measurements of such characteristics can be averaged. Using the Au/mica substrate, however, yields large areas of comparable conductive properties, which makes it more suitable for such investigations. Moreover, the strong lateral variation in the current map of Au/Si suggests that it is necessary to choose the points for averaging carefully. A suitable way to do so would be through imaging the surface as presented here.

## Conclusion

This report shows that the lateral variation of the conductive properties of molecular SAMs is governed by the choice of the substrate. To achieve comparable, well-measurable currents and conductive properties, flat substrates are favorable. The flatness of the substrate and homogeneity of the current distribution with and without the SAM should be studied in advance to ensure comparability. A rougher substrate surface leads to stronger variations in the conductive properties, limiting the areas over which conductive properties can be sensibly averaged, and should therefore be avoided.

Moreover, the studies presented here show, that a careful study of the correlation between topography and conductive properties of SAMs is strongly advised, especially if CAFM is used to perform the characterization of the conductive properties of the SAM. With such combined investigations, the areas for averaging can be chosen in a sensible way to reproducibly characterize the SAM's conductivity, for example, by using only the flat areas of the surface and excluding areas with large slopes in the topography.

## Supporting Information

### Supporting Information File 1

Additional figures.
[https://www.beilstein-journals.org/bjnano/content/supplementary/2190-4286-14-97-S1.pdf]

## Acknowledgements

SJ thanks Lukas Gerhard for discussions on the presentation of the data. SJ thanks Norman Blümel for helpful discussions during the stay at Leiden University. Parts of this article are based on the results reported in the doctoral thesis: J. A. Skolaut, "Molecular Motor Based on Single Chiral Tripodal Molecules Studied with STM", Doctoral Dissertation, Karlsruhe Institute of Technology, KIT Scientific Publishing, 2023.

## Funding

This work was partly funded by the Netherlands Organisation for Scientific Research (NWO), grant 680.92.18.01. The work was done during the PhD thesis of SJ within Deutsche Forschungsgemeinschaft (DFG) Grant No. GE 2989/2-1. The Karlsruhe House of Young Scientists (KHYS) supplied additional funds for the stay of SJ at Leiden University.

## ORCID® iDs

Julian Skolaut - https://orcid.org/0009-0004-2104-6785
Jędrzej Tepper - https://orcid.org/0000-0002-4841-1170
Federica Galli - https://orcid.org/0000-0002-1098-8150
Wulf Wulfhekel - https://orcid.org/0000-0001-6890-643X
Jan M. van Ruitenbeek - https://orcid.org/0000-0003-0381-0132

## References

1. Herwald, S. W.; Angello, S. J. *Science* **1960,** *132,* 1127–1133. doi:10.1126/science.132.3434.1127
2. Aviram, A.; Ratner, M. A. *Chem. Phys. Lett.* **1974,** *29,* 277–283. doi:10.1016/0009-2614(74)85031-1
3. Evers, F.; Korytár, R.; Tewari, S.; van Ruitenbeek, J. M. *Rev. Mod. Phys.* **2020,** *92,* 035001. doi:10.1103/revmodphys.92.035001
4. Akkerman, H. B.; de Boer, B. *J. Phys.: Condens. Matter* **2008,** *20,* 013001. doi:10.1088/0953-8984/20/01/013001
5. Mann, B.; Kuhn, H. *J. Appl. Phys.* **1971,** *42,* 4398–4405. doi:10.1063/1.1659785
6. Becucci, L.; Rosa Moncelli, M.; Guidelli, R. *J. Electroanal. Chem.* **1996,** *413,* 187–193. doi:10.1016/0022-0728(96)04637-2
7. Rampi, M. A.; Schueller, O. J. A.; Whitesides, G. M. *Appl. Phys. Lett.* **1998,** *72,* 1781–1783. doi:10.1063/1.121183
8. Nijhuis, C. A.; Reus, W. F.; Barber, J. R.; Whitesides, G. M. *J. Phys. Chem. C* **2012,** *116,* 14139–14150. doi:10.1021/jp303072a
9. Cademartiri, L.; Thuo, M. M.; Nijhuis, C. A.; Reus, W. F.; Tricard, S.; Barber, J. R.; Sodhi, R. N. S.; Brodersen, P.; Kim, C.; Chiechi, R. C.; Whitesides, G. M. *J. Phys. Chem. C* **2012,** *116,* 10848–10860. doi:10.1021/jp212501s
10. Jiang, L.; Sangeeth, C. S. S.; Wan, A.; Vilan, A.; Nijhuis, C. A. *J. Phys. Chem. C* **2015,** *119,* 960–969. doi:10.1021/jp511002b
11. Reus, W. F.; Thuo, M. M.; Shapiro, N. D.; Nijhuis, C. A.; Whitesides, G. M. *ACS Nano* **2012,** *6,* 4806–4822. doi:10.1021/nn205089u
12. Kiran, V.; Cohen, S. R.; Naaman, R. *J. Chem. Phys.* **2017,** *146,* 092302. doi:10.1063/1.4966237
13. Xie, Z.; Markus, T. Z.; Cohen, S. R.; Vager, Z.; Gutierrez, R.; Naaman, R. *Nano Lett.* **2011,** *11,* 4652–4655. doi:10.1021/nl2021637
14. Lu, H.; Wang, J.; Xiao, C.; Pan, X.; Chen, X.; Brunecky, R.; Berry, J. J.; Zhu, K.; Beard, M. C.; Vardeny, Z. V. *Sci. Adv.* **2019,** *5,* eaay0571. doi:10.1126/sciadv.aay0571
15. Ben Dor, O.; Morali, N.; Yochelis, S.; Baczewski, L. T.; Paltiel, Y. *Nano Lett.* **2014,** *14,* 6042–6049. doi:10.1021/nl502391t

16. Buchholz, S.; Fuchs, H.; Rabe, J. P. *J. Vac. Sci. Technol., B: Microelectron. Nanometer Struct.–Process., Meas., Phenom.* **1991,** *9,* 857–861. doi:10.1116/1.585527
17. Dishner, M. H.; Ivey, M. M.; Gorer, S.; Hemminger, J. C.; Feher, F. J. *J. Vac. Sci. Technol., A* **1998,** *16,* 3295–3300. doi:10.1116/1.581536
18. Oskam, G.; Searson, P. C. *Surf. Sci.* **2000,** *446,* 103–111. doi:10.1016/s0039-6028(99)01113-9
19. Poirier, G. E. *Chem. Rev.* **1997,** *97,* 1117–1128. doi:10.1021/cr960074m
20. Yang, G.; Liu, G.-y. *J. Phys. Chem. B* **2003,** *107,* 8746–8759. doi:10.1021/jp0219810
21. Mishra, S.; Mondal, A. K.; Pal, S.; Das, T. K.; Smolinsky, E. Z. B.; Siligardi, G.; Naaman, R. *J. Phys. Chem. C* **2020,** *124,* 10776–10782. doi:10.1021/acs.jpcc.0c02291
22. Tassinari, F.; Banerjee-Ghosh, K.; Parenti, F.; Kiran, V.; Mucci, A.; Naaman, R. *J. Phys. Chem. C* **2017,** *121,* 15777–15783. doi:10.1021/acs.jpcc.7b04194
23. Bloom, B. P.; Kiran, V.; Varade, V.; Naaman, R.; Waldeck, D. H. *Nano Lett.* **2016,** *16,* 4583–4589. doi:10.1021/acs.nanolett.6b01880
24. Kettner, M.; Göhler, B.; Zacharias, H.; Mishra, D.; Kiran, V.; Naaman, R.; Fontanesi, C.; Waldeck, D. H.; Sęk, S.; Pawłowski, J.; Juhaniewicz, J. *J. Phys. Chem. C* **2015,** *119,* 14542–14547. doi:10.1021/jp509974z

## License and Terms

BEILSTEIN JOURNAL OF NANOTECHNOLOGY

# *un*Drift: A versatile software for fast offline SPM image drift correction

Tobias Dickbreder*, Franziska Sabath, Lukas Höltkemeier, Ralf Bechstein and Angelika Kühnle

Full Research Paper

Open Access

Address:
Physical Chemistry I, Bielefeld University, Universitätsstraße 25, 33615 Bielefeld, Germany

Email:
Tobias Dickbreder* - dickbreder@uni-bielefeld.de

* Corresponding author

Keywords:
atomic force microscopy; calibration; drift correction; image correlation functions; periodic structures; scanning probe microscopy

*Beilstein J. Nanotechnol.* **2023,** *14,* 1225–1237.
https://doi.org/10.3762/bjnano.14.101

Received: 04 June 2023
Accepted: 28 November 2023
Published: 28 December 2023

This article is part of the thematic issue "Advanced atomic force microscopy techniques V".

Guest Editor: H. Mönig



## Abstract

Scanning probe microscopy (SPM) techniques are widely used to study the structure and properties of surfaces and interfaces across a variety of disciplines in chemistry and physics. One of the major artifacts in SPM is (thermal) drift, an unintended movement between sample and probe, which causes a distortion of the recorded SPM data. Literature holds a multitude of strategies to compensate for drift during the measurement (online drift correction) or afterwards (offline drift correction). With the currently available software tools, however, offline drift correction of SPM data is often a tedious and time-consuming task. This is particularly disadvantageous when analyzing long image series. Here, we present *un*Drift, an easy-to-use scientific software for fast and reliable drift correction of SPM images. *un*Drift provides three different algorithms to determine the drift velocity based on two consecutive SPM images. All algorithms can drift-correct the input data without any additional reference. The first semi-automatic drift correction algorithm analyzes the different distortion of periodic structures in two consecutive up and down (down and up) images, which enables *un*Drift to correct SPM images without stationary features or overlapping scan areas. The other two algorithms determine the drift velocity from the apparent movement of stationary features either by automatic evaluation of the cross-correlation image or based on positions identified manually by the user. We demonstrate the performance and reliability of *un*Drift using three challenging examples, namely images distorted by a very high drift velocity, only partly usable images, and images exhibiting an overall weak contrast. Moreover, we show that the semi-automatic analysis of periodic images can be applied to a long series containing hundreds of images measured at the calcite–water interface.

## Introduction

In science and technology, scanning probe microscopy (SPM) techniques are widely used to study the structure and properties of surfaces and interfaces from the micrometer scale down to the atomic level. The common element of SPM techniques is that surface structure and properties are revealed by moving a probe over the sample covering a given area or volume. During

this movement, the interaction between probe and sample is measured at fixed points in the scan area resulting in an image of the structure or a specific surface property. This scanning process is also the origin of two prominent artifacts in SPM image data, that is, an imperfect scanner calibration and thermal drift. Both of which cause a misalignment between probe and surface; thus, the measured SPM images are distorted and potentially shifted [1-6].

The calibration of an SPM scanner is used by the SPM instrument to convert the voltages applied to the scanner piezo into a probe position [2,7]. If this calibration is not correct, the position assumed by the SPM instrument deviates from the actual probe position; thus, the SPM image is distorted [1,2,4,8-17]. The determination of linear calibration parameters and scanner non-orthogonality based on atomic structures [1-3,8,9,18,19] and calibration gratings [1,20-22] have been discussed intensively. In addition to linear effects, non-linear scanner behavior such as creep [1,4,10-13] and hysteresis [1,2,4,10,14-17] has been analyzed and corrected.

The second prominent artifact causing distortion of SPM images is (thermal) drift. Because of the serial nature of the scanning process, recording an entire image takes at least several milliseconds in case of video-rate scanning [23,24]. Most SPM images, however, are measured at a much lower scan rate on the timescale of seconds to minutes. During this measurement time, the temperature in the SPM instrument can fluctuate, inducing thermal expansion or contraction of the instrument's components [5]. As a consequence, sample and probe experience an unintended movement relative to each other, that is, the thermal drift. This drift is not included in the measurement data, so the recorded SPM images appear distorted [5,6]. An effective way to reduce thermal drift to a minimum is to carry out SPM experiments under cryogenic conditions close to the temperature of liquid helium. The cryogenic temperature, however, also drastically reduces the rates of thermal processes such as on-surface reactions, diffusion, or desorption [25]. Hence, many processes relevant at room temperature or elevated temperatures are impossible to study in a cryogenic environment. The same applies to SPM studies at the solid–liquid interface. For these measurements, the effect of thermal drift needs to be compensated.

A variety of different strategies have been developed to characterize and correct thermal drift in SPM measurements. There are two types of drift correction strategies: In online drift correction, the drift velocity is determined during the measurement; then, the scanner movement is adjusted to compensate for drift [16,25-28]. Offline drift correction strategies, in contrast, correct the effect of drift in SPM images after the measurement. Drift correction has been carried out based on the apparent movement of stationary features (e.g., fixed defects or adsorbates) traceable in consecutive images [5,29-31] or images with opposing scan directions [12,32]. Instead of analyzing the apparent shift of individual features, the apparent movement of the scan window can also be determined from the maximum of the cross-correlation [26,27,33-36] between consecutive images. Moreover, the different distortion of periodic structures in images with opposing scan directions was used to determine drift and to calculate the undistorted structure [3,37]. Other authors proposed drift correction procedures based on rescanning a small area of an SPM image with the fast and slow scan directions reversed [13,38-40], splitting the scan of an image into several subscans [41], or periodically rescanning the first scan line [42]. For non-raster SPM, the drift velocity can be extracted without additional scans from the analysis of inherent crossing points in the scanning path [43,44]. Another approach to remove distortions from SPM images is to correct the images with regard to a known reference structure [4,6,18]. While the latter strategy can ensure distortion-free SPM images for known surface structures, it is not suited for investigation of unknown structures.

Here, we present *un*Drift, a free-to-use scientific software for the fast and reliable calibration and drift correction of SPM image data. *un*Drift implements three algorithms to determine the drift velocity based on two consecutive SPM images with or without periodic structures. The first semi-automatic algorithm extracts lattice vectors from two consecutive up and down (down and up) images exhibiting periodic structures. These lattice vectors are, then, used to analyze the distortion of the images and to calculate the drift velocity. This algorithm enables *un*Drift to drift-correct both SPM images without stationary features and SPM images without overlapping scan areas. The second and third drift correction algorithms extract drift velocities from the apparent movement of stationary features as described in [5,12,25-27,29-36,45]. Algorithm II implements the well-known cross-correlation method [26,27,33-36,45] to automatically determine the shift between two SPM images with identical scan directions. From this shift, we calculate the drift velocity. Algorithm III, in contrast, provides the possibility to manually identify stationary features in two SPM images with arbitrary scan direction and use their positions for drift correction [5,12,25,29-32]. Note that all drift correction algorithms applied by *un*Drift rely on information contained within the measurement data solely; thus, *un*Drift allows for the investigation of unknown structures. To demonstrate the performance of *un*Drift, we apply our software to three examples where the drift correction is especially challenging. Namely, we drift-correct SPM images with a very high drift velocity exceeding the slow scan rate, only partly usable images, and

images with an overall weak contrast and high noise level. Moreover, we show that *un*Drift is suitable for the drift correction and evaluation of measurement sessions spanning several hundred images.

## Software

*un*Drift is scientific software for the fast and accurate drift correction and calibration of SPM image data as necessary for quantitative data analysis. It is written in JavaScript and HTML and runs with all common browsers independent of the operating system. *un*Drift can be operated either on a local server or as a web-based version. Both versions are available from our website under [46]. All functions of *un*Drift, such as data import, leveling, calibration, and drift correction of SPM data, are free to use, that is, *un*Drift is entirely free to use. Analysis results including corrected SPM images as well as extracted lattice vectors and drift velocities are available in standard open data formats.

The full source code of *un*Drift is also available from our website. JavaScript modules for the import and analysis of SPM data are licensed under the GNU General Public License version 3.0. The visualization of SPM images in *un*Drift is realized with the proprietary library Kontrast [47], which is available under its own license. This means that all functions of *un*Drift are free-to-use for non-commercial purposes but the development of new features requires a Kontrast license.

## Input data

The import of SPM data into *un*Drift is designed to read files in the Gwyddion Native Format (gwy format) as created with the open source SPM data analysis software Gwyddion [48]. Gwyddion contains import modules for a wide variety of scanning probe microscopes as well as tools for SPM data processing and analysis. This enables the user to chose between data processing in *un*Drift and Gwyddion. *un*Drift supports basic data processing methods such as leveling (mean plane, polynomial) and an automatic color scale adaption; thus, the processing of most standard images can be done directly in *un*Drift. For more complex processing steps, the user is referred to Gwyddion. Then, the pre-processed SPM data can be calibrated and drift-corrected with *un*Drift. Moreover, *un*Drift can export data in the gwy format, which enables a seamless integration between *un*Drift and Gwyddion.

The gwy format does not contain standardized containers for scan direction, scan angle, and raster time per pixel, which constitute vital information for an accurate drift correction and calibration. *un*Drift extracts these parameters from the metadata, where they are typically stored with varying names depending on the manufacturer and version of the used microscope. Because of this, it is necessary to specify the matching between scanning parameters and metadata names for each microscope individually. We did this specification for the instruments and file formats listed in Table 1. For all other devices, this easy step needs to be done by the user in the preferences of *un*Drift.

## Drift correction

Next, we will discuss the main feature of *un*Drift, the offline drift correction of SPM images. Depending on the surface structure and scan directions of the SPM images, *un*Drift provides different algorithms to determine the drift velocity and to drift-correct the data. In terms of surface structure, we distinguish between images exhibiting a periodic structure and those without periodic structures. For images showing two-dimensional periodic structures, the drift velocity can be calculated from the different distortion of the surface periodicity in two SPM images with opposing slow scan direction (algorithm I). For the drift correction of SPM images without periodic structures, in contrast, *un*Drift implements two strategies (algorithms II and III) described in literature [5,12,25-27,29-36,45] to extract the drift velocity from the apparent movement of stationary features in consecutive images. Algorithm II uses the cross-correlation function between two images recorded in the same scan

**Table 1:** Overview of SPM devices and third-party file formats supported by *un*Drift.

| Device | Format | Direct import | Import via Gwyddion |
|---|---|---|---|
| Omicron MATRIX | .Amplitude_mtrx, .Damping_mtrx, .Phase_mtrx, .Df_mtrx, .Z_mtrx | no | yes |
| Bruker Nanoscope V | .001, .002, … | no | yes |
| Cypher ES AFM | .ibw | yes | yes |
| Nanonis controller | .sxm | yes | yes |
| other devices supported by Gwyddion | | no | limited[a] |
| others | | no | no |

[a]In principle, *un*Drift can read all SPM data saved with Gwyddion in the gwy format. However, as the gwy format lacks standardized containers for some of the information necessary for drift correction and calibration, the user needs to specify the mapping of meta data headers in the preferences of *un*Drift before use.

direction to evaluate the drift velocity [26,27,33-36,45], while algorithm III evaluates the position shift of stationary features between two images with arbitrary scan direction [5,12,25,29-32]. Both algorithms II and III also work for images exhibiting periodic structures if they contain stationary features. In the following two sections, we discuss the different algorithms clustered by the surface structures they are suitable for. Regardless of surface structure and scan direction, however, all drift correction algorithms applied by *un*Drift rely on information contained within the measurement data solely; thus, they allow for a quantitative data analysis without any knowledge on the surface geometry. Instead, all of the applied algorithms use the difference between two consecutive images to determine the drift velocity and to correct the SPM data. Hence, *un*Drift is, in contrast to drift correction schemes relying on known surface geometries, suited to investigate substrates with an unknown surface structure.

## Images with periodic structures

For the drift correction of images exhibiting periodic structures, *un*Drift uses the algorithm shown in Figure 1 (algorithm I). This algorithm takes advantage of the characteristic distortion of periodic structures in SPM images depending on drift velocity and scan direction [3,6,12,37]. For two consecutive SPM images with opposing slow scan directions, we will observe two different apparent surface structures, as drift distorts the real periodic surface structure differently for a different scan direction (see Figure 2a,d). As we know that the real surface structure is, indeed, independent of the scan direction, we can use the difference between distortions to calculate the drift velocity (and the real surface structure) as described in Supporting Information File 1. Algorithm I has the advantage that it relies only on the surface periodicity; thus, the scan areas of the two images used for drift correction do not need to overlap. The only requirements for this algorithm are a constant drift velocity and two SPM images exhibiting periodic structures measured with different slow scan directions. Note that, in principle, this strategy is not limited to images with opposing slow scan directions but should also work for images with different fast scan directions. In real measurements, however, we find that the difference in the distortion of images with different fast scan directions is too small compared to the uncertainty to achieve reliable results for the drift correction. Consequently, *un*Drift implements this algorithm for consecutive images with opposing slow scan directions solely.

As shown in Figure 1, algorithm I consists of five main steps, namely (1) import of input data, (2) extraction of primitive lattice vectors, (3) generation of linear combinations of these lattice vectors, (4) calculation of possible drift velocities, and (5) selection of the true drift velocity. After that, the obtained drift velocity is used to calculate the real lattice vectors and drift-correct the SPM images.

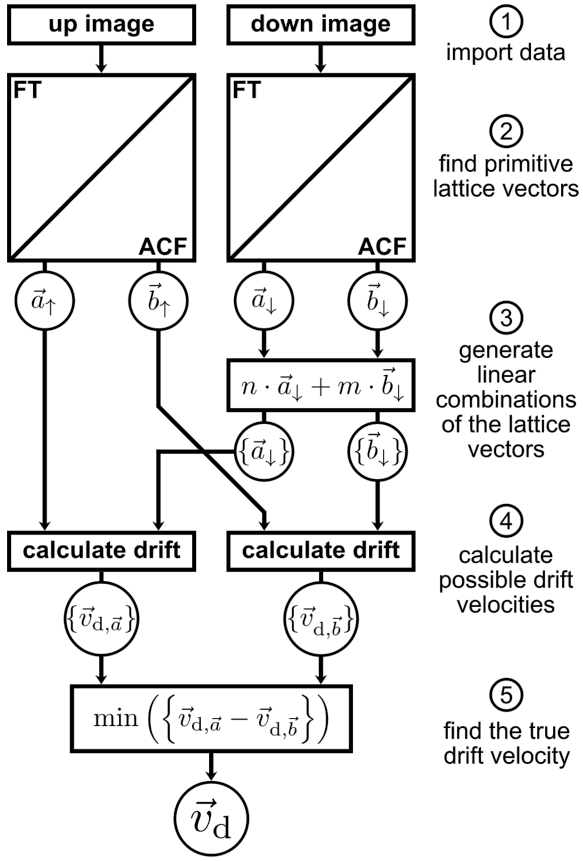


**Figure 1:** Schematic representation of algorithm I used to determine the drift velocity $v_\mathrm{d}$ from the distortion of periodic structures in consecutive SPM images with opposing slow scan directions.

First, two SPM images with opposing slow scan directions (i.e., one up and one down image) are imported as described before (step 1). Next, *un*Drift extracts primitive lattice vectors from both images as shown in Figure 2 (step 2). *un*Drift can determine the lattice vectors either based on the Fourier transforms (Figure 2b,e) or autocorrelations (Figure 2c,f). In both cases, our software searches for local maxima in the transformed image first (red dots in Figure 2). Then, it extracts guesses for the lattice vectors based on the maxima with the highest intensity, the maxima closest to the origin, or based on user selection. After that, these guessed lattice parameters and the spots belonging to the lattice are optimized with a least squares algorithm to obtain optimal lattice parameters. In Figure 2 the optimized lattice parameters are shown as a lattice drawn with red lines. For the Fourier transform, this fit yields lattice vectors of the inverse lattice, which are then transformed into real-space lattice vectors. For the autocorrelation, the optimization yields

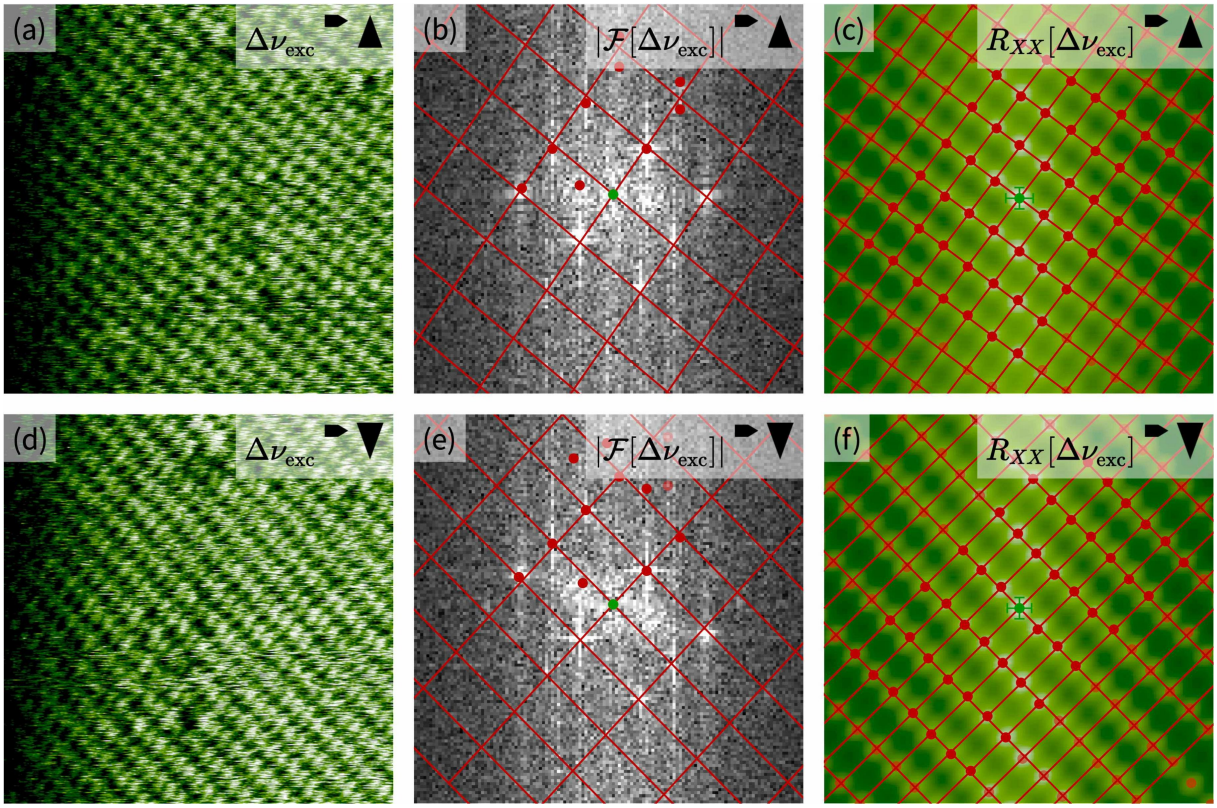


**Figure 2:** Extraction of lattice vectors from images exhibiting periodic structures. (a, d) High-resolution AFM images showing atomic resolution at the calcite (10.4)–water interface. (b, e) Fourier transform images of the real-space images shown in (a) and (d). The maxima in the Fourier transforms are marked by red circles, and the optimized lattice as found by *un*Drift is shown as red lines. Only the centers of the Fourier transformations are shown. (c, f) Autocorrelation images of the real-space images shown in (a) and (d). The maxima in the autocorrelation images are marked by red circles, and the optimized lattices as found by *un*Drift are shown as red lines. Only the centers of the autocorrelations are shown.

the real-space lattice vectors directly. To finish step 2, *un*Drift applies simple geometry to calculate the shortest possible lattice vectors for the lattice extracted in the optimization step.

This extraction of lattice vectors is a semi-automatic step, as the user needs to specify parameters for the peak finding. While these parameters need to be chosen manually, it can be easily determined from the fit quality whether these parameters are chosen correctly. We find that the optimal parameters for this step depend on the image size and contrast; thus, it can be necessary to change these parameters after a contrast change. Moreover, the user needs to choose whether the algorithm operates based on Fourier transform or autocorrelation. This choice mostly depends on the size of the image relative to the size of the observed periodic structure. For images showing many unit cells, we find that the Fourier transform yields better results, while the autocorrelation is superior for images containing very few unit cells. In between these extremes, there is a range where both methods work well as shown in our examples in Figure 2. The dependence of the optimal transformation for peak extraction on the image size is caused by the finite resolution of the measured SPM images. For images containing many unit cells, each unit cell only consists of few pixels; thus, the maxima in the autocorrelation are difficult to separate, as they also consist of few pixels. The Fourier transform, in contrast, works in the inverse space, which is why the maxima are very nicely separated by many pixels and easy to find by the algorithm. For images containing few unit cells, it is the other way around. The autocorrelation maxima are nicely separated, while the maxima in the Fourier transform sometimes even merge together.

After the extraction of lattice vectors, *un*Drift applies steps 3 to 5 to determine the drift velocity from these lattice vectors. It is important to note that the calculation of drift velocities requires a set of two differently distorted versions of the same vector (see Supporting Information File 1). The identification of a matching pair of lattice vectors, however, becomes increasingly difficult with increasing drift velocity and, thus, increasing image distortion. To solve this problem and to ensure that *un*Drift also works reliably for high drift velocities, we apply steps 3 to 5 of algorithm I. The idea behind this part of the algorithm is the following: Each pair of lattice vectors $(\left(\vec{a}_{\uparrow},\vec{a}_{\downarrow}\right)$ and

$\left(\vec{b}_{\uparrow},\vec{b}_{\downarrow}\right)$) yields one drift velocity. Hence, we can calculate two seemingly independent drift velocities $\vec{v}_{\mathrm{d},\vec{a}}$ and $\vec{v}_{\mathrm{d},\vec{b}}$. In reality, however, there is only one drift velocity $\vec{v}_{\mathrm{d}}$ that applies for both images. Hence, the drift velocities calculated for both lattice vectors need to be identical, that is, $\vec{v}_{\mathrm{d},\vec{a}} = \vec{v}_{\mathrm{d},\vec{b}}$.

Next, we can use this criterion to find matching pairs of lattice vectors and, thus, calculate the true drift velocity. We can start by choosing a set of lattice vectors for the first image, as this initial choice is arbitrary. For the second image, however, we need to find the matching lattice vectors. To realize this, we take the lattice vectors extracted from the image and generate a set of linear combinations for both vectors $\vec{a}_{\downarrow}$ and $\vec{b}_{\downarrow}$ (see Figure 1, step 3). These sets $\{\vec{a}_{\downarrow}\}$ and $\{\vec{b}_{\downarrow}\}$ then contain the matching vectors as well as several other vectors. In the next steps, the program subsequently calculates the corresponding sets of drift velocities $\{\vec{v}_{\mathrm{d},\vec{a}}\}$ and $\{\vec{v}_{\mathrm{d},\vec{b}}\}$ (step 4) and selects the pair of drift velocities with the smallest difference between $\vec{v}_{\mathrm{d},\vec{a}}$ and $\vec{v}_{\mathrm{d},\vec{b}}$ (step 5). Note that we cannot search for identical drift velocities, as the individual drift velocities are always slightly different because of experimental noise and a small nonlinearity in the drift. Instead, we use the two drift velocities with the smallest difference. Finally, the true drift velocity $\vec{v}_{\mathrm{d}}$ is calculated by averaging over the individual drift velocities.

For the selection of the drift velocity in step 5, *un*Drift provides an alternative selection procedure based on the lattice vectors. Not only the drift velocity needs to be identical for both pairs of lattice vectors, but also the primitive unit cell with the shortest lattice vectors has to be identical in both images after drift correction. The second selection procedure, thus, operates based on the difference between drift-corrected lattice vectors in both images. Again, we search for the minimum difference and select the corresponding drift velocity as the real drift velocity. The selection procedure used in step 5 can be chosen by the user under lattice matching. We find that this second selection procedure tends to work better for images with low signal-to-noise ratio.

## Images without periodic structures

As discussed before, *un*Drift features two algorithms to drift-correct SPM images without periodic structures based on the apparent movement of stationary features in consecutive images. In this section, we will describe these two algorithms, referred to as algorithm II and III, and discuss their applicability to different situations in terms of scan directions and experimental systems.

Algorithm II uses the cross-correlation between two consecutive images recorded in the same scan direction to evaluate the shift between the images and to calculate the drift velocity. The distortion of SPM images by drift only depends on drift velocity and scan direction (see Supporting Information File 1). Hence, two images measured with the same scan direction and a constant drift velocity are distorted in the same way. The only difference between these two images is that they are measured at a slightly different position on the surface, because drift moved the scanner and surface relative to each other. In SPM images, this effect manifests itself in an apparent movement of stationary surface features whose positions are actually constant, such as defects and step edges. This is illustrated in Figure 3, where the stationary surface features marked with colored crosses seem to move between Figure 3a and Figure 3b. Here, it is important to note that all stationary features "moved" by the same vector.

To evaluate this shift between images, we can apply the cross-correlation function between both images as described in

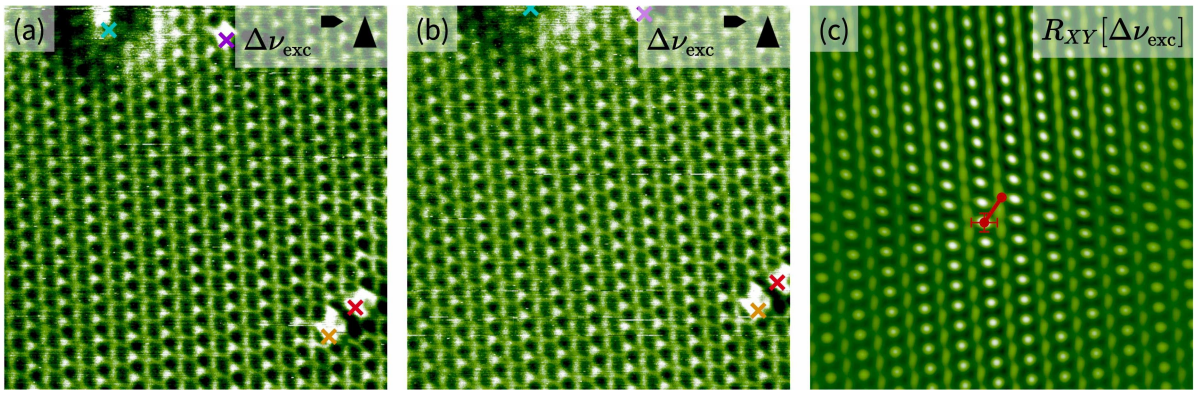


**Figure 3:** (a, b) Two consecutive up images recorded with high-resolution AFM on calcite(10.4) in ultrahigh vacuum. The images show several defects, whose positions are marked with colored crosses in both images. It is apparent that the defect positions are shifted in the second image compared to the first one. (c) Image of the cross-correlation function $R_{XY}$ between the images shown in (a) and (b). The center of the image and the position of the maximum are marked with red dots and connected with a red line. This line corresponds to the shift between images (a) and (b).

[26,27,33-36,45]. In the cross-correlation image, the global maximum corresponds to the shift necessary to achieve maximum similarity between both images [33,34], where a maximum in the image center means that both images are identical without any shift. We show the cross-correlation of our two example images (Figure 3a,b) in Figure 3c. We marked the center of the image and the global maximum with red dots connected by a red line to illustrate the shift between images. When we compare the shift derived from the cross-correlation image, it is evident that this shift is identical to the shift of the stationary features between the images in Figure 3a and Figure 3b.

In the next step, *un*Drift uses the shift derived from the cross-correlation function to calculate the drift velocity as described in Supporting Information File 1 and to drift-correct the input data. This algorithm is fully automatic and does not require any additional input from the user.

In addition to the global maximum, the cross-correlation image in our example in Figure 3c also exhibits a periodic structure. This periodicity stems from the periodic structure observed in the input images, and it can be evaluated by *un*Drift to obtain lattice parameters. For the drift correction with algorithm II, however, the stationary features in the input images are decisive and not the surface periodicity. This algorithm does not work reliably for perfectly periodic surfaces without any stationary features as all maxima would have the same intensity; thus, the algorithm cannot decide which maximum corresponds to the shift between the images [30]. For images exhibiting a periodic structure and stationary features, however, we find that algorithm II works with remarkable reliability.

In contrast to algorithm II, algorithm III does not evaluate the mean shift between images but the apparent shift of single stationary features as described by Rahe and co-workers [5]. It is necessary to subsequently identify stationary features in the SPM images and to determine their positions. For the determination of a feature position, *un*Drift provides the possibility to refine the manually selected positions to the closest maximum or minimum. The drift velocity is calculated for each feature individually; then, the mean drift velocity can be calculated by averaging over the individual drift velocities. The deviation between these yields information about the non-linearity of the drift. With algorithm III, *un*Drift provides the possibility to use positions of stationary features identified manually by the user. The software displays both images used for drift correction and a variable number of markers in different colors as shown in Figure 3a,b. The user can, then, move these markers to match the positions of stationary features and start the drift correction by clicking a button. As this positioning of markers on identical positions of the stationary features is never perfect, we recommend to use as many stationary features as possible for the drift correction.

Algorithm III is arguably the slowest algorithm in *un*Drift in terms of evaluation time per image, and the selection of feature positions is, at least, partly subjective. However, algorithm III has the important advantage that it works for all images with stationary features regardless of scan direction and image quality. As long as the user can identify features in the SPM images, this algorithm will work for the drift correction. Moreover, algorithm III offers the possibility to easily assess and quantify the effect of non-linear drift in the drift-corrected SPM data, which is not available from the other algorithms.

## Lateral calibration

In addition to the correction of drift, it is crucial for a quantitative analysis of SPM data that the scanner position is calibrated properly. While the drift correction will remove the effect of additional movement between scanner and sample surface, the obtained positions, distances, and angles will still be incorrect as long as the instrument is not properly calibrated. This situation is well known in literature, and there are several different strategies documented to determine the calibration parameters for a scanning probe microscope [1-3,7-9,12,18,19,21,22]. With these calibration parameters, the microscope can either be calibrated before the measurement, or the measured SPM data can be corrected afterwards. The calibration parameters can change over time because of, for example, piezo aging or measurements at different temperatures [3,20]. Thus, it is necessary to validate the calibration parameters regularly. *un*Drift provides features to (1) correct SPM data with a given set of lateral calibration parameters and (2) determine lateral calibration parameters based on a reference surface geometry.

The lateral calibration of SPM data in *un*Drift is based on the assumption of a linear relationship [3,7-9,19] between recorded and actual scanner movement as described in Supporting Information File 1. In this case, the calibration only depends on three parameters, namely the correction factors in the $x$ and $y$ directions, $\kappa_x$ and $\kappa_y$, respectively, and the angle between both directions, $\beta$. These parameters can be provided by the user for a lateral calibration of the drift-corrected SPM data. Alternatively, the default values can be used, which correspond to no additional calibration.

For SPM images exhibiting a periodic structure, *un*Drift can also calculate the expected lateral calibration parameters based on a reference. In order to do so, the user needs to provide the lattice parameters of the investigated periodic structure, that is, the edge lengths and opening angle of the surface unit cell.

*un*Drift then compares these reference data to the measured lattice parameters and calculates the lateral calibration parameters necessary to match the measured periodicity with the reference. Thus, *un*Drift makes it very easy to calibrate a previously not calibrated device or to check whether an existing calibration is still valid. Detailed information on the determination of calibration parameters are given in Supporting Information File 1.

## Output data

After calibration and drift correction, *un*Drift provides a variety of different methods to export the obtained data as shown in Table 2. Corrected SPM images including Fourier transforms and autocorrelations are available for export in the Gwyddion Simple Field and Gwyddion Native formats for further data evaluation or processing in Gwyddion. Moreover, images and image cutouts can be exported into the standard image formats png and svg. The svg exporter also includes the possibility to export ready-to-use figures with annotations and scale bars.

**Table 2:** Overview of output data and export types available from *un*Drift.

| Data type | Image type | Output formats |
|---|---|---|
| corrected SPM data | all | .gwy, .gsf |
| corrected images | all | .png, .svg |
| drift velocity | all | .csv |
| corrected lattice parameters | periodic | .csv |
| calibration parameters[a] | periodic | .csv |
| user input parameters | all | .csv |

[a]Requires the user to input reference data for the expected surface geometry.

In addition to the corrected SPM data, drift velocities and lattice parameters (only for images with periodic structures) calculated during drift correction are available as a session report in csv format. Calibration parameters are also available for images with periodic structures in the same session report file if the user specified a reference surface. User input parameters specified during the evaluation are recorded by *un*Drift and can be downloaded in a separate csv file.

# Results and Discussion

To demonstrate the performance of *un*Drift, we will now apply the software to experimental situations where the drift correction is either especially challenging or time-consuming.

## Challenging experimental conditions

For the above presentation of the working principle of our software, we used AFM images with good atomic contrast and reasonable drift velocities. In experiments, however, it is not always possible to reach these desirable conditions, which is why we want to show that our software can also deal with challenging experimental conditions. We will demonstrate that *un*Drift can handle (1) drift velocities exceeding the slow scan rate, (2) images with only small usable parts, and (3) images exhibiting a weak contrast or low signal-to-noise ratio.

First, we discuss a scenario with very high drift velocity. In Figure 4a,b, we show two consecutive AFM images of a calcium fluoride (111) surface recorded under ultrahigh vacuum conditions. The periodic structures observed in these two raw-data images (see red unit cells in Figure 4a,b) show a striking difference compared to each other and compared to the expected hexagonal structure. This obvious difference in appearance is caused by the strong image distortion associated with an exceptionally high drift velocity. High drift velocities can be challenging for drift correction, because the strong image distortion makes it difficult to identify pairs of features or corresponding lattice points. With *un*Drift, however, the images in Figure 4a,b can be drift-corrected easily, as algorithm I works reliably even for very high drift velocities.

We present the drift-corrected images corresponding to the images in Figure 4a,b in Figure 4c,d, respectively. Note that we cut the drift-corrected images to fit the form factor of this figure, while still being able to see the atomic structure. Figure 4c,d shows that the unit cell dimensions in both up and down image are now almost identical, and the surface now appears to be hexagonal. We find lattice parameters of $3.8 \times 10^{-10}$ m and $3.9 \times 10^{-10}$ m with an angle of 114°, which is very close to a hexagonal surface structure. The lattice parameters also agree well with lattice parameters documented in literature ($a = 3.86 \times 10^{-10}$ m and $\gamma = 120°$; [49]). We ascribe the slight deviation from the reference values to the experimental error, which we expect to be higher because of the exceptionally high drift velocity. We want to highlight that this is an extreme example where the absolute drift velocity ($3.8 \times 10^{-11}$ m·s$^{-1}$) exceeds the scan velocity in the slow scan direction ($3.7 \times 10^{-11}$ m·s$^{-1}$). For most experiments, the drift velocity will be much lower, as SPM experiments are typically optimized for stable conditions with low drift velocity. Nevertheless, this example shows that *un*Drift is not limited to low-drift environments but is also capable to correct SPM data recorded with (very) high drift velocities.

Second, we turn to images where only parts of the input images can be used for drift correction. During SPM experiments, sudden tip changes or collisions with the surface can significantly worsen or even destroy the observed contrast. Hence, it is quite common that only parts of an image can be used for evalu-

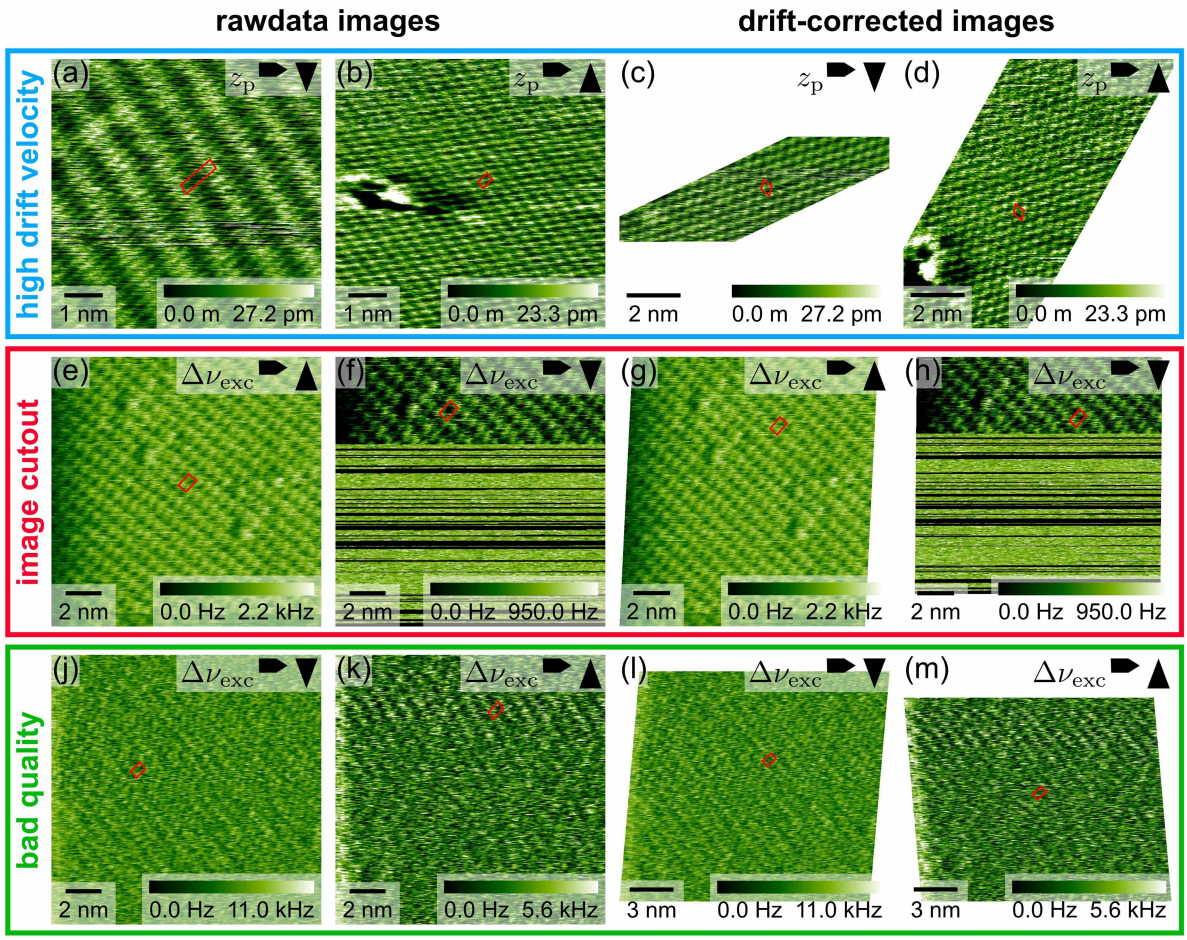


**Figure 4:** Example images demonstrating the applicability of *un*Drift to SPM experiments with high drift velocities (a–d), only partly usable images (e–h), and bad image quality (j–m). Raw-data images are shown on the left side of the figure, and the corresponding drift-corrected images are shown on the right side. In all images, the unit cell used for drift correction is shown as a red quadrangle. Images (a–d) show the atomic structure of calcium fluoride (111) recorded with high-resolution AFM in ultrahigh vacuum. Images (e–h) and (j–m) were recorded with high-resolution AFM at the calcite (10.4)–water interface.

ation. To demonstrate that *un*Drift can drift-correct these images by only considering (small) parts of an image, we show example images recorded at the calcite–water interface in Figure 4e,f. In our example, the sample drifted out of the scanner's $z$ range after the first third of the second image (Figure 4f), and the image contrast was completely lost. For drift correction, we used algorithm I based on the autocorrelation image and selected the usable part in Figure 4f manually, while the image in Figure 4e was used in its entirety. We show the drift-corrected results for both input images in Figure 4g,h, respectively. Comparison between the raw-data images (Figure 4e,f) and drift-corrected images (Figure 4g,h) shows that the unit cells of both images agree much better after drift correction. We conclude that the drift correction was successful, even though we could only use a small part of the second image for drift correction. This conclusion is confirmed by the derived unit cell dimensions of $5.1 \times 10^{-10}$ m × $8.2 \times 10^{-10}$ m with an angle of 89.8°, which fit the expected values ($4.99 \times 10^{-10}$ m × $8.10 \times 10^{-10}$ m, 90.0°; [50]) within the experimental accuracy of our AFM instrument (distance accuracy: $\pm 0.3 \times 10^{-10}$ m, angle accuracy: ±2°; see below).

Third, we discuss the arguably most challenging situation for drift correction, images with an overall weak contrast and low signal-to-noise ratio. The periodic structures of the calcite–water interface in Figure 4j,k are very faint and, thus, hard to recognize by eye. Based on the autocorrelation function, however, *un*Drift can extract unit cell dimensions even from images with such weak contrast. The different dimensions of the unit cells extracted here (see red quadrangles in Figure 4j,k) reveal that these raw-data images are distorted by drift. We drift-corrected the raw-data images with algorithm I based on the autocorrelation image to obtain the drift-corrected images shown in Figure 4l,m. In the drift-corrected images, the peri-

odic structures are still very faint, but the unit cell dimensions are now identical in both images. We derived lattice parameters of 5.0 × $10^{-10}$ m, 8.1 × $10^{-10}$ m, and 90.8°, which agree perfectly with the expected surface structure (4.99 × $10^{-10}$ m × 8.10 × $10^{-10}$ m, 90.0°; [50]). Hence, we conclude that *un*Drift also performs very well in the drift correction of images with weak contrast.

## Long image series

After discussing the performance of *un*Drift under different experimental conditions, we now demonstrate the applicability to long image series spanning several hundred SPM images with an example shown in Figure 5. The presented series comprises 530 high-resolution AFM images recorded at the calcite–water interface over a measurement time of approximately 4 h. We evaluated these images with the semi-automatic periodic analysis of *un*Drift (algorithm I) in approximately 1 h 40 min, which corresponds to a drift correction rate of 318 images per hour. In this series, the image contrast is rather stable over the full measurement time (see Figure 5a–c), facilitating drift correction. Thus, the given correction rate is likely to be the upper limit. We find that the number of drift-corrected images per hour and,

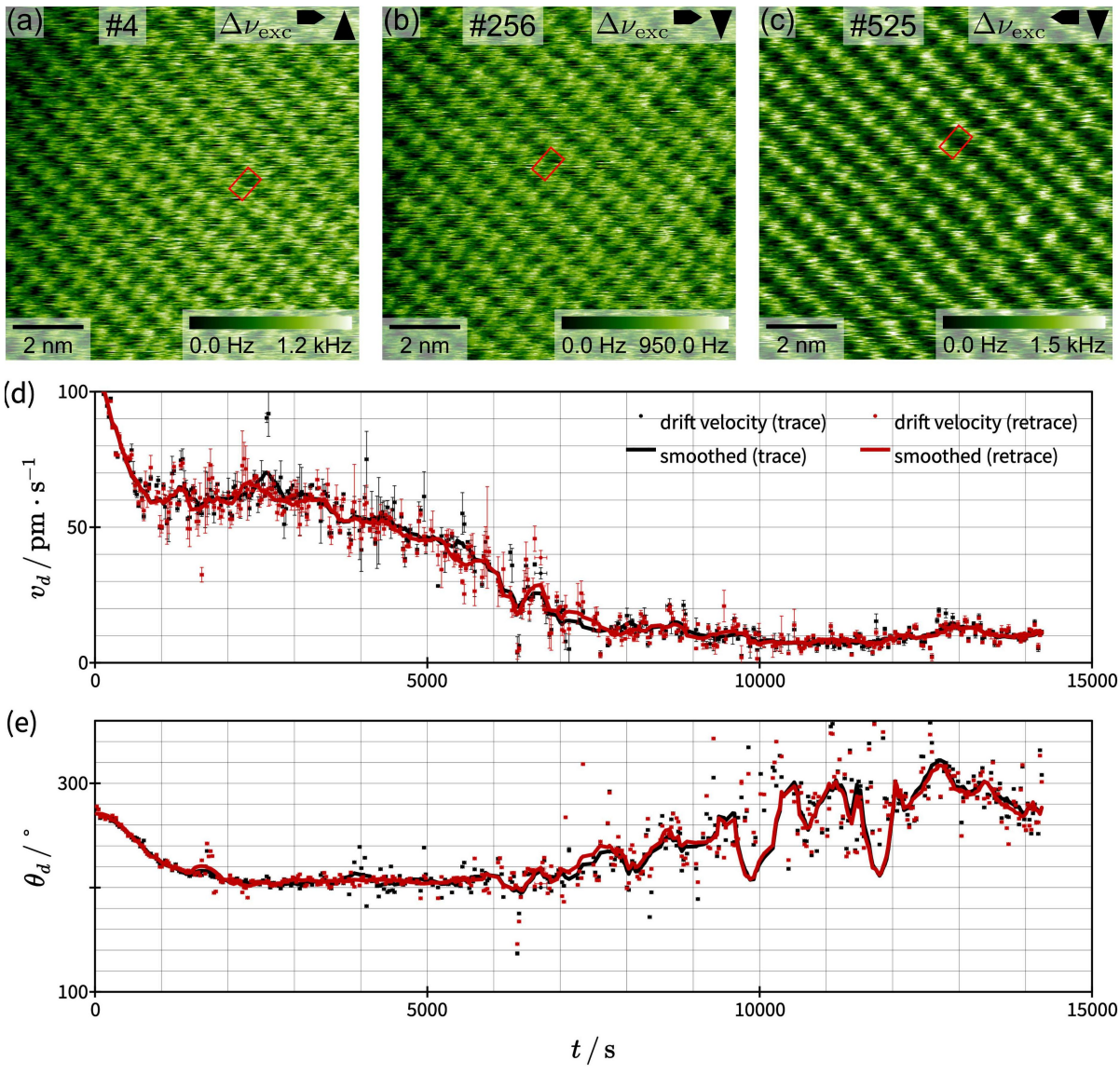


**Figure 5:** Application of *un*Drift to the analysis of a measurement session containing 530 AFM images recorded at the calcite–water interface. (a–c) Typical drift-corrected images from beginning, middle, and end of the evaluated AFM session. (d, e) Calculated drift velocities in polar coordinates as function of the measurement time *t*. The absolute values of $\vec{v}_d$ and the corresponding angle $\theta_d$ in are shown in (d) and (e), respectively. Results from trace and retrace images are shown as black and red circles, respectively, and the smoothed averages for both cases are shown as lines.

consequently, the performance of *un*Drift strongly depend on the image quality and contrast stability. Moreover, it is typically faster to evaluate longer image series than several series with few images. We find that the average drift correction rate with *un*Drift for typical AFM images is between 100 images per hour for short series and 200 images per hour for long series. Note that the analysis times discussed here are limited by the manual steps of the analysis (i.e., adjusting the analysis parameters and checking the results) rather than the computation time on all tested common desktop computers (e.g., Windows 10, Intel Core i5-9500, 6 cores @ 3.00 GHz, 8.00 GB RAM).

Next, we discuss the drift velocities measured during this image series and what they tell us about our AFM instrument. In Figure 5d,e, we show the absolute values of $v_d$ and polar angle $\theta_d$ of the drift velocity $\vec{v}_d$ as functions of the time. We observe a steep decrease of the drift velocity during the first 800 s (15 min) of our experiment. Then, the drift velocity decreases further, but with a lower change rate, until it reaches stable conditions approximately 8000 s (2 h 15 min) after starting the experiment. The polar angle $\theta_d$ (see Figure 5e) follows the same trend for the first 6000 s. After that, the change in the scan angle increases again. Compared to the change at the beginning of the experiment (before 800 s), however, the change in scan angle after 6000 s is much more random and looks more like noise. We explain this observation with the decreasing absolute value of the drift velocity. At the beginning of the experiment, the drift is caused by equilibration processes between sample surface, liquid, and AFM instrument, so the absolute drift velocity is high and has a stable direction. Then, with increasing measurement time, the system gets closer to equilibrium, which causes the drift velocity to decrease. Hence, the relative contribution of thermal fluctuations to the drift velocity increases and the direction of the drift velocity becomes less stable. The trends observed in Figure 5d,e show us that our AFM instrument needs to equilibrate for about 800 s (15 min) to reach a moderate drift velocity. Stable measurement conditions, however, are only reached after approximately 8000 s (2 h 15 min) of equilibration time.

In addition to the drift velocities, we want to discuss the lattice parameters derived by *un*Drift. Figure 6 shows histograms for all three lattice parameters derived from all 530 images in the session shown in Figure 5. Because of the applied drift correction scheme, we get two sets of lattice parameters for each image. One dataset originates from drift correction with the previous image, and the other dataset originates from drift correction with the next image. Here, we show the histograms of the average values calculated for each image. Figure 6 reveals that all three experimental lattice parameters ($5.0 \times 10^{-10}$ m × $8.1 \times 10^{-10}$ m, 90°) agree with the literature values ($4.99 \times 10^{-10}$ m × $8.10 \times 10^{-10}$ m, 90.0°; [50]) within an interval of the standard deviation ($\sigma_a = 0.06 \times 10^{-10}$ m, $\sigma_b = 0.12 \times 10^{-10}$ m, and $\sigma_\gamma = 1.0°$) from the average value. Moreover, these histograms give us detailed insight into the experimental accuracy of our AFM measurements. Figure 6a,b reveals that our instrument's distance accuracy after calibration and drift correction is $\pm 2.5 \times 10^{-11}$ m. In terms of angles, Figure 6c shows that the accuracy is ±2°. In both cases, we used the $2\sigma \approx 0.95\%$ confidence interval to determine the accuracy of our device. Note that the measurement accuracy also depends on the image quality, as the peaks in the autocorrelation and Fourier transform images get less defined with decreasing image quality. Hence, we expect the accuracy of distances and angles to decrease with decreasing image quality.

## Conclusion

We present *un*Drift, a versatile and powerful software for calibration and drift correction of SPM images. *un*Drift provides three different drift correction algorithms enabling the drift correction of SPM images, regardless of their scan direction and whether they exhibit periodic structures or not. We demonstrate the performance of *un*Drift in terms of image quality and experimental conditions with three examples,

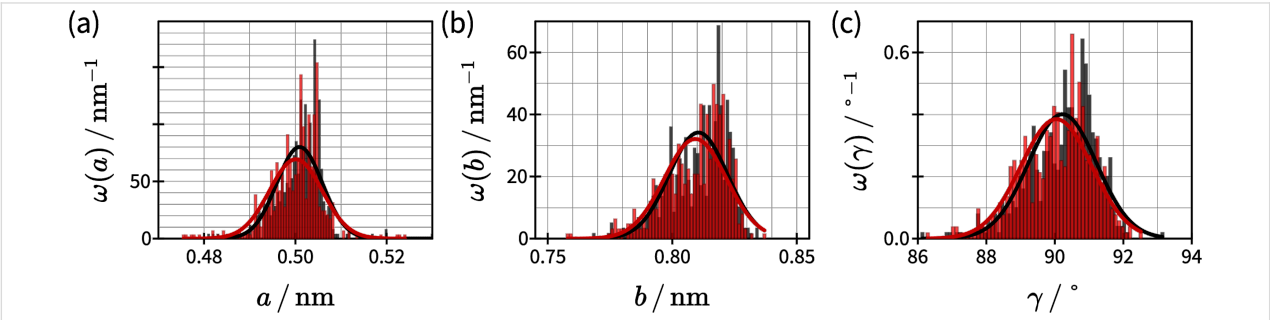


**Figure 6:** Histograms of lattice parameters *a*, *b*, and γ derived for the water structure at the calcite(10.4)–water interface based on the image series shown in Figure 5. Experimental results are shown as bar plots, and the corresponding normal distributions are shown as lines. Results for the trace (retrace) images are black (red). The average lattice parameters determined from these distributions are $a = 5.0 \times 10^{-10}$ m, $b = 8.1 \times 10^{-10}$ m, and γ = 90° for both trace and retrace data. The corresponding standard deviations are $\sigma_a = 0.06 \times 10^{-10}$ m, $\sigma_b = 0.12 \times 10^{-10}$ m, and $\sigma_\gamma = 1.0°$.

namely one image set with exceptionally high drift velocity, one with only a small usable part of an image, and one with an overall low image contrast and low signal-to-noise ratio. *un*Drift handles these three situations reliably. Moreover, we show that *un*Drift can be used for the fast evaluation of drift velocities and lattice parameters in long measurement sessions spanning several hundred images. We, thus, conclude that *un*Drift can be a valuable tool in the evaluation of SPM image data.

## Supporting Information

Supporting Information features derivations of the mathematical expressions used for the calibration and drift correction, a description of the procedure used to derive correction parameters as well as other technical aspects. Moreover, the gwy files for all shown AFM images and used analysis parameters are included in Supporting Information Files 2–5.

### Supporting Information File 1

Calibration and drift correction procedures
[https://www.beilstein-journals.org/bjnano/content/supplementary/2190-4286-14-101-S1.pdf]

### Supporting Information File 2

Experimental data shown in Figure 2.
[https://www.beilstein-journals.org/bjnano/content/supplementary/2190-4286-14-101-S2.zip]

### Supporting Information File 3

Experimental data shown in Figure 3.
[https://www.beilstein-journals.org/bjnano/content/supplementary/2190-4286-14-101-S3.zip]

### Supporting Information File 4

Experimental data shown in Figure 4.
[https://www.beilstein-journals.org/bjnano/content/supplementary/2190-4286-14-101-S4.zip]

### Supporting Information File 5

Experimental data shown in Figure 5.
[https://www.beilstein-journals.org/bjnano/content/supplementary/2190-4286-14-101-S5.zip]

## Acknowledgements

We acknowledge fruitful discussions with Philipp Rahe. We thank Adam Sweetman and Dylan Barker for kindly providing us with measurement data from a Nanonis controller, which enabled us to implement the import of Nanonis files.

## Funding

We acknowledge financial support from the DFG through grant INST 215/635-1 FUGG and KU 1980/11-1.

## ORCID® iDs

Tobias Dickbreder - https://orcid.org/0000-0002-7269-7236
Franziska Sabath - https://orcid.org/0000-0002-1562-7303

## References

1. Libioulle, L.; Ronda, A.; Taborelli, M.; Gilles, J. M. *J. Vac. Sci. Technol., B: Microelectron. Nanometer Struct.–Process., Meas., Phenom.* **1991,** *9,* 655–658. doi:10.1116/1.585480
2. van de Leemput, L. E. C.; Rongen, P. H. H.; Timmerman, B. H.; van Kempen, H. *Rev. Sci. Instrum.* **1991,** *62,* 989–992. doi:10.1063/1.1141989
3. Yurov, V. Y.; Klimov, A. N. *Rev. Sci. Instrum.* **1994,** *65,* 1551–1557. doi:10.1063/1.1144890
4. Yothers, M. P.; Browder, A. E.; Bumm, L. A. *Rev. Sci. Instrum.* **2017,** *88,* 013708. doi:10.1063/1.4974271
5. Rahe, P.; Bechstein, R.; Kühnle, A. *J. Vac. Sci. Technol., B: Microelectron. Nanometer Struct.–Process., Meas., Phenom.* **2010,** *28,* C4E31–C4E38. doi:10.1116/1.3360909
6. Henriksen, K.; Stipp, S. L. S. *Am. Mineral.* **2002,** *87,* 5–16. doi:10.2138/am-2002-0102
7. Adler, J. G.; Chen, T. T.; Gallagher, M. C.; Konkin, M. K.; Mullin, D. P. *J. Vac. Sci. Technol., B: Microelectron. Nanometer Struct.–Process., Meas., Phenom.* **1991,** *9,* 992–995. doi:10.1116/1.585443
8. Cai, C. Z.; Chen, X. Y.; Shu, Q. Q.; Zheng, X. L. *Rev. Sci. Instrum.* **1992,** *63,* 5649–5652. doi:10.1063/1.1143395
9. Carrara, S.; Facci, P.; Nicolini, C. *Rev. Sci. Instrum.* **1994,** *65,* 2860–2863. doi:10.1063/1.1145207
10. Stoll, E. P. *Rev. Sci. Instrum.* **1994,** *65,* 2864–2869. doi:10.1063/1.1144629
11. Trawick, M. L.; Megens, M.; Angelescu, D. E.; Harrison, C.; Vega, D. A.; Chaikin, P. M.; Register, R. A.; Adamson, D. H. *Scanning* **2003,** *25,* 25–33. doi:10.1002/sca.4950250106
12. Lapshin, R. V. *Meas. Sci. Technol.* **2007,** *18,* 907–927. doi:10.1088/0957-0233/18/3/046
13. Follin, N. D.; Taylor, K. D.; Musalo, C. J.; Trawick, M. L. *Rev. Sci. Instrum.* **2012,** *83,* 083711. doi:10.1063/1.4738646
14. Jørgensen, J. F.; Carneiro, K.; Madsen, L. L.; Conradsen, K. *J. Vac. Sci. Technol., B: Microelectron. Nanometer Struct.–Process., Meas., Phenom.* **1994,** *12,* 1702–1704. doi:10.1116/1.587267
15. Fu, J.; Chu, W.; Dixson, R.; Orji, G.; Vorburger, T.; Secula, E. M.; Seiler, D. G.; Khosla, R. P.; Herr, D.; Garner, C. M.; McDonald, R.; Diebold, A. C. *AIP Conf. Proc.* **2009,** *1173,* 280–284. doi:10.1063/1.3251234
16. Zhang, L.; Long, Q.; Liu, Y.; Zhang, J.; Feng, Z. *Ultramicroscopy* **2016,** *166,* 16–26. doi:10.1016/j.ultramic.2016.03.013
17. Zhang, L.; Chen, X.; Huang, J.; Li, H.; Chen, L.; Huang, Q. *Rev. Sci. Instrum.* **2019,** *90,* 023704. doi:10.1063/1.5052281
18. Jørgensen, J. F.; Madsen, L. L.; Garnaes, J.; Carneiro, K.; Schaumburg, K. *J. Vac. Sci. Technol., B: Microelectron. Nanometer Struct.–Process., Meas., Phenom.* **1994,** *12,* 1698–1701. doi:10.1116/1.587266
19. Staub, R.; Alliata, D.; Nicolini, C. *Rev. Sci. Instrum.* **1995,** *66,* 2513–2516. doi:10.1063/1.1145650

20. Poirier, G. E.; White, J. M. *Rev. Sci. Instrum.* **1990,** *61,* 3917–3918. doi:10.1063/1.1141526
21. Korpelainen, V.; Lassila, A. *Meas. Sci. Technol.* **2007,** *18,* 395–403. doi:10.1088/0957-0233/18/2/s11
22. Marinello, F.; Savio, E. *Meas. Sci. Technol.* **2007,** *18,* 462–468. doi:10.1088/0957-0233/18/2/s19
23. Rost, M. J.; Crama, L.; Schakel, P.; van Tol, E.; van Velzen-Williams, G. B. E. M.; Overgauw, C. F.; ter Horst, H.; Dekker, H.; Okhuijsen, B.; Seynen, M.; Vijftigschild, A.; Han, P.; Katan, A. J.; Schoots, K.; Schumm, R.; van Loo, W.; Oosterkamp, T. H.; Frenken, J. W. M. *Rev. Sci. Instrum.* **2005,** *76,* 053710. doi:10.1063/1.1915288
24. Patera, L. L.; Bianchini, F.; Africh, C.; Dri, C.; Soldano, G.; Mariscal, M. M.; Peressi, M.; Comelli, G. *Science* **2018,** *359,* 1243–1246. doi:10.1126/science.aan8782
25. Diao, Z.; Ueda, K.; Hou, L.; Yamashita, H.; Custance, O.; Abe, M. *Appl. Phys. Lett.* **2023,** *122,* 121601. doi:10.1063/5.0139330
26. Gómez-Rodríguez, J. M.; Sáenz, J. J.; Baró, A. M.; Veuillen, J.-Y.; Cinti, R. C. *Phys. Rev. Lett.* **1996,** *76,* 799–802. doi:10.1103/physrevlett.76.799
27. Huang, W.; Wang, W.; Xia, A.; Jin, N.; Hu, Z. *J. Vac. Sci. Technol., B: Microelectron. Nanometer Struct.–Process., Meas., Phenom.* **2000,** *18,* 2027–2029. doi:10.1116/1.1306302
28. Rahe, P.; Schütte, J.; Schniederberend, W.; Reichling, M.; Abe, M.; Sugimoto, Y.; Kühnle, A. *Rev. Sci. Instrum.* **2011,** *82,* 063704. doi:10.1063/1.3600453
29. Clifford, C. A.; Seah, M. P. *Meas. Sci. Technol.* **2009,** *20,* 095103. doi:10.1088/0957-0233/20/9/095103
30. Niu, D.; Li, J.; Chen, Y.; Huang, W. *J. Vac. Sci. Technol., B: Microelectron. Nanometer Struct.–Process., Meas., Phenom.* **2010,** *28,* 1070–1072. doi:10.1116/1.3478305
31. Gaponenko, I.; Tückmantel, P.; Ziegler, B.; Rapin, G.; Chhikara, M.; Paruch, P. *Sci. Rep.* **2017,** *7,* 669. doi:10.1038/s41598-017-00765-w
32. Luo, T.; Chen, Y.; Huang, W.; Gao, S. *Proc. SPIE* **2014,** *9283,* 928312. doi:10.1117/12.2072892
33. Sollböhmer, O.; May, K.-P.; Anders, M. *Thin Solid Films* **1995,** *264,* 176–183. doi:10.1016/0040-6090(95)05847-8
34. Mantooth, B. A.; Donhauser, Z. J.; Kelly, K. F.; Weiss, P. S. *Rev. Sci. Instrum.* **2002,** *73,* 313–317. doi:10.1063/1.1427417
35. Chen, Y.; Huang, W. *Rev. Sci. Instrum.* **2007,** *78,* 073701. doi:10.1063/1.2751091
36. Marinello, F.; Balcon, M.; Schiavuta, P.; Carmignato, S.; Savio, E. *Meas. Sci. Technol.* **2011,** *22,* 094016. doi:10.1088/0957-0233/22/9/094016
37. Woodward, J. T.; Schwartz, D. K. *J. Vac. Sci. Technol., B: Microelectron. Nanometer Struct.–Process., Meas., Phenom.* **1998,** *16,* 51–53. doi:10.1116/1.589834
38. Sun, Y.; Pang, J. H. L. *Nanotechnology* **2006,** *17,* 933–939. doi:10.1088/0957-4484/17/4/016
39. Marinello, F.; Bariani, P.; Chiffre, L. D.; Savio, E. *Meas. Sci. Technol.* **2007,** *18,* 689–696. doi:10.1088/0957-0233/18/3/019
40. Salmons, B. S.; Katz, D. R.; Trawick, M. L. *Ultramicroscopy* **2010,** *110,* 339–349. doi:10.1016/j.ultramic.2010.01.006
41. Degenhardt, J.; Tutsch, R.; Dai, G. *Meas. Sci. Technol.* **2021,** *32,* 035005. doi:10.1088/1361-6501/abc9f8
42. Kizu, R.; Misumi, I.; Hirai, A.; Gonda, S. *Meas. Sci. Technol.* **2020,** *31,* 054009. doi:10.1088/1361-6501/ab6b50
43. Meyer, T. R.; Ziegler, D.; Brune, C.; Chen, A.; Farnham, R.; Huynh, N.; Chang, J.-M.; Bertozzi, A. L.; Ashby, P. D. *Ultramicroscopy* **2014,** *137,* 48–54. doi:10.1016/j.ultramic.2013.10.014
44. Sun, X.; Heaps, E.; Yacoot, A.; Yang, Q.; Grolich, P.; Klapetek, P. *Meas. Sci. Technol.* **2021,** *32,* 115010. doi:10.1088/1361-6501/ac100f
45. Horcas, I.; Fernández, R.; Gómez-Rodríguez, J. M.; Colchero, J.; Gómez-Herrero, J.; Baro, A. M. *Rev. Sci. Instrum.* **2007,** *78,* 013705. doi:10.1063/1.2432410
46. *unDrift - SPM Image Drift Correction and Calibration,* version 1.0; Dickbreder, T., 2023. doi:10.4119/unibi/2984385
47. *Kontrast: interactive data visualization,* standalone distribution version 1.3.3; Söngen Development GmbH, 2021.
48. Nečas, D.; Klapetek, P. *Cent. Eur. J. Phys.* **2012,** *10,* 181–188. doi:10.2478/s11534-011-0096-2
49. Deer, W. A.; Howie, R. A.; Zussman, J. *An introduction to the rockforming minerals,* 2nd ed.; Pearson Education Limited: Edinburgh Gate, Harlow, England, 1992.
50. Effenberger, H.; Mereiter, K.; Zemann, J. *Z. Kristallogr.* **1981,** *156,* 233–243. doi:10.1524/zkri.1981.156.3-4.233


## License and Terms

BEILSTEIN JOURNAL OF NANOTECHNOLOGY

# Unveiling the nature of atomic defects in graphene on a metal surface

Karl Rothe*, Nicolas Néel and Jörg Kröger*

Full Research Paper

Open Access

Address:
Institut für Physik, Technische Universität Ilmenau, D-98693 Ilmenau, Germany

Email:
Karl Rothe* - karl.rothe@tu-ilmenau.de; Jörg Kröger* - joerg.kroeger@tu-ilmenau.de

* Corresponding author

Keywords:
atomic force microscopy and spectroscopy; graphene; scanning tunneling microscopy and spectroscopy

*Beilstein J. Nanotechnol.* **2024,** *15,* 416–425.
https://doi.org/10.3762/bjnano.15.37

Received: 31 December 2023
Accepted: 18 March 2024
Published: 15 April 2024

This article is part of the thematic issue "Advanced atomic force microscopy techniques V".

Guest Editor: P. Rahe



## Abstract

Low-energy argon ion bombardment of graphene on Ir(111) induces atomic-scale defects at the surface. Using a scanning tunneling microscope, the two smallest defects appear as a depression without discernible interior structure suggesting the presence of vacancy sites in the graphene lattice. With an atomic force microscope, however, only one kind can be identified as a vacancy defect with four missing carbon atoms, while the other kind reveals an intact graphene sheet. Spatially resolved spectroscopy of the differential conductance and the measurement of total-force variations as a function of the lateral and vertical probe–defect distance corroborate the different character of the defects. The tendency of the vacancy defect to form a chemical bond with the microscope probe is reflected by the strongest attraction at the vacancy center as well as by hysteresis effects in force traces recorded for tip approach to and retraction from the Pauli repulsion range of vertical distances.

## Introduction

Defects in lattices of two-dimensional (2D) materials are considered as promising building blocks for tailoring electronic and phononic band structures, magnetic texture, photon emission, and charge carrier concentration [1]. In addition, defects profoundly impact, in a beneficial or detrimental manner, characteristic properties of 2D materials [2].

A prominent 2D material is graphene. Intact graphene, the 2D $sp^2$ arrangement of C atoms in a honeycomb mesh, is well known for its appealing electronic and mechanical properties [3,4]. However, during its epitaxial growth in surface science experiments or its fabrication for applications, defects, that is, deviations from the ideal 2D lattice, inevitably occur. Examples for defects are vacancies, interstitial atoms, grain boundaries, stacking faults or wrinkles [5-23]. Even single missing C atoms were demonstrated to severely change electronic [11,13,14,18], mechanical [17], and magnetic [7,8,10,12] characteristics. It is therefore not surprising that the intentional

creation of defects, which has mainly been achieved by noble-gas ion irradiation [6,13,14,17,19,21,24], represents an opportunity for systematic defect studies.

The work presented here was stimulated by the lack of experimental data on the actual geometry of atomic-scale defects in graphene. So far, scanning tunneling microscope (STM) topographies have been claimed to be in accordance with, for example, single-C vacancy sites. However, clear-cut evidence for a missing C atom in the graphene lattice has remained elusive. Therefore, in addition to an STM, an atomic force microscope (AFM) has been used in the present study to unveil the geometric structure of the defect sites. Surprisingly, the smallest defect in graphene on Ir(111), which appears as a depression in STM images and, therefore, may readily be assigned to a single-C vacancy site, gives rise to an undistorted graphene lattice in AFM images. In contrast, slightly larger defects are indeed lacking the graphene atomic lattice structure in their interior. Spatially resolved spectroscopy of the differential conductance ($dI/dV$, $I$: tunneling current, $V$: bias voltage) and of the tuning fork resonance frequency change ($\Delta f$) further unravel marked differences between these two kinds of defects.

## Experimental

A combined STM-AFM was operated in ultrahigh vacuum ($5 \times 10^{-9}$ Pa) and at low temperature (5 K). Surfaces of Ir(111) were cleaned by $Ar^+$ ion bombardement and annealing. The epitaxial growth of graphene proceeded by exposing the heated (1300 K) Ir(111) surface to the gaseous molecular precursor $C_2H_4$ (purity: 99.9%) at a partial pressure of $10^{-5}$ Pa for 120 s [25,26]. Atomic-scale defects were created by bombarding graphene-covered Ir(111) with low-energy (140 eV) $Ar^+$ ions (purity of the Ar gas: 99.999%) [27-30] at room temperature for 5 s followed by annealing (900 K, 5 min). The $Ar^+$ beam enclosed an angle of 15° with the surface normal and exhibited a flux of ≈0.01 1/(nm$^2$·s). A chemically etched (NaOH, 0.1 M) W wire (purity: 99.99%, diameter: 50 µm) was used as the tip material. Tips were cleaned by field emission on and indentations into a clean Au(111) crystal and, presumably, coated with a Au film. The tip shape was further sharpened by single-atom transfers from the tip to the sample surface [31-36]. Topographic STM data were recorded in constant-current as well as constant-height modes with the bias voltage applied to the sample. Constant-height scanning tunneling spectroscopy (STS) of $dI/dV$ was performed by sinusoidally modulating (5 $mV_{rms}$, 725 Hz) the dc bias voltage and measuring the first harmonic of the ac current response of the tunneling junction with a lock-in amplifier. For AFM data acquisition, resonance frequency changes of an oscillating piezoelectric tuning fork sensor [37,38] (resonance frequency: 30.5 kHz, quality factor: 45000, amplitude: 50 pm) were mapped at constant height for topographic images. The vertical force between tip and sample was extracted from distance-dependent measurements of the resonance frequency shift [39,40]. Topographic STM and AFM data were processed using WSxM [41].

## Results and Discussion

### Scanning tunneling microscopy and spectroscopy findings

After gentle $Ar^+$ ion bombardment, graphene-covered Ir(111) gives rise to STM images as depicted in Figure 1a. The periodic superstructure of depressions with a measured repeat distance of 2.59 ± 0.05 nm reflects the moiré pattern that is caused by the lattice mismatch between graphene and Ir(111), where graphene $\langle 11\bar{2}0 \rangle$ directions are aligned with $\langle 10\bar{1} \rangle$ directions of the metal substrate [25,42-45]. The lozenge unit cell of the coincidence lattice is depicted in the bottom inset to Figure 1a, which shows an atomically resolved STM image of graphene. Mounds of the moiré pattern appear as depressions, while valleys show bright contrast at the specific tunneling parameters used for the STM topograph in Figure 1a. At higher tunneling currents, a contrast inversion occurs (top inset to Figure 1a), and mounds (valleys) appear bright (dark). A similar contrast inversion was previously reported for different tunneling voltages [42] and associated with the specific electronic structure of graphene on Ir(111) [45]. In the present experiments, the contrast inversion is induced by the reduction of the tip–graphene separation. As will be shown below, the involved junction currents correspond to a separation that is still larger than, but close to, the point of maximum attractive force. Therefore, a tentative rationale to the observed contrast inversion is the increased tip–graphene hybridization compared to the far tunneling range, which may entail a modification of the graphene electronic structure or enhance the contribution of substrate states to the junction current [46]. The mounds and adjacent valleys of the moiré superstructure are characterized by different graphene–Ir(111) stackings. Mounds of the moiré superstructure correspond to C hexagons of the graphene lattice residing atop an Ir atom, while adjacent valleys of the moiré superstructure are associated with C hexagons residing atop an hexagonal closed-packed (hcp) and a face-centered cubic (fcc) site of Ir(111). From STM images alone, hcp and fcc valleys cannot be distinguished, that is, the assignment in Figure 1a is tentative. In addition to the moiré superlattice, depressions with various sizes and shapes are visible, which are not present on the freshly prepared graphene surface (Supporting Information File 1, Figure S1). Therefore, the depressions are associated with defects of the graphene lattice induced by the $Ar^+$ ion impact. The most abundant defect types (≈58% of all observed defects) exhibit a triangular shape (top inset to Figure 1a). Type **1** (≈35%, Figure 1b) appears with a laterally larger and deeper

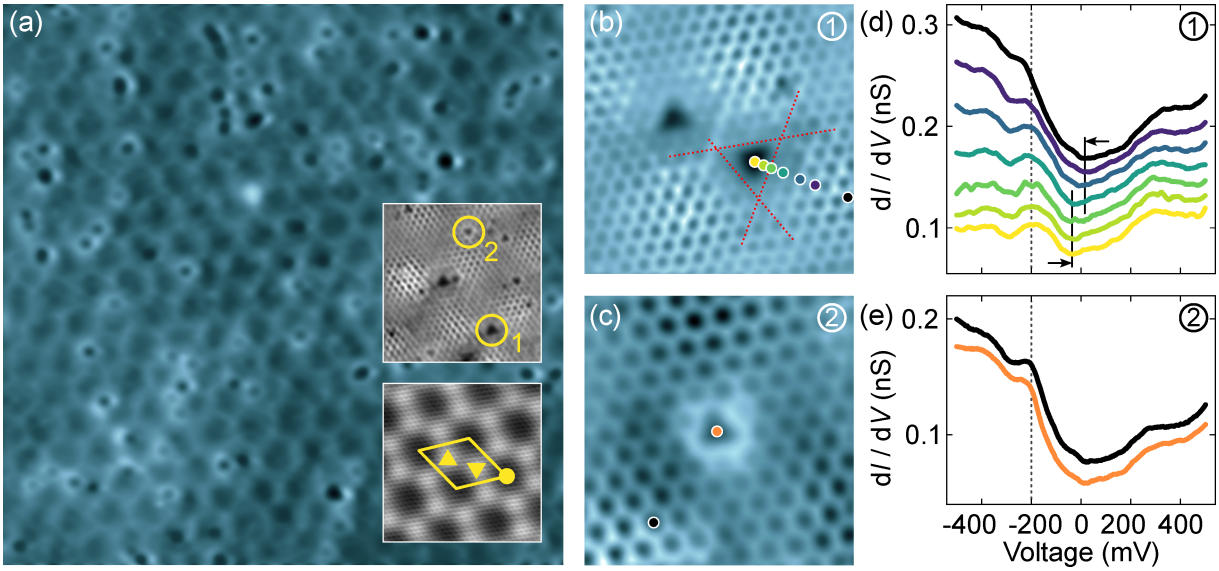


**Figure 1:** Scanning tunneling microscopy and spectroscopy of defect types **1** and **2** in graphene on Ir(111). (a) Constant-current STM image of $Ar^+$-bombarded graphene (bias voltage: 100 mV, tunneling current: 50 pA, size: 40 nm × 40 nm). Top inset: atomically resolved graphene lattice with defects **1** and **2** (10 mV, 40 nA, 5.9 nm × 5.9 nm). Bottom inset: moiré superstructure with lozenge unit cell (side length: ≈2.53 nm) and the atomically resolved graphene lattice. Triangles mark different valley stacking domains with ▲ and ▼ tentatively marking hcp and fcc stacking, while the dot (●) indicates the mound top site of the moiré lattice (10 mV, 5 nA, 8 nm × 8 nm). (b) Two adjacent type-**1** vacancies located at an hcp (left) and an fcc (right) position of the moiré lattice (10 mV, 55 nA, 3.6 nm × 3.6 nm). Red dashed lines approximate the defect edges (see text). (c) Single type-**2** defect at an fcc valley site (10 mV, 25 nA, 2.5 nm × 2.5 nm). The gray scale (from dark to bright) covers apparent heights from 0 to (a) 190 pm, (b) 50 pm and (c) 30 pm. (d) Series of constant-height d*I*/d*V* spectra recorded at the positions marked by the colored dots in (b). The steplike feature at ≈−200 mV (dashed line) corresponds to an Ir(111) surface resonance. The solid vertical lines mark the shift of the suggested Dirac cone signature. (e) Spectra of d*I*/d*V* recorded atop the positions indicated by the orange and black dots in (c). The STS data for defects **1** and **2** were acquired with the same tip. The spectra are shifted vertically by 0.02 nS. Feedback loop parameters prior to spectroscopy: 500 mV, 50 pA.

depression than type **2** (≈23%, Figure 1c). Moreover, type-**1** defects occur nearly exclusively (≈100%) at valley sites of the moiré lattice. The hcp and fcc stacking of the valley sites defines the orientation of the triangular shape of the defect, pointing in opposite directions at the two valley sites [24]. Defects of type **2** do not show a preferential moiré lattice site (top inset to Figure 1a). Other defects observed in the STM images are most likely due to Ir(111) surface impurities. These defects exhibit different shapes and contrasts in STM images and are already present on clean graphene-covered Ir(111) (Supporting Information File 1, Figure S1).

Figure 1b presents a close-up STM view of the first kind of equilateral triangular defects. The edges are oriented along the symmetry directions of the graphene lattice. To estimate the edge lengths, an equilateral triangle was circumscribed (dashed lines) that continues the edges of those C hexagons of intact graphene that are closest to the defect. A length of 0.65 ± 0.05 nm has been inferred in this manner. The apparent depth of the defect at 10 mV is 28 ± 9 pm. The second type of triangular defects (Figure 1c) exhibits a smaller side length of 0.46 ± 0.03 nm with the same orientations as observed for **1**. The apparent depth of type-**2** defects at 10 mV is 7 ± 3 pm. The uncertainty margins reflect the standard deviation of measured lengths of ten different defects of each type. Importantly, from STM data alone, both triangular defects appear as depressions with no identifiable interior structure. Therefore, they may be interpreted as graphene vacancy sites, that is, as sites with missing C atoms.

As shown by the spectra of d*I*/d*V* for the two defect types (Figure 1d,e) the electronic structure differs. Atop the center of **1** (bottom spectrum of Figure 1d) two prominent signatures contribute to the spectral data. The broad steplike variation at approx. −200 mV (dashed line) is due to the Ir(111) surface resonance at the $\bar{\Gamma}$-point of the surface Brillouin zone (BZ) [47], which is shifted toward the Fermi energy ($E_F$) because of the presence of graphene [48]. The ∨-shaped feature with minimum signal slightly below zero bias may be associated with the Dirac cone at the BZ $\bar{K}$-point. Figure 1d reveals the spatial evolution of the spectra, which shows a gradual quenching of the Ir(111) surface resonance signal accompanied by a small shift toward zero bias voltage upon laterally approaching the defect center. The Dirac cone signal shifts from ≈18 mV above undistorted graphene (top spectrum in Figure 1d) to ≈−40 mV atop the center of the defect. While the extracted energy of the Dirac point is in agreement with previously reported values from STS experiments [49-51], it is lower

than the energy observed in photoemission experiments [52]. A possible rationale is the locally lifted graphene in the presence of the tip [53], which in turn decreases the charge transfer from graphene to the metal and reduces the p-doping [52] and concomitantly causes a lowering of the Dirac point energy. Type-**1** defects exhibit the same behavior in spatially resolved STS measurements, independent of the moiré valley they reside at. In contrast, d$I$/d$V$ data acquired above **2** are essentially identical to spectroscopic data of pristine graphene (Figure 1e). The lateral evolution of the d$I$/d$V$ spectra hints at a markedly different character of defects **1** and **2**, which will further be explored on the basis of the AFM results to be discussed below. They will clarify structural aspects of the defects and help understand the different spectroscopic properties.

Before presenting the AFM results, a comparison of the defect spectra in Figure 1d,e with previous results obtained for atomic-scale defects in graphene on other surfaces is noteworthy. Very pronounced electronic resonances localized at vacancy defects were reported for graphite surfaces [13], graphene on Pt(111) [14], and SiC($000\bar{1}$) [16]. These resonances were interpreted as a collective excitation of the graphene $\pi$ orbitals near the void [54], which depends on the coupling of the C atoms to the substrate surface. Therefore, the graphene–surface hybridization plays an important role in the occurrence of this resonance. Indeed, the resonance was not observed at all graphene defects on Pt(111). At some sites, it was quenched because of an increased interaction between the defect and the metal [55]. Therefore, the absence of a similar resonance in d$I$/d$V$ spectra of graphene defects on Ir(111) may be due to an increased graphene–metal interaction compared with Pt(111), although both graphene–metal hybrid structures belong to the weak-hybridization regime [43]. Another rationale is the deviation of the observed defects **1** and **2** from a monatomic vacancy site, which will further be explored in the following.

## Atomic force microscopy and spectroscopy findings

Figure 2 compares constant-height AFM topographs of the defects (Figure 2a,c) with simultaneously recorded current maps

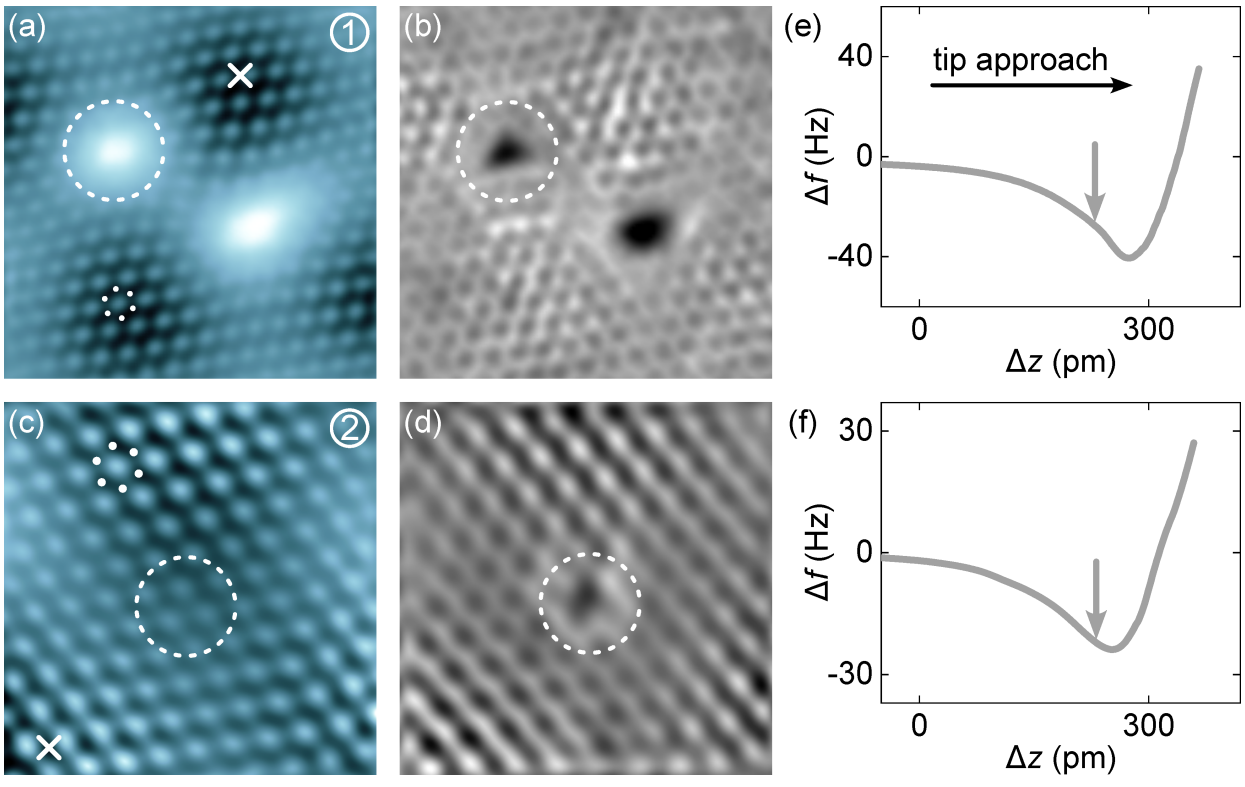


**Figure 2:** Atomic force and scanning tunneling microscopy of defect types **1** and **2** in graphene on Ir(111). (a) Constant-height AFM image and (b) simultaneously recorded tunneling current map of two adjacent defects (10 mV, 3.6 nm × 3.6 nm). (c),(d) As (a),(b) for a type-**2** defect (10 mV, 2.5 nm × 2.5 nm). The relevant defects in (a–d) are encircled by a dashed line. The gray scale (from dark to bright) covers changes in the resonance frequency shift from (a) −48 to −13 Hz and (c) −36 to −18 Hz as well as changes in the tunneling current from (b) 4 to 19 nA and (d) 4 to 7 nA. (e, f) Variation of $\Delta f$ with tip displacement $\Delta z$ (tip approach from left to right) on intact graphene (cross in (a) and (c)). The vertical arrow marks the tip excursion used for the constant-height $\Delta f$ current maps in (a–d). Displacement $\Delta z$ = 0 defines the tip–sample distance at which the feedback loop was deactivated above pristine graphene (10 mV, 50 pA).

of the same defects (Figure 2b,d). The tip–surface distance for the AFM and current maps was defined by the tip excursions marked with an arrow in the Δ*f* traces on clean graphene (Figure 2e,f). Tip approach, that is, the decrease of the tip–surface distance, is reflected by increasing tip excursions Δ*z* (horizontal arrow in Figure 2e). In Figure 2a, two adjacent defects appear as bright protrusions, where only the encircled defect is of kind **1**. It resides at a valley of the moiré lattice (data for a type-**1** defect at the other valley site are presented in Supporting Information File 1, Figure S2). Its brighter contrast compared to the intact graphene environment in the AFM topograph indicates that the attraction of type-**1** defects is considerably lower than that of intact graphene at the chosen tip–surface distance. In the associated current map (Figure 2b), defect **1** appears as a uniform depression without interior structure. Moreover, the graphene lattice, which appears via the protruding honeycomb cells in the AFM data, is distorted in the vicinity of the defects. The rows of honeycomb cells are not straight and rather follow curved trajectories that are bent towards the defect sites.

The Δ*f* map for a type-**2** defect (Figure 2c) was likewise acquired in the attractive regime (arrow in Figure 2f) where the graphene C atoms (white dots in Figure 2c) appear with lower contrast than the interior of the honeycomb cell [56]. Surprisingly, the AFM topograph of the assumed vacancy site hints at an intact graphene lattice (encircled area in Figure 2c) with no evidence of distortions, which clearly contrasts the result of the current map where defect **2** appears as a depression (Figure 2d).

Type-**1** defects were further analyzed by Δ*f* maps at different tip–surface distances (Figure 3a–c). The underlying tip excursions **A**–**C** are marked in the Δ*f*(Δ*z*) data sets obtained atop the defect and intact graphene (Figure 3d). The latter data were acquired at a lateral distance of a few graphene lattice constants apart from the defect (top right cross in Figure 3a). Atop the

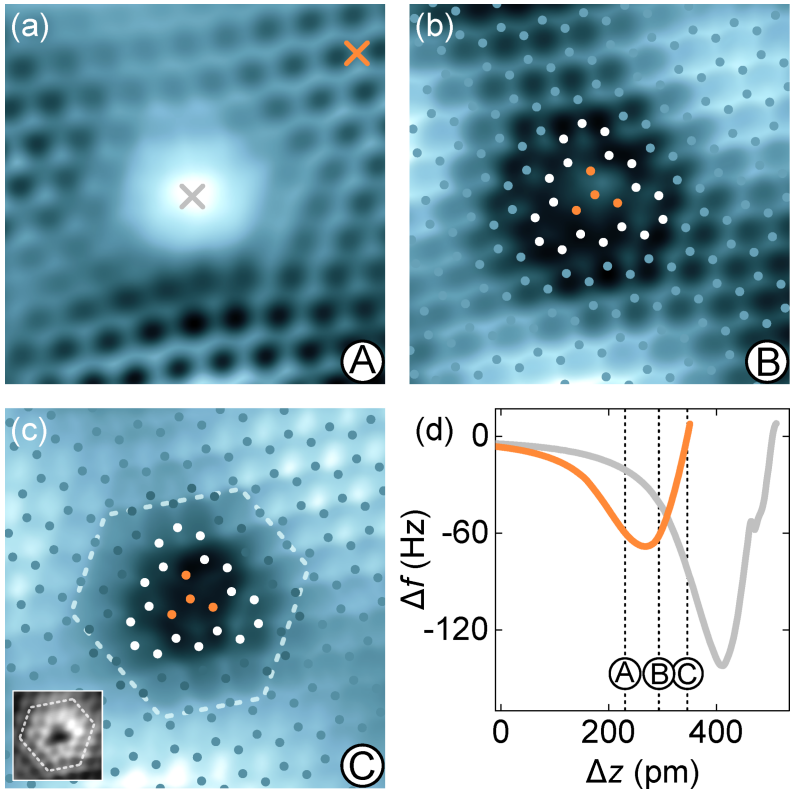


**Figure 3:** Vertical probe–surface distance dependence of AFM topographies of defect **1**. (a–c) Constant-height AFM images of a type-**1** defect (10 mV, 2.4nm × 2.4 nm). The tip–surface distance decreases from (a) to (c). The gray scale (from dark to bright) encodes resonance frequency changes from (a) −75 to −35 Hz, (b) −85 to −25 Hz, and (c) −120 to 40 Hz. Superimposed dots in (b) and (c) represent positions of C atoms (blue: C atom of intact graphene lattice; white: C atom at the defect edge; orange: missing C atom). White dashed line in (c) represents the edge of the dim rim surrounding the vacancy (see text). Inset to (c): constant-height current map (1.4 nm × 1.4 nm) of a type-**1** defect recorded at a comparable tip excursion as the Δ*f* map in (c). (d) Variation Δ*f*(Δ*z*) acquired atop intact graphene (orange line, top right cross in (a)) and above the defect (gray line, central cross in (a)). Labels **A**–**C** indicate the corresponding tip displacements for the topographic images in (a–c). The displacement Δ*z* = 0 is defined by the feedback loop parameters 10 mV and 50 pA above intact graphene. The same tip–surface distance prior to data acquisition above the defect is ensured by taking the apparent height difference at the feedback loop parameters into account.

defect center, $\Delta f(\Delta z)$ (gray line in Figure 3d) shows a minimum that is considerably lower and that occurs at larger tip excursions than observed for intact graphene.

At tip excursion **A**, defect **1** appears as a protrusion in $\Delta f$ maps (Figure 3a), while the surrounding graphene lattice exhibits lower $\Delta f$ contrast, which is in accordance with the $\Delta f$ behavior displayed in Figure 3d. In particular, the interior of the honeycomb unit cell is dark at this tip–graphene distance. Reaching the tip displacement **B**, which slightly exceeds the $\Delta f$ minimum, the formerly protruding defect turns into a depression with a weak central protrusion. Owing to the clearly resolved honeycomb mesh of graphene, the C atom positions can be superimposed as dots. The central protrusion of the $\Delta f$ map coincides with the position of a missing C atom. At even smaller tip–surface distances, which are well within the Pauli repulsion range (**C** in Figure 3d), the graphene honeycomb unit cell exhibits bright contrast, while defect **1** gives rise to a uniform depression without the central protrusion observed for tip excursion **B**. In addition, the depression of the $\Delta f$ map occupies an extended area that includes the three C atoms that are suggested to embrace the central protrusion in Figure 3b. Therefore, $\Delta f$ topographs acquired in the Pauli repulsion distance range are indicative of in total four missing C atoms, that is, defect **1** is compatible with a tetravacancy that was previously put forward by calculations accompanying an STM experiment [24]. The boundary of the tetravacancy is most likely lowered toward the metal surface allowing hybridization of the unsaturated C dangling bonds with substrate d bands. This scenario would explain the shift of the Dirac cone signature in d$I$/d$V$ spectra from positive sample voltages for intact graphene to negative voltages atop the defect (Figure 1d). While intact graphene on Ir(111) is slightly p-doped and exhibits the Dirac cone at energies above $E_F$ [52], hybridization of the graphene defect with the metal possibly induces electron transfer into graphene giving rise to local n-doping and the Dirac cone below $E_F$. In addition, the distortion of the graphene lattice that accompanies the increased hybridization with the surface may explain the dim rim of the vacancy in $\Delta f$ maps. The rim exhibits a hexagonal shape with nonuniform edge lengths (dashed lines in Figure 3c). It is also present as a blurry fringe in STM images (Figure 1b).

While topographic AFM data of type-**1** defects hint at a tetravacancy site, the actual origin of type-**2** defects remains elusive. The STS and AFM results presented here essentially exclude a monatomic vacancy site. Spectra of d$I$/d$V$ recorded atop defect-free graphene and above defect **2** are almost identical (Figure 1e), while AFM topographs show an undistorted graphene lattice (Figure 2c). A tentative rationale is then the presence of an $Ar^+$-induced Ir(111) surface defect [57].

In a next step, AFM imaging of the defects at different tip–surface distances was complemented by spatially resolved $\Delta f(\Delta z)$ measurements (Figure 4). Figure 4a shows the evolution of the total vertical force recorded along the path across a type-**1** defect indicated in the inset. The vertical force $F$ is extracted from $\Delta f$ data following a previously reported algorithm [39,40]. The minima $F^*$, which are defined by the points of maximum attraction attained at $\Delta z^*$ ($F^* = F(\Delta z^*)$), shifts towards larger tip excursions $\Delta z^*$ and larger magnitudes $|F^*|$ upon laterally approaching the defect center. The evolution of $F^*$ and $\Delta z^*$ with the consecutive positions along the path (from top to bottom) is depicted in Figure 4b. The strongest attraction

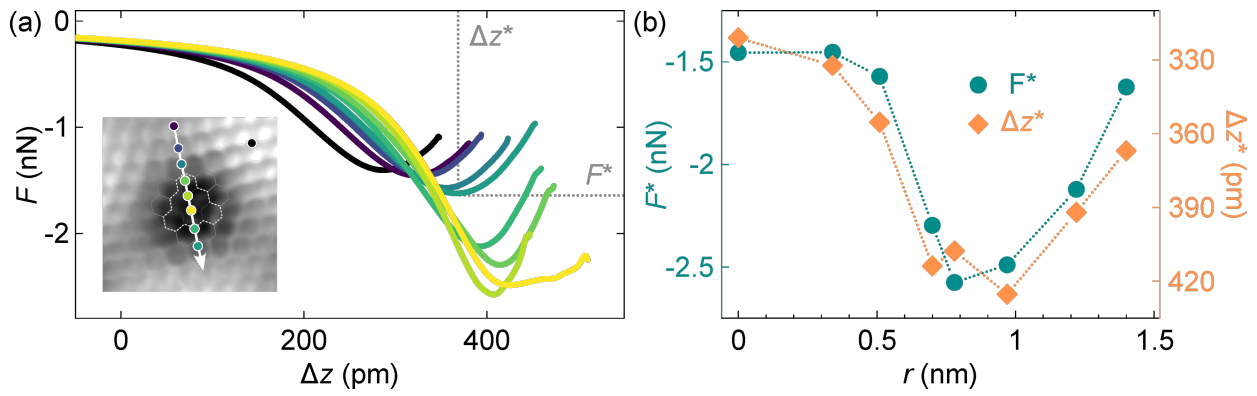


**Figure 4:** Total vertical force $F$ as a function of tip excursion and lateral evolution of the point of maximum attraction ($\Delta z^*$, $F^*$). (a) Variation of $F$ with tip displacement $\Delta z$ on the indicated path across a type-**1** defect. Displacement $\Delta z = 0$ is defined by the feedback loop parameters prior to the measurements (10 mV, 50 pA). Displacement $\Delta z^*$ and the associated force minimum $F^*$ are indicated in one data set. Inset: AFM image of a type-**1** defect with marked spectroscopy path oriented along $\langle 11\bar{2}0 \rangle$ (10 mV, 2.4 nm × 2.4 nm). (b) Evolution of $F^*$ (dots) and $\Delta z^*$ (lozenges) as a function of the distance $r$ with $r = 0$ at the top side of the path depicted in the inset to (a). Dotted lines serve as guides to the eye.

$\hat{F}^* \approx -2.6$ nN and largest tip excursion $\hat{z}^* \approx 425$ pm are observed at the defect center ($r = 0.78$ nm). These observations may be rationalized in terms of a more pronounced tendency of the defect center to form a chemical bond with the tip. In the case of defect **1**, dangling C bonds are most likely saturated by their hybridization with the Ir(111) surface. However, the proximity of a metal tip may offer a preferred bonding partner. A similar conclusion was inferred from spatially resolved force spectroscopy across a phthalocyanine molecule on Ag(111) whose pyrrolic H atoms had been removed. Despite the bonds formed by the H-detached N atoms of the molecule with the metal substrate, an increased reactivity was reported [58]. Intact graphene on Ru(0001) was previously demonstrated to exhibit locally different chemical reactivity on the basis of current-versus-distance characteristics [59]. For the second kind of defects, spatially resolved vertical-force traces are nearly identical and, therefore, do not hint at varying differences in bond formation (Supporting Information File 1, Figure S3).

The propensity to form a chemical bond between the Au tip apex atom and C atoms close to the center of type-**1** defects is likewise reflected by the occurrence of hysteresis loops in $\Delta f$ and $I$ approach and retraction traces. Figure 5 compares $\Delta f$ variations for tip approach (dots, $\Delta f\downarrow$) and retraction (circles, $\Delta f\uparrow$) on pristine graphene (Figure 5a) as well as on the boundary (Figure 5b) and the center (Figure 5c) of a type-**1** defect. The positions of data acquisition are marked in the inset to Figure 5d. While for graphene $\Delta f\downarrow$ and $\Delta f\uparrow$ data coincide, the $\Delta f$ traces for the tetravacancy exhibit a hysteresis loop in tip approach and retraction cycles. The width of the loop, defined as $\delta = \Delta z_p - \Delta z_a$ with $\Delta z_a$ and $\Delta z_p$ denoting the tip excursions where $\Delta f\downarrow$ and $\Delta f\uparrow$ intersect (Figure 5c), varies across the defect. Large values of δ are mostly observed at the boundary and in the central part of the proposed tetravacancy. Hysteresis widths exceeding 300 pm with a maximum of ≈330 pm were extracted from $\Delta f$ cycles in these regions. Lower values of δ including vanishing hysteresis loops were mainly probed in the interior part of the vacancy. A spatial map of δ is presented in Figure S4 of Supporting Information File 1.

For the interpretation of these observations, it is helpful to explore the simultaneously recorded $I(\Delta z)$ traces (Figure 5d–f). The hysteretic behavior that is present for $\Delta f$ at the defect site is likewise observed in approach ($I\downarrow$) and retraction ($I\uparrow$) current

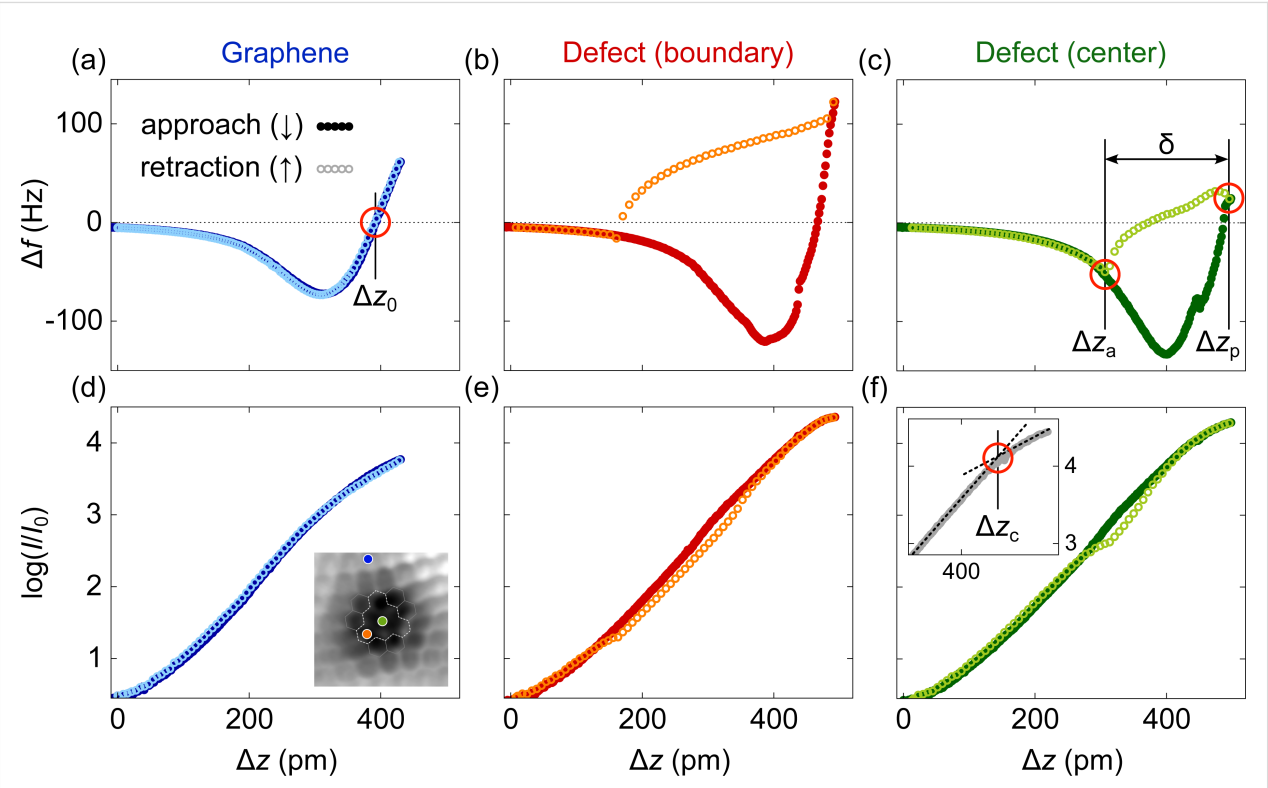


**Figure 5:** Hysteresis loops in approach (filled symbols) and retraction (open symbols) $\Delta f$ and $I$ traces. Variations $\Delta f(\Delta z)$ on (a) pristine graphene as well as atop (b) the defect-**1** boundary and (c) its interior. The zero of $\Delta f$ in (a) is marked $\Delta z_0$ and corresponds to the point of maximum attraction. The width of the hysteresis loop (δ) is defined by the difference of tip displacements associated with the intersections of $\Delta f$ approach and retraction traces in (e). (d–f) As (a–c), for $I(\Delta z)$ simultaneously recorded with $\Delta f(\Delta z)$. Zero tip displacement is defined by the feedback loop parameters 10 mV and $I_0 = 50$ pA. Inset to (d): Constant-height $\Delta f$ map of defect **1** (10 mV, 1.8 nm × 1.8 nm) with indicated positions for $\Delta f(\Delta z)$ and $I(\Delta z)$ data acquisition.

data, albeit with a smaller width of the hysteresis loop. The onset of deviations of $I\downarrow$ from a uniform exponential increase, marked $\Delta z_c$ in the inset to Figure 5f, signals the collapse of the tunneling barrier and the formation of a chemical bond between the tip and the surface [32,36,60,61], that is, between a Au and a C atom. In agreement with a previous report [62], $\Delta z_c \approx \Delta z_0$ with $\Delta z_0$ being the zero of $\Delta f\downarrow$ (Figure 5a), that is, the onset of bond formation corresponds to the point of maximum attraction. Importantly, at $\Delta z_c \approx \Delta z_0$ the equilibrium Au–C bond length has not yet been reached. To this end, the tip has to be displaced further by $\Delta z > \Delta z_c$ to reach the energy minimum.

The hysteresis loop in $\Delta f$ and $I$ data can, therefore, be rationalized in terms of a Au–C bond that is formed upon approaching the tip to the defect up to the point of maximum attraction at $\Delta z_c \approx \Delta z_0$. This bond remains intact during further tip approach up to $\Delta z_p$ and during tip retraction. The retraction of the tip may be accompanied by a partial detachment of graphene from the surface. As soon as the mechanical load surpasses the bond strength, it breaks at $\Delta z_a$. A comparable scenario was put forward previously for graphene on SiC(0001), where intact graphene was lifted from the surface after forming a Au tip–graphene bond and retracting the tip [63]. Hysteresis loops in $\Delta f$ and $I$ were then likewise observed. In the findings presented here, intact graphene does not exhibit hysteretic behavior, although one may expect a similar Au–C bond as proposed for graphene on SiC(0001). Most likely, the graphene–Ir(111) coupling is stronger than the graphene–SiC(0001) interaction and, thereby, prevents an identifiable lifting of graphene from the metal surface. The dangling bonds of the defect, however, can form a sufficiently strong bond with the tip apex atom. In addition, a voltage polarity effect was not observed, which renders the involvement of current-induced forces unlikely [64]. Another difference to the previous report concerns the actual behavior of $I\downarrow$ and $I\uparrow$. Within the hysteresis loop, the tunneling current during approach exceeds the current during retraction, $I\downarrow > I\uparrow$, which contrasts the opposite order for graphene on SiC(0001). On the basis of the experimental data alone it is difficult to identify a rationale for this observation. Indeed, electron transport across the junction depends on the tip–graphene and graphene–surface hybridization [23,65]. Therefore, simulations of the non-equilibrium charge transport across the junction are required for a detailed understanding of the observed current traces.

## Conclusion

A combination of STM and AFM experiments unravels the nature of defects in graphene on Ir(111) induced by rare-gas ion bombardment. Defects that are assigned to alleged monatomic vacancy sites by STM measurements represent an intact graphene lattice in AFM topographies. Possibly, a defect in the Ir(111) surface is the origin of the STM-derived contrast. The smallest vacancy defects are represented by triangular structures with four missing C atoms. These tetravacancies reveal an electronic structure clearly different from that of the surrounding intact graphene. Their interior exhibits the tendency to form bonds with the Au probe in close proximity, which is evidenced by shifts of the point of maximum attraction and hysteresis loops in force spectroscopy experiments.

## Supporting Information

### Supporting Information File 1

Additional data and figures.
[https://www.beilstein-journals.org/bjnano/content/supplementary/2190-4286-15-37-S1.pdf]

## Funding

Funding by the Deutsche Forschungsgemeinschaft through KR2912/17-1 and the German Federal Ministry of Education and Research within the “Forschungslabore Mikroelektronik Deutschland (ForLab)” initiative is acknowledged.

## ORCID® iDs

Karl Rothe - https://orcid.org/0000-0001-6672-398X
Nicolas Néel - https://orcid.org/0000-0003-0498-9138
Jörg Kröger - https://orcid.org/0000-0002-6452-5864

## Data Availability Statement

All data that supports the findings of this study is available in the published article and/or the supporting information to this article. Additional research data is not shared.

## References

1. Liu, Y.; Xiao, C.; Li, Z.; Xie, Y. *Adv. Energy Mater.* **2016,** *6,* 1600436. doi:10.1002/aenm.201600436
2. Komsa, H.-P.; Krasheninnikov, A. V. Physics and theory of defects in 2D materials: the role of reduced dimensionality. In *Defects in Two-Dimensional Materials;* Addou, R.; Colombo, L., Eds.; Materials Today; Elsevier: Amsterdam, Netherlands, 2022; pp 7–41. doi:10.1016/b978-0-12-820292-0.00008-2
3. Geim, A. K.; Novoselov, K. S. *Nat. Mater.* **2007,** *6,* 183–191. doi:10.1038/nmat1849
4. Castro Neto, A. H.; Guinea, F.; Peres, N. M. R.; Novoselov, K. S.; Geim, A. K. *Rev. Mod. Phys.* **2009,** *81,* 109–162. doi:10.1103/revmodphys.81.109
5. Marton, D.; Boyd, K. J.; Lytle, T.; Rabalais, J. W. *Phys. Rev. B* **1993,** *48,* 6757–6766. doi:10.1103/physrevb.48.6757
6. Hahn, J. R.; Kang, H. *Phys. Rev. B* **1999,** *60,* 6007–6017. doi:10.1103/physrevb.60.6007
7. Yazyev, O. V.; Helm, L. *Phys. Rev. B* **2007,** *75,* 125408. doi:10.1103/physrevb.75.125408

8. Palacios, J. J.; Fernández-Rossier, J.; Brey, L. *Phys. Rev. B* **2008,** *77,* 195428. doi:10.1103/physrevb.77.195428
9. Tapasztó, L.; Dobrik, G.; Nemes-Incze, P.; Vertesy, G.; Lambin, P.; Biró, L. P. *Phys. Rev. B* **2008,** *78,* 233407. doi:10.1103/physrevb.78.233407
10. Lehtinen, P. O.; Foster, A. S.; Ma, Y.; Krasheninnikov, A. V.; Nieminen, R. M. *Phys. Rev. Lett.* **2004,** *93,* 187202. doi:10.1103/physrevlett.93.187202
11. Pereira, V. M.; Guinea, F.; Lopes dos Santos, J. M. B.; Peres, N. M. R.; Castro Neto, A. H. *Phys. Rev. Lett.* **2006,** *96,* 036801. doi:10.1103/physrevlett.96.036801
12. Yazyev, O. V. *Phys. Rev. Lett.* **2008,** *101,* 037203. doi:10.1103/physrevlett.101.037203
13. Ugeda, M. M.; Brihuega, I.; Guinea, F.; Gómez-Rodríguez, J. M. *Phys. Rev. Lett.* **2010,** *104,* 096804. doi:10.1103/physrevlett.104.096804
14. Ugeda, M. M.; Fernández-Torre, D.; Brihuega, I.; Pou, P.; Martínez-Galera, A. J.; Pérez, R.; Gómez-Rodríguez, J. M. *Phys. Rev. Lett.* **2011,** *107,* 116803. doi:10.1103/physrevlett.107.116803
15. Kondo, T.; Honma, Y.; Oh, J.; Machida, T.; Nakamura, J. *Phys. Rev. B* **2010,** *82,* 153414. doi:10.1103/physrevb.82.153414
16. Ugeda, M. M.; Brihuega, I.; Hiebel, F.; Mallet, P.; Veuillen, J.-Y.; Gómez-Rodríguez, J. M.; Ynduráin, F. *Phys. Rev. B* **2012,** *85,* 121402. doi:10.1103/physrevb.85.121402
17. Blanc, N.; Jean, F.; Krasheninnikov, A. V.; Renaud, G.; Coraux, J. *Phys. Rev. Lett.* **2013,** *111,* 085501. doi:10.1103/physrevlett.111.085501
18. Ducastelle, F. *Phys. Rev. B* **2013,** *88,* 075413. doi:10.1103/physrevb.88.075413
19. Martín-Recio, A.; Romero-Muñiz, C.; Pou, P.; Pérez, R.; Gómez-Rodríguez, J. M. *Nanoscale* **2016,** *8,* 17686–17693. doi:10.1039/c6nr04978h
20. N'Diaye, A. T.; van Gastel, R.; Martínez-Galera, A. J.; Coraux, J.; Hattab, H.; Wall, D.; Meyer zu Heringdorf, F.-J.; Horn-von Hoegen, M.; Gómez-Rodríguez, J. M.; Poelsema, B.; Busse, C.; Michely, T. *New J. Phys.* **2009,** *11,* 113056. doi:10.1088/1367-2630/11/11/113056
21. Kim, H. W.; Ko, W.; Ku, J.; Jeon, I.; Kim, D.; Kwon, H.; Oh, Y.; Ryu, S.; Kuk, Y.; Hwang, S. W.; Suh, H. *Nat. Commun.* **2015,** *6,* 7528. doi:10.1038/ncomms8528
22. Néel, N.; Steinke, C.; Wehling, T. O.; Kröger, J. *Phys. Rev. B* **2017,** *95,* 161410. doi:10.1103/physrevb.95.161410
23. Kröger, J.; Néel, N.; Wehling, T. O.; Brandbyge, M. *Small Methods* **2020,** *4,* 1900817. doi:10.1002/smtd.201900817
24. Standop, S.; Lehtinen, O.; Herbig, C.; Lewes-Malandrakis, G.; Craes, F.; Kotakoski, J.; Michely, T.; Krasheninnikov, A. V.; Busse, C. *Nano Lett.* **2013,** *13,* 1948–1955. doi:10.1021/nl304659n
25. Hattab, H.; N'Diaye, A. T.; Wall, D.; Jnawali, G.; Coraux, J.; Busse, C.; van Gastel, R.; Poelsema, B.; Michely, T.; Meyer zu Heringdorf, F.-J.; Horn-von Hoegen, M. *Appl. Phys. Lett.* **2011,** *98,* 141903. doi:10.1063/1.3548546
26. Endlich, M.; Molina-Sánchez, A.; Wirtz, L.; Kröger, J. *Phys. Rev. B* **2013,** *88,* 205403. doi:10.1103/physrevb.88.205403
27. Esquinazi, P.; Spemann, D.; Höhne, R.; Setzer, A.; Han, K.-H.; Butz, T. *Phys. Rev. Lett.* **2003,** *91,* 227201. doi:10.1103/physrevlett.91.227201
28. Ohldag, H.; Tyliszczak, T.; Höhne, R.; Spemann, D.; Esquinazi, P.; Ungureanu, M.; Butz, T. *Phys. Rev. Lett.* **2007,** *98,* 187204. doi:10.1103/physrevlett.98.187204
29. Gómez-Navarro, C.; Pablo, P. J. D.; Gómez-Herrero, J.; Biel, B.; Garcia-Vidal, F. J.; Rubio, A.; Flores, F. *Nat. Mater.* **2005,** *4,* 534–539. doi:10.1038/nmat1414
30. Krasheninnikov, A. V.; Banhart, F. *Nat. Mater.* **2007,** *6,* 723–733. doi:10.1038/nmat1996
31. Limot, L.; Kröger, J.; Berndt, R.; Garcia-Lekue, A.; Hofer, W. A. *Phys. Rev. Lett.* **2005,** *94,* 126102. doi:10.1103/physrevlett.94.126102
32. Kröger, J.; Néel, N.; Limot, L. *J. Phys.: Condens. Matter* **2008,** *20,* 223001. doi:10.1088/0953-8984/20/22/223001
33. Kröger, J.; Jensen, H.; Berndt, R. *New J. Phys.* **2007,** *9,* 153. doi:10.1088/1367-2630/9/5/153
34. Kröger, J.; Néel, N.; Sperl, A.; Wang, Y. F.; Berndt, R. *New J. Phys.* **2009,** *11,* 125006. doi:10.1088/1367-2630/11/12/125006
35. Néel, N.; Kröger, J.; Berndt, R. *Phys. Rev. Lett.* **2009,** *102,* 086805. doi:10.1103/physrevlett.102.086805
36. Berndt, R.; Kröger, J.; Néel, N.; Schull, G. *Phys. Chem. Chem. Phys.* **2010,** *12,* 1022–1032. doi:10.1039/b908672m
37. Giessibl, F. J. *Appl. Phys. Lett.* **1998,** *73,* 3956–3958. doi:10.1063/1.122948
38. Giessibl, F. J. *Rev. Sci. Instrum.* **2019,** *90,* 011101. doi:10.1063/1.5052264
39. Giessibl, F. J. *Appl. Phys. Lett.* **2001,** *78,* 123–125. doi:10.1063/1.1335546
40. Sader, J. E.; Jarvis, S. P. *Appl. Phys. Lett.* **2004,** *84,* 1801–1803. doi:10.1063/1.1667267
41. Horcas, I.; Fernández, R.; Gómez-Rodríguez, J. M.; Colchero, J.; Gómez-Herrero, J.; Baro, A. M. *Rev. Sci. Instrum.* **2007,** *78,* 013705. doi:10.1063/1.2432410
42. N'Diaye, A. T.; Coraux, J.; Plasa, T. N.; Busse, C.; Michely, T. *New J. Phys.* **2008,** *10,* 043033. doi:10.1088/1367-2630/10/4/043033
43. Wintterlin, J.; Bocquet, M.-L. *Surf. Sci.* **2009,** *603,* 1841–1852. doi:10.1016/j.susc.2008.08.037
44. Meng, L.; Wu, R.; Zhang, L.; Li, L.; Du, S.; Wang, Y.; Gao, H.-J. *J. Phys.: Condens. Matter* **2012,** *24,* 314214. doi:10.1088/0953-8984/24/31/314214
45. Voloshina, E. N.; Fertitta, E.; Garhofer, A.; Mittendorfer, F.; Fonin, M.; Thissen, A.; Dedkov, Y. S. *Sci. Rep.* **2013,** *3,* 1072. doi:10.1038/srep01072
46. Park, C.; Yoon, M. *Sci. Rep.* **2022,** *12,* 7321. doi:10.1038/s41598-022-10870-0
47. Varykhalov, A.; Marchenko, D.; Scholz, M. R.; Rienks, E. D. L.; Kim, T. K.; Bihlmayer, G.; Sánchez-Barriga, J.; Rader, O. *Phys. Rev. Lett.* **2012,** *108,* 066804. doi:10.1103/physrevlett.108.066804
48. Altenburg, S. J.; Kröger, J.; Wehling, T. O.; Sachs, B.; Lichtenstein, A. I.; Berndt, R. *Phys. Rev. Lett.* **2012,** *108,* 206805. doi:10.1103/physrevlett.108.206805
49. Phark, S.-h.; Borme, J.; Vanegas, A. L.; Corbetta, M.; Sander, D.; Kirschner, J. *Phys. Rev. B* **2012,** *86,* 045442. doi:10.1103/physrevb.86.045442
50. Phark, S.-h.; Borme, J.; Vanegas, A. L.; Corbetta, M.; Sander, D.; Kirschner, J. *Nanoscale Res. Lett.* **2012,** *7,* 255. doi:10.1186/1556-276x-7-255
51. Liu, M.; Li, Y.; Chen, P.; Sun, J.; Ma, D.; Li, Q.; Gao, T.; Gao, Y.; Cheng, Z.; Qiu, X.; Fang, Y.; Zhang, Y.; Liu, Z. *Nano Lett.* **2014,** *14,* 6342–6347. doi:10.1021/nl502780u
52. Pletikosić, I.; Kralj, M.; Pervan, P.; Brako, R.; Coraux, J.; N'Diaye, A. T.; Busse, C.; Michely, T. *Phys. Rev. Lett.* **2009,** *102,* 056808. doi:10.1103/physrevlett.102.056808

53. Altenburg, S. J.; Berndt, R. *New J. Phys.* **2014,** *16,* 053036. doi:10.1088/1367-2630/16/5/053036
54. Huang, W.-M.; Tang, J.-M.; Lin, H.-H. *Phys. Rev. B* **2009,** *80,* 121404. doi:10.1103/physrevb.80.121404
55. Kim, H. W.; Ku, J.; Ko, W.; Cho, Y.; Jeon, I.; Hwang, S. W. *J. Phys. Chem. C* **2017,** *121,* 24641–24647. doi:10.1021/acs.jpcc.7b08161
56. Boneschanscher, M. P.; van der Lit, J.; Sun, Z.; Swart, I.; Liljeroth, P.; Vanmaekelbergh, D. *ACS Nano* **2012,** *6,* 10216–10221. doi:10.1021/nn3040155
57. Li, S.; Liu, M.; Qiu, X. *Chem. J. Chin. Univ.* **2020,** *41,* 49. doi:10.7503/cjcu20190570
58. Rothe, K.; Néel, N.; Bocquet, M.-L.; Kröger, J. *J. Phys. Chem. Lett.* **2022,** *13,* 8660–8665. doi:10.1021/acs.jpclett.2c02140
59. Altenburg, S. J.; Kröger, J.; Wang, B.; Bocquet, M.-L.; Lorente, N.; Berndt, R. *Phys. Rev. Lett.* **2010,** *105,* 236101. doi:10.1103/physrevlett.105.236101
60. Néel, N.; Kröger, J.; Limot, L.; Frederiksen, T.; Brandbyge, M.; Berndt, R. *Phys. Rev. Lett.* **2007,** *98,* 065502. doi:10.1103/physrevlett.98.065502
61. Néel, N.; Kröger, J.; Berndt, R. *Nano Lett.* **2011,** *11,* 3593–3596. doi:10.1021/nl201327c
62. Hauptmann, N.; Mohn, F.; Gross, L.; Meyer, G.; Frederiksen, T.; Berndt, R. *New J. Phys.* **2012,** *14,* 073032. doi:10.1088/1367-2630/14/7/073032
63. Omidian, M.; Leitherer, S.; Néel, N.; Brandbyge, M.; Kröger, J. *Phys. Rev. Lett.* **2021,** *126,* 216801. doi:10.1103/physrevlett.126.216801
64. Brand, J.; Leitherer, S.; Papior, N. R.; Néel, N.; Lei, Y.; Brandbyge, M.; Kröger, J. *Nano Lett.* **2019,** *19,* 7845–7851. doi:10.1021/acs.nanolett.9b02845
65. Halle, J.; Néel, N.; Fonin, M.; Brandbyge, M.; Kröger, J. *Nano Lett.* **2018,** *18,* 5697–5701. doi:10.1021/acs.nanolett.8b02295

## License and Terms

BEILSTEIN JOURNAL OF NANOTECHNOLOGY

# Stiffness calibration of qPlus sensors at low temperature through thermal noise measurements

Laurent Nony*[1], Sylvain Clair[1], Daniel Uehli[2], Aitziber Herrero[2], Jean-Marc Themlin[1], Andrea Campos[3], Franck Para[1], Alessandro Pioda[2] and Christian Loppacher[1]

Full Research Paper

Open Access

Address:
[1]Aix Marseille University, CNRS, IM2NP, UMR 7334, 13397 Marseille, France, [2]SPECS Zürich GmbH, Technoparkstrasse 1, 8005 Zürich, Switzerland and [3]Aix Marseille University, CNRS, Centrale Marseille, FSCM (FR1739), CP2M, 13397 Marseille, France

Email:
Laurent Nony* - laurent.nony@im2np.fr

* Corresponding author

Keywords:
low temperature; non-contact atomic force microscopy; qPlus sensors; quartz tuning fork; stiffness calibration; thermal noise; ultrahigh vacuum

*Beilstein J. Nanotechnol.* **2024,** *15,* 580–602.
https://doi.org/10.3762/bjnano.15.50

Received: 11 February 2024
Accepted: 25 April 2024
Published: 23 May 2024

This article is part of the thematic issue "Advanced atomic force microscopy techniques V".

Associate Editor: E. Meyer



## Abstract

Non-contact atomic force microscopy (nc-AFM) offers a unique experimental framework for topographical imaging of surfaces with atomic and/or sub-molecular resolution. The technique also permits to perform frequency shift spectroscopy to quantitatively evaluate the tip–sample interaction forces and potentials above individual atoms or molecules. The stiffness of the probe, $k$, is then required to perform the frequency shift-to-force conversion. However, this quantity is generally known with little precision. An accurate stiffness calibration is therefore mandatory if accurate force measurements are targeted. In nc-AFM, the probe may either be a silicon cantilever, a quartz tuning fork (QTF), or a length extensional resonator (LER). When used in ultrahigh vacuum (UHV) and at low temperature, the technique mostly employs QTFs, based on the so-called qPlus design, which actually covers different types of sensors in terms of size and design of the electrodes. They all have in common a QTF featuring a metallic tip glued at the free end of one of its prongs. In this study, we report the stiffness calibration of a particular type of qPlus sensor in UHV and at 9.8 K by means of thermal noise measurements. The stiffness calibration of such high-$k$ sensors, featuring high quality factors ($Q$) as well, requires to master both the acquisition parameters and the data post-processing. Our approach relies both on numerical simulations and experimental results. A thorough analysis of the thermal noise power spectral density of the qPlus fluctuations leads to an estimated stiffness of the first flexural eigenmode of ≈2000 N/m, with a maximum uncertainty of 10%, whereas the static stiffness of the sensor without tip is expected to be ≈3300 N/m. The former value must not be considered as being representative of a generic value for any qPlus, as our study stresses the influence of the tip on the estimated stiffness and points towards the need for the individual calibration of these probes. Although the framework focuses on a particular kind of sensor, it may be adapted to any high-$k$, high-$Q$ nc-AFM probe used under similar conditions, such as silicon cantilevers and LERs.

## Introduction

Since the 2000s, non-contact atomic force microscopy (nc-AFM) has established itself as a scanning probe method for the topographical, chemical, and electrical mapping of the surface of a sample down to the atomic scale [1-3]. When used in an ultrahigh-vacuum (UHV) system and at, or close to, liquid helium temperature (4–10 K, LT UHV), the method allows for the direct characterization of individual molecules with intramolecular contrast [4], opening up the field of studying on-surface reactions [5] or tip-induced chemistry [6].

The method also makes it possible to quantify the interatomic interaction forces that develop between the tip and the surface acquired in spectroscopic data cube modes [7,8] with both high sensitivity and high spatial resolution. Recently, the force sensitivity has been pushed forward, and forces as low as 100 fN have been reported on artificial atoms formed by quantum corrals [9].

In nc-AFM, the probe, whose mechanical behavior may advantageously be compared to that of a one-dimensional simple harmonic oscillator (SHO) of resonance frequency $f_1$ (flexural fundamental eigenmode) and stiffness $k_1$, is sinusoidally excited at $f_1$ by a phase-locked loop (PLL) that also guarantees a constant oscillation amplitude, $A_1$ [10]. If the tip is far enough from the surface, that is, at distances where the strength of the tip–surface interatomic forces is negligible with respect to the restoring force induced by the excitation, its resonance frequency remains unchanged, $f_1$. When the tip is in the range of attractive interatomic forces $F_{\text{int}}(r)$, that is, for tip–surface separations $r \lesssim 1$ nm, non-linear effects modify the oscillator dynamics, which shifts its resonance frequency down to lower values $\widetilde{f_1} < f_1$. The resulting frequency shift $\Delta f = \widetilde{f_1} - f_1 < 0$ is tracked by the PLL and used as the input of the *Z*-controller to form a "topographic image", which is actually a "constant-$\Delta f$" image. Alternatively, the image can also be acquired at constant height, which then forms a local $\Delta f$ map of the surface. $\Delta f$ is expressed according to [11,12]:

$$\Delta f\left(z\right)=\frac{f_1}{2\pi k_1 A_1}\int_0^{2\pi} F_{\text{int}}\left(r_u\left(z\right)\right)\cos\left(u\right)\mathrm{d}u, \qquad (1)$$

where $r_u(z) = z + A_1(1 - \cos(u))$ is the instantaneous tip–surface position, and $z$ is the shortest distance between the tip and the surface during one oscillation cycle. Thus, if $A_1$ and $k_1$ are properly calibrated, the interaction force may be quantified, however, through non-trivial inversion procedures [13-16]. The amplitude calibration in nc-AFM using the so-called constant-γ method is well documented and reasonably accurate [16-18], even if recently reported methods seem more accurate [16]. Conversely, it seems that the direct stiffness calibration of nc-AFM probes in UHV and at low temperature has never been reported. Furthermore, because the force sensitivity in nc-AFM critically depends on the mechanical stability of both probe and tip, it seems crucial to perform the probe stiffness calibration in situ, that is, within the LT UHV system, by means of a non-destructive method.

In UHV and at room temperature, nc-AFM experiments are mostly carried out with silicon cantilevers, similar to those used during AFM experiments in air or in liquid. Their stiffness rarely exceeds 100 N/m. In UHV and at low temperature, the use of cantilevers is more tedious because of the required in situ optical detection setup. Nc-AFM experiments are then mostly performed with quartz sensors, essentially implemented according to two geometries: quartz tuning fork (QTF) [19] or length-extensional resonator (LER) [20-22]. The commercial versions of these probes are the qPlus sensor (Scienta-Omicron) [19,23] and the KolibriSensor (SPECS) [24-26], respectively. It is known that these sensors offer several advantages: (i) Their large stiffness (≃1800 N/m for qPlus and ≃540 × $10^3$ N/m for KolibriSensor), much greater than that of silicon cantilevers. It prevents the snap of the tip into contact and enables the use of small oscillation amplitudes ($A_1 \simeq 50$ pm), which render the probe highly sensitive to the short-range regime of interatomic forces. (ii) Their high quality factor ($Q$, ≃$10^5$ in a LT UHV system), which renders the PLL highly sensitive to the frequency tracking. (iii) Their piezoelectric nature, which facilitates the readout of the tip deflection, based on the piezoelectric charge induced by the quartz upon oscillation through a simple *I*/*V*, or charge, preamplifier [27,28], as compared to the heavy optical detection setup required for silicon cantilevers.

Nowadays, the qPlus sensor is the probe that is most commonly used with LT UHV microscopes. This is why we focus on this type of probe in this work. In this design, only one prong of the QTF is fixed [19]. At the extremity of the free prong, a thin, etched wire (usually W or PtIr), less than a millimeter long, is glued, which forms the tip. The tip is electrically connected to an electrode that collects the tunneling current if scanning tunneling experiments are to be performed along with nc-AFM experiments. The qPlus sensors feature a resonance frequency of $f_1 \simeq 25$ kHz and a most commonly reported stiffness of 1800 N/m [19]. This estimate was first proposed in 2000 [29], following previous works [30,31], and was based on geometric criteria of the sensor that did not consider the influence of the added tip. Thus, this value of the stiffness reported for the early versions of qPlus, which is still used in most of the recent works to perform the frequency shift-to-force conversion (see, e.g., the supplementary material of [8] and [9]), is not necessarily com-

patible with that of modern ones. Furthermore, because the detailed geometry of each tip is never the same (regarding, e.g., diameter and length), and because it cannot be glued on the prong with high reproducibility (regarding, e.g, mass of glue and location on the prong), the mechanical properties of each sensor must differ in detail. Therefore, the actual stiffness of each probe must differ and has no reason to match a particular predefined value.

The stiffness calibration of silicon cantilevers at room temperature in air, liquid, or UHV by means of destructive and non-destructive methods has been discussed quite extensively in the literature [18,32-60], leading to a set of a dozen distinct approaches. A "global calibration initiative" has even been launched by Sader [58,61]. Conversely, much less references are available for qPlus sensors [62-67], and, among these, none of them deals with the direct stiffness calibration of the probe in a LT UHV system.

The goal of the present work is to propose a framework based on thermal noise measurement to calibrate the stiffness of qPlus sensors operated in a LT UHV system. The concept was introduced by Hutter and Bechhoefer, and Butt et al. in 1993 [33,34], and was further improved by Butt and Jaschke in 1995 [35]. It is based on the measurement of the spectrum of the fluctuations of the free end of the probe excited by thermal noise. The peak of the thermal noise spectrum at the resonance frequency of the probe may be related to its stiffness if the mechanical behavior of the probe can be modeled as that of an equivalent SHO. Our framework combines experimental measurements performed with qPlus sensors in UHV at 9.8 K and numerical simulations of the thermal fluctuations of a SHO under equivalent conditions. The numerical results permit to refine the experimental strategy, which allows us to achieve an uncertainty of 10% maximum in the calibration.

This work is inspired by, and based on, results from the literature, but extends the scope of AFM probes stiffness calibration through thermal noise measurement to very stiff ($k > 1000$ N/m) and large-$Q$ ($Q > 10^5$) probes, such as qPlus sensors. To this end, many theoretical and practical elements are detailed, which usually are either not clearly stated or little discussed in the literature because they are not salient with softer probes, but they become crucial with very rigid and high-$Q$ probes in LT UHV.

Finally, we want to stress that although this work treats the particular case of qPlus sensors, the framework can be adapted to any other kind of nc-AFM probes used in LT UHV, including other types of QTFs, silicon cantilevers, and LERs, with the KolibriSensor among the latter.

The paper is organized as follows. The section "Stiffness calibration methods: a brief review" briefly introduces the bibliographic context of the stiffness calibration methods, restricted to the main of our requirements. Section "Framework to the stiffness calibration" details the concepts of stiffness calibration based on thermal noise measurement, along with our assumptions. Section "Numerical simulations" details the numerical approach to the stiffness calibration. Section "Experimental results" presents the experimental results, which are discussed in section "Discussion" before the Conclusion.

Four Supporting Information files support our framework. They contain important results from the literature and are organized to help the reader to follow our developments. Supporting Information File 1 reminds the most salient results of the Euler–Bernoulli model and how it sustains the point-mass SHO equivalence. Supporting Information File 2 reminds fundamental elements of signal processing applied to discrete time signals, which include the power spectral density (PSD), a key tool for the stiffness calibration. Supporting Information File 3 reminds the expression of the thermal noise PSD of a SHO in thermal equilibrium within a thermostat. The PSD of the stochastic thermal force giving rise to the fluctuations of the SHO is derived as well, which is used in the numerical simulations. Supporting Information File 4 discusses the relevance of a digital antialiasing filter on the measured thermal noise PSD.

## Stiffness Calibration Methods: A Brief Review

This section reminds some salient results about stiffness calibration methods reported in the literature, which forms the context of the present study.

In the following, unless specified otherwise, the word "probe" either means a silicon cantilever or the free prong of a qPlus sensor. The discussion is restricted to probes with a rectangular cross section (length $l$, thickness $t$, width $w$ are such that $l \gg t$ and $l \gg w$) treated in the Euler–Bernoulli model of the embedded beam, extensively detailed, for example, in [35] (cf. also Supporting Information File 1). The displacement of the probe is assumed to occur vertically (along the $z$ axis, as defined in Figure 1) and to be small with respect to all its dimensions (elastic deformation only). The word "deflection" means the displacement that takes place at the free end of the probe with respect to its equilibrium position $z = 0$. Torsional effects are not accounted for, which is justified in the section "Framework to the stiffness calibration" (cf. subsection "Experimental context").

Since we focus on the stiffness calibration in UHV, we also restrict the context to cases where the hydrodynamic function of

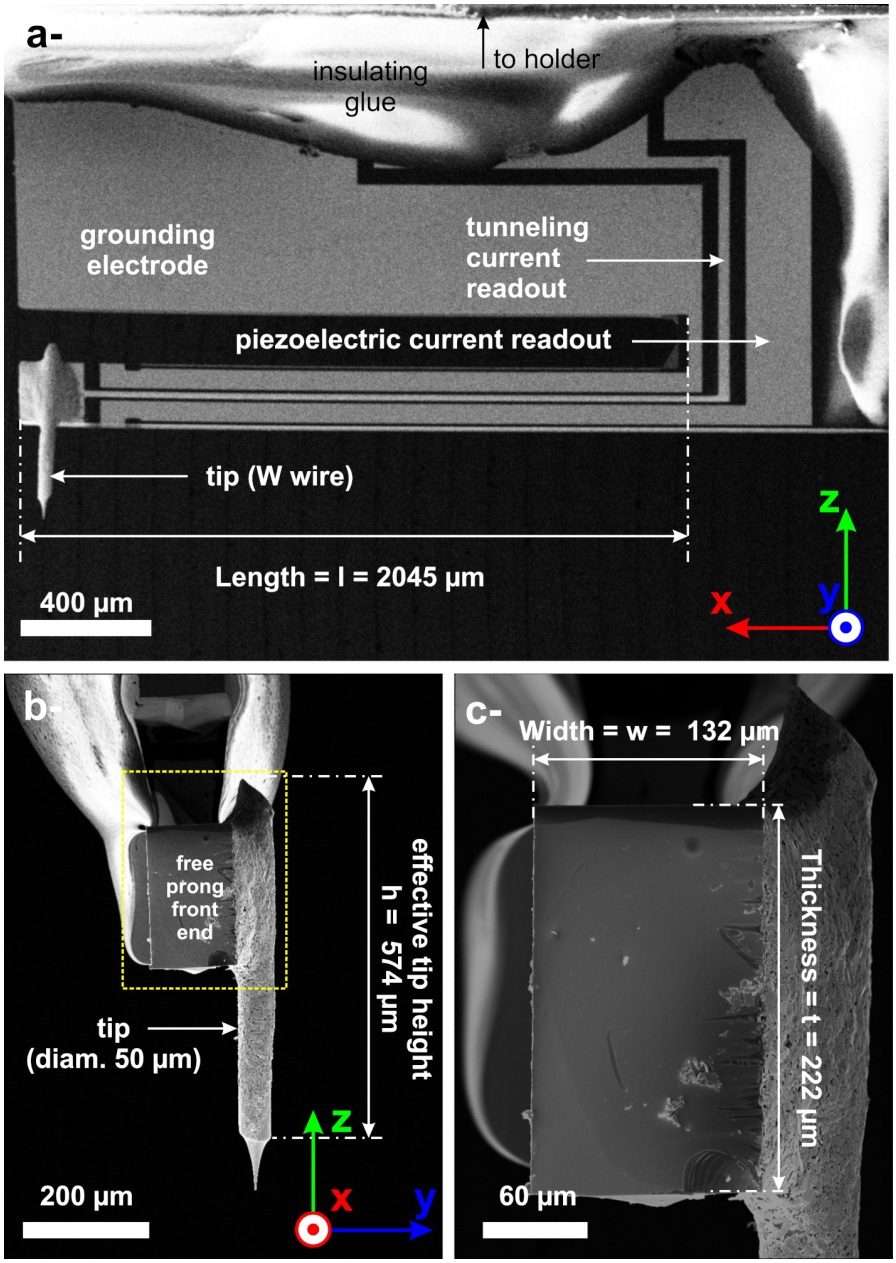


**Figure 1:** SEM images of the type of qPlus sensor used in this work. All dimensions are estimated with a relative uncertainty of 5%. a- Side view showing the complete geometry of the qPlus sensor. The circuitry of the electrodes is well identifiable. b- Front view of the qPlus free prong showing the tip glued to the right-hand side. c- Magnification of the dotted rectangle shown in b-.

the fluid surrounding the probe [38], if described in the model, plays no role.

Following Burnham's classification [40], we essentially focus on two categories of non-destructive calibration methods, referred to as "geometric" and "thermal" methods.

## Geometric methods

Geometric methods permit to calculate the stiffness of the probe from its dimensions and the mechanical properties of its constitutive material. When the load is applied at the free end of the probe, its static stiffness is given by:

$$k_s = \frac{Ewt^3}{4l^3}, \tag{2}$$

where $E$, $w$, $t$, and $l$ are Young's modulus, width, thickness, and length of the probe, respectively. Cleveland et al. early exploited this concept to determine the stiffness of soft levers

[32]. But these authors, as well as Sader et al. [38,68], also proposed a calibration method of the static stiffness based on the measurement of the unloaded resonant frequency of the probe flexural fundamental eigenmode ($f_1$), whose mass $m_{\text{probe}}$ is to be estimated then. In this framework, the probe is assumed to behave as an equivalent SHO; then, the static stiffness is derived from $f_1$ according to: $k_{s,f_1} = m_1^* (2\pi f_1)^2$. The quantity $m_1^* = \mu_{e,1} m_{\text{probe}}$ is the effective mass of the fundamental eigenmode of the probe; $m_{\text{probe}} = \rho wtl$ is calculated from the density ρ, thickness $t$, and plan view dimensions (length $l$ and width $w$) of the probe. The quantity $\mu_{e,1}$ is the probe's normalized effective mass of the fundamental eigenmode, taking the value $\mu_{e,1} \simeq 0.2427$ for $l/w > 5$ [32,38] (cf. also Supporting Information File 1). Because the experimental determination of the length of the probe is prone to less error than that of its thickness ($l \gg t$), Cleveland et al. and Sader et al. removed the thickness dependence from Equation 2 and came to an equivalent expression for $k_{s,f_1}$:

$$k_{s,f_1} = 2w(\pi l f_1)^3 \sqrt{\frac{\rho^3}{E}}. \tag{3}$$

As discussed by Burnham et al. [40], for rectangular probes with a stiffness of ≃1 N/m, Cleveland/Sader's calibration methods agree within 17% of the manufacturer's nominal value.

In 2012, Lübbe et al. extended Cleveland/Sader's approach to the Euler–Bernoulli model and derived an expression giving the static stiffness of the probe from the resonance frequency of any of its flexural eigenmodes [51]:

$$k_{s,f_n} = \frac{2w(\pi l f_n)^3}{\alpha_n^6} \sqrt{\frac{12^3 \rho^3}{E}}, \tag{4}$$

where $\alpha_n$ is a term occurring in functions that define the Euler–Bernoulli model used to describe the probe oscillation. $\alpha_n$ is the solution of a so-called dispersion relation, written as [35,48,49,55]:

$$1 + \cos(\alpha_n)\cosh(\alpha_n) = 0, \tag{5}$$

leading to $\alpha_1 = 1.875$, $\alpha_2 = 4.694$, $\alpha_3 = 7.864$, …, $\alpha_n \simeq (n - 1/2)\pi$.

The latter formalisms consider a homogeneous probe without influence of the added mass due to the presence of the tip at its free end (unloaded case). This added mass changes the eigenmodes geometry, though. This results in a change of the value of the constant $\alpha_n$ of each eigenmode. Lozano et al. [49], Lübbe et al. [51], and Yamada et al. [69] have addressed the issue of the tip mass correction in the Euler–Bernoulli model. To this end, an extended probe oscillation model is used [70], which leads to a new equation for $\alpha_n$ (loaded case), now written $\tilde{\alpha}_n$ in order to not confuse it with the solution of the unloaded case:

$$1 + \cos(\tilde{\alpha}_n)\cosh(\tilde{\alpha}_n) + \mu\tilde{\alpha}_n\left[\sinh(\tilde{\alpha}_n)\cos(\tilde{\alpha}_n) - \sin(\tilde{\alpha}_n)\cosh(\tilde{\alpha}_n)\right] = 0, \tag{6}$$

where $\mu = m_{\text{tip}}/m_{\text{probe}}$ is the ratio between the tip mass and the probe mass. Hence, μ must now be established before obtaining the value of $\tilde{\alpha}_n$.

In their work, Lübbe et al. [51] point out that the direct stiffness calibration from the probe dimensions yields values with an uncertainty of ±25% as the result critically depends on the probe thickness, which is difficult to determine experimentally. But the uncertainty is reduced to ±7% when the measured fundamental eigenfrequency is included in the calculation and a tip mass correction is applied.

## Thermal noise methods

Thermal methods are based on the measurement of the probe's thermal fluctuations when it is in thermal equilibrium within a thermal bath [35,40,43,44,46-48,55-57,59,60,71]. The influence of thermal noise on a system has first been investigated by Nyquist and Johnson in 1928 with electric resistors [72,73]. Their seminal work has later been formalized by the linear response theory and the fluctuation–dissipation theorem (FDT) [74,75], establishing a connection between fluctuations about equilibrium and the response of a system to external forces upon its susceptibility (or response function).

Thermal energy and probe fluctuations are linked by the equipartition theorem, which states that the energy transferred from a thermal bath to a dynamic system equals $k_B T/2$ for each of its degrees of freedom, $k_B$ being the Boltzmann constant and $T$ the temperature of the thermostat. Here, as discussed in [35,48,56], the probe is described as an equivalent point-mass SHO that features stochastic deflections of its free end along the vertical $z$ axis over time due to thermal noise, forming a signal $z_{\text{th}}(t)$. The equipartition theorem is written as:

$$\frac{1}{2} k_B T = \frac{1}{2} k_s \left\langle z_{\text{th}}^2 \right\rangle, \tag{7}$$

where ⟨⟩ represents a virtually infinite time averaging. The quantity

$$\left\langle z_{\mathrm{th}}^2 \right\rangle \triangleq \lim_{T_\mathrm{w}\to\infty} \frac{1}{T_\mathrm{w}} \int_0^{T_\mathrm{w}} z_{\mathrm{th}}^2(t)\,\mathrm{d}t$$

is the power of the probe fluctuations (mean quadratic deflections) induced by thermal noise over time. For a qPlus sensor of stiffness $k_\mathrm{s} \simeq 1800$ N/m at $T = 9.8$ K, the rms deflection induced by thermal noise is $\sqrt{\left\langle z_{\mathrm{th}}^2 \right\rangle} \simeq 270$ fm.

As discussed early by Butt and Jaschke [35] and explicitly measured by others [48,55], the rigorous analysis of the thermal fluctuations is to be performed in terms of modal decomposition of the probe deflections over its eigenmodes. Then, the total deflection of the probe's free end due to thermal fluctuations results from the superposition of the deflections of equivalent SHOs embodying the eigenmodes of the probe, which are assumed to be independent [49]. Because of their high quality factors, the former assumption is particularly valid for qPlus sensors (cf. also Supporting Information File 1). Thus:

$$\left\langle z_{\mathrm{th}}^2 \right\rangle = \sum_{n=1}^{+\infty} \left\langle z_{\mathrm{th},n}^2 \right\rangle, \tag{8}$$

where $\left\langle z_{\mathrm{th},n}^2 \right\rangle$ is the power of the thermal fluctuations of the $n$-th flexural eigenmode (resonance frequency $f_n$, quality factor $Q_n$, and stiffness $k_n$), and the summation represents all eigenmodes of the probe. Under the assumption of thermal equilibrium, the thermal noise-induced deflection of each eigenmode follows the equipartition theorem, such that:

$$\frac{1}{2} k_\mathrm{B} T = \frac{1}{2} k_n \left\langle z_{\mathrm{th},n}^2 \right\rangle. \tag{9}$$

Upon proper normalization of the solution functions of the Euler–Bernoulli model, the modal stiffness $k_n$ of an unloaded probe may be connected to the static one $k_\mathrm{s}$ (or equivalently $k_{\mathrm{s},f_n}$) according to [35,76]:

$$\frac{k_n}{k_\mathrm{s}} = \frac{\alpha_n^4}{12}. \tag{10}$$

Thus, for the fundamental eigenmode of an unloaded probe ($\alpha_1 = 1.875$), $k_1 / k_\mathrm{s} = \alpha_1^4 / 12 \simeq 1.03$.

Combining Equation 8, Equation 9, and Equation 10 yields:

$$\left\langle z_{\mathrm{th}}^2 \right\rangle = k_\mathrm{B} T \sum_{n=1}^{+\infty} \frac{1}{k_n} = \frac{k_\mathrm{B} T}{k_\mathrm{s}} \sum_{n=1}^{+\infty} \frac{12}{\alpha_n^4}. \tag{11}$$

Equation 11 is similar to Equation 7 if the summation is performed over all the eigenmodes of the probe ($\sum_{n=1}^{+\infty} 12/\alpha_n^4 = 1$, cf. [35,77]).

From an experimental point of view, the number of accessible eigenmodes ($m$) is limited because the detection bandwidth of the fluctuations is restricted. Then, the relative error introduced in the estimated static stiffness is $\mathrm{err} = \sum_{n>m}^{+\infty} 12/\alpha_n^4 = 1 - \sum_{n=1}^{m} 12/\alpha_n^4 = 1 - \left(12/\alpha_1^4 + 12/\alpha_2^4 + \ldots + 12/\alpha_m^4\right)$, which may be estimated. For instance, restricting the detection bandwidth to the fundamental eigenmode of an unloaded probe ($\alpha_1 = 1.875$) sets $m = 1$ and $\mathrm{err} = 1 - 12/\alpha_1^4 \simeq 3\%$. In other words, the modal stiffness $k_1$ of the fundamental eigenmode of an unloaded probe exceeds the static stiffness $k_\mathrm{s}$ by 3%, or equivalently, 97% of the thermal fluctuations are due to the probe's fundamental eigenmode.

Equation 9 states that the measurement of the thermal fluctuations of the deflection of the $n$-th eigenmode over an arbitrary long time interval might allow us to derive the corresponding modal stiffness. But this is not feasible in practice because of measurement noise, which usually exceeds thermal noise. There are several origins to measurement noise. For qPlus sensors, two main noise sources may be considered: the preamplifier, which converts the piezoelectric current of the QTF into a scalable voltage signal, and the subsequent analog/digital converter (ADC), which converts the analog signal into a digital signal to be processed by the digital control unit of the microscope. It is difficult to quantify the strength of those sources with respect to that of the thermal noise based on the time trace of the fluctuations as it gives no idea on how the noise is spectrally spread within the system. This is why the analysis of noisy signals is rather performed from their PSD. The PSD $S_z(f)$ of an analog signal $z(t)$ featuring thermal fluctuations with measurement noise is defined according to:

$$\left\langle z^2 \right\rangle = \int_{-\infty}^{\infty} S_z(f)\,\mathrm{d}f. \tag{12}$$

It is also usually assumed that thermal noise and measurement noise are uncorrelated. Thus, noting the power of the measurement noise:

$$\left\langle z_{\mathrm{mn}}^2 \right\rangle = \int_{-\infty}^{\infty} S_{z_{\mathrm{mn}}}(f)\,\mathrm{d}f, \tag{13}$$

the power of the measured thermal noise probe deflections is such that:

$$\left\langle z^2 \right\rangle = \left\langle z_{\mathrm{th}}^2 \right\rangle + \left\langle z_{\mathrm{mn}}^2 \right\rangle. \tag{14}$$

The power of the thermal fluctuations without measurement noise is ultimately given by integration of a quantity we name the thermal noise PSD (tn-PSD) $S_{z_{\mathrm{th}}}(f)$, according to:

$$\left\langle z_{\mathrm{th}}^2 \right\rangle = \int_{-\infty}^{\infty} S_{z_{\mathrm{th}}}(f)\,\mathrm{d}f = \int_{-\infty}^{\infty} \left[ S_z(f) - S_{z_{\mathrm{mn}}}(f) \right] \mathrm{d}f. \tag{15}$$

Technically, the PSD is defined from the Fourier transform $\hat{z}(f)$ of the time trace of the signal $z(t)$ forming the Fourier pair $z(t) \rightleftharpoons \hat{z}(f)$, according to:

$$S_z(f) = \lim_{T_w \to \infty} \frac{1}{T_w} \left| \hat{z}(f) \right|^2. \tag{16}$$

Thus, if the measurement noise PSD $S_{z_{\mathrm{mn}}}(f)$ is quantified, the quantity $\left\langle z_{\mathrm{th}}^2 \right\rangle$ depicting the thermal fluctuations of the probe can be estimated from the measurement of $S_z(f)$ (Equation 15) and, thus, also the probe stiffness (Equation 7).

Because the Fourier transform is intrinsically two-sided ($f \in \mathbb{R}$), the integration in Equation 12, Equation 13, and Equation 15 spreads from $-\infty$ to $+\infty$. The two-sided representation of the DFT forms a strict, self-consistent, mathematical background; however, in the case of the PSD, its one-sided representation is preferred ($f \in [0;+\infty[$). In addition, the observables that are measured from stochastic signals usually relate to rms values (e.g., $V_{\mathrm{rms}}$). It is therefore preferable to express their corresponding PSD from the rms value of their Fourier transform. Supporting Information File 2 explicitly details the connection between the two-sided expression of the PSD and that of the one-sided rms PSD (cf. Supporting Information File 2, Equations S14 and S15). In the following, we will only use the spectral expression/representation of the one-sided rms PSD of the signal $z_{\mathrm{th}}(t)$, which is defined for $f \geq 0$ only. Unlike in Supporting Information File 2, the "rms" superscript will be systematically omitted in the notations in order to lighten them, but it is maintained in the units.

A large part of the thermal fluctuations stems from the probe's fundamental eigenmode. Thus, it is interesting to compare $S_{z_{\mathrm{th}}}(f)$ to the formal expression of the one-sided rms tn-PSD of an equivalent SHO (resonance frequency $f_1$, quality factor $Q_1$, and stiffness $k_1$), which is established in Supporting Information File 3 (cf. Equation S8). This quantity is written as:

$$S_{\mathrm{SHO}}\left(u = f/f_1\right) = \frac{2k_{\mathrm{B}}T}{\pi k_1 Q_1 f_1} \frac{1}{\left[1-u^2\right]^2 + \frac{u^2}{Q_1^2}}. \tag{17}$$

The function exhibits a resonance for $f = f_1$ ($u = 1$), and then:

$$S_{\mathrm{SHO}}(u=1) = \frac{2k_{\mathrm{B}}TQ_1}{\pi k_1 f_1}. \tag{18}$$

Equation 15, Equation 16, Equation 17, and Equation 18 form the analytical framework for the analysis of the thermal fluctuations, which ultimately allows for the probe stiffness calibration from Equation 7. They are used according to three methodological approaches, which all are reported in the literature:

- **Method 1**: $\left\langle z_{\mathrm{th}}^2 \right\rangle$ is derived by integration of the tn-PSD $S_{z_{\mathrm{th}}}(f)$ (Equation 15), that is, the as-measured thermal noise PSD $S_z(f)$ corrected from its measurement noise $S_{z_{\mathrm{mn}}}(f)$. $S_z(f)$ may either be measured with a properly calibrated spectrum analyzer or derived from the Fourier transform of the time trace of the thermal fluctuations (Equation 16) [48]. Depending on the acquisition bandwidth, $k_{\mathrm{s}}$ may be estimated from Equation 10 or Equation 11.
- **Method 2**: The stiffness of the probe's fundamental eigenmode $k_1$ may as well be fitted from $S_{z_{\mathrm{th}}}(f)$ from the tn-PSD of the SHO (Equation 17) [56], provided that (i) the probe's mechanical behavior satisfactorily compares to that of an equivalent SHO, and (ii) resonance frequency $f_1$ and quality factor $Q_1$ of the probe are known. Then, $k_{\mathrm{s}}$ may be derived from Equation 10.
- **Method 3**: $k_1$ may be directly estimated from the maximum of $S_{z_{\mathrm{th}}}(f)$ (Equation 18) [40], provided that $f_1$ and $Q_1$ are known. Then, $k_{\mathrm{s}}$ may be derived from Equation 10.

These methods all require a good estimate of the measurement noise PSD $S_{z_{\mathrm{mn}}}(f)$, otherwise the estimated stiffness will be uncertain (cf. hereafter).

## Other non-destructive methods

Finite element method (FEM) modeling has been applied successfully to calibrate the stiffness of both silicon cantilevers [59,76,78-82] and qPlus sensors [18,65]. For qPlus sensors, however, FEM does not offer a generic approach. Indeed, as presented in the Introduction, the fact whether the sensors are custom-made or commercial, the tip shape (nature, diameter, and length of the wire), the precise location where it is glued on the free prong, along with the nature and quantity of glue used to hold the wire, imply a large range of geometric parameters, which ultimately influence the resulting stiffness of the probe.

Falter et al. pointed out this issue [65], and the authors outlined the urge of stiffness calibration for each sensor. The main conclusion of their FEM modeling shows quantitative agreement with the beam formula (Equation 2) if the beam origin is shifted to the position of zero stress onset inside the tuning fork base; however, there was a systematic overestimation of the experimental stiffness due to the tip gluing geometry.

In the 2000s, Rychen et al. proposed an approach to the calibration of the modal stiffness of QTFs used below 4.2 K and at 5 mbar [62,63]. The method is based on the measurement of the admittance of the piezoelectric current produced by the fork upon oscillation. The authors fitted that quantity with a Butterworth–Van Dyke-type electrical equivalence, and they put in relation the fitted electrical parameters with those of an equivalent mechanical SHO. This approach is valuable as it is performed in situ (however here not in UHV) and is non-destructive. However, it requires the precise knowledge of the piezoelectric constant of the quartz, and, with current qPlus designs, it was shown that the Butterworth–Van Dyke equivalent circuit failed at describing all their features [83].

## Framework to the Stiffness Calibration

### Methodology

Our experimental results are interpreted with the help of numerical simulations, but experimental and numerical approaches rely both on the same methodology.

Our framework to the stiffness calibration consists in processing the time trace of the qPlus thermal fluctuations to extract the quantity $\langle z_{\mathrm{th}}^2 \rangle$. To this end, the time signal of the thermal fluctuations including, or not (in the case of numerical simulations), measurement noise, is acquired over a windowing duration $T_{\mathrm{w}}$. This process is repeated to form a statistic set of $M$ time traces of the fluctuations ($M_{\mathrm{exp}} \geq 500$, $M_{\mathrm{num}} \geq 60$). Then, the properly normalized one-sided rms PSD spectrum of each trace is calculated. The $M$ rms PSD spectra are ultimately averaged resulting in a single final spectrum.

The value of the stiffness is then deduced according to the methods 1–3 described before. However, as discussed in detail by Cole [46] or Sader et al. [53], in the case of noisy signals like the tn-PSD, the use of non-linear least-squares fits, such as those required in method 2, is problematic. Their convergence and the accuracy of the fit coefficients may depend on type of noise, type of fit functional, minimization algorithm, and number of coefficients to fit along with their boundary conditions and may lead to erroneous results. Because some of these difficulties were faced when processing our data, we do not use method 2 for the experimental stiffness calibration and restrict the analysis to methods 1 and 3.

### Experimental context

The experimental results presented in this work have been acquired with a closed-cycle UHV SPM Infinity microscope from Scienta-Omicron, operated at 9.8 K. We use commercial qPlus sensors purchased from Scienta-Omicron.

Scanning electron microscopy (SEM) pictures of one of these probes are shown in Figure 1. SEM analysis was performed with a Zeiss GeminiSEM 500 ultrahigh-resolution FESEM at 15 kV. Secondary electron detection was used for imaging. At 15 kV, the resolution is 0.6 nm. Energy-dispersive X-ray spectroscopy (EDS) chemical analyses have been performed too, for which an EDAX Octane Silicon Dri Detector (129 eV energy resolution for manganese) coupled to the SEM was used at 15 kV. A large side view (cf. Figure 1a) shows the overall probe geometry. The qPlus sensors we use feature QTFs whose prong geometry is asymmetric. The sensor is glued by means of an insulating epoxy glue (white areas) on a massive metallic holder, not visible in the figure, that is mechanically clamped into the scanning piezo featuring a ring electrode for mechanical excitation. The QTF surface features a set of three metallic electrodes evaporated on it. Their chemical composition has been characterized by EDS as consisting of a ≃200 nm thick layer of Au on a thinner chromium layer to favor the adhesion and wetting of Au. The massive electrode is for grounding. The two thinner ones, running along the free prong, are for the piezoelectric current and tunneling current readouts. The free prong is $l = (2045 \pm 100)$ µm long. The tip, indicated at the end of the free prong, consists of a W wire that is 50 µm in diameter, better visible in Figure 1b. It is glued with a conducting epoxy, visible in the pictures, on the side of the free prong, near its end. With this asymmetry, oscillations due to the first torsional eigenmode of the qPlus sensor might occur and perturb the detection of the thermal motion due to the first bending mode. However with regular QTFs, the first torsional eigenmode is expected to be above, or near, our sampling frequency of ≃155 kHz [84] (cf. subsection "Acquisition parameters of the thermal fluctuations as a discrete time signal"). The torsional resonance is, therefore, far away from our considered frequency range, and torsional effects should not influence, to a large extent, our measurements. The W wire has been cut at the top end and etched at the bottom end to form the tip. One can estimate its height as that of an effective cylinder, as indicated in the picture, $h = (574 \pm 30)$ µm. However, this quantity is only representative of this particular qPlus sensor and is expected to vary from one sensor to another. The free prong has a width $w = (132 \pm 7)$ µm and a thickness $t = (222 \pm 12)$ µm, as measured from Figure 1c, which is the magnification of the dotted rectangle shown in Figure 1b. From these geometric quantities, the estimated static stiffness of the probe (cf. Equation 2) is $k_{\mathrm{s}} = (3322 \pm 1270)$ N/m. To get this value, we

have considered Young's modulus and density of quartz, $E$ = (78.7 ± 1.6) GPa and ρ = (2.65 ± 0.06) × $10^3$ kg·$m^{-3}$, respectively. It is also reminded that Equation 2 does not include the contribution of the tip.

The qPlus sensor is assumed to be in thermal equilibrium at $T$ = 9.8 K. The temperature is measured within the head of the microscope by a Si diode and readout by a Lakeshore 335 Controller. The microscope being in closed-cycle has been thermalized at that temperature for several weeks. A HQA-15M-10T charge preamplifier from Femto collects the piezoelectric current generated by the qPlus sensor [28] and sends the preamplified signal into a Nanonis OC4 oscillation control unit for digital conversion and a Nanonis Mimea SPM control system from SPECS for processing this signal. An analog low-pass filter in the OC4 acts as an antialiasing filter before digital conversion by an ADC. It is implemented as a third-order overall Butterworth filter with a Sallen–Key topology and with a fixed cut-off frequency of 5 MHz, meaning that dampening is 60 dB per decade. There is no additional filter in the analog part, and there is no antialiasing filter in the digital domain. Before thermal noise measurements, the qPlus deflections are accurately calibrated into metric units with a custom-made script implemented in the Nanonis MIMEA control unit that performs the constant-γ calibration procedure of the oscillation amplitude in nc-AFM mode [16-18]. The accuracy of the calibration is cross-checked in STM mode, which guarantees an accuracy of 5% in the amplitude calibration.

A dedicated software data acquisition module implemented by SPECS into the Nanonis MIMEA control software is used to acquire the $M_{\mathrm{exp}}$ time traces of the signal $z(t)$ featuring the thermal fluctuations of the qPlus sensor and to process them accordingly to yield the averaged rms PSD spectrum of the thermal fluctuations (cf. subsection "Acquisition parameters of the thermal fluctuations").

Because $M_{\mathrm{exp}} \simeq 500$ time traces are acquired, lasting $T_{\mathrm{w}} \simeq 50$ s each (cf. also subsection "Acquisition parameters of the thermal fluctuations"), the total acquisition lasts a couple of hours. In order to lower the parasitic noise level, these measurements are carried out overnight. The protocol might seem long and demanding, but it is the properties of the qPlus sensor that constrain one to drastic acquisition parameters. In 2013, Lübbe et al. had already come to the same conclusion in the case of silicon cantilevers in UHV at room temperature [56]. To overcome the drawback of the acquisition duration with high-$Q$ probes, they introduced a quick and efficient alternative method based on the spectral analysis of the frequency shift detected by the PLL. If their concept was transposable to the case of qPlus sensors without loss of accuracy in the calibration, which is not established so far, it would be an advantage over the current method.

During the thermal noise measurement ($S_z(f)$), the qPlus sensor is located far from the sample such that no interaction force may develop between tip and surface. All inputs to the microscope are grounded (e.g., high voltage lines of the $X$, $Y$, and $Z$ scanner, coarse motor, and bias). The tunneling current readout is also grounded. It is also made sure that no parasitic external noise source (mechanical or electrical) adds to the measurement. The measurement noise PSD ($S_{z_{\mathrm{mn}}}(f)$) is recorded under similar conditions, except that the input of the charge amplifier is not connected and let open (qPlus sensor not connected). The acquisition parameters of $S_z(f)$ and $S_{z_{\mathrm{mn}}}(f)$ are detailed hereafter.

## The qPlus sensor seen as an equivalent SHO

As with many other results dealing with that topic, a central assumption of this work is that the mechanical behavior of the qPlus sensor may be described by that of an equivalent SHO of resonance frequency $f_1$, quality factor $Q_1$, amplitude at the resonance $A_1$, and stiffness $k_1$. The relevance of that approximation is verified by recording the resonance curve around $f_1$ and checking to which extent the measured amplitude $A(f)$ and phase φ($f$) can be fitted by the SHO model for large quality factors (cf. section "Experimental results", subsection "Equivalent SHO"):

$$\begin{cases} A(f) = \dfrac{A_1}{\sqrt{Q_1^2\left[1-\left(\dfrac{f}{f_1}\right)^2\right]^2+\left(\dfrac{f}{f_1}\right)^2}} \\ \varphi(f) = \arctan\left(\dfrac{f f_1}{Q_1\left(f^2-f_1^2\right)}\right) \end{cases}. \tag{19}$$

Doing so, $f_1$ and $Q_1$ will be determined accurately. For the sake of the forthcoming discussions, we use typical orders of magnitude for qPlus sensors operated in LT UHV, namely $f_1 \simeq 25$ kHz and $Q_1 \simeq 2 \times 10^5$.

## Acquisition parameters of the thermal fluctuations as a discrete time signal

The concept of PSD applied to the measurement of thermal fluctuations was introduced by assuming a continuous, that is, analog time signal. But on the experimental level, the thermal fluctuations are meant to be processed by the Nanonis MIMEA control unit, which is based on a digital FPGA architecture, such that the signal is ultimately discrete in time and of finite duration $T_{\mathrm{w}}$. Let us assume the signal to be sampled with a

period $T_s$, that is, a sampling frequency $f_s = 1/T_s$, yielding a buffer of $N$ samples. The windowing duration is then:

$$T_w = NT_s = \frac{N}{f_s}. \quad (20)$$

In UHV and at low temperature, the qPlus sensor's thermal fluctuations stem from stochastic phonons of the quartz in thermal equilibrium with the thermostat at the energy $k_BT$. The phonons excite the qPlus sensor and statistically repeat over time with a frequency spectrum yielding a thermal noise rms PSD described by that of an equivalent SHO (Equation 17). The spectrum conceals the mechanical properties of the SHO and exhibits a resonance at $f_1$. Thus, stochastic phonons with frequencies at, or close to, the SHO resonance frequency, produce long-standing oscillations, particularly if the SHO's quality factor is large, which is the case with qPlus sensors. It is therefore mandatory to acquire the thermal fluctuations over a duration window $T_w$ that is much larger than the intrinsic equilibration time of the SHO defined as $\tau_1 = 2Q_1/f_1$, hence, $T_w \gg \tau_1$. With the orders of magnitude that were chosen above, $\tau_1 \simeq 16$ s.

Furthermore, setting $T_w$ implicitly means setting $\delta f$, that is, the frequency resolution $\delta f$ of the rms PSD spectrum:

$$\delta f = \frac{f_s}{N} = \frac{1}{NT_s} = \frac{1}{T_w}. \quad (21)$$

Therefore, the problem is to determine a correct value for $\delta f$ that must satisfy $\delta f \ll \tau_1^{-1}$. With our parameters, $\delta f \ll 60$ mHz. We arbitrarily set $\delta f = 20$ mHz, that is, $T_w = 50$ s. According to the definition of the quality factor, the SHO bandwidth is $w_f = f_1/Q_1$, that is, here $w_f \simeq 125$ mHz. Thus, it is essential to have at least ≃7 samples within the $w_f$ bandwidth around $f_1$ in the tn-PSD.

On the hardware level, the analog signal of the qPlus deflections is sampled at the maximum rate imposed by the MIMEA control unit, $f_{s,max} = 40$ MHz, resulting in a Shannon–Nyquist frequency of 20 MHz. At that frequency, because of the analog antialiasing filter, the digital signal provided by the ADC is dampened by 36 dB. However, $f_{s,max}$ is not the sampling frequency used to perform the thermal noise analysis, as $T_w \simeq 50$ s would imply a too large buffer of samples to handle ($N = T_w f_{s,max} \simeq 2 \times 10^9$). Therefore the discrete time signal is downsampled at $f_s$ while making sure that $f_s$ fulfills the Shannon–Nyquist sampling theorem $f_s > 2f_1$. To limit memory usage on the hardware, the maximum buffer size is limited to $N = 8{,}388{,}544$ samples. Thus, because $f_1 \simeq 25$ kHz, we set $f_s = 156.250$ kHz ($T_w = N/f_s \simeq 53.6$ s). This results in an acquisition bandwidth of the thermal fluctuations of $B_s = f_s/2 = 78.125$ kHz. Note that, because the second flexural eigenmode features a resonance frequency $f_2 \simeq 6.27\, f_1 \simeq 156.750$ kHz $> f_s/2$, the corresponding discrete time signal will be downsampled and, hence, not properly detected. Therefore, our framework to the stiffness calibration restricts the detection bandwidth of the qPlus sensor's thermal fluctuations to its fundamental eigenmode. It is reminded that no additional digital filtering that might act as an antialiasing filter is used for the acquisition of the thermal noise (cf. section "Numerical Simulations", subsection "Ideal case: no measurement noise").

To summarize, for qPlus sensors operated in LT UHV, typical sampling parameters of the discrete time signal of the thermal fluctuations are: $T_w \simeq 53$ s, $f_s = 156.250$ kHz, $T_s = 1/f_s = 6.4$ µs, $\delta f \simeq 19$ mHz, yielding a buffer of $N \simeq 8.4 \times 10^6$ samples.

## Numerical Simulations

The simulation of AFM experiments affected by stochastic noise and its consequences on the statistics of the PSD has been addressed by Labuda and coworkers [85,86]. Specifically, the authors use inverse Fourier transform for generating time-domain stochastic noise directly from a numerically defined PSD of stationary noise. The method is valuable as the defined PSD may, for example, be fitted from an experimental measurement.

Our approach is the opposite. We simulate the time trace of the thermal fluctuations and derive the tn-PSD consistently via direct discrete Fourier Transform. Our framework restricts the experimental detection bandwidth of the qPlus sensor's thermal fluctuations to its fundamental eigenmode. However, the numerical description of the qPlus sensor's mechanical behavior must be as accurate as possible. As already mentioned, the Euler–Bernoulli model accounts for the probe deflection from the superposition of the deflections of each of its eigenmodes described as independent SHOs. With our computational means however, it is unrealistic to describe a too large number of eigenmodes presenting high-$Q$ factors. To gain computational time, we restrict the numerical analysis to the first three eigenmodes of the qPlus sensor ($n$ = 1–3). Furthermore, we do not account for the influence of the tip ($m_{tip} = 0$). The as-calculated values of the set ($f_n$, $Q_n$, $k_n$) are reported in Table 1. We chose for ($f_1$, $Q_1$, $k_1$) the values (25 kHz, $10^5$, 1800 N/m). The values of $f_2$ ($f_3$) and $k_2$ ($k_3$) are given by Equations S9 and S10 of Supporting Information File 1, respectively, with $\alpha_n$ given by Equation 5. As for $Q_2$ and $Q_3$, there are few results in the literature on how they are expected to vary in UHV. Usually, the quality factor decreases with $n$ (cf. [87] and silicon cantilever P5 in [56]). We therefore have set arbitrary values following that trend. The simulated temperature is 9.8 K.

**Table 1:** Values of $f_n$, $Q_n$, and $k_n$ for the first three eigenmodes of the simulated qPlus sensor. We only set the values of the fundamental eigenmode ($n$ = 1), the others are derived from the corresponding equations.

| Eigenmode ($n$) | $\alpha_n$ () (Equation 5) | $f_n$ (kHz) (cf. Supporting Information File 1, Equation S9) | $Q_n$ () | $k_n$ (N/m) (cf. Supporting Information File 1, Equation S10) |
|---|---|---|---|---|
| **1** | 1.875 | 25.000 | $10^5$ | 1800 |
| **2** | 4.694 | 156.680 | $50 \times 10^3$ | 70 703 |
| **3** | 7.864 | 438.650 | $25 \times 10^3$ | 554 150 |

We first consider the ideal case where there is no measurement noise and then introduce measurement noise, whose characteristics reproduce those of the experimental noise.

## Ideal case: no measurement noise

Assuming $F_{\mathrm{th},n}(t)$ to be the instantaneous value of the thermal force applied to the qPlus sensor's $n$-th eigenmode, the corresponding instantaneous deflection $z_{\mathrm{th},n}(t)$ obeys the classical second-order differential equation for the SHO:

$$m_n \ddot{z}_{\mathrm{th},n}(t) + m_n \frac{\omega_n}{Q_n} \dot{z}_{\mathrm{th},n}(t) + k_n z_{\mathrm{th},n}(t) = F_{\mathrm{th},n}(t), \quad (22)$$

where $\omega_n = 2\pi f_n$ and $m_n = k_n / \omega_n^2$ are the resonance angular frequency and mass of the equivalent SHO representing the $n$-th eigenmode, respectively.

The thermal noise is simulated as stemming from a random stationary process, a reasonable assumption for thermal noise. Then, the FDT states that the thermal force inducing thermal fluctuations of each eigenmode is normally distributed with a rms standard deviation given by (cf. Supporting Information File 3, Equation S11):

$$F_{\mathrm{th},n}(t) = \sqrt{\frac{2k_{\mathrm{B}}Tk_n}{\pi Q_n f_n} B_{\mathrm{s,max}}}, \quad (23)$$

where $B_{\mathrm{s,max}} = f_{\mathrm{s,max}}/2$ is the acquisition bandwidth of $z_{\mathrm{th},n}(t)$. It is important to notice that $B_{\mathrm{s,max}}$ is not to be confused with $B_{\mathrm{s}}$, which was described as the experimental acquisition bandwidth of the thermal fluctuations. Here, $B_{\mathrm{s,max}}$ is the acquisition bandwidth of the numerical signal $z_{\mathrm{th},n}(t)$, which describes the instantaneous deflection of the qPlus sensor, that is, a continuous time signal, whose experimental counterpart is sampled by the control unit at a maximum rate $f_{\mathrm{s,max}}$ = 40 MHz, as already mentioned.

With our computational means it is not possible to account for such a large sampling frequency. We, therefore, have restricted it to an integer multiple of $f_{\mathrm{s}}$ = 156.250 kHz, namely $f_{\mathrm{s,max}}^{\mathrm{num}} = 20 \times f_{\mathrm{s}}$ = 3.125 MHz. Thus, Equation 22 is integrated with a Runge–Kutta 4 scheme by using a sampling period $T_{\mathrm{s,min}}^{\mathrm{num}} = 1/f_{\mathrm{s,max}}^{\mathrm{num}}$ = 320 ns, embodying the discrete time signal processed by the control unit for thermal noise analysis. We have noticed that the relevance of Runge–Kutta methods to solve stochastic differential equations seems debated [88,89]; however, at our level, this algorithm was found to be more accurate than the Symplectic Euler or the Verlet (Leapfrog) algorithms (data not shown).

Consistently with the estimated acquisition parameters, we simulate a window duration $T_{\mathrm{w}}$ = 60 s. Because the three SHOs are independent, the total deflection of the qPlus sensor is given by:

$$z_{\mathrm{th}}(t) = z_{\mathrm{th},1}(t) + z_{\mathrm{th},2}(t) + z_{\mathrm{th},3}(t). \quad (24)$$

An example of a single simulated time trace of $z_{\mathrm{th}}(t)$ is reported in Figure 2, along with the stochastic force (first eigenmode only). The thermal force histogram exhibits a normal distribution with a rms standard deviation given by Equation 23. The corresponding probability density function (cf. Supporting Information File 3, Equation S12) is shown in black.

A set of $M_{\mathrm{num}}$ = 64 time traces of $z(t)$ is thus calculated. Then, each trace $z(t)$ is downsampled with a rate $r = f_{\mathrm{s,max}}/f_{\mathrm{s}}$ = 20 to form a signal $z_d(t)$ of duration $T_{\mathrm{w}}$ = 60 s sampled at $f_{\mathrm{s}}$ = 156.250 kHz. This results in a thermal noise acquisition bandwidth $B_{\mathrm{s}} = f_{\mathrm{s}}/2$ = 78.125 kHz, consistent with the experimental conditions.

A typical spectrum is reported in Figure 3a in the spectral range [0;$B_{\mathrm{s}}$] (black curve). A zoom around $f_1$ = 25 kHz (spectral range [24.987 kHz; 25.013 kHz]) is shown in Figure 3b. The curve exhibits a pronounced resonance, representing the resonance frequency of the first eigenmode of the simulated qPlus sensor with $Q_1 = 10^5$. The continuous red curve is the theoretical tn-PSD calculated with Equation 17. Around the resonance, the

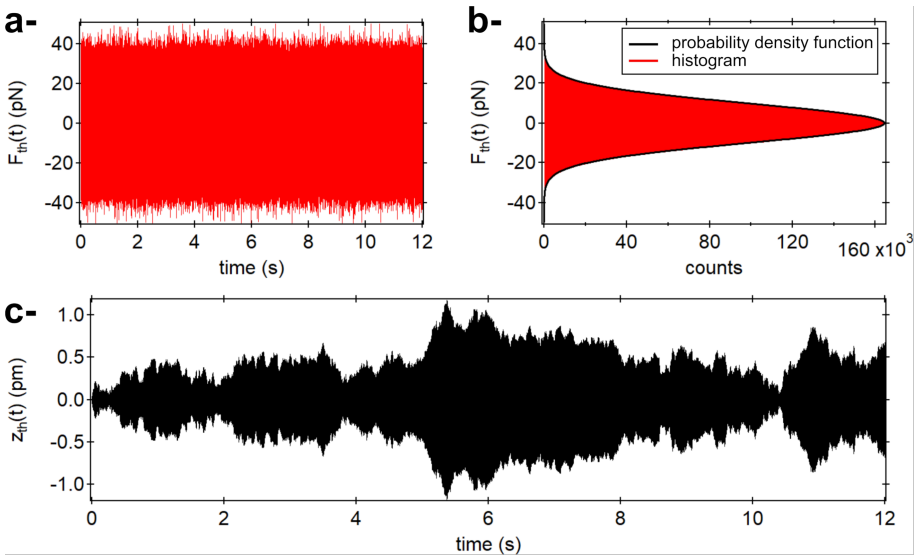


**Figure 2:** a- Time trace of the simulated thermal force for the first eigenmode displayed over an arbitrary duration of 12 s. b- Corresponding histogram and probability density function showing its normal distribution (thick black curve). c- Corresponding time trace of the fluctuations of the simulated qPlus (superposition of the first three eigenmodes, cf. text).

agreement between both curves is excellent. Deriving the stiffness according to method 1 (PSD integral over the range $[0;B_s]$, Equation 15) gives $k_{1,\mathrm{est}}^{(1)}$ = 1750 N/m. Method 2, using Equation 17 as fit functional, gives $k_{1,\mathrm{est}}^{(2)}$ = 1765 N/m, while method 3 gives $S_{z_{\mathrm{th}}}(f=f_1)=1.900\times10^{-25}\ \mathrm{m_{rms}^2/Hz}$, that is, $k_{1,\mathrm{est}}^{(3)}$ = 1813 N/m. The results are gathered in Table 2. The relative error is less than 3% with respect to the nominal value $k_1$ = 1800 N/m, regardless of the method.

In addition to the resonance peak at $f_1$, the black curve in Figure 3a exhibits two additional unexpected peaks, resembling resonance peaks, at $f_a \simeq 433$ Hz and $f_b \simeq 31.7$ kHz. However, their magnitudes are by several decades smaller than that of the $f_1$ peak. These peaks are aliases of the eigenmodes 2 and 3 of the qPlus sensor due to spectral aliasing within the band $[0;B_s]$. The spectral aliasing is also responsible for the discrepancy between the simulated tn-PSD and the theoretical tn-PSD of the SHO in the low-frequency part of the spectrum, which is discussed in Supporting Information File 4, along with the influence of an additional digital antialiasing filter.

## Influence of measurement noise

The experimental data are subject to measurement noise. To assess how it might influence the stiffness calibration, two types of measurement noise sources that embody the experimental measurement noise are introduced in the simulations. The first one is white noise featuring a constant rms PSD spectrum, $S_{z_{\mathrm{mn}}}^{(0)}$. The second source has a $1/f^n$ rms PSD spectrum, $S_{z_{\mathrm{mn}}}^{(1)}(f)$. For $n$ = 1, one has a regular $1/f$ noise. The discussion is carried out with the theoretical tn-PSD of the SHO (Equation 17), and a

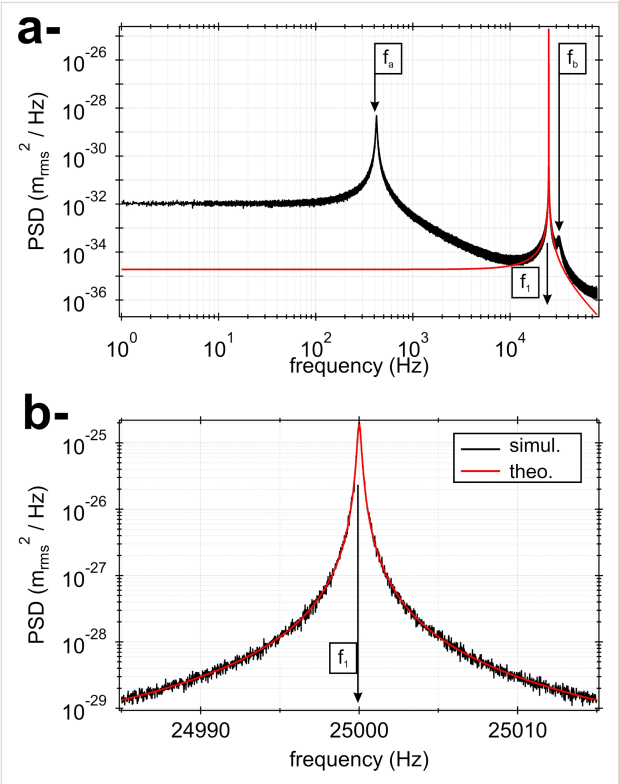


**Figure 3:** a- Simulated tn-PSD spectrum at 9.8 K (spectral range $[0;B_s]$) for the qPlus sensor whose mechanical parameters are given in Table 1 (black curve). The resonance peak due to the fundamental eigenmode ($f_1$ = 25.000 kHz) largely dominates the tn-PSD. The theoretical tn-PSD for the SHO is displayed in red. Additional peaks ($f_a$ and $f_b$) stemming from eigenmodes 2 and 3 are visible because of spectral aliasing, which also explains the discrepancy with respect to the SHO tn-PSD (cf. text). b- tn-PSD displayed in the spectral range ±15 Hz around $f_1$ (simulated data: black curve, SHO tn-PSD: red curve).

**Table 2:** Calibrated stiffness using methods 1, 2 or 3. The number of averaged time traces is $M_{num}$ = 64 in each case. The estimated stiffness is in excellent agreement with the nominal value.

| Method ($n$) | Nominal $k_1$ (N/m) | $k_{1,est}^{(n)}$ (N/m) (rel. err.) |
|---|---|---|
| **1** | 1800 | 1750 (–2.8%) |
| **2** | 1800 | 1765 (–1.9%) |
| **3** | 1800 | 1813 (+0.7%) |

similar acquisition bandwidth $B_s$ = 78.125 kHz is considered. Then, the total rms PSD of the system is written as:

$$S_z(f) = S_{SHO}(f) + S_{z_{mn}}(f), \tag{25}$$

where:

$$S_{z_{mn}}(f) = S_{z_{mn}}^{(0)} + S_{z_{mn}}^{(1)}(f) = S_{z_{mn}}^{(0)} + \frac{K}{f^n}. \tag{26}$$

To make the discussion relevant, the numerical parameters defining $S_{z_{mn}}(f)$ are those deduced empirically from the experimental PSD (cf. section "Experimental results" and Figure 6), namely:

$$S_{z_{mn}}(f) = 3.765\times10^{-27} + \frac{1.1\times10^{-20}}{f^{1.6}}. \tag{27}$$

As for $S_{SHO}(f)$, $(f_1, Q_1, k_1)$ = (25 kHz, $10^5$, 1800 N/m). The corresponding spectrum is reported in Figure 4a.

According to method 1, we first make sure that

$$k_{1,est}^{(1)} = \frac{k_B T}{\langle z_{th}^2 \rangle} = \frac{k_B T}{\int_0^{B_s}\left[S_z(f) - S_{z_{mn}}(f)\right]df} = \frac{k_B T}{\int_0^{B_s} S_{SHO}(f)\,df} \tag{28}$$

accurately leads to the nominal value $k_{1,est}^{(1)}$ = 1800 N/m.

Practically, the measurement noise PSD may be difficult to account for with a functional as simple as Equation 27. This is why, in the literature, the stiffness may also be found to be estimated by integration of the PSD within a restricted bandwidth around the resonance [48], where its behavior is easier to describe. In the mentioned reference, however, the authors state that they compensate for the finite integration range, but without detailing how. We hereafter propose an analysis of the in-

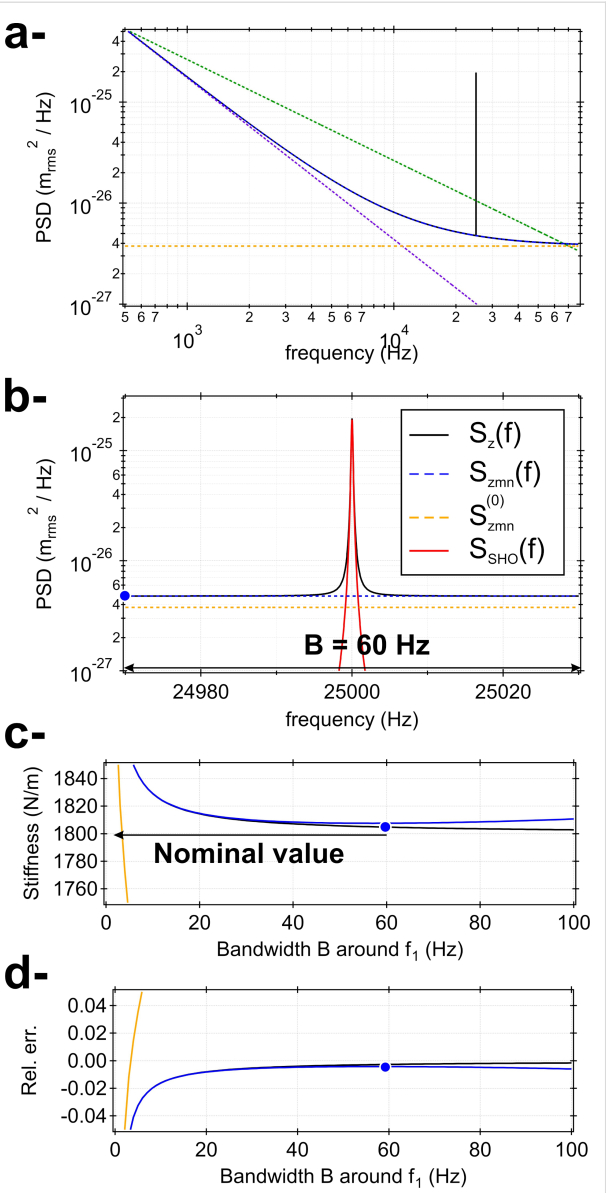


**Figure 4:** a- Numerical tn-PSD including measurement noise displayed in the range [500 Hz;$B_s$]: $S_z(f) = S_{SHO}(f) + S_{z_{mn}}(f)$ (black curve). The measurement noise PSD, $S_{z_{mn}}(f)$, is displayed as a dotted blue curve on top of $S_z(f)$, except at the resonance. The numerical parameters are given in the text. $S_{z_{mn}}(f)$ is built as the superposition of a constant background $S_{z_{mn}}^{(0)}$ (dotted orange curve) and a $1/f^n$-like contribution $S_{z_{mn}}^{(1)}(f) = K/f^n$ (dotted purple curve). Here, $n$ = 1.6 to match with the experimental PSD (cf. text). A $1/f$ component has been displayed as a guide to the eye (dotted green curve). b- Zoom in the spectral range $\pm B/2$ = ±30 Hz around $f_1$. The theoretical PSD of the equivalent SHO is overlaid (red curve). In that area of the PSD, the noise floor may be estimated from the value of $S_{z_{mn}}(f_1 - B/2)$ (blue circle). c- Estimated stiffness upon integration of (i) $S_z(f) - S_{z_{mn}}(f)$ (black curve), (ii) $S_z(f) - S_{z_{mn}}(f_1 - B/2)$ (blue curve), and (iii) $S_z(f) - S_{z_{mn}}^{(0)}$ (orange curve), for an increasing bandwidth around $f_1$. The nominal stiffness is $k_1$ = 1800 N/m. d- Corresponding relative errors.

fluence of a finite PSD integration range on the stiffness calibration.

In a ±30 Hz wide area around $f_1$, the PSD noise background looks flat (cf. Figure 4b), as if the measurement noise only consisted of a constant, that is, white background noise. This effect essentially stems from the high $Q$ value of the qPlus sensor, which imposes a weak bandwidth $w_f = f_1/Q_1$ = 125 mHz around $f_1$, over which the $1/f^n$ attenuation, with our parameters, is barely visible. To assess how much the estimated stiffness is sensitive to the PSD integration interval, we derive the stiffness upon integration of the quantity $S_z(f) - S_{z_{\mathrm{mn}}}(f)$ over an increasing bandwidth $B$ around $f_1$ according to:

$$k_{1,\mathrm{est}}^{(1)}(B) = \frac{k_\mathrm{B}T}{\left\langle z_{\mathrm{th}}^2 \right\rangle} = \frac{k_\mathrm{B}T}{\int_{f_1-B/2}^{f_1+B/2}\left[S_z(f) - S_{z_{\mathrm{mn}}}(f)\right]\mathrm{d}f}. \quad (29)$$

The result is reported in Figure 4c (black curve). The estimated stiffness fits to better than 2% with the nominal value as soon as the integration bandwidth is larger than $B/2$ = 5 Hz (cf. Figure 4d, black curve).

Then, we assess how much the estimated stiffness is falsified if only a constant background is subtracted from $S_z(f)$ instead of $S_{z_{\mathrm{mn}}}(f)$, regardless of the PSD power-law dependence at low frequencies. Following the same methodology, the estimated stiffness is derived for two cases, namely by integration of (i) $S_z(f) - S_{z_{\mathrm{mn}}}^{(0)}$ (removal of the white noise only, cf. orange curve in Figure 4c), and (ii) $S_z(f) - \left[S_{z_{\mathrm{mn}}}^{(0)} + S_{z_{\mathrm{mn}}}^{(1)}(f_1 - B/2)\right]$ (removal of the white noise and the $1/f^n$ noise, but the former is estimated at $f = f_1 - B/2$; here $S_{z_{\mathrm{mn}}}(f_1 - B/2) = 4.785\times10^{-27}\ \mathrm{m_{rms}^2/Hz}$, cf. blue curve and blue circle in Figure 4c). The accuracy of the estimated stiffness remains excellent by integration of the quantity $S_z(f) - \left[S_{z_{\mathrm{mn}}}^{(0)} + S_{z_{\mathrm{mn}}}^{(1)}(f_1 - B/2)\right]$ and nearly equal to that obtained upon integration of $S_z(f) - S_{z_{\mathrm{mn}}}(f)$ (black vs blue curve in Figure 4c) up to $B/2$ = 30 Hz. Conversely, $S_{z_{\mathrm{mn}}}^{(0)}$ underestimates the background noise in the area around $f_1$ such that the integration of the quantity $S_z(f) - S_{z_{\mathrm{mn}}}^{(0)}$ yields a largely underestimated stiffness value (orange curves in Figure 4c,d).

In summary, this section has proven that the stiffness of a qPlus sensors may be accurately calibrated by integration of the tn-PSD in a restricted bandwidth $B$ around $f_1$, provided that (i) $S_z(f)$ presents a homogeneous background measurement noise without parasitic peaks within $B$, (ii) $B$ is much larger than the equivalent SHO bandwidth $w_f$, and (iii) $S_z(f)$ is corrected from the measurement noise, whose spectral dependence has been estimated over $B$ or corrected from a constant measurement noise estimated nearby $f_1$; however, depending on how the constant background is determined, that former approach is less accurate.

# Experimental Results

The experimental stiffness calibration was performed with two distinct qPlus sensors, referred to as qPlus 1 and 2 in the following. For qPlus 1, the tip was removed so as to reproduce the behavior of a perfectly free prong, which allows us to benchmark the thermal noise measurement method on two probes with expected distinct mechanical behaviors.

## Equivalent SHO

In order to assess whether the mechanical behavior of the qPlus sensor reasonably compares to that of a SHO, several resonance curves (fundamental eigenmode) were measured for both qPlus sensors with decreasing excitation amplitudes (cf. Figure 5). Each curve is fitted with Equation 19 (amplitude dependence only), from which the resonance frequency $f_1$, the resonance amplitude $A_1$, and the quality factor $Q_1$ are deduced. A constant background, $A_{\mathrm{bkg}}$, has been added to Equation 19 to account for the noise floor. A set of four coefficients is therefore ultimately used for the fits, namely $A_1$, $Q_1$, $f_1$, and $A_{\mathrm{bkg}}$. The fits are performed by means of the software Igor Pro from Wavemetrics®. For the non-linear least-squares fit process used here, Igor uses the Levenberg–Marquardt algorithm looking for the minimum value of chi-squared. The confidence interval for the fit coefficients is set to 99%. The residual of each fit, Δ, is built according to $\Delta = A_{\mathrm{exp}}(f) - A_{\mathrm{fit}}(f)$. Doing so, we not only want to measure these parameters while estimating the fit quality, but also want to verify whether the qPlus quality factor is independent from the excitation amplitude ($A_{\mathrm{exc}}$), as expected in the SHO model. Since the thermal noise measurements are performed without mechanical excitation of the qPlus sensor and its quality factor is required to perform the stiffness calibration (methods 2 and 3), this value must reflect an intrinsic property of the probe. We name that quantity $Q_1^*$. The quality factor used to perform the stiffness calibration must be as close as possible to $Q_1^*$, meaning that it must have been determined without any influence of the mechanical transfer function of the qPlus sensor holder within the microscope, that is, at extremely low excitation amplitude.

A set of excitation amplitudes yielding $A_1$ values ranging from ≃500 pm down to ≃10 pm has been selected. The resonance curves are reported in Figure 5a and Figure 5e (qPlus 1 and 2, respectively). Each curve is acquired over an interval of ±4.8 Hz around the resonance (qPlus 1: $f_1$ = 29,182.99 Hz, qPlus 2: $f_1$ = 24,661.76 Hz) and features a spectral resolution equal to, or better than, the required one, $\delta f$ = 20 mHz. Each curve is acquired within a one hour time lap because of the

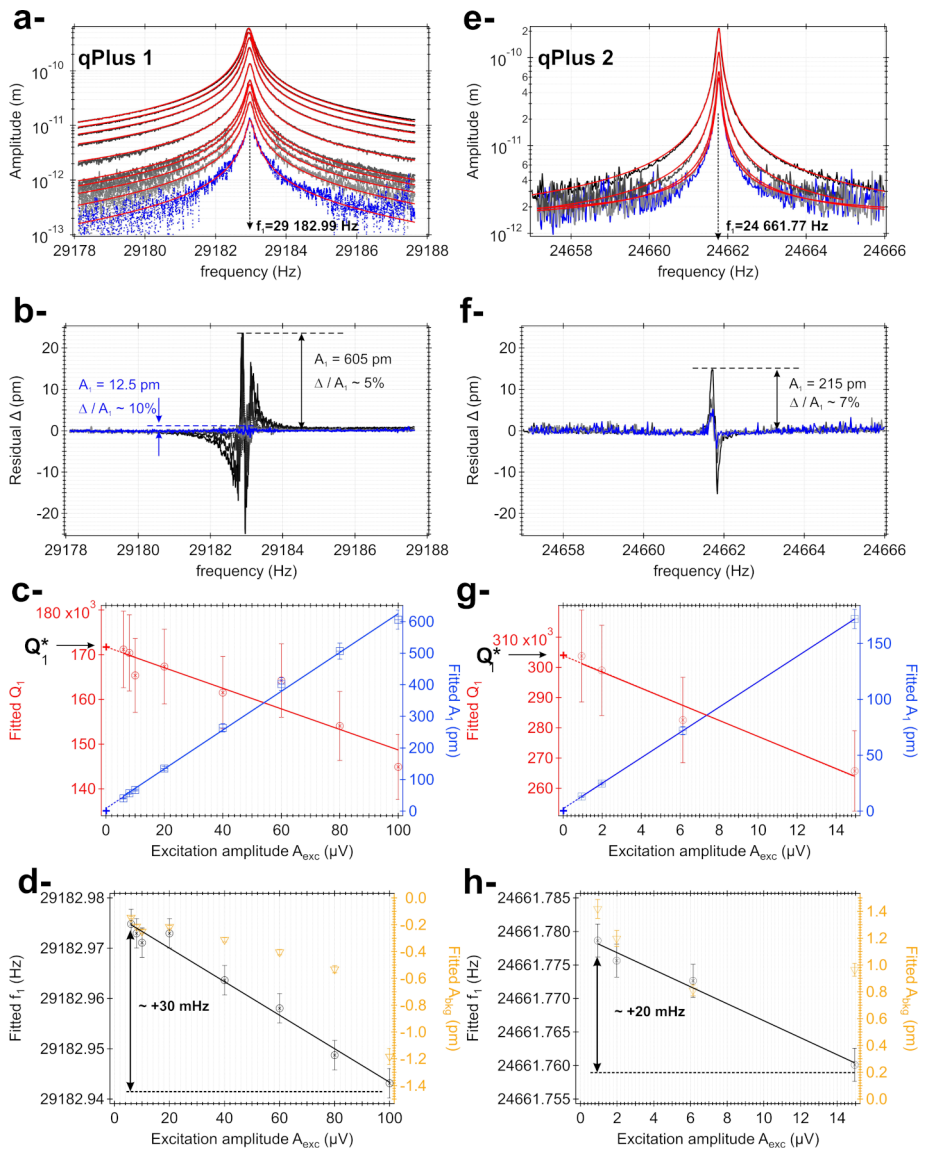


**Figure 5:** Experimental resonance curves of the fundamental eigenmode for two distinct qPlus sensors recorded with decreasing excitation amplitudes $A_{exc}$ (a- and e-). For each curve, a fit with the SHO equations gives the values of resonance frequency $f_1$, resonance amplitude $A_1$, background $A_{bkg}$, and quality factor $Q_1$ (red curves). The curves acquired with the smallest excitation amplitude are shown in blue to discriminate them from the less noisy data. The residual Δ of each fit is shown in panels b- and f-. The relative magnitude of the ratio $\Delta/A_1$ at the resonance is between 5% and 10%. The evolution of $A_1$ and $Q_1$ vs $A_{exc}$ is reported in panels c- and g- (right and left axes, blue and red markers, respectively). The evolution of $A_{bkg}$ and $f_1$ vs $A_{exc}$ is reported in panels d- and h- (right and left axes, orange and black markers, respectively). The evolution of the fitted quality factor allows us to extract the intrinsic quality factor of each qPlus sensor, $Q^*_1$ (cf. text).

large quality factor, which is enough to prevent any non-adiabatic effect from occurring. The fits with Equation 19 as fit functional are overlaid on each acquisition (red curves). The residuals are reported in Figure 5b and Figure 5f (qPlus 1 and 2, respectively).

Figure 5b,f shows that the magnitude of the residuals increases when $A_{exc}$ is decreased owing to the degraded signal-to-noise ratio. Overall, in the vicinity of the resonance, the relative magnitude increases from less than 5% ($A_1$ = 605 pm) to less than 10% ($A_1$ = 12.5 pm). Although the following statement is not rigorous, we estimate that a relative uncertainty of ±5% is quite representative for the fit coefficients (except $f_1$, which is estimated with a much better accuracy; cf. below). They are plotted consistently, but note that these error bars are much larger than the standard deviations given by the fit process for each coefficient. We have noticed that some approaches are reported to achieve specified tolerances on the fit coefficients of spectra exhibiting a Lorentzian response; however, we did not employ them here [53,90].

The evolution of the fitted quality factor as a function of $A_{exc}$ for qPlus 1 and 2 is reported in Figure 5c and Figure 5g, respectively (red symbols and continuous red line, left axis). The evolution of the fitted value of $A_1$ as a function of $A_{exc}$ is reported as well (blue symbols and continuous blue line, right axis). For $A_1 \simeq 100$ pm, the quality factor of qPlus 1 is in the range of 168,000, whereas for qPlus 2, it is rather 280,000. The correct expected linear dependence between $A_1$ and $A_{exc}$ is observed down to $A_{exc} = 0$ (dotted line and blue cross), which testifies that, with these excitations, non-linearities due to the mechanical transfer function of the qPlus excitation system are not likely to occur.

The evolution of the fitted value of the resonance frequency as a function of $A_{exc}$ for qPlus 1 and 2 is reported in Figure 5d and Figure 5h, respectively (black symbols and continuous black line, left axis). The evolution of the fitted value of $A_{bkg}$ as a function of $A_{exc}$ is reported as well (orange symbols and orange curve, right axis). Because of the high quality factors, the fits yield values of $f_1$ with a high accuracy, such that it is irrelevant to plot the fitted value for that coefficient with 5% error bars. We rather use the standard deviation given by the fit, which is about $\pm f_1 \times 10^{-7} \simeq \pm 3$ mHz. We note that the fitted values for $A_{bkg}$ remain consistently small compared to $A_1$ and that a significant offset error in the estimation of the amplitude is unlikely to occur.

For both qPlus sensors, the quality factor and the resonance frequency feature a moderate linear dependence with $A_{exc}$. Both $Q_1$ and $f_1$ increase as $A_{exc}$ decreases. $Q_1$ increases by about 20% (140,000→170,000 for qPlus 1, 260,000→310,000 for qPlus 2) and $f_1$ by about +30 mHz. A similar effect on $f_1$, with comparable magnitudes, has been reported by Dagdeviren et al. with other types of qPlus sensors [91]. The reference states that the drop of the resonance frequency upon increase of the oscillation amplitude results from an in-plane surface stress near the clamp of the free prong of the QTF. In the mentioned reference, the evolution of the quality factor is not reported. Hence, it is difficult to conclude whether the in-plane surface stress is the main cause for the observed trend of the quality factor. Thus, even though the observations by Dagdeviren et al. are consistent with ours, we do not exclude the additional influence of the mechanical transfer function of the excitation system onto the QTF. Indeed, it is known that the way the probes are mounted on their holders, along with the mechanical transfer function of the probe excitation system, may influence their quality factor [92], which is detrimental to the decoupling of conservative and dissipative forces in nc-AFM [93]. Because much less mechanical energy is injected into the system when $A_{exc}$ is decreased, energy losses are reduced, and it is the most reactive part of the system, namely the QTF, that reacts to the excitation.

From these measurements, we deduce the $Q_1^*$ value of each qPlus sensor (extrapolation at $A_{exc} = 0$, dotted line and red cross). For qPlus 1 and 2, we get, respectively, $Q_1^* = 172{,}000$ and 304,000. These values are used in the following to perform the stiffness calibration.

## Measurement noise PSD

Figure 6a reports the measured tn-PSD spectrum with measurement noise, $S_z(f)$, for qPlus 2 (black curve), for which we now have identified $f_1 = 24{,}661.76$ Hz and $Q_1^* = 304{,}000$. The spectrum was acquired with the parameters $f_s = 156.250$ kHz, $N = 8{,}388{,}544$ samples, and $M_{exp} = 512$ time traces. It is reported over the bandwidth [500 Hz;$B_s$] since the qPlus charge preamplifier features a cut-off high-pass frequency of ≃500 Hz [28]. The spectrum exhibits a bunch of parasitic peaks for frequencies above 10 kHz. Owing to the large spectral resolution, extremely narrow ones can be identified, tracing the influence of purely sinusoidal noise components. Some others look wider. As mentioned earlier, one expects some of these to stem from aliasing effects, although this was not investigated in detail and neither was the origin of the purely sinusoidal noise components.

The magnified area of the spectrum around the qPlus resonance is reported in Figure 6b (40 Hz wide), where no parasitic peak is visible. The resonance is superimposed on a seemingly constant background measurement noise that is estimated to be $S_{z_{mn}}^{cst} = 4.796 \times 10^{-27}\ m_{rms}^2/Hz$ (orange dotted line in Figure 6b). $S_{z_{mn}}^{cst}$ is the noise floor of the experimental setup in this frequency range. In Figure 6b, the experimental spectrum can qualitatively be compared with that of the numerical simulations (cf. Figure 4b). In the log–log scale, the spectrum features a linear decay from 500 to ≃5000 Hz (cf. Figure 6a). The estimated background measurement noise using Equation 26 as functional yields Equation 27. We name this quantity $S_{z_{mn}}^{fit}(f)$, although it was not deduced from a fit, but estimated empirically with the constraint to make it match $S_{z_{mn}}^{cst}$ for $f = f_1 - 20$ Hz (cf. blue dot in Figure 6b). The corresponding curve is reported in blue in Figure 6a,b. We notice that the charge preamplifier transfer function of the experimental setup induces a measurement noise drop ($\propto 1/f^{1.6}$) that decays faster than regular $1/f$ noise.

The measurement noise PSD has also been estimated by direct measurement, that is, without connecting the qPlus sensor to the charge preamplifier input (green curve in Figure 6a,b). This third estimate of the measurement noise is named $S_{z_{mn}}^{dir}(f)$. For this acquisition, similar sampling parameters have been used. In the log–log scale, the spectrum exhibits a nearly linear decay all over the acquisition bandwidth. Some residual narrow noise components are still visible; but, overall, the spectrum is much

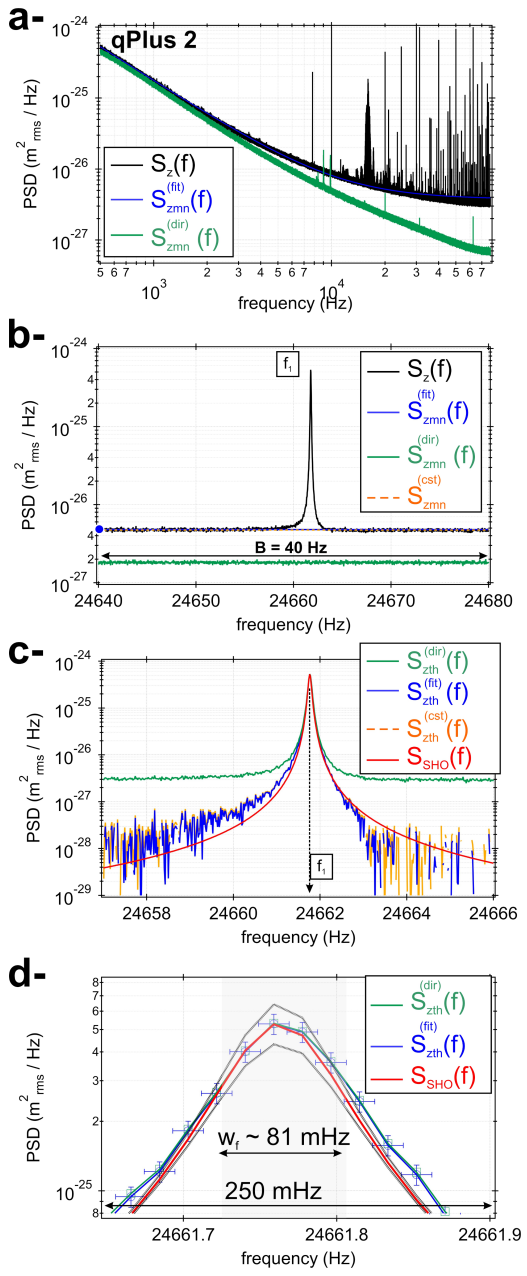


**Figure 6:** a- Experimental tn-PSD featuring measurement noise, $S_z(f)$, for qPlus 2 (black curve). The empirically derived measurement noise PSD $S^{\text{fit}}_{z_{\text{mn}}}(f)$ is displayed in blue, whereas the directly measured homologous quantity $S^{\text{dir}}_{z_{\text{mn}}}(f)$ is displayed in green (cf. text). b- Zoom area around the resonance of the qPlus sensor (40 Hz wide). The traces of $S^{\text{fit}}_{z_{\text{mn}}}(f)$ and $S^{\text{dir}}_{z_{\text{mn}}}(f)$ are visible. The dotted orange curve depicts a constant noise background $S^{\text{cst}}_{z_{\text{mn}}}$ that coincides with $S^{\text{fit}}_{z_{\text{mn}}}(f)$ in that spectral range. c- tn-PSD for qPlus 2 $S_{z_{\text{th}}}(f)$ derived according to (i) $S_z(f) - S^{\text{cst}}_{z_{\text{mn}}}$ (dotted orange curve), (ii) $S_z(f) - S^{\text{fit}}_{z_{\text{mn}}}(f)$ (blue curve), and (iii) $S_z(f) - S^{\text{dir}}_{z_{\text{mn}}}(f)$ (green curve). The estimated stiffness is derived from these measurements and gathered in Table 3. The red curve is the theoretical SHO PSD calculated from the experimentally deduced parameters of the qPlus sensor. d Zoom area on top of the resonance shown in panel c- (250 mHz wide). The bandwidth of the equivalent SHO, $w_f \simeq 81$ mHz, has been overlaid in light grey. The experimental data are framed by the theoretical SHO PSD with an uncertainty smaller than 10% (cf. text).

cleaner than the tn-PSD one. The fact that both PSDs (qPlus connected and disconnected) are so different points towards an additional influence of noise when the qPlus sensor is connected. This is most probably due to the qPlus cabling inside the microscope; however, this issue was not addressed so far. It is, however, clear that $S^{\text{dir}}_{z_{\text{mn}}}(f)$ will be insufficient to account for all the noise in the system and will, therefore, not be reliable to perform the stiffness calibration (cf. section below).

## Stiffness calibration

The tn-PSD $S_{z_{\text{th}}}(f)$ of qPlus 2 deduced from $S^{\text{cst}}_{z_{\text{mn}}}$, $S^{\text{fit}}_{z_{\text{mn}}}(f)$, and $S^{\text{fit}}_{z_{\text{mn}}}(f)$ is reported in Figure 6c over a 9 Hz wide spectral range. The orange curve in Figure 6c shows the tn-PSD $S^{\text{cst}}_{z_{\text{th}}}(f) = S_z(f) - S^{\text{cst}}_{z_{\text{mn}}}$, the blue curve shows $S^{\text{fit}}_{z_{\text{th}}}(f) = S_z(f) - S^{\text{fit}}_{z_{\text{mn}}}(f)$, and the green curve shows $S^{\text{dir}}_{z_{\text{th}}}(f) = S_z(f) - S^{\text{dir}}_{z_{\text{mn}}}(f)$.

As mentioned earlier, we use no curve-fitting process for $S_{z_{\text{th}}}(f)$ and only focus on methods 1 and 3. Method 1 is used with an integration range of ±60 Hz around $f_1$, where no parasitic peak is visible while ensuring a good accuracy of the stiffness calibration, based on the numerical results. The stiffness thus derived from $S^{\text{cst}}_{z_{\text{th}}}(f)$, $S^{\text{fit}}_{z_{\text{th}}}(f)$, and $S^{\text{dir}}_{z_{\text{th}}}(f)$ gives $k^{(1)}_{1,\text{est}}$ = 1800, 1995, and 318 N/m, respectively. Method 3 applied to $S^{\text{fit}}_{z_{\text{th}}}(f)$ gives $S^{\text{fit}}_{z_{\text{th}}}(f = f_1) = 5.2907 \times 10^{-25}\ \text{m}^2_{\text{rms}}/\text{Hz}$, and $k^{(3)}_{1,\text{est}}$ = 2007 N/m. We cannot straightforwardly establish error bars on those measurements at that stage, but this is done hereafter. Therefore methods 1 and 3 applied to $S^{\text{fit}}_{z_{\text{th}}}(f)$ are found to be in excellent agreement. As suspected, the estimated stiffness deduced from $S^{\text{dir}}_{z_{\text{th}}}(f)$ is critically underestimated and unreliable. Furthermore, because we have numerically established that the calibration stiffness is more accurate when using a background measurement noise estimated over the entire acquisition bandwidth rather than a constant one, the most realistic stiffness of qPlus 2 is that derived from $S^{\text{fit}}_{z_{\text{th}}}(f)$, namely $k^{(1)}_{1,\text{est}}$ = 1995 N/m. The continuous red curve in Figure 6c is the theoretical tn-PSD of the SHO (Equation 17) calculated with the now established values of $f_1$, $Q^*_1$, and $k^{(1)}_{1,\text{est}}$. The curve overlays with a good agreement on top of the experimental tn-PSDs over three decades.

Figure 6d is a zoom area on top of the tn-PSD shown in Figure 6c. The frequency range is now 250 mHz. The experimental samples of $S^{\text{fit}}_{z_{\text{th}}}(f)$ are displayed with their error bars of ±10 mHz in frequency, consistent with the frequency resolution, and ±10% in $\text{m}^2_{\text{rms}}/\text{Hz}$, consistent with our amplitude calibration uncertainty. The two thick, light grey curves depict the tn-PSD of the SHO (Equation 17) with 10% deviations of $Q^*_1$ and $k^{(1)}_{1,\text{est}}$. Because the quality factor and the stiffness have opposite contributions in the tn-PSD (cf. Equation 18), the upper curve is obtained with $Q^*_1$ + 10% and $k^{(1)}_{1,\text{est}}$ − 10%, and

the lower one with $Q_1^*$ − 10% and $k_{1,\mathrm{est}}^{(1)}$ + 10%. It may be seen from the figure that the relevant experimental samples located within the qPlus bandwidth, $w_f = f_1/Q_1^* \simeq 81$ mHz, depicted with the shaded rectangle, sit all well within this interval. Therefore, we conclude that the stiffness is estimated with a maximum relative uncertainty of 10%, which is reported in Table 3.

The same processing was reproduced with qPlus 1 ($f_1$ = 29,182.99 Hz and $Q_1^*$ = 172,000) featuring no tip. The estimated stiffness with methods 1 and 3 using $S_{z_{\mathrm{mn}}}^{\mathrm{fit}}(f)$ as background measurement noise (±60 Hz integration range) gives $k_{1,\mathrm{est}}^{(1)}$ = (1289 ± 130) N/m and $k_{1,\mathrm{est}}^{(3)}$ = (1544 ± 155) N/m, respectively. Like with qPlus 2, we note a slightly larger value of $k_{1,\mathrm{est}}^{(3)}$ with respect to $k_{1,\mathrm{est}}^{(1)}$. The results are gathered in Table 3 and are discussed in the section below.

## Discussion

In this section, we discuss the advantage of method 1 over method 3, and we compare the thermal noise-based estimated stiffness to values derived from other approaches (cf. Table 3).

Our results indicate that method 3 tends to slightly overestimate the stiffness with respect to method 1. But the latter method forces the experimentalist to point the maximum of the PSD at the resonance, which introduces a somewhat subjective bias in the stiffness estimate. Conversely, method 1 integrates the PSD without subjective input. Thus, any potential statistical bias is smeared out as compared to method 3. This is why method 1 is likely more robust and, hence, preferred to method 3.

It is reminded that qPlus 1 features no tip and that the SEM imaging has been performed with a qPlus sensor that is neither qPlus 1 nor qPlus 2. Thus, we cannot guarantee that the tip dimensions that are used hereafter are consistent with those of the qPlus 2. The discussion is adapted consistently.

For the static stiffness derived from the geometrical parameters of a qPlus sensor (Equation 2, model without tip), we have yet calculated $k_s$ = (3322 ± 1270) N/m. Lübbe's approach [51] (Equation 4 with $\alpha_1$ = 1.875), leads for qPlus 1 to: $k_{s,f_1}$ = (809 ± 162) N/m. We also estimate the stiffness from Cleveland's approach [32] $k_{s,f_1} = m_1^*(2\pi f_1)^2$, where $m_1^* = \mu_{e,1} m_{\mathrm{probe}} = 3m_{\mathrm{probe}}/\alpha_1^4$ is the effective mass of the fundamental eigenmode (cf. also Supporting Information File 1, Equation S5). With the geometric parameters introduced, the prong mass is estimated to be $m_{\mathrm{probe}}$ = (160 ± 24) ng (thus, $m_1^*$ = (39 ± 6) ng). The mass of the metallic electrodes is neglected compared to $m_{\mathrm{probe}}$. For qPlus 1, Cleveland's approach [32] leads to $k_{s,f_1}$ = (1296 ± 195) N/m.

The latter values stand for the qPlus static stiffness and are not strictly comparable to $k_{1,\mathrm{est}}^{(1)}$ (or $k_{1,\mathrm{est}}^{(3)}$), which depict the modal stiffness of the probe's fundamental eigenmode. Nevertheless, because qPlus 1 features no tip, its static stiffness can be derived from $k_{1,\mathrm{est}}^{(1)}$ (or $k_{1,\mathrm{est}}^{(3)}$) from Equation 10. Then, we get $k_{s,f_1}$ = (1252 ± 125) N/m. Cleveland's approach [32] and ther-

**Table 3:** Estimated stiffness of the two qPlus sensors used in this study. Various methods have been used. When the tip mass correction is applied, one assumes the tip geometry to be the same as that given in Figure 1, which is a strong hypothesis and explains the dispersion between the data (cf. text).

| Method | Estimated stiffness | Tip mass correction | qPlus 1 (no tip) (N/m) | qPlus 2 (with tip) (N/m) |
|---|---|---|---|---|
| geometry (Equation 2) | $k_s$ | no | (3322 ± 1270) | not applicable |
| Lübbe et al. [51] (Equation 4) | $k_{s,f_1}$ | no | (809 ± 162) | not applicable |
| Cleveland et al. [32] (cf. Supporting Information File 1, Equation S5) | $k_{s,f_1}$ | no | (1296 ± 195) | not applicable |
| Cleveland et al. [32] (cf. Supporting Information File 1, Equation S14) | $k_{s,f_1}$ | yes | not applicable | (1447 ± 223) |
| Lozano et al. [49] (cf. Supporting Information File 1, Equation S12) | $k_{s,f_1}$ | yes | not applicable | (1636 ± 164) |
| tn-PSD | | implicit | | |
| method 1, bkg = $S_{z_{\mathrm{mn}}}^{\mathrm{fit}}(f)$ | $k_{1,\mathrm{est}}^{(1)}$ | | (1289 ± 130) | (1995 ± 200) |
| method 3, bkg = $S_{z_{\mathrm{mn}}}^{\mathrm{fit}}(f)$ | $k_{1,\mathrm{est}}^{(3)}$ | | (1544 ± 155) Equation 10 | (2007 ± 200) Supporting Information File 1, Equation S13 |
| Equation 10, or Supporting Information File 1, Equation S13, with $k_{1,\mathrm{est}}^{(1)}$ | $k_{s,f_1}$ | | (1252 ± 125) | (3012 ± 301) |

mal noise measurements are, therefore, in good agreement. However, we notice a strong discrepancy between the former results and the stiffness derived from the geometrical parameters of the qPlus (overestimate) and Lübbe's approach [51] (underestimate). The reason for that has not been investigated, but both approaches rely on the embedded beam theory. It might be that such a description does not perfectly suit to the type of qPlus sensors investigated here, as discussed in the bibliographic section of the work by Falter and coworkers [65]. Besides, the tip of qPlus 1 has been removed with the goal to have a perfectly free prong, whose behavior might be compared to the geometrical model. But again, we cannot guarantee that there is no glue left at the end of the free prong, which might falsify the comparison to the model.

Regarding qPlus 2, the influence of both tip and glue used to hold it must change its stiffness. This is not accounted for in Equation 2 or Equation 4 and must now be considered. In their article, Cleveland et al. had proposed a simple approach to that problem [32] (cf. also Supporting Information File 1, Equation S14). The stiffness of the loaded prong is $k_{s,f_1} = m(2\pi f_1)^2$, where $m$ is not the total mass of the probe including the tip, but given by $m = m_1^* + m_{tip}$. Doing so, they do not consider the modification of the first eigenmode geometry due to the added mass, which makes the approach approximate. $m_1^*$ has been established. As for $m_{tip}$, based on Figure 1, we assume for the tip an effective cylinder of 50 µm diameter and of $h$ = (570 ± 29) µm height (cf. Figure 1b). The mass of the glue is neglected compared to $m_{tip}$. We get $m_{tip}$ = (22 ± 4) ng. Thus, for qPlus 2, Cleveland's approach [32] now yields $k_{s,f_1}$ = (1447 ± 223) N/m. The approach by Lozano et al. [49] improves Cleveland's one. As mentioned, the tip changes the geometry of the probe eigenmodes compared to the unloaded case. This results in a change of the value of the constant $\alpha_n$ of each eigenmode (now becoming $\tilde{\alpha}_n$, cf. Equation 6). To derive the value of $\tilde{\alpha}_1$ for the first eigenmode, Equation 6 is to be solved with a selected value of $\mu = m_{tip}/m_{probe}$. With our estimations, $\mu \simeq 13.8\%$. The numerical solution of Equation 6 yields $\tilde{\alpha}_1 = 1.679$. Thus, we derive the stiffness of the equivalent SHO featuring a total mass $m = m_{probe} + m_{tip}$ according to (cf. Supporting Information File 1, Equation S12):

$$k_{s,f_1} = \frac{3}{\tilde{\alpha}_1^4} m\left(2\pi f_1\right)^2. \tag{30}$$

For the qPlus 2, the approach by Lozano et al. [49] yields $k_{s,f_1}$ = (1636 ± 164) N/m, closer to $k_{1,est}^{(1)}$ (or $k_{1,est}^{(3)}$), and, thus, more consistent than Cleveland's one [32]. However, it is again outlined that $k_{s,f_1}$ and $k_{1,est}^{(1)}$ (or $k_{1,est}^{(3)}$) do not depict the same stiffness. The connection between them is not given by Equation 10 anymore, but by:

$$\frac{k_n}{k_s} = \frac{\tilde{\alpha}_n^4}{12}. \tag{31}$$

For the qPlus 2, we ultimately get $k_{s,f_1}$ = (3012 ± 301) N/m. The estimated static stiffness is about twice as large as Lozano's one. However as already mentioned, the tip geometry is not guaranteed; hence, the relevance of the comparison is neither.

At last, a large discrepancy between the estimated modal stiffness values of qPlus 1 and 2 is also noticed, which is assigned to the absence/presence of the tip. Our results highlight both the fundamental role played by the tip in the estimated stiffness and the urge for the stiffness calibration of each qPlus sensor. For us, measuring the tip geometry cannot be performed in situ because the SEM is not connected to the experimental setup. Hence, the interest in thermal noise measurements.

Our final conclusion is that the most relevant value we can rely on for qPlus 2 is its modal stiffness $k_{1,est}^{(1)}$ = (1995 ± 200) N/m, determined through thermal noise measurements from method 1. The fact that this value coincides to within 10% of the value of 1800 N/m reported for the early versions of qPlus sensor is purely fortuitous and specific to this qPlus sensor. This value will be different for other qPlus sensors since they will feature different tips.

## Conclusion

This work details a combined numerical and experimental framework for the stiffness calibration ($k$) of a particular type of non-contact atomic force microscopy (nc-AFM) probes, the so-called qPlus sensors, in ultrahigh vacuum (UHV) and at low temperature (9.8 K), based on thermal noise measurements. The qPlus design for which the stiffness calibration is performed is shown in Figure 1. These sensors are based on a quartz tuning fork with one prong fixed and a metallic wire glued at the front end of their free prong forming the tip. The stiffness calibration of such high-$k$ sensors, featuring high-quality factors ($Q$) as well, requires to master both the acquisition parameters and the data post-processing. Our approach relies on the statistical analysis of the thermal noise power spectral density (tn-PSD) of the fluctuations of the qPlus sensor's free prong. The estimated stiffness is derived upon analysis of the tn-PSD by means of the Euler–Bernoulli model and the simple harmonic oscillator equivalence, an otherwise common approach in the literature. Our numerical framework allows us to optimize the experimental acquisition parameters and draw conclusions about the most efficient way to treat the measurement noise that interferes with

the tn-PSD. Among several methods introduced for estimating the stiffness from the tn-PSD, it has been shown that the most reliable is to perform the tn-PSD integration over a limited bandwidth around the resonance of the qPlus sensor. The subsequent analysis of the experimental tn-PSD yields a value for the modal stiffness of the qPlus of ≃2000 N/m, with an uncertainty of 10% maximum, whereas the corresponding static stiffness of the sensor featuring no tip, derived from geometric criteria, is 3300 N/m.

Our work highlights the influence of the tip on the estimated stiffness, as well as the need for individual calibration of these probes. Calibrating the stiffness by measuring thermal noise also proves to be more reliable than geometric methods that not only require highly accurate measurements of probe and tip dimensions, but also an ad hoc mechanical model.

Our framework details many technical and practical aspects of the stiffness calibration of qPlus sensors in UHV and at low temperature. From this point of view, it may be adapted to any high-$k$, high-$Q$ nc-AFM probe used under similar conditions, such as silicon cantilevers and length extensional resonators, the latter including the KolibriSensor.

Nowadays, a lot of nc-AFM experiments based on qPlus sensors use frequency shift spectroscopy to deduce the forces and potentials above individual atoms or molecules in order to quantitatively evaluate the tip–sample interaction. Most of these publications use a value of 1800 N/m for the stiffness, reported more than 20 years ago for the original qPlus sensor design. However, as we have shown, this can lead to wrong estimates, as the stiffness is used in the frequency shift-to-force conversion.

## Supporting Information

Supporting information features four files. File Supporting Information File 1 reminds the most salient results of the Euler–Bernoulli model and how it sustains the point-mass SHO equivalence. File Supporting Information File 2 reminds fundamental elements of signal processing applied to discrete time signals, among which the Power Spectral Density. File Supporting Information File 3 reminds the expression of the thermal noise PSD of a SHO in thermal equilibrium within a thermostat. The PSD of the stochastic thermal force giving rise to the fluctuations of the SHO is derived as well, which is used in the numerical simulations. File Supporting Information File 4 illustrates the influence of a digital antialiasing filter on the measured tn-PSD.

### Supporting Information File 1

The Euler–Bernoulli model and the point-mass SHO equivalence
[https://www.beilstein-journals.org/bjnano/content/supplementary/2190-4286-15-50-S1.pdf]

### Supporting Information File 2

Discrete Fourier transform and power spectral density of a discrete time signal
[https://www.beilstein-journals.org/bjnano/content/supplementary/2190-4286-15-50-S2.pdf]

### Supporting Information File 3

Power Spectral densities of a SHO and of the thermal force – Probability density function of the thermal force
[https://www.beilstein-journals.org/bjnano/content/supplementary/2190-4286-15-50-S3.pdf]

### Supporting Information File 4

Influence of a digital antialiasing filter on the measured tn-PSD
[https://www.beilstein-journals.org/bjnano/content/supplementary/2190-4286-15-50-S4.pdf]

## Acknowledgements

LN gratefully acknowledges Ludovic Bellon (ENS Lyon) for his advices about the numerical simulations. LN, SC and CL acknowledge Mélissa Hankache and Elie Geagea (IM2NP) for fruitful discussions and experimental support.

## Funding

The following source of funding is acknowledged: Agence Nationale de la Recherche (ANR Grants No. ANR-21-CE09-0002 “CROSS”, ANR-21-CE09-0004 “Light4Net” and ANR-21-CE09-0025 “Ganesh”).

## Author Contributions

Laurent Nony: conceptualization; data curation; formal analysis; funding acquisition; investigation; methodology; project administration; resources; software; supervision; validation; visualization; writing – original draft; writing – review & editing. Sylvain Clair: investigation; validation; writing – review & editing. Daniel Uehli: software; validation; writing – review & editing. Aitziber Herrero: software; validation; writing – review & editing. Jean-Marc Themlin: formal analysis; validation; writing – review & editing. Andrea Campos: investigation; validation; writing – review & editing. Franck Para: writing – review & editing. Alessandro Pioda: supervision; validation;

writing – review & editing. Christian Loppacher: writing – review & editing.

## ORCID® iDs

Laurent Nony - https://orcid.org/0000-0002-9211-4237
Sylvain Clair - https://orcid.org/0000-0002-8751-1887
Franck Para - https://orcid.org/0000-0002-0295-0451
Christian Loppacher - https://orcid.org/0000-0002-4853-6897

## Data Availability Statement

The data that supports the findings of this study is available from the corresponding author upon reasonable request.

## References

1. Morita, S.; Wiesendanger, R.; Meyer, E., Eds. *Noncontact Atomic Force Microscopy;* NanoScience and Technology, Vol. 1; Springer Berlin: Berlin, Germany, 2002. doi:10.1007/978-3-642-56019-4
2. Morita, S.; Giessibl, F. J.; Wiesendanger, R., Eds. *Noncontact Atomic Force Microscopy;* NanoScience and Technology, Vol. 2; Springer Berlin: Berlin, Germany, 2009. doi:10.1007/978-3-642-01495-6
3. Morita, S.; Giessibl, F. J.; Meyer, E.; Wiesendanger, R., Eds. *Noncontact Atomic Force Microscopy;* NanoScience and Technology, Vol. 3; Springer International Publishing: Cham, Switzerland, 2015. doi:10.1007/978-3-319-15588-3
4. Gross, L.; Mohn, F.; Moll, N.; Liljeroth, P.; Meyer, G. *Science* **2009,** *325,* 1110–1114. doi:10.1126/science.1176210
5. Clair, S.; de Oteyza, D. G. *Chem. Rev.* **2019,** *119,* 4717–4776. doi:10.1021/acs.chemrev.8b00601
6. Albrecht, F.; Fatayer, S.; Pozo, I.; Tavernelli, I.; Repp, J.; Peña, D.; Gross, L. *Science* **2022,** *377,* 298–301. doi:10.1126/science.abo6471
7. Mohn, F.; Gross, L.; Moll, N.; Meyer, G. *Nat. Nanotechnol.* **2012,** *7,* 227–231. doi:10.1038/nnano.2012.20
8. Mallada, B.; Gallardo, A.; Lamanec, M.; de la Torre, B.; Špirko, V.; Hobza, P.; Jelinek, P. *Science* **2021,** *374,* 863–867. doi:10.1126/science.abk1479
9. Stilp, F.; Bereczuk, A.; Berwanger, J.; Mundigl, N.; Richter, K.; Giessibl, F. J. *Science* **2021,** *372,* 1196–1200. doi:10.1126/science.abe2600
10. Nony, L.; Baratoff, A.; Schär, D.; Pfeiffer, O.; Wetzel, A.; Meyer, E. *Phys. Rev. B* **2006,** *74,* 235439. doi:10.1103/physrevb.74.235439
11. Giessibl, F. J. *Appl. Phys. Lett.* **2001,** *78,* 123–125. doi:10.1063/1.1335546
12. Giessibl, F. J. *Rev. Mod. Phys.* **2003,** *75,* 949–983. doi:10.1103/revmodphys.75.949
13. Sader, J. E.; Jarvis, S. P. *Appl. Phys. Lett.* **2004,** *84,* 1801–1803. doi:10.1063/1.1667267
14. Huber, F.; Giessibl, F. J. *J. Appl. Phys.* **2020,** *127,* 184301. doi:10.1063/5.0003291
15. Dagdeviren, O. E. *Rev. Sci. Instrum.* **2021,** *92,* 063703. doi:10.1063/5.0052126
16. Heile, D.; Olbrich, R.; Reichling, M.; Rahe, P. *Phys. Rev. B* **2021,** *103,* 075409. doi:10.1103/physrevb.103.075409
17. Giessibl, F. J.; Bielefeldt, H. *Phys. Rev. B* **2000,** *61,* 9968–9971. doi:10.1103/physrevb.61.9968
18. Simon, G. H.; Heyde, M.; Rust, H.-P. *Nanotechnology* **2007,** *18,* 255503. doi:10.1088/0957-4484/18/25/255503
19. Giessibl, F. J. *Rev. Sci. Instrum.* **2019,** *90,* 011101. doi:10.1063/1.5052264
20. Giessibl, F. J.; Pielmeier, F.; Eguchi, T.; An, T.; Hasegawa, Y. *Phys. Rev. B* **2011,** *84,* 125409. doi:10.1103/physrevb.84.125409
21. Sugimoto, Y.; Onoda, J. *Appl. Phys. Lett.* **2019,** *115,* 173104. doi:10.1063/1.5112062
22. Kirpal, D.; Qiu, J.; Pürckhauer, K.; Weymouth, A. J.; Metz, M.; Giessibl, F. J. *Rev. Sci. Instrum.* **2021,** *92,* 043703. doi:10.1063/5.0041369
23. Scienta Omicron: Danmarksgatan 22, 75323 Uppsala, Sweden. https://scientaomicron.com/en (accessed April 22, 2024).
24. SPECS GmbH: Berlin, Germany: https://www.specs-group.com/ (accessed April 22, 2024).
25. Torbrügge, S.; Schaff, O.; Rychen, J. *J. Vac. Sci. Technol., B: Nanotechnol. Microelectron.: Mater., Process., Meas., Phenom.* **2010,** *28,* C4E12–C4E20. doi:10.1116/1.3430544
26. Berger, J.; Spadafora, E. J.; Mutombo, P.; Jelínek, P.; Švec, M. *Small* **2015,** *11,* 3686–3693. doi:10.1002/smll.201500092
27. Huber, F.; Giessibl, F. J. *Rev. Sci. Instrum.* **2017,** *88,* 073702. doi:10.1063/1.4993737
28. cf. e.g. model HQA-15M-10T from Femto®. https://www.femto.de/en/products/current-amplifiers.html (accessed April 22, 2024).
29. Giessibl, F. J. *Appl. Phys. Lett.* **2000,** *76,* 1470–1472. doi:10.1063/1.126067
30. Giessibl, F. J. *Appl. Phys. Lett.* **1998,** *73,* 3956–3958. doi:10.1063/1.122948
31. Giessibl, F. J. *Appl. Phys. Lett.* **1999,** *74,* 4070. doi:10.1063/1.123265
32. Cleveland, J. P.; Manne, S.; Bocek, D.; Hansma, P. K. *Rev. Sci. Instrum.* **1993,** *64,* 403–405. doi:10.1063/1.1144209
33. Hutter, J. L.; Bechhoefer, J. *Rev. Sci. Instrum.* **1993,** *64,* 1868–1873. doi:10.1063/1.1143970
34. Butt, H.-J.; Siedle, P.; Seifert, K.; Fendler, K.; Seeger, T.; Bamberg, E.; Weisenhorn, A. L.; Goldie, K.; Engle, A. J. *J. Microsc. (Oxford, U. K.)* **1993,** *169,* 75–84. doi:10.1111/j.1365-2818.1993.tb03280.x
35. Butt, H.-J.; Jaschke, M. *Nanotechnology* **1995,** *6,* 1–7. doi:10.1088/0957-4484/6/1/001
36. Sader, J. E.; Larson, I.; Mulvaney, P.; White, L. R. *Rev. Sci. Instrum.* **1995,** *66,* 3789–3798. doi:10.1063/1.1145439
37. Gibson, C. T.; Watson, G. S.; Myhra, S. *Nanotechnology* **1996,** *7,* 259–262. doi:10.1088/0957-4484/7/3/014
38. Sader, J. E.; Chon, J. W. M.; Mulvaney, P. *Rev. Sci. Instrum.* **1999,** *70,* 3967–3969. doi:10.1063/1.1150021
39. Holbery, J. D.; Eden, V. L.; Sarikaya, M.; Fisher, R. M. *Rev. Sci. Instrum.* **2000,** *71,* 3769–3776. doi:10.1063/1.1289509
40. Burnham, N. A.; Chen, X.; Hodges, C. S.; Matei, G. A.; Thoreson, E. J.; Roberts, C. J.; Davies, M. C.; Tendler, S. J. B. *Nanotechnology* **2003,** *14,* 1–6. doi:10.1088/0957-4484/14/1/301
41. Green, C. P.; Lioe, H.; Cleveland, J. P.; Proksch, R.; Mulvaney, P.; Sader, J. E. *Rev. Sci. Instrum.* **2004,** *75,* 1988–1996. doi:10.1063/1.1753100
42. Hutter, J. L. *Langmuir* **2005,** *21,* 2630–2632. doi:10.1021/la047670t
43. Cook, S. M.; Schäffer, T. E.; Chynoweth, K. M.; Wigton, M.; Simmonds, R. W.; Lang, K. M. *Nanotechnology* **2006,** *17,* 2135–2145. doi:10.1088/0957-4484/17/9/010
44. Matei, G. A.; Thoreson, E. J.; Pratt, J. R.; Newell, D. B.; Burnham, N. A. *Rev. Sci. Instrum.* **2006,** *77,* 083703. doi:10.1063/1.2336115
45. Gates, R. S.; Reitsma, M. G. *Rev. Sci. Instrum.* **2007,** *78,* 086101. doi:10.1063/1.2764372

46. Cole, D. G. *Meas. Sci. Technol.* **2008,** *19,* 125101. doi:10.1088/0957-0233/19/12/125101
47. Chung, K.-H.; Shaw, G. A.; Pratt, J. R. *Rev. Sci. Instrum.* **2009,** *80,* 065107. doi:10.1063/1.3152335
48. Paolino, P.; Tiribilli, B.; Bellon, L. *J. Appl. Phys.* **2009,** *106,* 094313. doi:10.1063/1.3245394
49. Lozano, J. R.; Kiracofe, D.; Melcher, J.; Garcia, R.; Raman, A. *Nanotechnology* **2010,** *21,* 465502. doi:10.1088/0957-4484/21/46/465502
50. Gates, R. S.; Reitsma, M. G.; Kramar, J. A.; Pratt, J. R. *J. Res. Natl. Inst. Stand. Technol.* **2011,** *116,* 703–727. doi:10.6028/jres.116.015
51. Lübbe, J.; Doering, L.; Reichling, M. *Meas. Sci. Technol.* **2012,** *23,* 045401. doi:10.1088/0957-0233/23/4/045401
52. Sader, J. E.; Sanelli, J. A.; Adamson, B. D.; Monty, J. P.; Wei, X.; Crawford, S. A.; Friend, J. R.; Marusic, I.; Mulvaney, P.; Bieske, E. J. *Rev. Sci. Instrum.* **2012,** *83,* 103705. doi:10.1063/1.4757398
53. Sader, J. E.; Hughes, B. D.; Sanelli, J. A.; Bieske, E. J. *Rev. Sci. Instrum.* **2012,** *83,* 055106. doi:10.1063/1.4709496
54. Grutzik, S. J.; Gates, R. S.; Gerbig, Y. B.; Smith, D. T.; Cook, R. F.; Zehnder, A. T. *Rev. Sci. Instrum.* **2013,** *84,* 113706. doi:10.1063/1.4832978
55. Laurent, J.; Steinberger, A.; Bellon, L. *Nanotechnology* **2013,** *24,* 225504. doi:10.1088/0957-4484/24/22/225504
56. Lübbe, J.; Temmen, M.; Rahe, P.; Kühnle, A.; Reichling, M. *Beilstein J. Nanotechnol.* **2013,** *4,* 227–233. doi:10.3762/bjnano.4.23
57. Borysov, S. S.; Forchheimer, D.; Haviland, D. B. *Beilstein J. Nanotechnol.* **2014,** *5,* 1899–1904. doi:10.3762/bjnano.5.200
58. Sader, J. E.; Borgani, R.; Gibson, C. T.; Haviland, D. B.; Higgins, M. J.; Kilpatrick, J. I.; Lu, J.; Mulvaney, P.; Shearer, C. J.; Slattery, A. D.; Thorén, P.-A.; Tran, J.; Zhang, H.; Zhang, H.; Zheng, T. *Rev. Sci. Instrum.* **2016,** *87,* 093711. doi:10.1063/1.4962866
59. Labuda, A.; Kocun, M.; Lysy, M.; Walsh, T.; Meinhold, J.; Proksch, T.; Meinhold, W.; Anderson, C.; Proksch, R. *Rev. Sci. Instrum.* **2016,** *87,* 073705. doi:10.1063/1.4955122
60. Labuda, A.; Cao, C.; Walsh, T.; Meinhold, J.; Proksch, R.; Sun, Y.; Filleter, T. *Rev. Sci. Instrum.* **2018,** *89,* 093701. doi:10.1063/1.5045679
61. https://sadermethod.org/ (accessed April 22, 2024).
62. Rychen, J.; Ihn, T.; Studerus, P.; Herrmann, A.; Ensslin, K.; Hug, H. J.; van Schendel, P. J. A.; Güntherodt, H. J. *Appl. Surf. Sci.* **2000,** *157,* 290–294. doi:10.1016/s0169-4332(99)00541-3
63. Rychen, J.; Ihn, T.; Studerus, P.; Herrmann, A.; Ensslin, K.; Hug, H. J.; van Schendel, P. J. A.; Güntherodt, H. J. *Rev. Sci. Instrum.* **2000,** *71,* 1695–1697. doi:10.1063/1.1150521
64. Berger, J.; Švec, M.; Müller, M.; Ledinský, M.; Fejfar, A.; Jelínek, P.; Majzik, Z. *Beilstein J. Nanotechnol.* **2013,** *4,* 1–9. doi:10.3762/bjnano.4.1
65. Falter, J.; Stiefermann, M.; Langewisch, G.; Schurig, P.; Hölscher, H.; Fuchs, H.; Schirmeisen, A. *Beilstein J. Nanotechnol.* **2014,** *5,* 507–516. doi:10.3762/bjnano.5.59
66. Kim, J.; Won, D.; Sung, B.; An, S.; Jhe, W. *Ultramicroscopy* **2014,** *141,* 56–62. doi:10.1016/j.ultramic.2014.03.009
67. Melcher, J.; Stirling, J.; Shaw, G. A. *Beilstein J. Nanotechnol.* **2015,** *6,* 1733–1742. doi:10.3762/bjnano.6.177
68. Sader, J. E. *Rev. Sci. Instrum.* **1995,** *66,* 4583–4587. doi:10.1063/1.1145292
69. Yamada, Y.; Ichii, T.; Utsunomiya, T.; Kimura, K.; Kobayashi, K.; Yamada, H.; Sugimura, H. *Nanoscale Adv.* **2023,** *5,* 840–850. doi:10.1039/d2na00686c
70. Elmer, F.-J.; Dreier, M. *J. Appl. Phys.* **1997,** *81,* 7709–7714. doi:10.1063/1.365379
71. Hutter, J. L.; Bechhoefer, J. *J. Appl. Phys.* **1993,** *73,* 4123–4129. doi:10.1063/1.352845
72. Nyquist, H. *Phys. Rev.* **1928,** *32,* 110–113. doi:10.1103/physrev.32.110
73. Johnson, J. B. *Phys. Rev.* **1928,** *32,* 97–109. doi:10.1103/physrev.32.97
74. Kubo, R. *Rep. Prog. Phys.* **1966,** *29,* 255–284. doi:10.1088/0034-4885/29/1/306
75. Coleman, P. 9 – Fluctuation-dissipation theorem and linear response theory. *Introduction to Many-Body Physics;* Cambridge University Press, 2015; pp 292–331. doi:10.1017/cbo9781139020916.011
76. Melcher, J.; Hu, S.; Raman, A. *Appl. Phys. Lett.* **2007,** *91,* 053101. doi:10.1063/1.2767173
77. Rayleigh, J. W. S. *The theory of sound;* New York, Dover, 1945. doi:10.1017/cbo9781139058087
78. Neumeister, J. M.; Ducker, W. A. *Rev. Sci. Instrum.* **1994,** *65,* 2527–2531. doi:10.1063/1.1144646
79. Hazel, J. L.; Tsukruk, V. V. *J. Tribol.* **1998,** *120,* 814–819. doi:10.1115/1.2833784
80. Hazel, J. L.; Tsukruk, V. V. *Thin Solid Films* **1999,** *339,* 249–257. doi:10.1016/s0040-6090(98)00961-4
81. Stark, R. W.; Drobek, T.; Heckl, W. M. *Ultramicroscopy* **2001,** *86,* 207–215. doi:10.1016/s0304-3991(00)00077-2
82. Espinoza-Beltrán, F. J.; Geng, K.; Muñoz Saldaña, J.; Rabe, U.; Hirsekorn, S.; Arnold, W. *New J. Phys.* **2009,** *11,* 083034. doi:10.1088/1367-2630/11/8/083034
83. Nony, L.; Bocquet, F.; Para, F.; Loppacher, C. *Phys. Rev. B* **2016,** *94,* 115421. doi:10.1103/physrevb.94.115421
84. Friedt, J.-M.; Carry, É. *Am. J. Phys.* **2007,** *75,* 415–422. doi:10.1119/1.2711826
85. Labuda, A.; Lysy, M.; Paul, W.; Miyahara, Y.; Grütter, P.; Bennewitz, R.; Sutton, M. *Phys. Rev. E* **2012,** *86,* 031104. doi:10.1103/physreve.86.031104
86. Labuda, A.; Lysy, M.; Grütter, P. *Appl. Phys. Lett.* **2012,** *101,* 113105. doi:10.1063/1.4745781
87. Kawai, S.; Glatzel, T.; Such, B.; Koch, S.; Baratoff, A.; Meyer, E. *Phys. Rev. B* **2012,** *86,* 245419. doi:10.1103/physrevb.86.245419
88. Wilkie, J. *Phys. Rev. E* **2004,** *70,* 017701. doi:10.1103/physreve.70.017701
89. Burrage, K.; Burrage, P.; Higham, D. J.; Kloeden, P. E.; Platen, E. *Phys. Rev. E* **2006,** *74,* 068701. doi:10.1103/physreve.74.068701
90. Sader, J. E.; Yousefi, M.; Friend, J. R. *Rev. Sci. Instrum.* **2014,** *85,* 025104. doi:10.1063/1.4864086
91. Dagdeviren, O. E.; Miyahara, Y.; Mascaro, A.; Enright, T.; Grütter, P. *Sensors* **2019,** *19,* 4510. doi:10.3390/s19204510
92. Lübbe, J.; Tröger, L.; Torbrügge, S.; Bechstein, R.; Richter, C.; Kühnle, A.; Reichling, M. *Meas. Sci. Technol.* **2010,** *21,* 125501. doi:10.1088/0957-0233/21/12/125501
93. Labuda, A.; Miyahara, Y.; Cockins, L.; Grütter, P. H. *Phys. Rev. B* **2011,** *84,* 125433. doi:10.1103/physrevb.84.125433

BEILSTEIN JOURNAL OF NANOTECHNOLOGY

# AFM-IR investigation of thin PECVD $SiO_x$ films on a polypropylene substrate in the surface-sensitive mode

Hendrik Müller[1], Hartmut Stadler[2], Teresa de los Arcos[1], Adrian Keller[1] and Guido Grundmeier[*1]

Full Research Paper

Open Access

Address:
[1]Technical and Macromolecular Chemistry, Paderborn University, Warburger Str. 100, 33098 Paderborn, Germany and [2]Bruker Nano Surfaces and Metrology Division, Östliche Rheinbrückenstr. 49, 76187 Karlsruhe, Germany

Email:
Guido Grundmeier[*] - guido.grundmeier@uni-paderborn.de

* Corresponding author

Keywords:
AFM-IR; polypropylene; surface-sensitive mode; silicon oxide; thin films; XPS

*Beilstein J. Nanotechnol.* **2024,** *15,* 603–611.
https://doi.org/10.3762/bjnano.15.51

Received: 31 January 2024
Accepted: 02 May 2024
Published: 24 May 2024

This article is part of the thematic issue "Advanced atomic force microscopy techniques V".

Guest Editor: I. Bald



## Abstract

Thin silicon oxide films deposited on a polypropylene substrate by plasma-enhanced chemical vapor deposition were investigated using atomic force microscopy-based infrared (AFM-IR) nanospectroscopy in contact and surface-sensitive mode. The focus of this work is the comparison of the different measurement methods (i.e., contact mode and surface-sensitive mode) with respect to the chemical surface sensitivity. The use of the surface-sensitive mode in AFM-IR shows an enormous improvement for the analysis of thin films on the IR-active substrate. As a result, in this mode, the signal of the substrate material could be significantly reduced. Even layers that are so thin that they could hardly be measured in the contact mode can be analyzed with the surface-sensitive mode.

## Introduction

Photothermal AFM-IR nanospectroscopy is a technique that combines the chemical information from infrared (IR) spectroscopy with the high spatial resolution of atomic force microscopy (AFM). For this, the sample is illuminated with a tunable IR laser [1]. When a suitable IR wavelength is chosen, resonant absorption of IR photons results in molecular vibrations in the material under investigation. This photon absorption also causes the thermal expansion of the material. The resulting photothermally generated tip–sample force is measured via changes in the deflection signal of the AFM cantilever. The correlation between the IR wavelength of the laser and the thermal expansion of the material enables the recording of IR absorption spectra with this technique which correspond to the spectra of bulk IR spectroscopy [2-4]. Compared to ATR-FTIR spectroscopy, AFM-IR provides a drastic improvement in terms of spatial resolution. In ATR-IR spectroscopy, the resolution is theoretically limited by λ/2, which corresponds to several µm [3]. In contrast, the development of new and powerful tunable IR laser

sources, such as optical parametric oscillator (OPO) and quantum cascade lasers (QCL), enabled a nanoscale resolution of AFM-IR down to 10 nm [3]. Nowadays, the limit of the spatial resolution is given by the apex of the AFM tip.

One of the first AFM-IR demonstrations was reported in 2005 by Dazzi et al. [4], who presented AFM-IR spectra of single bacterial cells. Further on, this technique became more refined and found its way into many and highly diverse fields of application, including virology, DNA nanotechnology, polymer science, and materials science [5-9]. The importance of AFM-IR steadily grew over the past decade and its development has been described in detail in several review papers [1,3,9,10].

A general restriction of AFM-IR is its rather large depth of information, which depends on the sample structure and the chosen measurement mode such as contact mode or tapping mode. In general, the incident IR light excites a large volume of material beneath the AFM tip, and the tip–sample force generated by the thermal expansion of the total excited volume is detected. This makes it very challenging to characterize thin films with a small thermal expansion coefficient (e.g., inorganic oxides) deposited on bulk materials with a large thermal expansion coefficient (e.g., polymers). To tackle this problem, the surface-sensitive mode was developed.

## Surface-sensitive AFM-IR

Surface-sensitive AFM-IR mode [10] operates in contact mode on the absorbing sample and utilizes nonlinear frequency mixing of IR-laser-induced photothermal and an additional dither piezo-induced mechanical surface excitation at two different frequencies schematically shown in Figure 1. Due to their different propagation characteristics in the material, the evanescent mechanical waves created by these two processes can only interact in a small volume directly beneath the tip (typically to a depth of less than 10–30 nm below the top surface).

As this is a higher-order nonlinear effect, the resulting tip–surface force is very small compared to that of classical contact-mode-based AFM-IR techniques, such as the ring-down method or resonance-enhanced AFM-IR, where the photothermal tip–sample force can be measured in a first-order detection scheme with or without additional resonance enhancement. However, it contains chemical information from a much larger depth (hundreds of nanometers to several micrometers). If the difference or sum of freely selectable laser pulse repetition frequency and mechanical modulation (i.e., drive frequency) in surface-sensitive AFM-IR mode equals a mechanical resonance of the tip–surface contact, sufficient IR signal enhancement can be obtained at this frequency (i.e., detection frequency). This is used to measure the IR signature of thin material sections close to the top surface without (or at least with severely limited) contributions from the bulk. In this description scheme, surface-sensitive AFM-IR shows similarities to the tapping-mode-based AFM-IR technique (i.e., the transduction of the IR absorption via nonlinear frequency mixing of photothermal and piezo-induced sample excitation). However, it is much more flexible in the choice of the drive and detection frequencies, as only the mixing frequency needs to match a system resonance and not the individual frequencies themselves.

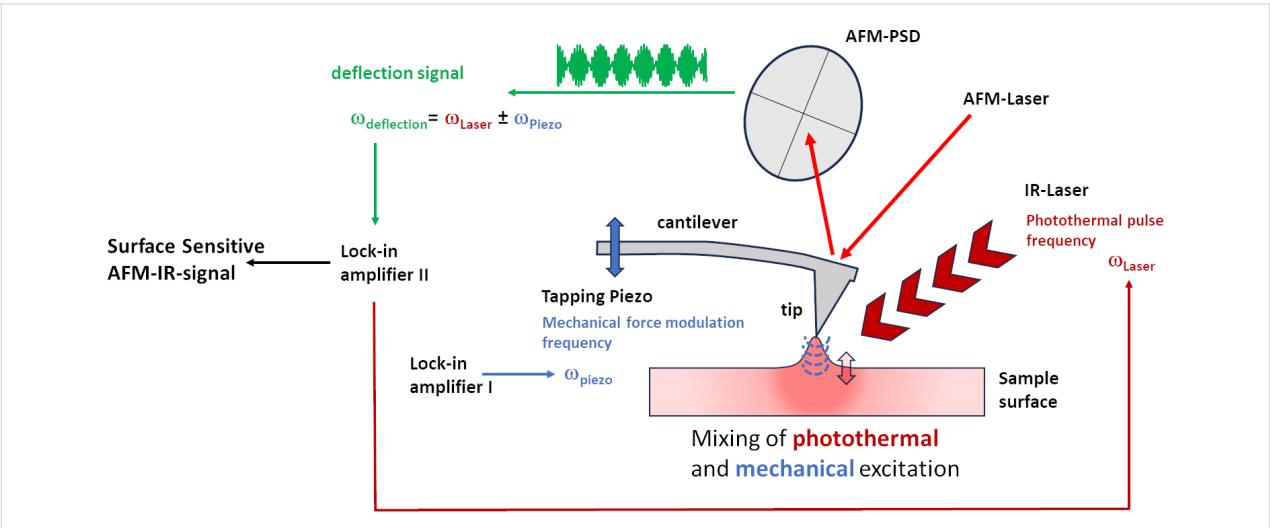


**Figure 1:** Detection scheme in surface-sensitive AFM-IR mode. Photothermal and mechanical surface excitation is achieved by driving the dither piezo and the IR laser source with two lock-in amplifiers. Nonlinear coupling of these processes in a small volume underneath the tip generates a surface expansion behavior containing the mixing frequencies, which are transferred into the cantilever deflection. Either the sum (C+M) or difference (C–M) frequency is chosen for detection. The chosen detection frequency should equal a mechanical contact resonance of the tip–sample contact for a sufficiently large signal level.

Here, we use AFM-IR in the surface-sensitive mode to investigate thin silicon oxide films on polypropylene substrates. Polypropylene is widely used as packaging material [11] and in other industrial applications [12-14]; however, it is commonly known for its poor gas barrier properties [11,13]. Therefore, silicon oxide coatings are used to improve the gas barrier properties [13]. In this study thin coatings of $SiO_x$ were deposited by plasma-enhanced chemical vapor deposition (PECVD) in an oxygen-rich plasma process with hexamethyldisiloxane (HMDSO) used as monomer. With this process, the thickness of the coating can be controlled and homogeneous films can be produced [15].

# Experimental

## Materials and chemicals

The substrates used were polypropylene foils (LyondellBasell, Moplen Hp640J) onto which a thin layer of $SiO_x$ was deposited by PECVD. Therefore, the samples were placed onto the grounded electrode. The basis pressure was below $5 \times 10^{-5}$ mbar and the working pressure ranged between 0.2 and 0.5 mbar. As the gas mixture, argon, oxygen, and HMDSO (98.5% purity, Sigma-Aldrich) were used in different ratios. First, the surface was pretreated for five seconds with an oxygen-rich plasma. For this step, the argon-to-oxygen ratio was set to 1:2. For the deposition of silicon oxide, the partial pressure of argon was set to 0.1 mbar and the partial pressure of oxygen was set to 0.3 mbar. The monomer partial pressure was set to 0.05 mbar. The high partial pressure of oxygen in a ratio of 3:1 promotes the formation of $SiO_x$ structures.

The film thickness was measured with a quartz crystal microbalance (QCM) during deposition. Samples were prepared with a $SiO_x$ thickness of 5 nm and 50 nm. The PECVD process is described elsewhere [16].

## Surface and thin film analysis

The infrared spectroscopic studies were performed using an Anasys NanoIR 3s system from Bruker Nano GmbH, Germany, equipped with a broadband Carmina OPO Laser (Angewandte Physik & Elektronik GmbH, Germany). Contact Mode NIR2 cantilevers from Anasys Instruments (PR-EX-nIR2-10) were used. The samples were first scanned in contact mode with a resolution between 512 × 256 and 256 × 256 pixels and an image size between 10 µm × 5 µm and 5 µm × 5 µm. In the AFM images, we selected a suitable spot to optimize the laser parameters. After the alignment of the laser, the pulse frequency was tuned. For the measurements in contact mode, the frequency was set to 69 kHz and, for the surface-sensitive mode, the second eigenmode of the cantilever was used as detection mode at 205 kHz. The drive mode was set to 845 kHz, which equals a higher contact resonance mode. The spectra were collected with a spectral resolution of 4 $cm^{-1}$, and the phase-locked loop (PLL) was disabled for collecting the spectra.

In addition to these, measurements were performed comparing contact mode measurements, collected at a laser frequency tuned to the contact resonance mode of 771 kHz, and surface-sensitive measurements with the drive mode set to 764 kHz, the detection mode to 195 kHz, and the laser pulse was tuned to 566 kHz. Therefore, the sample with a 5 nm $SiO_x$ coating was used and, additionally to the AFM-IR spectra, a hyperspectral image was collected in contact mode.

In addition to photothermal AFM-IR measurements in contact mode and surface-sensitive mode, the surface was analyzed with near-ambient pressure X-ray photoelectron spectroscopy (NAP-XPS) using a NAP-XPS system with a Phoibos150 NAP analyzer from Specs Surface Nano Analysis GmbH. The setup has a µ-FOCUS 600 X-ray monochromator NAP source working with monochromatic Al Kα radiation at 1468.7 eV. The power was set to 50 W for all measurements. For the environmental charge compensation of the isolating polymer foils, the measurement was carried out in a 1.5 mbar $N_2$ atmosphere. The survey spectra were recorded with a pass energy of 100 eV, while the core level spectra were taken with a 40 eV pass energy. The analysis was done using the software Unifit 2019 [17]. For all core level spectra, a Shirley type background was used. The Si 2p peak was fitted with doublet peaks with a Si $2p_{3/2\text{-}1/2}$ splitting of 0.6 eV [18].

# Results and Discussion

## XPS analysis

The XPS data in Figure 2 and Figure 3 show that the deposition of silicon oxide thin films was successful. In the survey spectra, the peaks of oxygen, nitrogen, carbon, and silicon are visible. The N 1s peak originates from the nitrogen atmosphere which was used for the environmental charge compensation [18]. The C 1s peak can be assigned to adventitious carbon for the sample with a 50 nm $SiO_x$ layer. For the sample with a 5 nm $SiO_x$ layer, the C 1s is a mixture of adventitious carbon and the signal from the underlying polypropylene substrate.

The core levels of O 1s, C 1s, and Si 2p are shown in Figure 2 and Figure 3. In the figures, the spectra are arbitrarily charge corrected by fixing the binding energy of the Si 2p peak at 103.5 eV, which approximately corresponds to silicon oxide [19]. However, due to the impossibility to fix the BE scale in this case due to the nonconducting nature of the samples [20], the chemical identification of the oxide film is done by evaluation of the BE difference between the O 1s and Si 2p peaks. The O 1s–Si 2p distance is 429.6 eV for the 50 nm film and 429.9 eV for the 5 nm film. This is in good agreement with

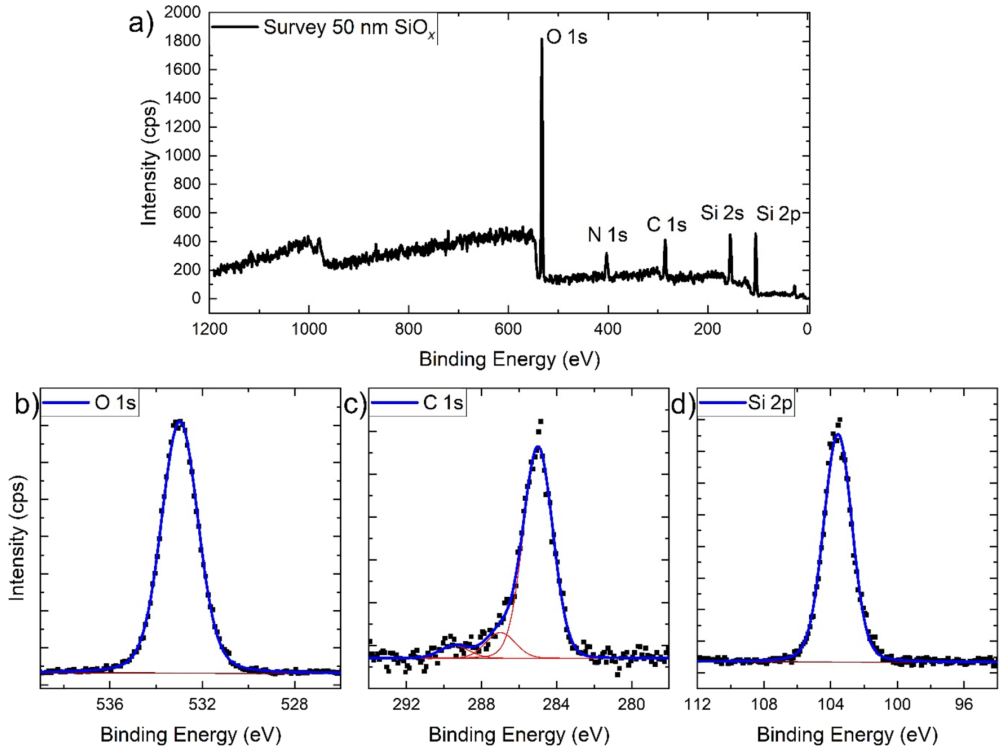


**Figure 2:** NAP-XPS survey (a) and high-resolution core level spectra of oxygen O 1s (b), carbon C 1s, (c) and silicon Si 2p (d) of the polypropylene foil covered with 50 nm $SiO_x$ measured in a 1.5 mbar $N_2$ atmosphere for environmental charge compensation. Black dots represent measured data, while the blue lines are fits to the data that incorporate different components as indicated by the red lines.

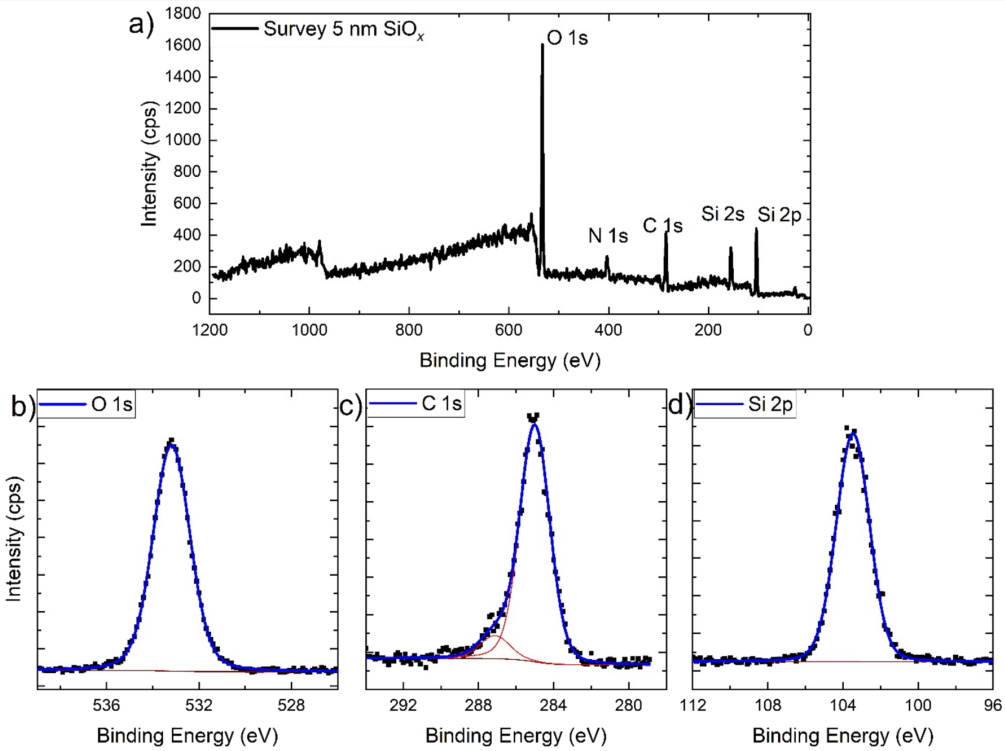


**Figure 3:** NAP-XPS survey (a) and high-resolution core level spectra of oxygen O 1s (b), carbon C 1s, (c) and silicon Si 2p (d) of the polypropylene foil covered with 5 nm $SiO_x$ measured in a 1.5 mbar $N_2$ atmosphere for environmental charge compensation. Black dots represent measured data, while the blue lines are fits to the data that incorporate different components as indicated by the red lines.

values found in the literature for the PECVD deposition of $SiO_x$ films from HMDSO/$O_2$/Ar gas mixtures [21]. A comparison of the relative intensities of the O 1s and Si 2p peaks of the two samples (shown in Table 1) additionally supports the result that the chemistry of both $SiO_x$ layers is the same.

**Table 1:** Quantification of the surface composition of the silicon oxide films on the polypropylene foil.

| Sample | O 1s–Si 2p (eV) | Relative areas [%] |
|---|---|---|
| 50 nm $SiO_x$ | 429.6 | 64 |
| | | 36 |
| 5 nm $SiO_x$ | 429.9 | 65 |
| | | 35 |

## AFM-IR analysis

The prepared samples were analyzed by photothermal AFM-IR. First, AFM images were collected in contact mode to visualize the sample surface (Figure 4). In the image of the sample with the 50 nm $SiO_x$ layer (Figure 4a), a column-like grown $SiO_x$ film is visible. The surface became rougher. In addition to that, small cracks in the $SiO_x$ layer are recognizable. These cracks were induced by uniaxial stretching of about 10%. The topography of the 5 nm sample (Figure 4b) shows a smooth surface with elevations and valleys. These occur from the used polypropylene foil.

The photothermal AFM-IR spectra in contact and surface-sensitive mode were collected at the spots marked in the AFM images, shown in Figure 4. The resulting spectra are shown in Figure 5 (contact mode) and Figure 6 (surface-sensitive mode). The spectra are normalized for a better comparison.

The contact mode AFM-IR spectra in Figure 5 show peaks according to $CH_3$ asymmetric deformation vibration and $CH_2$ bending at 1455 $cm^{-1}$, $CH_3$ symmetric deformation vibration at 1376 $cm^{-1}$, and $CH_3$ rocking bands at 1168 $cm^{-1}$, all of which originate from the polymer foil [21,22]. In the spectra of the sample with a 50 nm $SiO_x$ film, a broad peak occurs around 1080 $cm^{-1}$, which corresponds to Si–O–Si transversal oscillation modes [23-25]. In contrast, the sample with the thin $SiO_x$ film shows no broad peak around 1080 $cm^{-1}$. Nevertheless, the XPS spectra in Figure 3 have shown that the $SiO_x$ deposition was successful. Therefore, these results indicate that the sensitivity limit of photothermal AFM-IR spectroscopy in contact mode is reached due to the small thickness of the deposited $SiO_x$ film.

To improve the chemical sensitivity of the 5 nm $SiO_x$ film, the surface-sensitive mode was employed (see Figure 6). Here, photothermal AFM-IR spectra were collected on the same samples; however, this time a drive frequency of 847 kHz and a detection frequency of 205 kHz were used. In addition, the laser was tuned to 646 kHz.

The surface-sensitive mode AFM-IR spectra in Figure 6 show a high intensity in the area between 1000 and 1200 $cm^{-1}$, while the intensity of the $CH_3$ and $CH_2$ absorption bands at 1455 $cm^{-1}$ and 1376 $cm^{-1}$ weakened. In the surface-sensitive mode, the measured signal contains less information of the

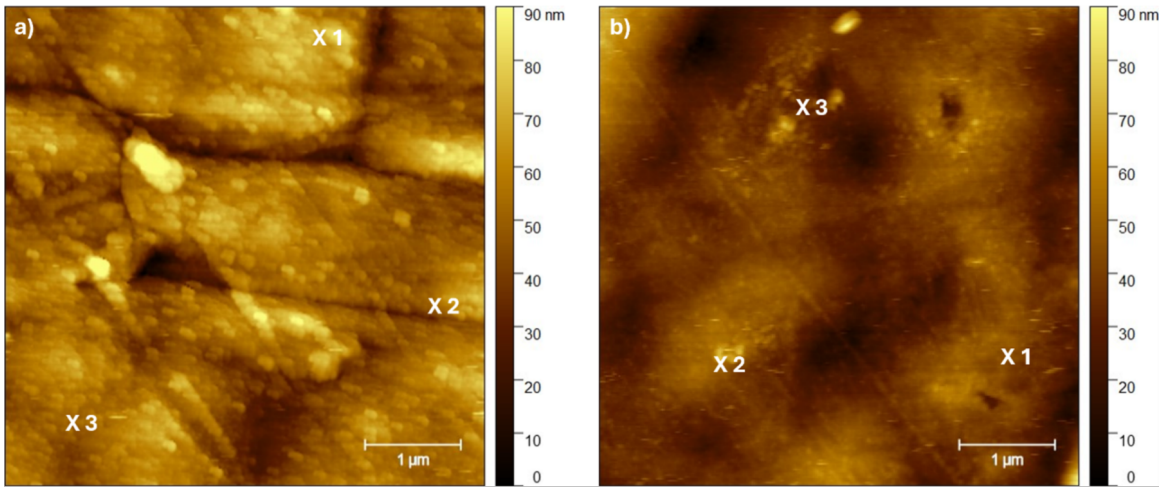


**Figure 4:** AFM height images of the polypropylene foil covered with 50 nm (a) and 5 nm $SiO_x$ film (b). The highlighted spots in the images represent the spots where the surface-sensitive AFM-IR spectra were recorded.

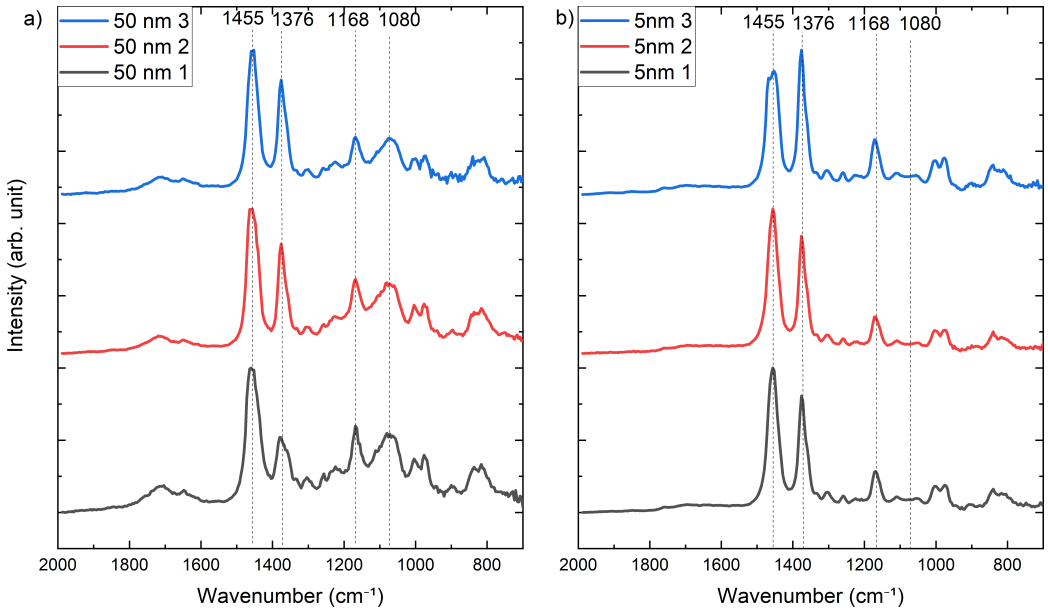


**Figure 5:** Contact mode AFM-IR spectra of each of the polypropylene samples with 50 nm (a) and 5 nm $SiO_x$ (b) recorded in the AFM image in Figure 4.

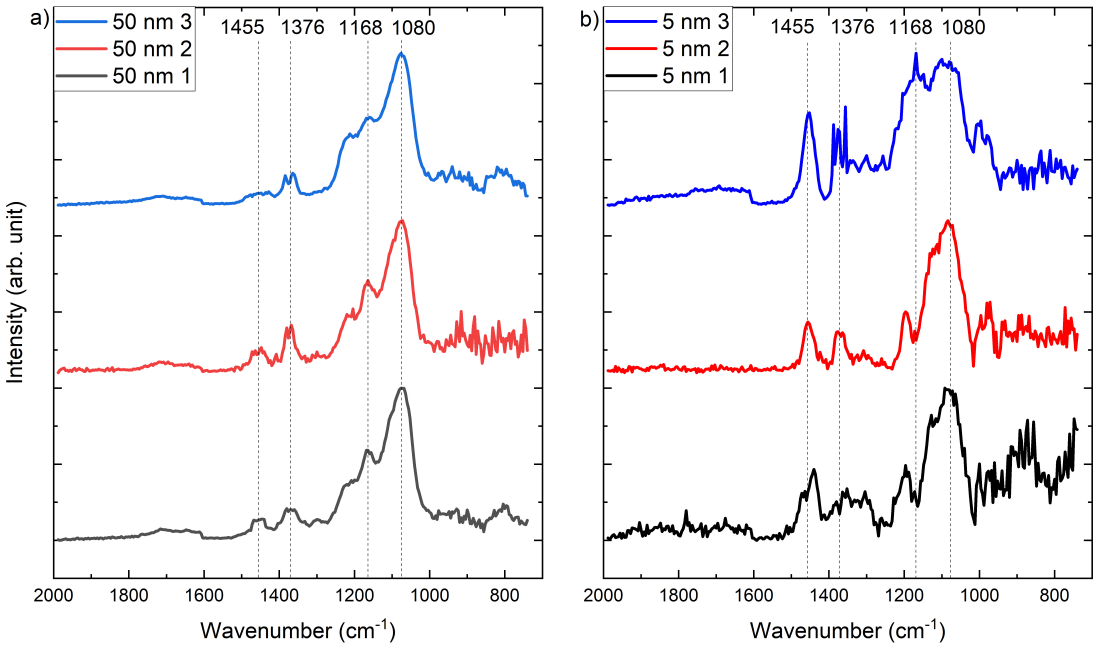


**Figure 6:** Surface-sensitive mode AFM-IR spectra of each of the polypropylene samples with 50 nm (a) and 5 nm thin PECVD $SiO_x$ film (b) recorded in the AFM image in Figure 4.

deeper bulk phase of the substrate and more information of the near-surface region. In samples with a thicker layer of $SiO_x$, this results in an improved signal-to-noise ratio. Even though the spectra of the sample with a low $SiO_x$ thickness still show sizable peaks originating from the substrate underneath the $SiO_x$ layer, improved surface sensitivity is achieved for both samples.

Upon a closer look at the spectra, the broad peak corresponding to the TO Si–O–Si vibration at 1080 $cm^{-1}$ can be clearly identified and even dominate the overall spectra [23,26].

The peak at 1168 $cm^{-1}$ corresponding to the $CH_3$ rocking is superposed to the broad Si–O–Si band, as can be seen in all

spectra measured for the sample with the 50 nm $SiO_x$ layer. Interestingly, this peak appears as a negative peak in some of the spectra measured for the 5 nm $SiO_x$ sample (spectra 1 and 2) of the sample with a 5 nm $SiO_x$ layer (Figure 6b, black and red spectra). It is unclear at present whether this effect is due to a tip-induced artifact.

It is interesting to note that the relative intensity of the polypropylene band at 1455 $cm^{-1}$ decreases when the 50 nm $SiO_x$ sample is measured in the surface-sensitive mode. The relative intensity of this band increases again in the measurement of the 5 nm $SiO_x$ layer. The results seem to indicate that the band at 1455 $cm^{-1}$ could be associated to bulk regions within the polypropylene, further away from the interface to the $SiO_x$.

To highlight the advantage of the surface-sensitive mode and to show the homogeneity of the coating, further measurements on the sample with the 5 nm $SiO_x$ coating were performed. Therefore, a comparison of surface-sensitive AFM-IR using contact mode AFM-IR and with the laser tuned to a higher contact resonance mode for a higher surface sensitivity was done.

The topography image in Figure 7a shows a surface with elevations and valleys. The hyperspectral measurement of this area indicates an overall signal of the Si–O–Si stretching band at 1080 $cm^{-1}$ with some islands with a higher intensity. These can originate from small differences in the film thickness. The hyperspectral image (Figure 7c) shows the ratio of the Si–O–Si stretching band at 1080 $cm^{-1}$ (blue) and the absorption band according to the $CH_3$ asymmetric deformation vibration and the

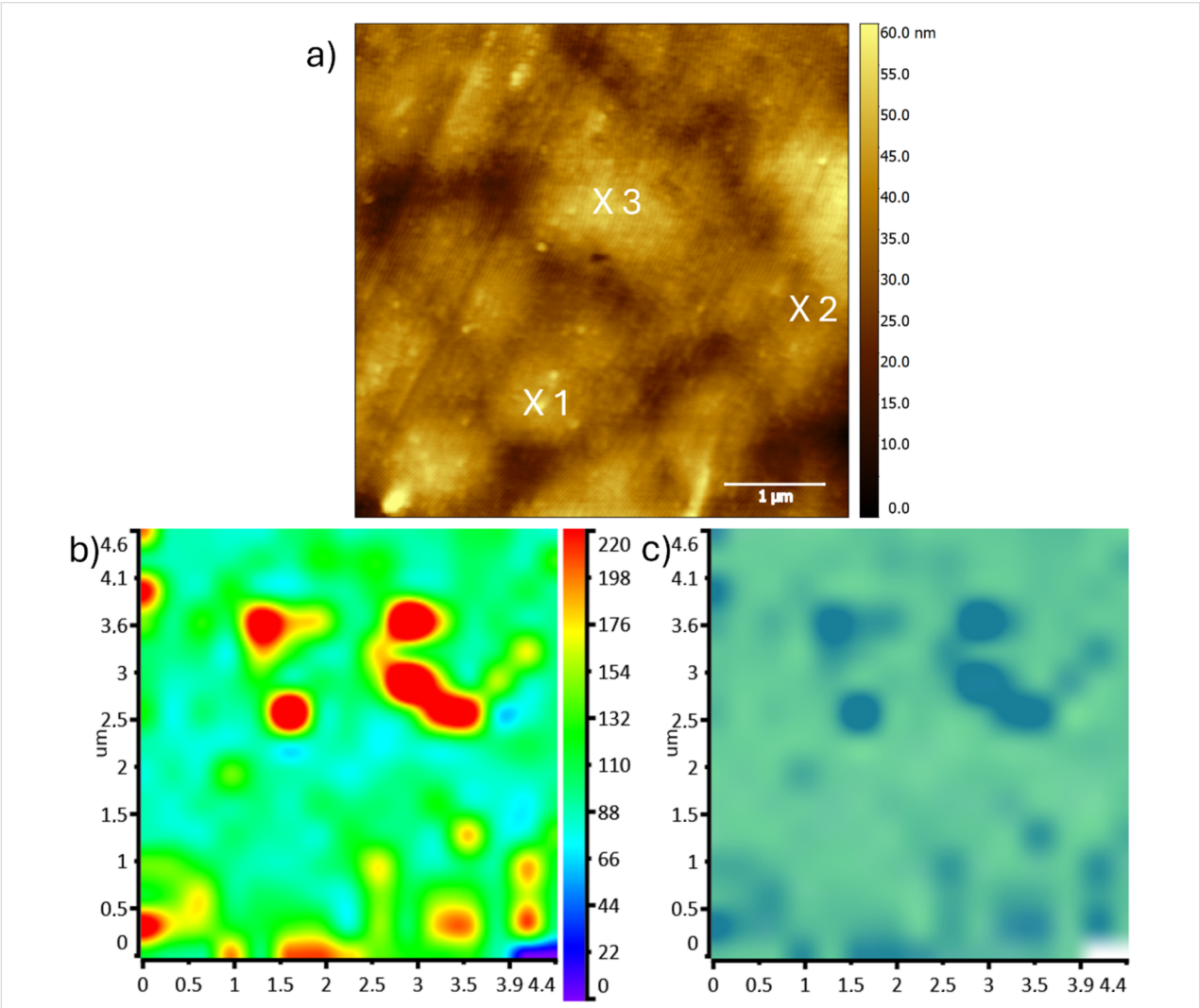


**Figure 7:** a) Height image recorded in contact mode of the investigated area of the 5 nm thin $SiO_x$ film coated sample. The markings in this image correspond to the spots where the AFM-IR spectra were collected. Images b) and c) show the hyperspectral image of the area measured with 15 × 15 single IR-spectra recorded with a laser pulse tuned to 771 kHz in contact mode. Image b) shows the intensity distribution of the 1080 $cm^{-1}$ absorption band. In image c) the intensity ratio of the absorption bands at 1080 $cm^{-1}$ (blue) and 1455 $cm^{-1}$ (green) are shown.

$CH_2$ bending at 1455 $cm^{-1}$ (green). As expected, the intensity of the polypropylene peak over the full image is more intense. It must be noted that, at the end of the measurement, the last two spectra showed no signal which can be seen in the hyperspectral images in the lower right corner.

In addition to the hyperspectral image, single AFM-IR spectra were recorded at selected spots shown in Figure 7a. Here, the spectra were collected in surface-sensitive mode with a drive frequency of 764 kHz and a detection frequency of 195 kHz. The laser pulse was tuned to 566 kHz, as well as in contact mode with a laser pulsed corresponding to the higher contact resonance mode at 771 kHz. The images reveal that at such small thickness the film is not perfectly homogeneous.

The AFM-IR spectra in Figure 8a show the measurement in contact mode. The peaks corresponding to the polypropylene substrate at 1455 $cm^{-1}$, 1376 $cm^{-1}$, and 1168 $cm^{-1}$ are clearly visible. Additionally, in these measurements with the laser pulse tuned to 771 kHz, the peak of the Si–O–Si layer at 1080 $cm^{-1}$ is also detectable. This is a significant improvement compared to the previous spectra recorded in contact mode where the laser pulse was set to 69 kHz. Nevertheless, the spectra in Figure 8b were recorded in surface-sensitive mode and show the potential of this technique. The signal of the 5 nm thin $SiO_x$ layer has increased enormously. These measurements show the high sensitivity of this technique by detecting even 5 nm ultra-thin coatings on top of a polymeric substrate. This effect could have been supported by the choice of substrate material as shown in the work of Rosenberger et al. [27], where a polymeric substrate supports the sensitivity of AFM-IR detecting thin carbon nanotubes. Nevertheless, the system shown here is not completely transferable, as samples with a continuous coating were examined in this study.

These results highlight the potential of the AFM-IR surface-sensitive mode for the investigation of ultra-thin films and the interfaces to the supporting materials.

## Conclusion

The benefits of the surface-sensitive mode in the AFM-IR characterization of thin PECVD $SiO_x$ films on polymer substrates were investigated in this study. Our results exemplify the enormous improvements in thin film sensitivity that can be achieved by this mode in comparison to the established contact mode measurements. While the measurements in contact mode were dominated by the signal of the polypropylene substrate, we were able to record clear and well-defined signals of the $SiO_x$ thin films in surface-sensitive mode. This way, we were able to record AFM-IR spectra of a 5 nm thin PECVD $SiO_x$ layer grown on the polypropylene substrate.

AFM-IR enabled for the first time the analysis of PECVD $SiO_x$ thin film inhomogeneities during the initial layer growth.

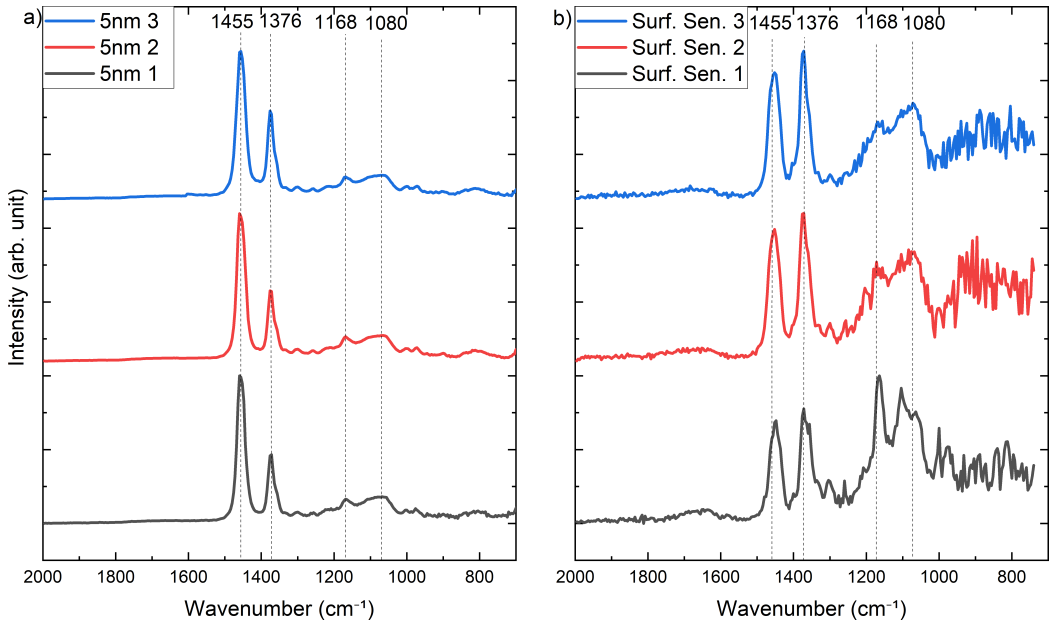


**Figure 8:** AFM-IR spectra collected in contact mode with a laser pulse frequency of 771 kHz corresponding to the fourth eigenmode frequency of the cantilever (a). In b) the AFM-IR spectra collected in surface-sensitive mode with a drive frequency of 764 kHz, a detection frequency of 195 kHz, and a laser pulse frequency of 566 kHz are shown.

Overall, this work demonstrates the significant improvement in sensitivity of the surface-sensitive mode for AFM-IR near-surface measurements of thin films.

## Funding

This work was financially supported by the German Research Foundation (DFG) within the project "Functional PECVD coatings as migration barrier for the use of postconsumer recycled materials in food contact" (TRR 87 - T07 Project number 138690629).

## ORCID® iDs

Hendrik Müller - https://orcid.org/0000-0002-3758-3305
Teresa de los Arcos - https://orcid.org/0000-0002-8684-273X
Adrian Keller - https://orcid.org/0000-0001-7139-3110
Guido Grundmeier - https://orcid.org/0000-0003-2550-4048

## Data Availability Statement

The data that supports the findings of this study is available from the corresponding author upon reasonable request.

## References

1. Dazzi, A.; Prater, C. B. *Chem. Rev.* **2017,** *117,* 5146–5173. doi:10.1021/acs.chemrev.6b00448
2. Dazzi, A.; Saunier, J.; Kjoller, K.; Yagoubi, N. *Int. J. Pharm.* **2015,** *484,* 109–114. doi:10.1016/j.ijpharm.2015.02.046
3. Schwartz, J. J.; Jakob, D. S.; Centrone, A. *Chem. Soc. Rev.* **2022,** *51,* 5248–5267. doi:10.1039/d2cs00095d
4. Dazzi, A.; Prazeres, R.; Glotin, F.; Ortega, J. M. *Opt. Lett.* **2005,** *30,* 2388–2390. doi:10.1364/ol.30.002388
5. Dou, T.; Li, Z.; Zhang, J.; Evilevitch, A.; Kurouski, D. *Anal. Chem. (Washington, DC, U. S.)* **2020,** *92,* 11297–11304. doi:10.1021/acs.analchem.0c01971
6. Hanke, M.; Grundmeier, G.; Keller, A. *Nanoscale* **2022,** *14,* 11552–11560. doi:10.1039/d2nr02701a
7. He, S.; Stadler, H.; Huang, X.; Zheng, X.; Yuan, G.; Kuball, M.; Unger, M.; Ward, C.; Hamerton, I. *Appl. Surf. Sci.* **2023,** *607,* 154925. doi:10.1016/j.apsusc.2022.154925
8. Leppänen, I.; Arola, S.; King, A. W. T.; Unger, M.; Stadler, H.; Nissen, G. S.; Zborowski, C.; Virtanen, T.; Salmela, J.; Setälä, H.; Lésage, S.; Österberg, M.; Tammelin, T. *Adv. Mater. Interfaces* **2023,** *10,* 2300162. doi:10.1002/admi.202300162
9. Kurouski, D.; Dazzi, A.; Zenobi, R.; Centrone, A. *Chem. Soc. Rev.* **2020,** *49,* 3315–3347. doi:10.1039/c8cs00916c
10. Mathurin, J.; Deniset-Besseau, A.; Bazin, D.; Dartois, E.; Wagner, M.; Dazzi, A. *J. Appl. Phys.* **2022,** *131,* 010901. doi:10.1063/5.0063902
11. Tsuji, K.; Nakaya, M.; Uedono, A.; Hotta, A. *Surf. Coat. Technol.* **2015,** *284,* 377–383. doi:10.1016/j.surfcoat.2015.10.027
12. Bellel, A.; Sahli, S.; Ziari, Z.; Raynaud, P.; Segui, Y.; Escaich, D. *Surf. Coat. Technol.* **2006,** *201,* 129–135. doi:10.1016/j.surfcoat.2005.11.100
13. Körner, L.; Sonnenfeld, A.; von Rohr, P. R. *Thin Solid Films* **2010,** *518,* 4840–4846. doi:10.1016/j.tsf.2010.02.006
14. Wang, Z.; Zhu, H.; Yang, L.; Wang, X.; Liu, Z.; Chen, Q. *Plasma Sci. Technol. (Bristol, U. K.)* **2016,** *18,* 424–429. doi:10.1088/1009-0630/18/4/16
15. Böke, F.; Giner, I.; Keller, A.; Grundmeier, G.; Fischer, H. *ACS Appl. Mater. Interfaces* **2016,** *8,* 17805–17816. doi:10.1021/acsami.6b04421
16. Varghese, J.; Vieth, P.; Xie, X.; Grundmeier, G. *SN Appl. Sci.* **2023,** *5,* 29. doi:10.1007/s42452-022-05244-0
17. *Unifit Scientific Software;* Universal Spectrum Processing, 2019.
18. de los Arcos, T.; Müller, H.; Weinberger, C.; Grundmeier, G. *J. Electron Spectrosc. Relat. Phenom.* **2023,** *264,* 147317. doi:10.1016/j.elspec.2023.147317
19. Finster, J.; Schulze, D.; Bechstedt, F.; Meisel, A. *Surf. Sci.* **1985,** *152–153,* 1063–1070. doi:10.1016/0039-6028(85)90521-7
20. Greczynski, G.; Hultman, L. *Sci. Rep.* **2021,** *11,* 11195. doi:10.1038/s41598-021-90780-9
21. Hoppe, C.; Mitschker, F.; Awakowicz, P.; Kirchheim, D.; Dahlmann, R.; de los Arcos, T.; Grundmeier, G. *Surf. Coat. Technol.* **2018,** *335,* 25–31. doi:10.1016/j.surfcoat.2017.12.015
22. Liang, C. Y.; Pearson, F. G. *J. Mol. Spectrosc.* **1961,** *5,* 290–306. doi:10.1016/0022-2852(61)90094-7
23. de los Arcos, T.; Müller, H.; Wang, F.; Damerla, V. R.; Hoppe, C.; Weinberger, C.; Tiemann, M.; Grundmeier, G. *Vib. Spectrosc.* **2021,** *114,* 103256. doi:10.1016/j.vibspec.2021.103256
24. Liu, C.-N.; Ozkaya, B.; Steves, S.; Awakowicz, P.; Grundmeier, G. *J. Phys. D: Appl. Phys.* **2013,** *46,* 084015. doi:10.1088/0022-3727/46/8/084015
25. Deshmukh, S. C.; Aydil, E. S. *J. Vac. Sci. Technol., B: Microelectron. Nanometer Struct.–Process., Meas., Phenom.* **1996,** *14,* 738–743. doi:10.1116/1.588707
26. Brunet-Bruneau, A.; Fisson, S.; Gallas, B.; Vuye, G.; Rivory, J. *Thin Solid Films* **2000,** *377–378,* 57–61. doi:10.1016/s0040-6090(00)01386-9
27. Rosenberger, M. R.; Wang, M. C.; Xie, X.; Rogers, J. A.; Nam, S.; King, W. P. *Nanotechnology* **2017,** *28,* 355707. doi:10.1088/1361-6528/aa7c23

## License and Terms

BEILSTEIN JOURNAL OF NANOTECHNOLOGY

# Exploring surface charge dynamics: implications for AFM height measurements in 2D materials

Mario Navarro-Rodriguez*, Andres M. Somoza and Elisa Palacios-Lidon*

Full Research Paper

Open Access

Address:
Centro de Investigación en Óptica y Nanofísica (CIOyN), Department of Physics, University of Murcia, E-30100, Spain

Email:
Mario Navarro-Rodriguez* - mario.navarror@um.es;
Elisa Palacios-Lidon* - elisapl@um.es

* Corresponding author

Keywords:
2D materials; incorrect height measurements; Joule dissipation; surface conductivity; tip influence

*Beilstein J. Nanotechnol.* **2024,** *15,* 767–780.
https://doi.org/10.3762/bjnano.15.64

Received: 19 January 2024
Accepted: 13 June 2024
Published: 01 July 2024

This article is part of the thematic issue "Advanced atomic force microscopy techniques V".

Guest Editor: P. Rahe



## Abstract

An often observed artifact in atomic force microscopy investigations of individual monolayer flakes of 2D materials is the inaccurate height derived from topography images, often attributed to capillary or electrostatic forces. Here, we show the existence of a Joule dissipative mechanism related to charge dynamics and supplementing the dissipation due to capillary forces. This particular mechanism arises from the surface conductivity and assumes significance specially in the context of 2D materials on insulating supports. In such scenarios, the oscillating tip induces in-plane charge currents that in many circumstances constitute the main dissipative contribution to amplitude reduction and, consequently, affect the measured height. To investigate this phenomenon, we conduct measurements on monolayer flakes of co-deposited graphene oxide and reduced graphene oxide. Subsequently, we introduce a general model that elucidates our observations. This approach offers valuable insights into the dynamics of surface charges and their intricate interaction with the tip.

## Introduction

Two-dimensional (2D) materials have emerged as a promising platform for next-generation electronic devices [1], sensors [2], and biomedical applications [3,4], among other areas [5-8]. Graphene-related materials [8], transition metal dichalcogenides [9], boron nitride [10], and MXenes [11], among many others, exhibit novel and exotic properties, which markedly differ from their bulk counterparts [12]. This has sparked considerable interest spanning from fundamental research to practical device applications. The distinctive physical and chemical properties of 2D materials, composed of one atom- or a few atom-thick sheets, stem from their thin, flat structure, providing an exceptional surface-to-volume ratio. Moreover, their exten-

sive surface exposure renders them highly sensitive to ambient and external influences, amplifying chemical reactivity [13] and bestowing attractive properties regarding electrochemical and catalytic reactions [14]. Furthermore, the ability to stack these materials facilitates the creation of new heterostructures with tailored properties [15,16], making 2D materials suitable for different applications.

Understanding the correlation between structural and topographical variations and their impact on mechanical [17,18], optical [19,20], magnetic [21,22], electronic [23,24], or electrochemical properties [25] is a key topic of research. Factors such as flake size and shape, composition, density of defects, or doping significantly influence the response of 2D materials. Given the nanoscopic scale underlying the functionality of 2D materials, atomic force microscopy (AFM) techniques emerge as ideal tools to investigate them [26,27]. Depending on the operation mode and under controlled environmental conditions, AFM offers the possibility to record morphology along with relevant electronic, mechanical, or magnetic properties with nanoscale resolution. In addition, it can be integrated with classical optical spectroscopy methods such as Raman and fluorescence [20,28,29], enabling a multidimensional characterization approach.

A well-recognized issue within the AFM community is the inaccurate height determination derived from topography images on heterogeneous samples. This discrepancy arises from various sources depending on the operation mode and working parameters. In the frequency modulation mode (FM-AFM), a non-compensated bias voltage between tip and sample, from differences in the surface potential (SP), results in inaccurate height measurements [30]. This issue can be addressed with Kelvin probe force microscopy (KPFM). Under ambient conditions, the most common mode is amplitude modulation (AM-AFM), which uses the oscillation amplitude reduction as the input for the topography feedback. Its main aspects are summarized in [31]. At large free oscillation amplitudes, the tip mechanically touches the surface during part of the oscillation. This mode is known as "intermittent contact" or tapping mode, and incorrect height measurements are usually ascribed to variations in the local elasticity [32,33] or differences in the local adhesion, related to differences of the wetting properties [34]. At moderate oscillation amplitudes, intimate tip–sample contact is avoided, and the energy dissipation takes place at the lower turning point of the oscillation cycle because of the formation and rupture of liquid necks [35-37]. When operating in this less invasive mode, the driving excitation frequency can be fixed at, or near, the free resonance frequency of the cantilever, or tracked by using a phase-locked loop (PLL) to keep the system always in resonance. If the driving excitation frequency is kept fixed, the phase variations contain information about the dissipation. In this mode, the amplitude reduction may be due to (i) the tip–sample interaction (conservative or non-conservative), which shifts the resonance frequency and, therefore, makes the excitation go out of resonance, (ii) non-conservative interactions, which dissipate parts of the system's energy and, thus, reduce the amplitude, or (iii) a combination of both. Operating in this mode, erroneous height measurements derived from topography images are then attributed to local variations of hydrophilicity or hydrophobicity, which affect the dissipative capillary forces between tip and sample [38-41], or to typically electrostatic conservative forces [42]. In the latter case, using KPFM to minimize these forces mitigates the problem. Finally, if the driving excitation frequency is tracked to follow the resonance frequency shift induced by the tip–sample interactions, the system is always excited at resonance. Then, the amplitude is reduced because of non-conservative forces only, and topography images can be understood as constant-dissipation images [43]. Larger dissipative interactions necessitate the tip to retract further from the surface to maintain a constant amplitude. Consequently, in this mode, highly hydrophilic materials may appear thicker than their hydrophobic counterparts [39,40].

Erroneous height measurements are especially important in AFM studies of 2D materials [8,44-46]. The use of dynamic modes enhanced the problem; measured heights tend to be overestimated, especially in comparison to those obtained in contact mode [8,47-52]. As discussed above, the extent of the discrepancy depends on the operation mode [53,54] and environmental conditions [8] and is notably pronounced in samples grown on insulating substrates [55-57]. The origin of incorrect height measurements in 2D materials has been ascribed to the same sources as those mentioned above, including capillary forces and adhesion [8,46], electrostatic forces [58-60], or residues of the solvent [8]. However, in many cases, this is not enough to fully explain the measurements, suggesting that there may be additional interactions directly related to the 2D nature of these materials affecting the height measurements.

To explore this issue, in this work, we conducted a study on single-layer flakes of graphene oxide (GO) and reduced graphene oxide (rGO) co-deposited on an insulating substrate. Measurements on these two materials, which exhibit very different properties in terms of hydrophilicity and conductivity, allowed us to clarify the most relevant factors of the problem and how they affect the apparent height measured with AM-AFM. This has enabled us to identify, in addition to the previously described interactions, an additional contribution to the tip–sample interaction due to the movement of charges on the surface induced by the oscillating tip. To understand and

quantify this mechanism, we have proposed a very general model that solves Maxwell's equations for the system, including the presence of the tip, which we have subsequently particularized for 2D materials on insulating supports.

## Experimental

Co-deposited samples of GO and rGO were prepared following the methodology outlined in [61]. In summary, ultradiluted ($4 \times 10^{-4}$ wt %) dispersions of GO and/or rGO in Milli-Q type-I water (MQ water) were utilized. A drop of these dispersions was cast onto highly doped p-type silicon (1–10 Ω·cm, Siltronix) with a 300 nm $SiO_2$ layer thermally grown on top. Before deposition, the substrate underwent a thorough cleaning process, which involved rinsing with ethanol and MQ water. Subsequently, the substrate was exposed to UV/ozone for 15 min to eliminate organic contaminants and promote the hydrophilicity of the $SiO_2$ surface. GO (Graphenea), was employed without further treatment, while rGO was obtained through chemical reduction using hydrazine hydrate (50–60%, Sigma-Aldrich). After deposition, we heated the sample for a minimum of 3 h at 60 °C on a hot plate to remove some of the physisorbed water. While still hot, it was transferred to the AFM and left to cool down in a nitrogen atmosphere. Before starting measurements under controlled humidity, we waited for a minimum of 1 h until the humidity stabilized.

The experiments were performed at room temperature and low relative humidity (RH < 10%) in a dry nitrogen atmosphere. Topography images were acquired in AM-AFM mode by using the oscillation amplitude as the topography feedback channel. To maintain the system at resonance and track the frequency shift, a wide-bandwidth PLL (0.5–32 kHz) was enabled. In this operation mode, the amplitude signal carries information about dissipative interactions, as conservative forces only modify the resonant frequency. KPFM was operated in the frequency modulation mode (FM-KPFM) with an AC voltage of 700 mV at 7 kHz using platinum-coated silicon tips (Olympus AC240TM-R3, $k$ = 2 N/m and $f_0$ = 70 kHz). Using a dual lock-in amplifier (Zurich instruments, HF2LI), in addition to the KPFM channel, which provides information on the sample's SP, the $2\omega_{elec}$ capacitance signal was also recorded, as explained in [61].

Spectroscopy data were acquired using a variant of the 3D-mode dynamic force spectroscopy [62], explained in detail in [63]. Briefly, force, frequency shift, amplitude, and phase channels are recorded simultaneously at a fixed sample point as a function of the applied bias voltage ($V_{bias}$) for different tip–sample distances ($z$). This way, interaction images $I(V_{bias}, z)$ are obtained and later processed to obtain the relevant information from each channel.

## Results and Discussion

GO and rGO belong to the graphene family. In GO, the carbon basal plane is randomly decorated with oxygen-containing functional groups, including hydroxy, epoxy, and carboxyl groups [64,65]. In contrast, rGO is derived from the partial removal of these functionalities [66-69]. Further details about the structure and properties of GO and rGO are given in section SI.1 of Supporting Information File 1. Beyond their significance in various applications such as materials science, electronics, and biomedicine [70], these materials serve as benchmark systems for fundamental studies in 2D materials because of their markedly distinct properties [71]. Specifically, GO is a hydrophilic insulating material [72], while rGO exhibits a hydrophobic and more conductive nature [69,73-75], both dependent on the degree of reduction. This stark contrast provides an ideal heterogeneous sample to study the tip–sample interaction of co-deposited GO and rGO on insulating substrates.

In Figure 1, we present a stack of single-layer GO and rGO flakes co-deposited on $SiO_2$, measured under $N_2$ atmosphere (RH < 10%). Distinguishing between GO and rGO flakes based solely on the topography image proves to be challenging, as both materials exhibit similar heights. Therefore, additional AFM interaction channels are necessary for accurate differentiation. As explained in [61], this distinction is achieved unequivocally by using the KPFM and $2\omega_{elec}$ electrostatic channels. In KPFM images (Figure 1c), GO flakes are identified by their signature localized charge domains related to its low conduction and disordered nature [76]. Conversely, rGO presents a roughly uniform surface potential consistent with the presence of larger $sp^2$ regions, which increase the localization length, and with its enhanced conductivity as compared to GO. The $2\omega_{elec}$ signal (Figure 1d), related to the tip–sample capacitance [77], also allows one to discriminate GO from rGO. While a quantitative interpretation of the $2\omega_{elec}$ contrast in 2D materials necessitates further elucidation, it has proven reliable and robust for distinguishing materials with distinct electronic properties and, in particular, for identifying rGO with different reduction degrees [61]. In this channel, GO displays no contrast, whereas rGO shows a larger value compared with the substrate. With the unambiguous identification of each type of flake, we can proceed to study their thickness and its dependency on various external parameters. A line profile comprising both types of flake (Figure 1b) reveals a height of approximately 2 nm, larger than the expected nominal heights of ≈0.9 nm for GO and ≈0.3 nm for rGO. Moreover, the rGO flake appears to be slightly thicker than the GO flake, contradicting the anticipated reduction in thickness due to the removal of functionalities during the transition from GO to rGO. As mentioned above, in our AM-AFM measurements, the inconsistencies in height arise from the dissipative contrast between different materials. Under

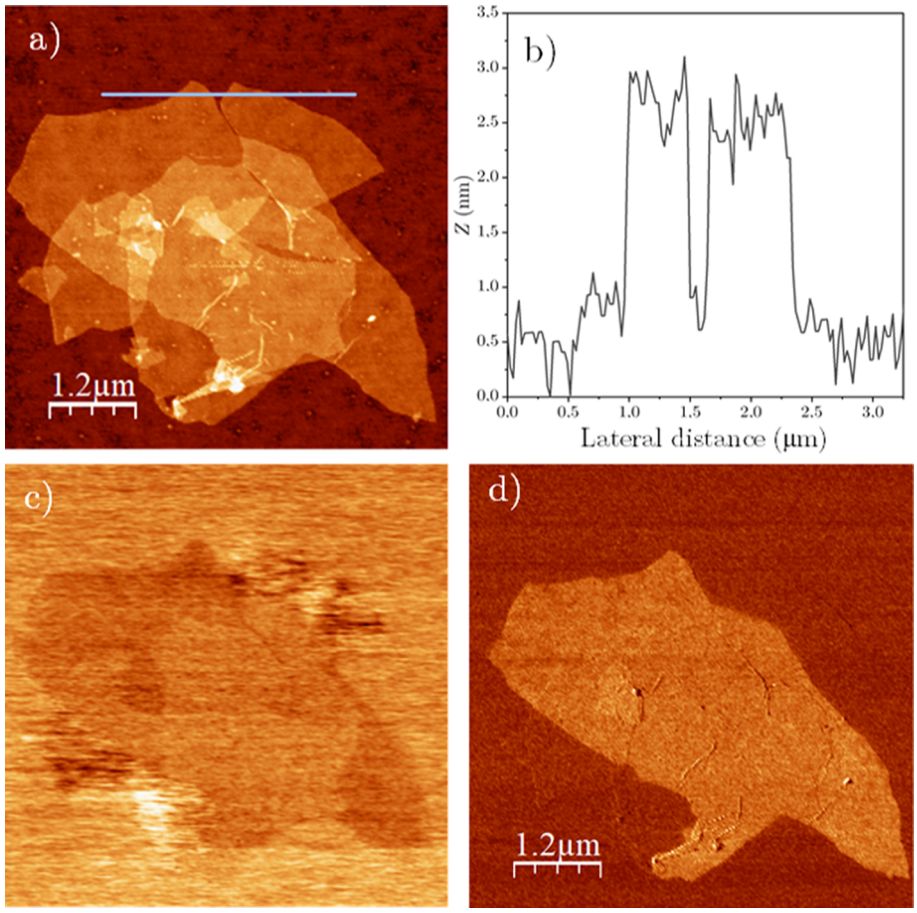


**Figure 1:** (a) Topography of a stack of GO and rGO flakes, *z* scale = 10 nm. (b) Profile along the blue line in (a). (c) KPFM (*z* scale = 320 mV) and (d) $2\omega_{elec}$ images corresponding to the topography in (a).

ambient conditions, this is typically dominated by capillary forces [39,40]. However, despite rGO being hydrophobic and both GO and the $SiO_2$ substrate being hydrophilic, the rGO sheet is observed as thicker than the GO sheet, where the formation of liquid necks between the tip and the sample should be more favorable [37]. It is worth noting that the measurements in Figure 1 were conducted at RH < 10% to minimize any potential influence of this effect, although no significant differences were observed compared to measurements at 45% RH. Additionally, KPFM operation does not seem to play a crucial role in this specific situation (see Supporting Information File 1, section SI.2).

Nevertheless, there are situations in which compensating the local surface potential through KPFM significantly enhances the precision of topography measurements, especially when the voltage between tip and sample is large. This is exemplified in Figure 2, where the tip–rGO voltage is intentionally modified by charging the flakes through bringing the tip into contact while applying an external bias voltage to the tip [78] (see Supporting Information File 1, section SI.3 for further details). Following the charging process, without activating the KPFM feedback (Figure 2a), there is a noticeable increase in the flake's apparent height, reaching approximately 9 nm, while the typical height (about 2 nm) is restored only after turning on the KPFM loop (Figure 2b and Supporting Information File 1, section SI.3). This has significant implications in multilayer systems, where height is commonly used to determine the number of layers, and measurements without KPFM might give an erroneous layer count. Moreover, a line profile along one and two layers (Figure 2c) reveals that, after charging, the height increase of the first layer with respect to the substrate is much more pronounced than the increase of the second layer with respect to the first one, which remains essentially unchanged. Additional charging experiments (not shown) reveal that the measured flake height depends on the charging state; this effect is magnified as the amount of charge is increased, regardless of its sign. We could associate this behavior with the existence of an uncompensated electrostatic force that is nullified when KPFM is activated. However, it is crucial to remember that,

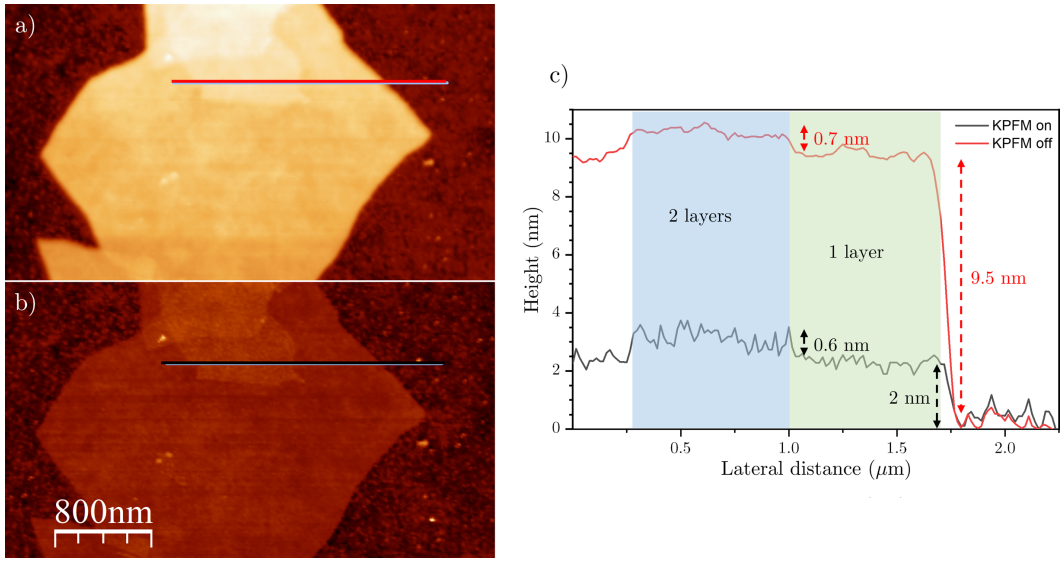


**Figure 2:** Topography images of charged rGO flakes. (a) KPFM off and (b) KPFM on, *z* scale = 15 nm. (c) Profiles along the red and black lines shown in (a) and (b).

under our measurement conditions, the tip always oscillates at resonance and amplitude variations are related to dissipative interactions. Since the electrostatic force is conservative, it should not change the oscillation amplitude [39]. Therefore, an increase in height correlates with larger dissipation, which prompts a tip retraction to maintain a constant amplitude. This suggests the presence of a voltage-dependent dissipation mechanism.

Since the apparent flake height seems to depend on both the tip–sample voltage and on the material, we explore these correlations on both GO and rGO flakes by biasing the tip with a DC voltage. To prevent any interaction between flakes arising from charge transfer through the substrate [79], we deliberately chose two well-separated rGO and GO single-layer flakes (Figure 3a,b). The AC voltage and the *y* scan are turned off at the highlighted profile in Figure 3a, and a DC voltage is applied

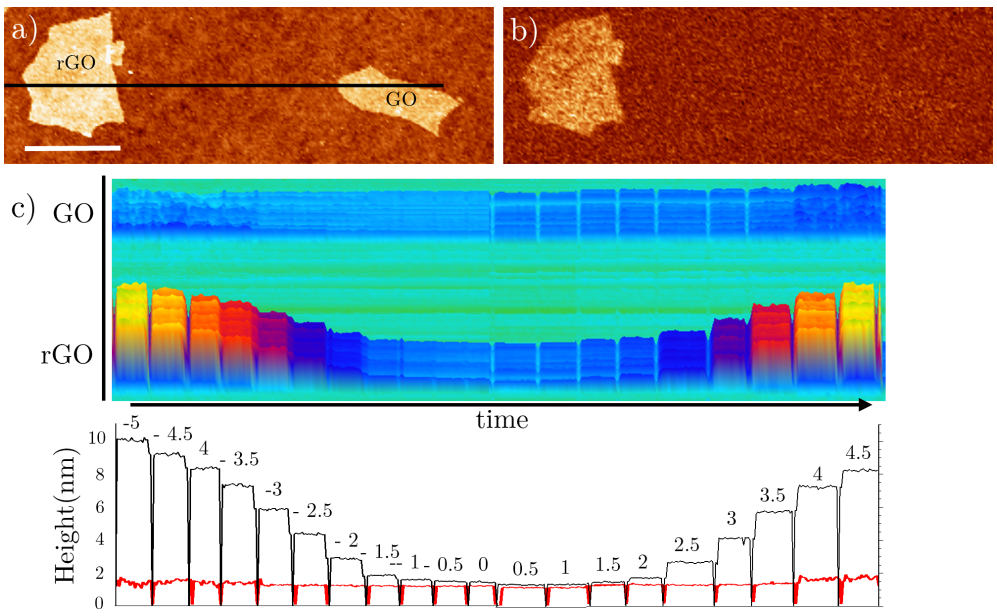


**Figure 3:** (a) Topography and (b) $2\omega_{elec}$ images of rGO and GO monolayer flakes. (c) The top image corresponds to the 3D representation of the topography along the black line shown in (a) as a function of time as $V_{bias}$ is changed in 0.5 V increments. The bottom plot corresponds to the average height of rGO (black) and GO (red) as a function of time for several discrete values of $V_{bias}$. Each data point is calculated by averaging the height over each flake profile at a given time.

to the tip ($V_{bias}$) for a few seconds, which is then changed to another voltage in steps of 0.5 V. In Figure 3c, we display the variations in height as a function of $V_{bias}$ along the line profile. In the case of GO, the height remains relatively constant with respect to the applied bias, showing only a slight increase at significantly positive and negative voltages (above ±4 V). In contrast, the rGO flake exhibits a much more pronounced dependence. At low bias voltages around the SP, the height is independent of $V_{bias}$, but it rapidly increases at higher bias voltages. This confirms the presence of a voltage-dependent dissipation mechanism, particularly enhanced on rGO. However, it is important to emphasize that this height dependence with the voltage is not seen when the flakes are supported on a conducting substrate (see Supporting Information File 1, section SI.4).

Moreover, we can examine a nanoscale heterogeneous sample, such as a partially reduced rGO flake. The transition from GO to rGO under reduction with hydrazine involves a non-homogeneous process, in which, at the intermediate reduction stages, the rGO flakes are composed of regions with different reduction degrees and, therefore, different properties [61]. As depicted in Figure 4a, when the tip–sample voltage is compensated (KPFM on), the height of rGO is roughly homogeneous along the flake. Conversely, when biasing the tip, not only does the overall height increase, but the increase is more pronounced in certain regions (Figure 4c,d). Comparing these regions with the $2\omega_{elec}$ image (Figure 4b), we find that the height increase is correlated to the local degree of reduction, with a lateral size for the domains that varies from tens to hundreds of nanometers. This confirms, on the one hand, that this mechanism achieves nanoscale resolution, primarily attributable to the tip, and, on the other hand, that the voltage dissipation mechanism depends on the local properties of the material.

To gain a deeper understanding of this voltage-dependent dissipative interaction, we conducted 3D spectroscopy measure-

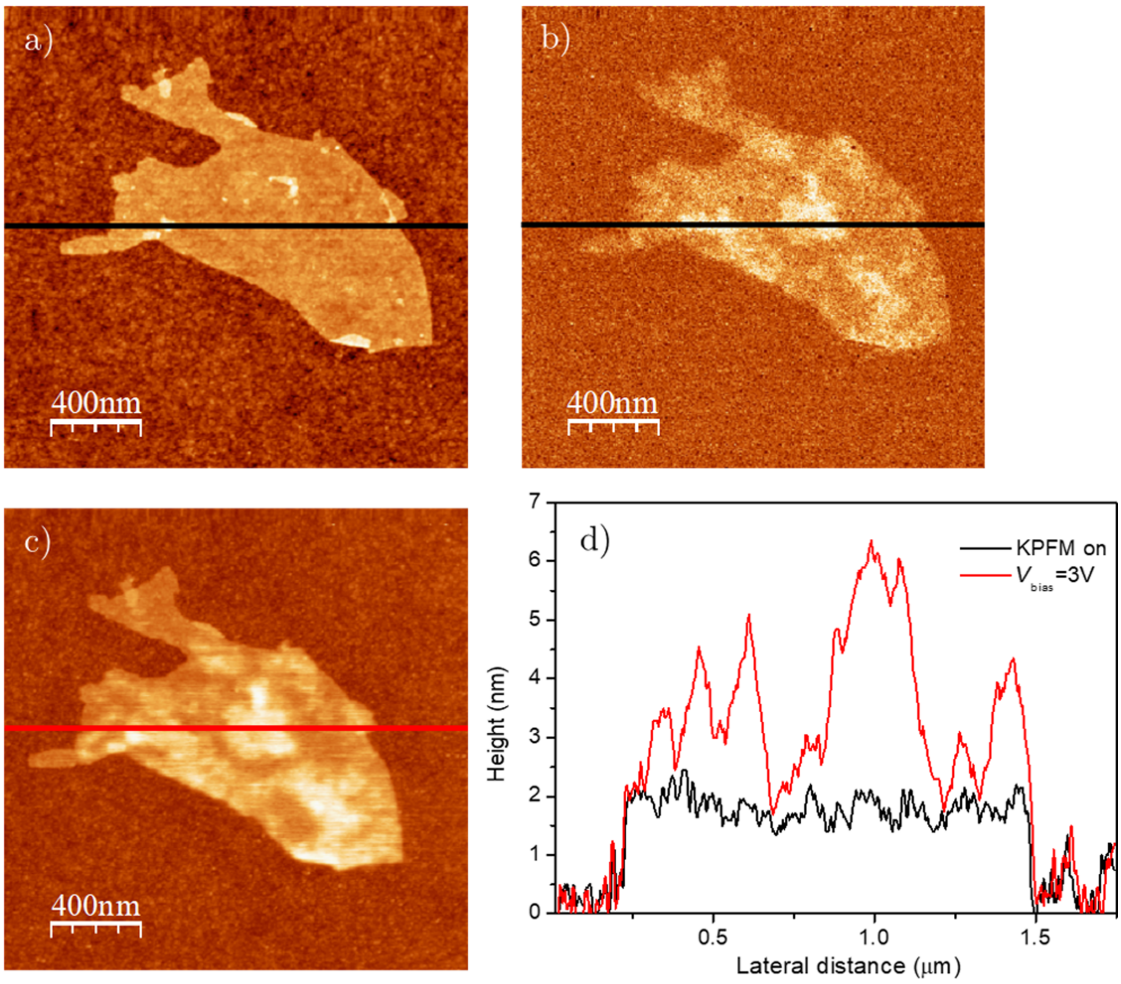


**Figure 4:** (a) Topography and (b) $2\omega_{elec}$ images with KPFM on of a partially reduced rGO flake. (c) Topography of the same flake but with KPFM off and $V_{bias}$ = 3 V. (d) Line profiles along the black and red lines in (a–c).

ments on rGO. The amplitude vs $V_{bias}$ as a function of tip–sample distance images ($A(V_{bias}, z)$) for two different free oscillation amplitudes ($A_0$) are shown in Figure 5a ($A_0$ = 4 nm) and Figure 5b ($A_0$ = 2 nm). From the corresponding normal force and frequency shift channels (not shown) and following the data processing described in [63], we derived the deflection–distance curve, as well as the SP for each tip–sample distance, SP($z$). This approach enabled us to accurately calibrate the tip–sample distance and the oscillation amplitude as shown in Figure 5c, where, in addition to the deflection–distance curve, we also include the upper and lower turning points of the oscillating tip at the minimum tip–sample voltage $A(V_{bias}$ = SP, $z)$, where $z$ is the mean tip–sample distance around which the tip is oscillating. In Figure 5c, we identify the two well-known non-contact interaction regimes, namely, (I) distances far from the sample, where capillary forces are negligible, and (II) distances close to sample, where the formation and rupture of liquid necks starts, and the amplitude reduction due to capillary forces becomes relevant [35,37]. The boundary between these regimes, of course, depends on $A_0$ since, at the same average tip–sample distance, for larger amplitudes, the lower turning point is closer to the sample, favoring the earlier formation of liquid necks.

In Figure 5d, representative amplitude vs $V_{bias}$ curves at different tip–sample distances are displayed. To facilitate comparison between various oscillation amplitudes, we present the amplitude referred to its free amplitude in each case ($A/A_0$). At large distances ($z$ = 15 nm), the amplitude exhibits a clear parabolic dependence on the bias voltage, being equal to the free oscillation ($A/A_0$ = 1) at $V_{bias}$ = SP and lower than the free oscillation ($A/A_0$ < 1) when $V_{bias} \neq$ SP. This confirms the presence of a dissipation mechanism depending on the tip–sample voltage even at large tip–sample distances. As the tip approaches ($z$ = 10 nm), the purely parabolic dependence is retained only for the lower oscillation amplitude. Conversely, a nearly voltage-independent flat region around the SP is superimposed on the curve with the larger oscillation amplitude. This is explained by considering that, at this mean tip–sample distance, we are still in regime I for the low amplitude while transitioning to regime II for the larger amplitude. In regime II, dissipation due to liquid necks dominates at low tip–sample bias voltages [35], while the voltage-dependent dissipative term becomes prominent at higher $V_{bias}$. Finally, at $z$ = 8 nm, where both amplitudes are in regime II, the curves exhibit a combination of voltage-independent dissipation at $V_{bias}$ around the SP and a voltage-dependent dissipative contribution at large tip–sample voltages. The relative contribution of each term to the total dissipation depends on the free oscillation amplitude. In contrast to the voltage-independent contribution mediated by capillary forces [38,63], the voltage-dependent dissipation

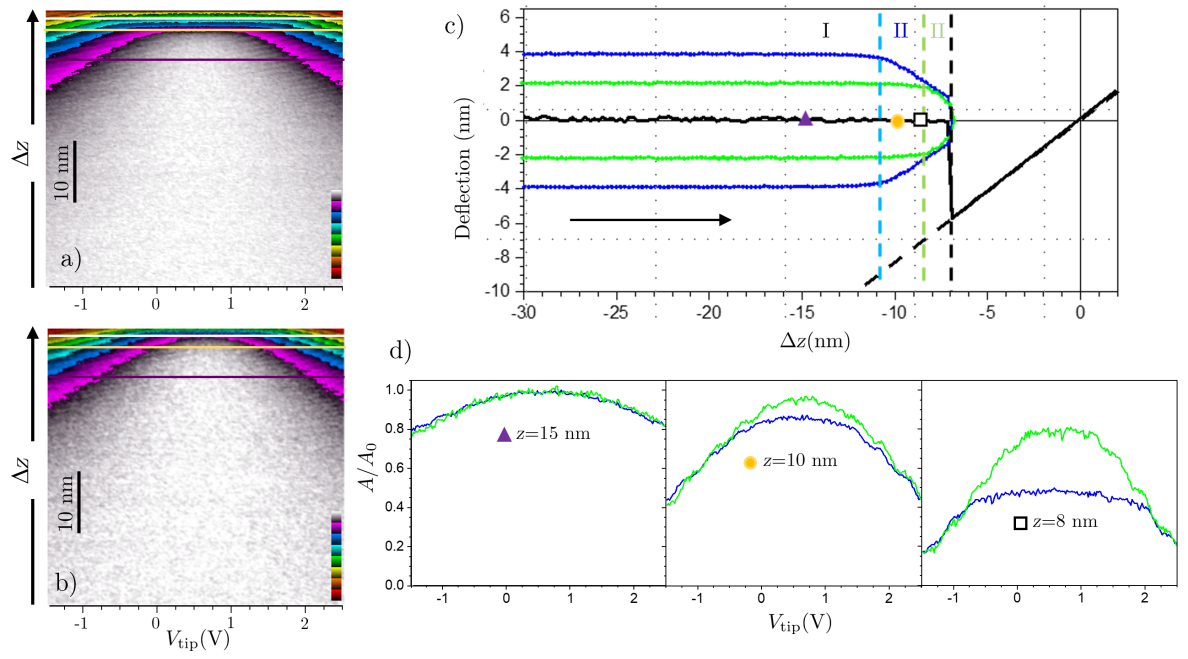


**Figure 5:** A($V_{bias}$, $z$) 3D spectroscopy images acquired on a rGO monolayer flake for (a) $A_0$ = 4 nm and (b) $A_0$ = 2 nm. Only the non-contact region is shown. (c) Deflection vs mean distance curve (black). The green ($A_0$ = 2 nm) and blue ($A_0$ = 4 nm) curves represent the upper and lower turning points of the oscillating tip at $V_{bias}$ = SP. The corresponding green and blue dashed lines mark the boundary between regions I and II for the amplitudes, while the black dashed line indicates the jump to the contact point. (d) $A/A_0$ vs $V_{bias}$ for different tip–sample distances; the green and blue curves correspond to $A_0$ = 2 nm and $A_0$ = 4 nm, respectively.

contribution perfectly scales with the free oscillation amplitude. This scaling suggests that, for low to moderate amplitudes, this dissipation mechanism is proportional to $A_0$. The same experiments were conducted on the GO flake (see Supporting Information File 1, section SI.5), revealing that, in this material, the voltage-dependent contribution is significantly lower, aligning well with the observations of Figure 3.

In summary, our experimental results confirm that, in addition to the well-known dissipative interaction due to capillary forces, in 2D materials, there is another dissipative interaction, whose magnitude is tightly related to the tip–sample voltage and strongly depends on the 2D material itself. Moreover, this mechanism achieves nanoscale resolution and is sensitive to local heterogeneities in the material's properties. We also show that this effect is particularly relevant whenever the 2D material is supported on an insulating substrate and can be an important source of error when determining its thickness.

According to its voltage dependence, it is reasonable to assume an electronic origin. Previously, it has been proposed in other systems that a plausible explanation to this effect is related to Joule dissipation [80,81]. The physical processes that lead to Joule dissipation are as follows: (i) In the presence of an effective tip–sample voltage, the oscillating AFM tip generates a time-dependent electrical field, which induces a current and Joule dissipation due to the non-zero resistance of the material. These currents induce an oscillating charge movement. (ii) Simultaneously, these moving charges also generate a time-dependent electric field, which needs to be considered consistently. We think that our findings align well with this explanation, as a key difference between GO and rGO is their electrical conductivity. Moreover, the conduction mechanism in GO and rGO flakes is variable-range hopping [75], and slight changes in the reduction degree may vary the conductivity by many orders of magnitude [69], which would explain the high sensitivity of the measurements to the local reduction degree within one partially reduced rGO flake.

To account for Joule dissipation, different models have been derived with different approximations, most of them treating the metal–metal situation or modeling the tip–sample system as a series of capacitors [80-84]. In this work, we follow a different approach. We derive the general equations in the macroscopic limit for the charge dynamics near the surface between two media. In a previous work, we studied the tip-less case, which we will use as the starting point for our model. Here, we just summarize the main aspects and refer to [78] for further details. Then, we include the tip influence by adding the appropriate boundary condition, which is time-dependent when the tip is oscillating and/or an AC voltage is applied. After adding this contribution, we particularize to 2D materials on insulating supports, where the current through the bulk is minimal and the induced currents are confined to the surface.

As shown in Figure 6, the sample is modelled as a semi-infinite medium with permittivity $\varepsilon_2$ and bulk conductivity $\sigma_2$ embedded in a medium with permittivity $\varepsilon_1$ and conductivity $\sigma_1$. A well-known key feature is that, for an homogeneous bulk system, an arbitrary initial charge density, $\rho(\mathbf{r}, t = 0)$, decays in time as $\rho(\mathbf{r}, t) = \rho(\mathbf{r}, t = 0)\cdot\exp(-t/\tau)$. This result is directly derived from the Poisson equation ($\nabla\cdot\mathbf{E} = \rho/\varepsilon$), the continuity equation ($\nabla\cdot\mathbf{J} = -\partial\rho/\partial t$), and Ohm's law ($\mathbf{J} = \sigma\mathbf{E}$). According to this result, we assume that bulk regions not initially charged will remain uncharged, that is, all charge (if any) will be located at the surface. In order to avoid possible singularities, we assume that all non-negligible charge density is located in a region of height $a$ inside the sample (from $z = 0 + \varepsilon \to 0^+$ to $z = -a$, see Figure 6). We note that, as long as $a$ is finite, we must handle three-dimensional quantities (charge density and conductivity). Only when we take the limit $a \to 0$, two-dimensional quantities will become properly defined. We assume that for currents parallel to the surface inside the gray region, $J_\parallel = \sigma_\parallel E_\parallel$, the conductivity is different to the bulk value. Then, the final surface conductivity will be defined as $\sigma_s = \lim_{a\to 0} a\sigma_\parallel$. Similarly, the two-dimensional charge density is defined as $n(x, y, t) = \lim_{a\to 0} a\rho(x, y, z = 0, t)$. Now, applying charge conservation (continuity equation), Ohm's law, and Gauss' theorem to the gray surface element in the sample plotted in Figure 6 leads to [78]:

$$a\frac{\partial\rho}{\partial t} = \frac{\sigma_\parallel}{\varepsilon_2}a\rho + \left(\sigma_2 - \sigma_\parallel\right)E_z\left(z=-a\right) - \left(\sigma_1 - \sigma_\parallel\frac{\varepsilon_1}{\varepsilon_2}\right)E_z\left(z=0^+\right). \quad (1)$$

$E_z(x, y, z, t)$ is the $z$ component of the electric field. The electric field is induced by both the presence of the tip (at voltage $V_{bias}$) and by the surface charge density. The electric field must then verify Maxwell's first equation, $\nabla\cdot\mathbf{E} = \rho/\varepsilon$, above and below the surface, whose general solution is

$$V\left(x,y,z,t\right) = V_{tip}\left(x,y,z,t\right) + \int dx' \int dy'\, n\left(x',y',t\right)V_1\left(x',y',z';x,y,z,t\right), \quad (2)$$

where $V_{tip}(x, y, z , t)$ is the potential generated by the tip in the absence of charges, the second term on the right-hand side is the potential generated by the charges at the surface, $n(x, y, t)$ is the surface charge density, and $V_1(x', y', z'; x, y, z, t)$ is the potential at position $(x, y, z)$ generated by a unit charge located at $(x', y', z')$. $V_{tip}(x, y, z, t)$ is calculated through solving the Laplace equation with the boundary condition $V(\mathbf{r} \in$ tip surface$) = V_{bias}$. This term may depend on time if the tip oscillates or if

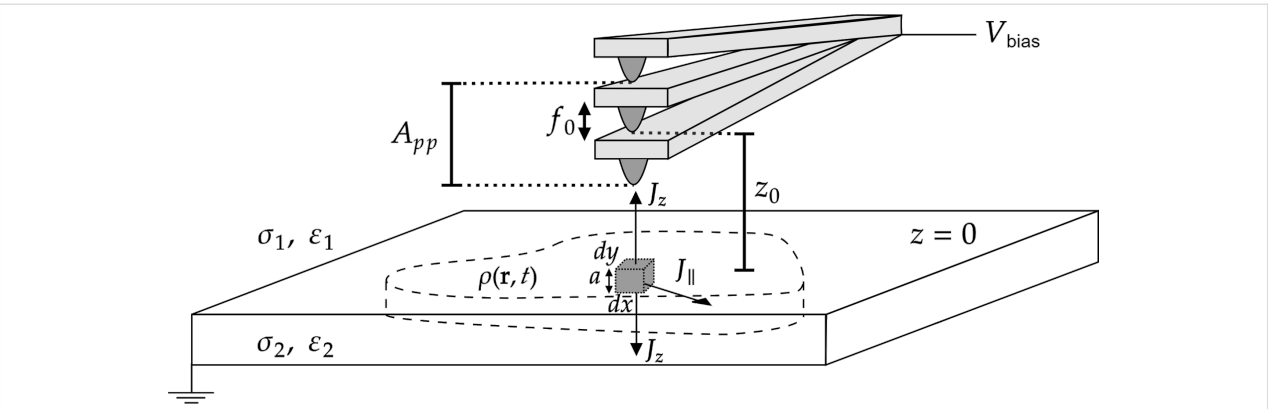


**Figure 6:** Scheme of the modelled system with an oscillating tip above the sample's surface. The tip is oscillating at its resonant frequency, $f_0$, with a peak-to-peak amplitude $A_{pp}$. The current density ($\mathbf{J}(x, y, z, t)$) leaving the differential volume element ($dV = dxdy\,a$) has components parallel ($J_\parallel = \sigma_\parallel E_\parallel$) and perpendicular ($J_{i,z} = \sigma_i E_{i,z}$, with $i$ = 1,2 above and below the surface, respectively) to the surface.

an AC voltage is applied. $V_1(x', y', z'; x, y, z, t)$ is calculated with the boundary condition $V(\mathbf{r}\in$ tip surface$) = 0$ and is proportional to the standard Green function of the problem (in some textbooks $G(\mathbf{r}, \mathbf{r}')$ is the potential at $\mathbf{r}$ due to a charge of value $q = -4\pi\varepsilon$ located at $\mathbf{r}'$ [85]).

Equation 1 and Equation 2, together with initial and boundary conditions constitute a closed set to determine $n(x, y, t)$. It is possible to differentiate Equation 2 to obtain a similar equation for $E_z(\mathbf{r})$. Then, inserting it into Equation 1 and taking the limit $a\to 0$, we obtain an integro-differential equation for $n(x, y, t)$ that defines the exact macroscopic limit of the problem of charge dynamics at the surface including the effect of the tip. The complexity of this equation impedes an analytical treatment unless we introduce certain approximations that enable us to analyze it and deduce some of its consequences. In our case, (i) the tip is described as a sphere of radius $R$ located at ($x = 0$, $y = 0$, $z = z_0$), and (ii) we take the long-distance limit, where the tip is far away from the surface; thus, we only keep the leading-order terms in $z_0\to\infty$. This approximation allows for a simple treatment in terms of image charges, see for example [86,87]. In general, verifying the boundary conditions at the surface and at the tip surface requires to treat an infinite series of image charges, but for large $z_0$ these charges become rapidly negligible. Taking this into account, the term $V_{tip}(x, y, z ,t)$ can be written as

$$V_{\text{tip}}(x,y,z,t)\approx\begin{cases}\dfrac{q}{4\pi\varepsilon_1}\left(\dfrac{1}{\sqrt{x^2+y^2+(z-z_0)^2}}-\dfrac{s}{\sqrt{x^2+y^2+(z+z_0)^2}}\right) & \text{for } z>0,\\ \dfrac{q}{4\pi\varepsilon_2}\dfrac{(1+s)}{\sqrt{x^2+y^2+(z-z_0)^2}} & \text{for } z<0,\end{cases} \tag{3}$$

where $s = (\varepsilon_2 - \varepsilon_1)/(\varepsilon_2 + \varepsilon_1)$, and $q = 4\pi\varepsilon_1 R V_{bias}$. $V_{bias}$ and $z_0$ may be time-dependent if the tip is oscillating or a variable voltage is applied. Similarly, the potential generated by a unit charge, $V_1(x', y', z'; x, y, z)$, for $z, z' < 0$, is written as

$$V_1(x',y',z';x,y,z)\approx\frac{1}{4\pi\varepsilon_2\sqrt{(x-x')^2+(y-y')^2+(z-z')^2}}+\frac{s}{4\pi\varepsilon_2\sqrt{(x-x')^2+(y-y')^2+(z-z')^2}}. \tag{4}$$

We note that, once $E_z$ is calculated and substituted into Equation 1, the right-hand side of the integro-differential equation contains two kind of terms, namely, (i) terms independent of $n(x, y, t)$ and (ii) terms linear in $n(x, y, t)$. The interpretation of the first kind of terms is straightforward. In the absence of charges, the tip produces electric fields and, thus, currents. These currents modify the charge density through the continuity equation. Collecting all the terms of the first kind and taking the limit $a\to\ 0$ leads to

$$f_{\text{tip}}(x,y)=\frac{2Rz_0V_{\text{bias}}}{\varepsilon_1+\varepsilon_2}\frac{(\varepsilon_2\sigma_1-\varepsilon_1\sigma_2)}{\left(x^2+y^2+z_0^2\right)^{3/2}}+\frac{2\varepsilon_1V_{\text{bias}}R\sigma_s}{\varepsilon_1+\varepsilon_2}\frac{\left(x^2+y^2-2z_0^2\right)}{\left(x^2+y^2+z_0^2\right)^{5/2}}. \tag{5}$$

Furthermore, within our approximations, $V_1$ is not affected by the tip, so it can be written as $V_1(x - x', y - y', z, z')$. Then, the second kind of terms in Equation 1 become a pure convolution

and can be easily Fourier-transformed in the plane (see Appendices A and B in [78] for details). After Fourier transformation and taking the limit $a \to 0$, Equation 1 becomes [78]:

$$\frac{\partial n(k,t)}{\partial t} = \frac{-n(k,t)}{\tau(k)} + f_{\text{tip}}(k), \tag{6}$$

where $\tau(k)^{-1} = \tau_0^{-1} + \sigma_s k / (\varepsilon_1 + \varepsilon_2)$, $\tau_0 = (\varepsilon_1 + \varepsilon_2)/(\sigma_1 + \sigma_2)$, and

$$f_{\text{tip}}(k) = \frac{4\pi R V_{\text{bias}}}{\varepsilon_1 + \varepsilon_2}\left(\varepsilon_2\sigma_1 - \varepsilon_1\sigma_2 - \varepsilon_1 k\sigma_s\right)e^{-kz_0}.$$

It should be noted that Equation 6 only depends on $k = |\mathbf{k}|$ since radial symmetry is assumed. For a non-oscillating tip ($z_0$ and $V$ constant), this equation can be solved analytically in Fourier space. A first consequence in this case is that, as $t \to \infty$, there will be a surface charge density that will depend on the bulk conductivities and the surface conductivity,

$$\begin{aligned} n(k, t\to\infty) &= f_{\text{tip}}(k)\tau(k) \\ &= 4\pi R V_{\text{bias}} \frac{\varepsilon_2\sigma_1 - \varepsilon_1\sigma_2 - \sigma_s\varepsilon_1 k}{\sigma_1 + \sigma_2 + k\sigma_s} e^{-kz_0}. \end{aligned} \tag{7}$$

This equation shows that, initially, the tip generates an electric field that gives rise to currents at the surface, charging it in the process. This process stops when there is no net electric field parallel to the surface, and thus the whole surface is set at a constant voltage. The surface charge distribution is such that it cancels the electric field parallel to the surface, $E_\parallel$, generated by the tip. The final voltage depends on the geometry of the problem and the conductivity of each media. Solutions of this kind will exist regardless of the model used for the tip.

In our model, a 2D material supported on an insulating substrate is described by setting $\sigma_1, \sigma_2 \approx 0$, that is, bulk conduction is negligible, but surface conductivity is not. Then, for an initially uncharged surface ($n(r, t = 0) = 0$), we get

$$n(r,t) = -8\pi^2\varepsilon_1 R V_{\text{bias}} \cdot \left( \frac{z_0}{\left(r^2 + z_0^2\right)^{3/2}} - \frac{\left(\varepsilon_1 + \varepsilon_2\right)^2}{\left[\sigma_s t + \left(\varepsilon_1 + \varepsilon_2\right) z_0\right]^2 \left( 1 + \frac{\left(\varepsilon_1 + \varepsilon_2\right)^2 r^2}{\left[\sigma_s t + \left(\varepsilon_1 + \varepsilon_2\right) z_0\right]^2} \right)^{3/2}} \right), \tag{8}$$

where $r = \sqrt{x^2 + y^2}$. This solution shows that there is a relatively slow charging of the surface with a characteristic time

$$\tau\left(k = 1/z_0\right) \approx \frac{\left(\varepsilon_1 + \varepsilon_2\right) z_0}{\sigma_s}, \tag{9}$$

such that for $t \ll \tau$, the surface remains uncharged, but for times larger than $\tau$, the surface will be charged, even if no charges were present at $t = 0$. When $\tau$ is much larger than any relevant time, this charge will be negligible, while as $\tau \to 0$, the surface charge density will correspond to the metallic case. In our samples, the local surface conductivity varies by many orders of magnitude and, thus, this effect may influence the measurements. A rough estimation for GO and highly reduced GO gives an idea of typical timescales for an insulating and a conducting 2D material. At a typical working distance, $z_0 \approx 10$ nm, and using the $\sigma_\parallel$ values from [69] ($\sigma_\parallel^{\text{GO}} \approx 10^{-8}$ S/m and $\sigma_\parallel^{\text{rGO}} \approx 10^5$ S/m), the surface conductivity is calculated as $\sigma_s = \sigma_\parallel a$, with $a \approx 1$ nm, the thickness of the flake. We also consider $\varepsilon_1 = \varepsilon_0$ and $\varepsilon_2 = \varepsilon_{SiO_2} = 4\varepsilon_0$. This yields relaxation times that span many orders of magnitude, from tens of milliseconds to few femtoseconds ($\tau_{\text{GO}} \approx 40$ ms and $\tau_{\text{rGO}} \approx 4$ fs). Comparing these with typical acquisition times for a data point, $t_p \approx 10^{-3}$ s, yields two opposite situations. For GO, $t_p < \tau_{\text{GO}}$, the surface charge distribution does not reach the equilibrium configuration during the acquisition time, while for rGO, $t_p \gg \tau_{\text{rGO}}$, measurements are carried out in equilibrium. It is important to note that the time evolution in Equation 8 is entirely a consequence of a non-negligible $\sigma_s$; if we set $\sigma_s = 0$, the time evolution cancels, and we recover the expected solution for a dielectric interface.

When the tip oscillates or an AC voltage is applied, the oscillating electric field produces Joule dissipation at the surface as well as an oscillating surface charge. For simplicity, we consider the case of an AC voltage ($V_{\text{bias}} = V_{\text{DC}} + V_{\text{AC}}\cos(\omega t)$), although solutions will be very similar for small tip oscillation amplitudes, since only $f_{\text{tip}}(k)$ depends on $z_0$ or $V$. In order to properly calculate them, we need to solve Equation 1 including the oscillating term $V_{\text{AC}}\cos(\omega t)$. As this change only affects

$f_{tip}(k)$, we can find the oscillating part of the solution for each $k$ applying the variation of constants method, thus:

$$n_{AC}(k,t) = \frac{V_{AC} f_{tip}(k)}{1+\tau^2(k)\omega^2}\left[\cos(\omega t)+\tau(k)\omega\sin(\omega t)\right]. \quad (10)$$

We note that this oscillating charge must be taken into account in order to properly calculate the tip–sample interaction. To our knowledge, the effect of this time-dependent charge distribution has not been taken into account, and it could be important when using KPFM, specially when $\tau^{-1}$ is comparable to the oscillation frequency and when the AC voltage is large.

Now $V(k, z, t)$ can be calculated substituting $n_{AC}(k, t)$ into the Fourier transform of Equation 2. From $V(k, z, t)$, it is possible to calculate the Joule dissipation. In particular, for our case ($\sigma_1$, $\sigma_2 = 0$), the dissipated power, $P$, takes the simple expression:

$$P = \sigma_s \frac{\omega}{2\pi}\int_0^{2\pi/\omega} dt \int d\mathbf{k}\, k^2 \left|V(k, z=0, t)\right|^2. \quad (11)$$

Because of the linearity of Equation 2, the oscillating part of the total electrostatic potential at the surface will be linear in $V_{AC}$. Hence, this equation predicts the parabolic dependence of the dissipation with the applied bias voltage and shows that, in 2D materials, there is an a priori non-negligible dissipation mechanism related to the in-plane conductivity. This might also explain why the application of KPFM mostly mitigates the issue of incorrect height measurements in 2D materials, although it does not entirely correct the problem. Through the use of KPFM, the overall tip–sample voltage across a specific region beneath the tip is nullified, minimizing the mean electric field in that area and, consequently, effectively reducing the currents. However, it is important to note that, locally, complete nullification of the electric field may not occur, resulting in residual small surface currents with an associated Joule dissipation.

## Conclusion

We conducted a study on a system involving GO and rGO flakes supported on $SiO_2$/Si to elucidate the origin behind consistently inaccurate AM-AFM height measurements of 2D materials when they are deposited on insulating substrates. Our experimental results reveal that this discrepancy arises from a dissipation mechanism directly proportional to the free oscillation amplitude for low to moderate amplitudes. Additionally, we observed a parabolic dependence on the tip–sample bias voltage, with the dissipation effect being more pronounced as the in-plane conductivity of the material increases.

We have linked this phenomenon to an in-plane Joule dissipation due to an oscillating charge induced by the oscillating tip, which is enhanced when the underlying substrate is insulating. To comprehensively understand this 2D Joule dissipation, we have established the equations governing surface charge dynamics, accounting for the presence of the oscillating tip. While solving the exact equations proves challenging without resorting to numerical techniques, we have derived a comprehensive explanation of the experimental observations by considering the long-distance limit. Moreover, our model reveals that, aside from the impact of Joule dissipation on height measurements in AM-AFM mode, the presence of an oscillating surface charge introduces additional dynamic effects typically overlooked, which, under certain conditions, should be considered when calculating the tip–sample interaction. Also, we have identified a relaxation time required to reach the stationary or periodic state for a static or oscillating tip, respectively. This relaxation time is crucial to the overall charge dynamics and depends on the material's in-plane conductivity and on the measurement parameters. When this relaxation time is comparable to, or even significantly exceeds, the characteristic AFM measurement times, it may influence not only the topography, but also other interaction channels, particularly, those related to electrostatic properties.

Finally, it is worth noting that the oscillating surface charge on the material's surface may not only be induced by the scanning tip but also by applying an external AC voltage. This approach presents distinct advantages, allowing for precise tuning of both amplitude and frequency, providing an alternative path for exploring the electronic properties of 2D materials, which will be addressed in the future.

## Supporting Information

Supporting information includes: SI.1. Structure of GO and rGO. SI.2. Experiments at different relative humidity. SI.3. Charging of rGO flakes. SI.4. rGO on a conducting substrate. SI.5. 3D spectroscopy on a GO monolayer flake.

### Supporting Information File 1

Additional data.
[https://www.beilstein-journals.org/bjnano/content/supplementary/2190-4286-15-64-S1.pdf]

## Funding

The following sources of funding are acknowledged: MCIN/AEI/10.13039/501100011033 through projects PID2019-104272RB-C52 and PID2022-139191OB-C31 "ERDF A way of making Europe"; M.N work was financed by the grant PID2019-104272RB-C52/PRE2020-094503 funded by MCIN/AEI/ 10.13039/501100011033 and by "ESF Investing in your future".

## Author Contributions

Mario Navarro-Rodriguez: formal analysis; investigation; visualization; writing – original draft. Andres M. Somoza: conceptualization; methodology; validation; writing – original draft. Elisa Palacios-Lidon: conceptualization; funding acquisition; methodology; supervision; validation; writing – original draft.

## ORCID® iDs

Mario Navarro-Rodriguez - https://orcid.org/0000-0001-7676-6609
Andres M. Somoza - https://orcid.org/0000-0002-7402-4668
Elisa Palacios-Lidon - https://orcid.org/0000-0002-0785-8566

## Data Availability Statement

The data that supports the findings of this study is available from the corresponding author upon reasonable request.

## References

1. Lemme, M. C.; Akinwande, D.; Huyghebaert, C.; Stampfer, C. *Nat. Commun.* **2022,** *13,* 1392. doi:10.1038/s41467-022-29001-4
2. Sulleiro, M. V.; Dominguez-Alfaro, A.; Alegret, N.; Silvestri, A.; Gómez, I. J. *Sens. Bio-Sens. Res.* **2022,** *38,* 100540. doi:10.1016/j.sbsr.2022.100540
3. Murali, A.; Lokhande, G.; Deo, K. A.; Brokesh, A.; Gaharwar, A. K. *Mater. Today* **2021,** *50,* 276–302. doi:10.1016/j.mattod.2021.04.020
4. Li, K.; Ji, Q.; Liang, H.; Hua, Z.; Hang, X.; Zeng, L.; Han, H. *J. Nanobiotechnol.* **2023,** *21,* 181. doi:10.1186/s12951-023-01920-4
5. Kumbhakar, P.; Jayan, J. S.; Sreedevi Madhavikutty, A.; Sreeram, P. R.; Saritha, A.; Ito, T.; Tiwary, C. S. *iScience* **2023,** *26,* 106671. doi:10.1016/j.isci.2023.106671
6. Shanmugam, V.; Mensah, R. A.; Babu, K.; Gawusu, S.; Chanda, A.; Tu, Y.; Neisiany, R. E.; Försth, M.; Sas, G.; Das, O. *Part. Part. Syst. Charact.* **2022,** *39,* 2200031. doi:10.1002/ppsc.202200031
7. Lin, Y.-C.; Torsi, R.; Younas, R.; Hinkle, C. L.; Rigosi, A. F.; Hill, H. M.; Zhang, K.; Huang, S.; Shuck, C. E.; Chen, C.; Lin, Y.-H.; Maldonado-Lopez, D.; Mendoza-Cortes, J. L.; Ferrier, J.; Kar, S.; Nayir, N.; Rajabpour, S.; van Duin, A. C. T.; Liu, X.; Jariwala, D.; Jiang, J.; Shi, J.; Mortelmans, W.; Jaramillo, R.; Lopes, J. M. J.; Engel-Herbert, R.; Trofe, A.; Ignatova, T.; Lee, S. H.; Mao, Z.; Damian, L.; Wang, Y.; Steves, M. A.; Knappenberger, K. L., Jr.; Wang, Z.; Law, S.; Bepete, G.; Zhou, D.; Lin, J.-X.; Scheurer, M. S.; Li, J.; Wang, P.; Yu, G.; Wu, S.; Akinwande, D.; Redwing, J. M.; Terrones, M.; Robinson, J. A. *ACS Nano* **2023,** *17,* 9694–9747. doi:10.1021/acsnano.2c12759
8. Backes, C.; Abdelkader, A. M.; Alonso, C.; Andrieux-Ledier, A.; Arenal, R.; Azpeitia, J.; Balakrishnan, N.; Banszerus, L.; Barjon, J.; Bartali, R.; Bellani, S.; Berger, C.; Berger, R.; Ortega, M. M. B.; Bernard, C.; Beton, P. H.; Beyer, A.; Bianco, A.; Bøggild, P.; Bonaccorso, F.; Barin, G. B.; Botas, C.; Bueno, R. A.; Carriazo, D.; Castellanos-Gomez, A.; Christian, M.; Ciesielski, A.; Ciuk, T.; Cole, M. T.; Coleman, J.; Coletti, C.; Crema, L.; Cun, H.; Dasler, D.; De Fazio, D.; Díez, N.; Drieschner, S.; Duesberg, G. S.; Fasel, R.; Feng, X.; Fina, A.; Forti, S.; Galiotis, C.; Garberoglio, G.; García, J. M.; Garrido, J. A.; Gibertini, M.; Gölzhäuser, A.; Gómez, J.; Greber, T.; Hauke, F.; Hemmi, A.; Hernandez-Rodriguez, I.; Hirsch, A.; Hodge, S. A.; Huttel, Y.; Jepsen, P. U.; Jimenez, I.; Kaiser, U.; Kaplas, T.; Kim, H.; Kis, A.; Papagelis, K.; Kostarelos, K.; Krajewska, A.; Lee, K.; Li, C.; Lipsanen, H.; Liscio, A.; Lohe, M. R.; Loiseau, A.; Lombardi, L.; Francisca López, M.; Martin, O.; Martín, C.; Martínez, L.; Martin-Gago, J. A.; Ignacio Martínez, J.; Marzari, N.; Mayoral, Á.; McManus, J.; Melucci, M.; Méndez, J.; Merino, C.; Merino, P.; Meyer, A. P.; Miniussi, E.; Miseikis, V.; Mishra, N.; Morandi, V.; Munuera, C.; Muñoz, R.; Nolan, H.; Ortolani, L.; Ott, A. K.; Palacio, I.; Palermo, V.; Parthenios, J.; Pasternak, I.; Patane, A.; Prato, M.; Prevost, H.; Prudkovskiy, V.; Pugno, N.; Rojo, T.; Rossi, A.; Ruffieux, P.; Samorì, P.; Schué, L.; Setijadi, E.; Seyller, T.; Speranza, G.; Stampfer, C.; Stenger, I.; Strupinski, W.; Svirko, Y.; Taioli, S.; Teo, K. B. K.; Testi, M.; Tomarchio, F.; Tortello, M.; Treossi, E.; Turchanin, A.; Vazquez, E.; Villaro, E.; Whelan, P. R.; Xia, Z.; Yakimova, R.; Yang, S.; Yazdi, G. R.; Yim, C.; Yoon, D.; Zhang, X.; Zhuang, X.; Colombo, L.; Ferrari, A. C.; Garcia-Hernandez, M. *2D Mater.* **2020,** *7,* 022001. doi:10.1088/2053-1583/ab1e0a
9. Chowdhury, T.; Sadler, E. C.; Kempa, T. J. *Chem. Rev.* **2020,** *120,* 12563–12591. doi:10.1021/acs.chemrev.0c00505
10. Gonzalez-Ortiz, D.; Salameh, C.; Bechelany, M.; Miele, P. *Mater. Today Adv.* **2020,** *8,* 100107. doi:10.1016/j.mtadv.2020.100107
11. Ronchi, R. M.; Arantes, J. T.; Santos, S. F. *Ceram. Int.* **2019,** *45,* 18167–18188. doi:10.1016/j.ceramint.2019.06.114
12. Bondavalli, P. *2D Materials: And Their Exotic Properties;* Walter de Gruyter GmbH & Co KG, 2022. doi:10.1515/9783110656336
13. Jeong, J. H.; Kang, S.; Kim, N.; Joshi, R.; Lee, G.-H. *Phys. Chem. Chem. Phys.* **2022,** *24,* 10684–10711. doi:10.1039/d1cp04831g
14. Deng, D.; Novoselov, K. S.; Fu, Q.; Zheng, N.; Tian, Z.; Bao, X. *Nat. Nanotechnol.* **2016,** *11,* 218–230. doi:10.1038/nnano.2015.340
15. Velický, M.; Toth, P. S. *Appl. Mater. Today* **2017,** *8,* 68–103. doi:10.1016/j.apmt.2017.05.003
16. Shi, B.; Qi, P.; Jiang, M.; Dai, Y.; Lin, F.; Zhang, H.; Fang, Z. *Mater. Adv.* **2021,** *2,* 5542–5559. doi:10.1039/d1ma00263e
17. Baimova, J.; Polyakova, P.; Shcherbinin, S. *Fibers* **2021,** *9,* 85. doi:10.3390/fib9120085
18. Cao, G.; Gao, H. *Prog. Mater. Sci.* **2019,** *103,* 558–595. doi:10.1016/j.pmatsci.2019.03.002
19. Sriram, P.; Wen, Y.-P.; Manikandan, A.; Hsu, K.-C.; Tang, S.-Y.; Hsu, B.-W.; Chen, Y.-Z.; Lin, H.-W.; Jeng, H.-T.; Chueh, Y.-L.; Yen, T.-J. *Chem. Mater.* **2020,** *32,* 2242–2252. doi:10.1021/acs.chemmater.9b02886
20. Cong, X.; Liu, X.-L.; Lin, M.-L.; Tan, P.-H. *npj 2D Mater. Appl.* **2020,** *4,* 13. doi:10.1038/s41699-020-0140-4
21. Huang, Y.; Sun, M.; Wang, Y.; Wee, A. T. S.; Chen, W. *ChemPhysMater* **2023,** *2,* 282–294. doi:10.1016/j.chphma.2023.04.001
22. Hossain, M.; Qin, B.; Li, B.; Duan, X. *Nano Today* **2022,** *42,* 101338. doi:10.1016/j.nantod.2021.101338

23. Murata, Y.; Mashoff, T.; Takamura, M.; Tanabe, S.; Hibino, H.; Beltram, F.; Heun, S. *Appl. Phys. Lett.* **2014,** *105,* 221604. doi:10.1063/1.4902988
24. Hu, Y.-J.; Tandoc, C.; Barsoum, M. W.; Rosen, J.; Björk, J. *2D Mater.* **2023,** *10,* 015019. doi:10.1088/2053-1583/aca8b7
25. Muthu, J.; Khurshid, F.; Chin, H.-T.; Yao, Y.-C.; Hsieh, Y.-P.; Hofmann, M. *Chem. Eng. J.* **2023,** *465,* 142852. doi:10.1016/j.cej.2023.142852
26. Zhang, H.; Huang, J.; Wang, Y.; Liu, R.; Huai, X.; Jiang, J.; Anfuso, C. *Opt. Commun.* **2018,** *406,* 3–17. doi:10.1016/j.optcom.2017.05.015
27. Xu, R.; Guo, J.; Mi, S.; Wen, H.; Pang, F.; Ji, W.; Cheng, Z. *Mater. Futures* **2022,** *1,* 032302. doi:10.1088/2752-5724/ac8aba
28. Shang, J.; Ma, L.; Li, J.; Ai, W.; Yu, T.; Gurzadyan, G. G. *Sci. Rep.* **2012,** *2,* 792. doi:10.1038/srep00792
29. Jie, W.; Yang, Z.; Bai, G.; Hao, J. *Adv. Opt. Mater.* **2018,** *6,* 1701296. doi:10.1002/adom.201701296
30. Sadewasser, S.; Lux-Steiner, M. C. *Phys. Rev. Lett.* **2003,** *91,* 266101. doi:10.1103/physrevlett.91.266101
31. García, R. *Amplitude modulation atomic force microscopy;* John Wiley & Sons, 2011. doi:10.1002/9783527632183
32. Guo, S.; Akhremitchev, B. B. *Langmuir* **2008,** *24,* 880–887. doi:10.1021/la7018605
33. Zhuang, W.; Ecker, C.; Metselaar, G. A.; Rowan, A. E.; Nolte, R. J. M.; Samorí, P.; Rabe, J. P. *Macromolecules* **2005,** *38,* 473–480. doi:10.1021/ma048786z
34. Köber, M.; Sahagún, E.; Fuss, M.; Briones, F.; Luna, M.; Sáenz, J. J. *Phys. Status Solidi RRL* **2008,** *2,* 138–140. doi:10.1002/pssr.200802033
35. Colchero, J.; Storch, A.; Luna, M.; Gómez Herrero, J.; Baró, A. M. *Langmuir* **1998,** *14,* 2230–2234. doi:10.1021/la971150z
36. de Pablo, P. J.; Colchero, J.; Luna, M.; Gómez-Herrero, J.; Baró, A. M. *Phys. Rev. B* **2000,** *61,* 14179–14183. doi:10.1103/physrevb.61.14179
37. Wei, Z.; Sun, Y.; Ding, W.; Wang, Z. *Sci. China: Phys., Mech. Astron.* **2016,** *59,* 694611. doi:10.1007/s11433-016-0241-7
38. Sahagún, E.; García-Mochales, P.; Sacha, G. M.; Sáenz, J. J. *Phys. Rev. Lett.* **2007,** *98,* 176106. doi:10.1103/physrevlett.98.176106
39. Palacios-Lidón, E.; Munuera, C.; Ocal, C.; Colchero, J. *Ultramicroscopy* **2010,** *110,* 789–800. doi:10.1016/j.ultramic.2010.01.015
40. Verdaguer, A.; Santos, S.; Sauthier, G.; Segura, J. J.; Chiesa, M.; Fraxedas, J. *Phys. Chem. Chem. Phys.* **2012,** *14,* 16080–16087. doi:10.1039/c2cp43031b
41. Santos, S.; Verdaguer, A.; Chiesa, M. *J. Chem. Phys.* **2012,** *137,* 044201. doi:10.1063/1.4737516
42. Riedel, C.; Alegría, A.; Arinero, R.; Colmenero, J.; Sáenz, J. J. *Nanotechnology* **2011,** *22,* 345702. doi:10.1088/0957-4484/22/34/345702
43. Jaafar, M.; Iglesias-Freire, Ó.; García-Mochales, P.; Sáenz, J. J.; Asenjo, A. *Nanoscale* **2016,** *8,* 16989–16994. doi:10.1039/c6nr04356a
44. Shearer, C. J.; Slattery, A. D.; Stapleton, A. J.; Shapter, J. G.; Gibson, C. T. *Nanotechnology* **2016,** *27,* 125704. doi:10.1088/0957-4484/27/12/125704
45. Serron, J.; Minj, A.; Spampinato, V.; Franquet, A.; Rybalchenko, Y.; Boulon, M.-E.; Brems, S.; Silva, H. M.; Shi, Y.; Groven, B.; Villarreal, R.; Conard, T.; van der Heide, P.; Hantschel, T. *ACS Appl. Mater. Interfaces* **2023,** *15,* 26175–26189. doi:10.1021/acsami.3c03057
46. Godin, K.; Cupo, C.; Yang, E.-H. *Sci. Rep.* **2017,** *7,* 17798. doi:10.1038/s41598-017-18077-4
47. Harvey, A.; Backes, C.; Gholamvand, Z.; Hanlon, D.; McAteer, D.; Nerl, H. C.; McGuire, E.; Seral-Ascaso, A.; Ramasse, Q. M.; McEvoy, N.; Winters, S.; Berner, N. C.; McCloskey, D.; Donegan, J. F.; Duesberg, G. S.; Nicolosi, V.; Coleman, J. N. *Chem. Mater.* **2015,** *27,* 3483–3493. doi:10.1021/acs.chemmater.5b00910
48. Harvey, A.; He, X.; Godwin, I. J.; Backes, C.; McAteer, D.; Berner, N. C.; McEvoy, N.; Ferguson, A.; Shmeliov, A.; Lyons, M. E. G.; Nicolosi, V.; Duesberg, G. S.; Donegan, J. F.; Coleman, J. N. *J. Mater. Chem. A* **2016,** *4,* 11046–11059. doi:10.1039/c6ta02811j
49. Hanlon, D.; Backes, C.; Doherty, E.; Cucinotta, C. S.; Berner, N. C.; Boland, C.; Lee, K.; Harvey, A.; Lynch, P.; Gholamvand, Z.; Zhang, S.; Wang, K.; Moynihan, G.; Pokle, A.; Ramasse, Q. M.; McEvoy, N.; Blau, W. J.; Wang, J.; Abellan, G.; Hauke, F.; Hirsch, A.; Sanvito, S.; O'Regan, D. D.; Duesberg, G. S.; Nicolosi, V.; Coleman, J. N. *Nat. Commun.* **2015,** *6,* 8563. doi:10.1038/ncomms9563
50. Backes, C.; Smith, R. J.; McEvoy, N.; Berner, N. C.; McCloskey, D.; Nerl, H. C.; O'Neill, A.; King, P. J.; Higgins, T.; Hanlon, D.; Scheuschner, N.; Maultzsch, J.; Houben, L.; Duesberg, G. S.; Donegan, J. F.; Nicolosi, V.; Coleman, J. N. *Nat. Commun.* **2014,** *5,* 4576. doi:10.1038/ncomms5576
51. Paton, K. R.; Varrla, E.; Backes, C.; Smith, R. J.; Khan, U.; O'Neill, A.; Boland, C.; Lotya, M.; Istrate, O. M.; King, P.; Higgins, T.; Barwich, S.; May, P.; Puczkarski, P.; Ahmed, I.; Moebius, M.; Pettersson, H.; Long, E.; Coelho, J.; O'Brien, S. E.; McGuire, E. K.; Sanchez, B. M.; Duesberg, G. S.; McEvoy, N.; Pennycook, T. J.; Downing, C.; Crossley, A.; Nicolosi, V.; Coleman, J. N. *Nat. Mater.* **2014,** *13,* 624–630. doi:10.1038/nmat3944
52. Fan, X.; Xu, P.; Li, Y. C.; Zhou, D.; Sun, Y.; Nguyen, M. A. T.; Terrones, M.; Mallouk, T. E. *J. Am. Chem. Soc.* **2016,** *138,* 5143–5149. doi:10.1021/jacs.6b01502
53. Nemes-Incze, P.; Osváth, Z.; Kamarás, K.; Biró, L. P. *Carbon* **2008,** *46,* 1435–1442. doi:10.1016/j.carbon.2008.06.022
54. Lai, C.-Y.; Santos, S.; Chiesa, M. *RSC Adv.* **2015,** *5,* 80069–80075. doi:10.1039/c5ra16695k
55. Shen, Y.; Guo, S.; Hu, J.; Zhang, Y. *Appl. Phys. Lett.* **2012,** *101,* 183109. doi:10.1063/1.4765359
56. Shen, Y.; Zhang, S.; Sun, Y.; Hai, C.; Li, X.; Zeng, J.; Ren, X.; Zhou, Y. *J. Phys. Chem. C* **2020,** *124,* 14371–14379. doi:10.1021/acs.jpcc.0c03499
57. Yalcin, S. E.; Galande, C.; Kappera, R.; Yamaguchi, H.; Martinez, U.; Velizhanin, K. A.; Doorn, S. K.; Dattelbaum, A. M.; Chhowalla, M.; Ajayan, P. M.; Gupta, G.; Mohite, A. D. *ACS Nano* **2015,** *9,* 2981–2988. doi:10.1021/nn507150q
58. Nie, Y.; Barton, A. T.; Addou, R.; Zheng, Y.; Walsh, L. A.; Eichfeld, S. M.; Yue, R.; Cormier, C. R.; Zhang, C.; Wang, Q.; Liang, C.; Robinson, J. A.; Kim, M.; Vandenberghe, W.; Colombo, L.; Cha, P.-R.; Wallace, R. M.; Hinkle, C. L.; Cho, K. *Nanoscale* **2018,** *10,* 15023–15034. doi:10.1039/c8nr02280a
59. Lin, Y.-C.; Zhang, W.; Huang, J.-K.; Liu, K.-K.; Lee, Y.-H.; Liang, C.-T.; Chu, C.-W.; Li, L.-J. *Nanoscale* **2012,** *4,* 6637–6641. doi:10.1039/c2nr31833d
60. Yang, K.-M.; Chung, J. Y.; Hsieh, M. F.; Ferng, S.-S.; Lin, D.-S.; Chiang, T.-C. *Phys. Rev. B* **2006,** *74,* 193313. doi:10.1103/physrevb.74.193313
61. Navarro-Rodriguez, M.; Camús, V.; Cros, A.; Garro, N.; Somoza, A. M.; Palacios-Lidon, E. *Appl. Surf. Sci.* **2024,** *642,* 158611. doi:10.1016/j.apsusc.2023.158611

62. Gómez-Navarro, C.; Gil, A.; Álvarez, M.; De Pablo, P.; Moreno-Herrero, F.; Horcas, I.; Fernández-Sánchez, R.; Colchero, J.; Gómez-Herrero, J.; Baró, A. M. *Nanotechnology* **2002,** *13,* 314–317. doi:10.1088/0957-4484/13/3/315
63. Palacios-Lidón, E.; Colchero, J. *Nanotechnology* **2006,** *17,* 5491–5500. doi:10.1088/0957-4484/17/21/033
64. Krishnamoorthy, K.; Veerapandian, M.; Yun, K.; Kim, S.-J. *Carbon* **2013,** *53,* 38–49. doi:10.1016/j.carbon.2012.10.013
65. Mouhat, F.; Coudert, F.-X.; Bocquet, M.-L. *Nat. Commun.* **2020,** *11,* 1566. doi:10.1038/s41467-020-15381-y
66. Park, S.; An, J.; Potts, J. R.; Velamakanni, A.; Murali, S.; Ruoff, R. S. *Carbon* **2011,** *49,* 3019–3023. doi:10.1016/j.carbon.2011.02.071
67. Ren, P.-G.; Yan, D.-X.; Ji, X.; Chen, T.; Li, Z.-M. *Nanotechnology* **2011,** *22,* 055705. doi:10.1088/0957-4484/22/5/055705
68. Agarwal, V.; Zetterlund, P. B. *Chem. Eng. J.* **2021,** *405,* 127018. doi:10.1016/j.cej.2020.127018
69. Mattevi, C.; Eda, G.; Agnoli, S.; Miller, S.; Mkhoyan, K. A.; Celik, O.; Mastrogiovanni, D.; Granozzi, G.; Garfunkel, E.; Chhowalla, M. *Adv. Funct. Mater.* **2009,** *19,* 2577–2583. doi:10.1002/adfm.200900166
70. Jiříčková, A.; Jankovský, O.; Sofer, Z.; Sedmidubský, D. *Materials* **2022,** *15,* 920. doi:10.3390/ma15030920
71. Smith, A. T.; LaChance, A. M.; Zeng, S.; Liu, B.; Sun, L. *Nano Mater. Sci.* **2019,** *1,* 31–47. doi:10.1016/j.nanoms.2019.02.004
72. Saxena, S.; Tyson, T. A.; Shukla, S.; Negusse, E.; Chen, H.; Bai, J. *Appl. Phys. Lett.* **2011,** *99,* 013104. doi:10.1063/1.3607305
73. Wang, Y.; Chen, Y.; Lacey, S. D.; Xu, L.; Xie, H.; Li, T.; Danner, V. A.; Hu, L. *Mater. Today* **2018,** *21,* 186–192. doi:10.1016/j.mattod.2017.10.008
74. Chen, Y.; Fu, K.; Zhu, S.; Luo, W.; Wang, Y.; Li, Y.; Hitz, E.; Yao, Y.; Dai, J.; Wan, J.; Danner, V. A.; Li, T.; Hu, L. *Nano Lett.* **2016,** *16,* 3616–3623. doi:10.1021/acs.nanolett.6b00743
75. Joung, D.; Khondaker, S. I. *Phys. Rev. B* **2012,** *86,* 235423. doi:10.1103/physrevb.86.235423
76. Palacios-Lidón, E.; Colchero, J.; Ortuno, M.; Colom, E.; Benito, A. M.; Maser, W. K.; Somoza, A. M. *ACS Mater. Lett.* **2021,** *3,* 1826–1831. doi:10.1021/acsmaterialslett.1c00550
77. Sadewasser, S.; Glatzel, T., Eds. *Kelvin Probe Force Microscopy - From Single Charge Detection to Device Characterization;* Springer Series in Surface Sciences; Springer International Publishing: Cham, Switzerland, 2018. doi:10.1007/978-3-319-75687-5
78. Navarro-Rodriguez, M.; Palacios-Lidon, E.; Somoza, A. M. *Appl. Surf. Sci.* **2023,** *610,* 155437. doi:10.1016/j.apsusc.2022.155437
79. Shen, Y.; Zhang, X.; Wang, Y.; Zhou, X.; Hu, J.; Guo, S.; Zhang, Y. *Appl. Phys. Lett.* **2013,** *103,* 053107. doi:10.1063/1.4817252
80. Volokitin, A. I.; Persson, B. N. J. *Rev. Mod. Phys.* **2007,** *79,* 1291–1329. doi:10.1103/revmodphys.79.1291
81. Gnecco, E.; Meyer, E., Eds. *Fundamentals of Friction and Wear on the Nanoscale;* NanoScience and Technology; Springer International Publishing: Cham, Switzerland, 2015. doi:10.1007/978-3-319-10560-4
82. Hasan, M. M.; Arai, T.; Tomitori, M. *Jpn. J. Appl. Phys.* **2022,** *61,* 065006. doi:10.35848/1347-4065/ac6b02
83. Chumak, A. A.; Milonni, P. W.; Berman, G. P. *Phys. Rev. B* **2004,** *70,* 085407. doi:10.1103/physrevb.70.085407
84. Yildiz, D.; Kisiel, M.; Gysin, U.; Gürlü, O.; Meyer, E. *Nat. Mater.* **2019,** *18,* 1201–1206. doi:10.1038/s41563-019-0492-3
85. Jackson, J. D. *Classical electrodynamics,* 3rd ed.; John Wiley & Sons: Hoboken, NJ, USA, 2021.
86. Sadeghi, A.; Baratoff, A.; Goedecker, S. *Phys. Rev. B* **2013,** *88,* 035436. doi:10.1103/physrevb.88.035436
87. Orihuela, M. F.; Somoza, A. M.; Colchero, J.; Ortuño, M.; Palacios-Lidón, E. *Nanotechnology* **2017,** *28,* 025703. doi:10.1088/1361-6528/28/2/025703

## License and Terms

BEILSTEIN JOURNAL OF NANOTECHNOLOGY

# Signal generation in dynamic interferometric displacement detection

Knarik Khachatryan*, Simon Anter, Michael Reichling* and Alexander von Schmidsfeld

Full Research Paper

Open Access

Address:
Institut für Physik, Universität Osnabrück, Barbarastr. 7, 49076 Osnabrück, Germany

Email:
Knarik Khachatryan* - knarik.khachatryan@uos.de;
Michael Reichling* - reichling@uos.de

* Corresponding author

Keywords:
amplitude calibration; displacement detection; force microscopy; interferometer signal; NC-AFM

*Beilstein J. Nanotechnol.* **2024,** *15,* 1070–1076.
https://doi.org/10.3762/bjnano.15.87

Received: 08 May 2024
Accepted: 26 July 2024
Published: 20 August 2024

This article is part of the thematic issue "Advanced atomic force microscopy techniques V".

Associate Editor: E. Meyer



## Abstract

Laser interferometry is a well-established and widely used technique for precise displacement measurements. In a non-contact atomic force microscope (NC-AFM), it facilitates the force measurement by recording the periodic displacement of an oscillating microcantilever. To understand signal generation in a NC-AFM-based Michelson-type interferometer, we evaluate the non-linear response of the interferometer to the harmonic displacement of the cantilever in the time domain. As the interferometer signal is limited in amplitude because of the spatial periodicity of the interferometer light field, an increasing cantilever oscillation amplitude creates an output signal with an increasingly complex temporal structure. By the fit of a model to the measured time-domain signal, all parameters governing the interferometric displacement signal can precisely be determined. It is demonstrated, that such an analysis specifically allows for the calibration of the cantilever oscillation amplitude with 2% accuracy.

## Introduction

Optical interferometry is a reliable technique utilizing light waves to measure distance and displacement with high precision [1,2]. With the light wavelength as the length standard, a highly stable interferometer can detect displacements with an accuracy far beyond nanometer resolution [3], where the final physical limit is set by the photon emission statistics of the light source [4]. In non-contact atomic force microscopy (NC-AFM), interferometry is used to measure the periodic displacement of a (quasi) harmonically oscillating microcantilever, acting as one mirror of the interferometer, while the second mirror is the even surface of an optical fiber delivering the light to the microcantilever [5-10].

As illustrated in Figure 1, interference occurs in the optical fiber between the light beams reflected from the fiber end (reference beam) and the cantilever (cavity beam), creating a standing

wave pattern in the fiber with a spatial periodicity given by the light wavelength λ and a phase ϕ determined by the distance $d$ between the fiber end and the cantilever. Any variation in $d$ results in a variation of the intensity $I_M$ recorded by a detector placed at a fixed distance to the fiber end [11]. In our setup, there is a strong imbalance of reflectivity coefficients between fiber ($r_f$) and cantilever ($r_c$), yielding an interferometer signal with a large average $\bar{I}_M$ and a small intensity variation upon a change in $d$.

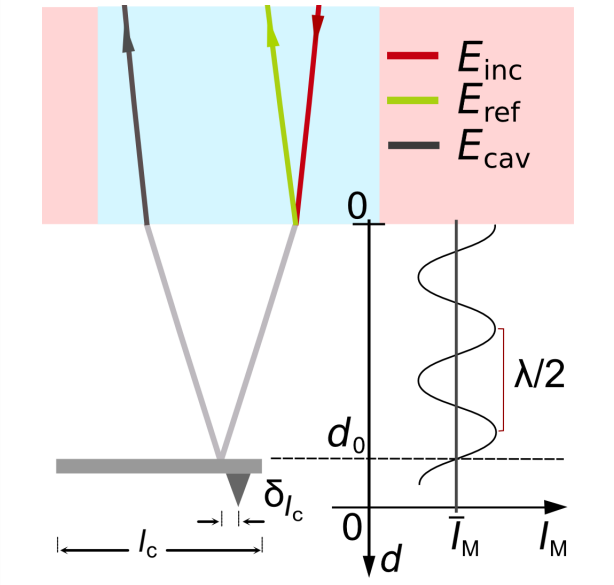


**Figure 1:** Michelson-type interferometer formed by an optical fiber end and a microcantilever. Graph and physical quantities are explained in the text.

As light exits the fiber with a certain divergence, and the fiber core has a small diameter (4 µm), there is a finite number of multiple reflections between the cantilever and fiber. At large distance $d$, this number is small, and the setup basically acts as a Michelson interferometer. Experiments reported here are performed with the dielectric/vacuum interface of the bare fiber end acting as the first mirror and a metal-coated silicon cantilever as the second mirror. We keep the fiber–cantilever distance $d$ always large enough to work in the Michelson regime characterized by a low Fabry–Pérot enhancement factor [12].

To obtain a model description of the interference light intensity at the detector, we virtually place the detector inside the fiber at its end and consider the electric field of the incident light beam $E_{inc}$ at this position, the electric field of the reference light beam $E_{ref} = r_f E_{inc}$, and the electric field reflected from the cantilever and entering the fiber $E_{cav} = t_f^2 r_c s_{loss}(2d) e^{i[\phi(d)+\pi]} E_{inc}$. As interference occurs in the fiber, the relevant transmissivity is $T_f = t_f^2$, and it depends on the polarisation for (quasi) normal incidence. The a priori unknown function $s_{loss}(2d)$ describes the loss of light in the gap between the fiber end and the cantilever due to beam divergence. The spatial variation of the electric field strength due to interference is governed by the path difference $2d$ determining the phase of the interference electric fields $\phi(d) = 2\pi\frac{2d}{\lambda}$.

Linear superposition of reference and cavity beams yields, as the intensity measured at the detector position,

$$I_M = \left\{ E_{inc} \left[ r_f - T_f r_c s_{loss}(2d) e^{i\phi(d)} \right] \right\}^2 . \quad (1)$$

By introducing the incoming light intensity $I_0 = \frac{1}{2} c \varepsilon_0 E_{inc}^2$, where $c$ is the speed of light in vacuum and $\varepsilon_0$ is the vacuum permittivity, and the reflectivities $R_f = (r_f)^2$, $R_c = (r_c)^2$ and cavity loss $S_{loss}(2d) = (s_{loss}(2d))^2$, Equation 1 is transformed into

$$I_M(d) = I_0 \Big[ R_f + (1-R_f)^2 R_c S_{loss}(2d) - 2\sqrt{R_f R_c}(1-R_f) \cdot \sqrt{S_{loss}(2d)} \cos\left(2\pi \frac{2d}{\lambda}\right) \Big], \quad (2)$$

where the transmissivity $T_f$ is substituted by $1 - R_f$, representing the law of energy conservation. A sketch of the intensity measured at the detector of the Michelson-type interferometer $I_M$ as a function of $d$ is shown in the right part of Figure 1, where the distance dependence $S_{loss}(2d)$ has been neglected. The interference pattern has a periodicity of λ/2, while the curve crosses the mean value of intensity $\bar{I}_M$ every $n\lambda/4$, where $n$ is a positive integer. Usually, the interferometer is adjusted to positions $d_0 = m\lambda/8$, where $m$ is an odd integer representing inflection points of the interference curve, where the slope of $I_M(d)$ is a maximum. Such an adjustment facilitates a most sensitive displacement detection. Note, that it is not possible to adjust the interferometer to $d_0$ with a small number $m$ because of limitations in positioning the fiber end face parallel to the cantilever surface.

Upon excitation, the freely oscillating cantilever exhibits a harmonic displacement $q(t)$ as a function of time. If a tip–surface force $F_{ts}$ is present, this will introduce a slight anharmonicity, and there will be a static displacement $q_s$ [13]. Within the harmonic approximation, which is well justified for small tip–surface forces, the cantilever displacement is [13]:

$$q(t) = q_s + A \cdot \sin(2\pi f_{exc} t), \quad (3)$$

where $A$ is the cantilever oscillation amplitude and $f_{exc}$ is the excitation frequency kept at the resonance frequency of the cantilever for frequency-modulation NC-AFM. Further taking into account that the interferometer may be misaligned by the amount $d_{err}$, we find for the time-dependent fiber-cantilever distance:

$$d(t) = d_0 + d_{err} - q(t) = d_0 + d_{err} - q_s - A \cdot \sin(2\pi f_{exc} t). \quad (4)$$

Combining Equation 2 and Equation 4 yields the time dependence of the light intensity at the detector. As the detector measures the total incident light power, we introduce the circular illuminated effective area of the detector $\pi r_{eff}^2$. The factor $f_{loss}$ takes all optical losses into account occurring in the fiber delivering the light to the cantilever and to the detector. The time domain signal of the interferometer is then given as

$$\begin{aligned} P_M(t) = f_{loss}\pi r_{eff}^2 I_0 \Big\{ & R_f + (1-R_f)^2 R_c S_{loss}(2d(t)) \\ & + 2\sqrt{R_f R_c}(1-R_f)\sqrt{S_{loss}(2d(t))} \\ & \cdot \sin\left[\frac{4\pi}{\lambda}\begin{pmatrix} d_0 + d_{err} - q_s \\ -A\cdot\sin(2\pi f_{exc} t)\end{pmatrix} - \frac{\pi}{2}\right]\Big\}. \end{aligned} \quad (5)$$

Analyzing the result, we find that the characteristics of the oscillatory part of $P_M$ is determined by the ratio between the cantilever oscillation amplitude $A$ and the wavelength λ. For $A \ll \lambda/8$, the detector signal oscillates quasi-sinusoidal with the fundamental frequency $f_{exc}$; for $A \approx \lambda/8$, the signal is a strongly distorted sine and when increasing the amplitude further, the signal is more and more dominated by higher-frequency oscillations. Exemplary waveforms are shown schematically below in Figure 4.

## Results and Discussion

The interferometer used for our experiments is part of a custom-built NC-AFM, operated under ultrahigh-vacuum (UHV) conditions [14]. The cantilever is a highly reflective ($R_c$ = 0.81) aluminum-coated silicon microcantilever (type PPP-NCLR, NanoWorld AG, Neuchâtel, Switzerland) having dimensions of (225 ± 10) µm × (38 ± 8) µm × (7 ± 1) µm according to the specification of the manufacture. Using our standard procedure [15], we determined the eigenfrequency as $f_0$ = 169.67622 kHz and a quality factor of $Q$ = 9000. After transfer of the cantilever, which is glued to a cantilever holder, the cantilever is mechanically firmly attached to the AFM scan head, while the optical fiber and the sample are approached to the cantilever and the tip by piezoelectric motors for coarse motion [16] and tube piezos [17] for fine positioning in all directions. The scanhead with cantilever, sample support, and the respective motion elements are shown in Figure 2a. The fine adjustment of $d$ is accomplished by the fiber tube piezo, which is in its relaxed position at $z_f$ = 0, according to the coordinate system given in Figure 2b. Note, that the tube piezo allows for an adjustment of $d$ with high accuracy; however, the absolute distance between the fiber end and the cantilever can practically neither be set nor measured. The interferometer is adjusted to a fairly large value $d_0$ to assure operation in the Michelson mode resulting in a detector signal $I_M$ that is much smaller than what could be obtained by working in the Fabry–Pérot mode [12].

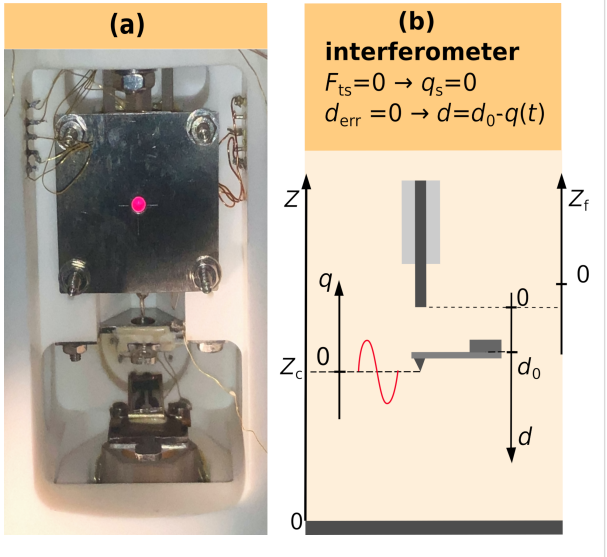


**Figure 2:** (a) Photo of the AFM scanhead showing the fiber and fiber coarse approach assembly (top), the removable cantilever holder (middle) and the sample plate with a mirror inserted for inspection purposes (bottom). (b) Coordinates for fiber movement $z_f$, fiber cantilever distance $d$ and cantilever displacement $q$ in relation to the tip–sample coordinate $z$ [18]. The cantilever is shown in its relaxed position where the static displacement $q_s$ = 0 and $A\sin(2\pi f_{exc}t)$ = 0. Note, that the origin of the $d$-axis is fixed at the fiber end. The interferometer yields maximum sensitivity for $d = d_0$ as explained in the text.

A temperature- and intensity-stabilized laser diode light source (type 48TA-1-42037, Schäfter + Kirchhoff GmbH, Hamburg, Germany) operating at a vacuum wavelength of λ = 796.42 nm delivers the light to the cantilever via a single-mode optical fiber (type Hi780, Corning Inc., New York, USA) with a core having a refractive index of $n_f$ = 1.45 and 4 µm diameter. Before entering the UHV system, the light passes a 3 dB beam splitter, where it is divided into two beams with almost identical power. The first part is directed to a power meter for control purposes, while the second part is guided to the interferometer in the UHV [11]. The fiber end in the interferometer is carefully cleaved to achieve high optical quality for the dielectric/vacuum interface having a reflectivity of $R_f$ = 0.04. The fourth end of the 3 dB coupler is connected to the detector,

which is a photoreceiver (model HBPR-200M-30K-SI-FC, FEMTO Messtechnik, Berlin, Germany) converting the incoming light power into a voltage signal. The photoreceiver allows for high-sensitivity low-noise measurements of DC and AC signals with a bandwidth of 200 MHz.

The interferometer is precisely aligned via a tube piezo controlled by the R9 control system (RHK Technology Inc., Troy, MI, USA). Cantilever excitation with a sine wave voltage with a well-defined amplitude $V_{exc}$ and overall experiment control is accomplished by a HF2LI (Zurich Instruments, Zürich, Switzerland). Experiments are performed with the freely oscillating cantilever. Therefore, the cantilever excitation frequency $f_{exc}$ is set to the eigenfrequency of the cantilever, which is determined by taking a resonance curve before each experiment. By temperature stabilisation of the laboratory and the scan head, care is taken to avoid any thermal drift of the cantilever eigenfrequency that might compromise measurements. A model MDO3000 oscilloscope (Tektronix Inc., Beaverton, OR, USA) is used to record the AC output signal of the photoreceiver, $V_{sig}$, which is a voltage between 0 and 10 m$V_{pp}$ with a typical noise level of less than 150 μ$V_{RMS}$. Time traces with a length of 4 μs at a sampling rate of 250 MS/s are taken and quantized with a resolution of 10 bits. Each experiment comprises a set of 20 to 30 measurements with the excitation voltage amplitude $V_{exc}$ ramped from 0 to 7 V. This voltage is reduced by a 100:1 voltage divider before it is applied to the excitation piezo. For each amplitude, 512 traces of $V_{sig}$ are taken and averaged, where the start of sampling is triggered by the zero crossing of the low-noise sinusoidal cantilever excitation voltage signal recorded on the second oscilloscope channel.

For data evaluation, a simplified form of Equation 5 is fitted to the averaged trace for each amplitude. In the fit function of Equation 6, linearly depending parameters are gathered into one

$$V_{sig} = V_{DC} + V_0 \sin\left\{\frac{4\pi}{\lambda}\left[D - A\cdot\sin\left(2\pi f_s t - \varphi\right)\right] - \frac{\pi}{2}\right\}, \quad (6)$$

where $V_{DC}$ represents the constant part of the interferometer signal voltage, $V_0$ the voltage amplitude of the interference signal oscillation, $D = d_0 + d_{err} - q_s$ the actual distance of the center of oscillation from the fiber end, $f_s$ the frequency referenced to the time base of the oscilloscope, and φ a phase factor covering any phase shift introduced by the electronics in the signal path. The time dependence of $S_{loss}$ is neglected as it is of minute influence on the amplitudes used here. However, for experiments with a very large amplitude, it is expected to influence the interference signal.

We find that Equation 6 fits the experimental data for all amplitudes perfectly, as demonstrated for one example in Figure 3. However, for lower amplitudes, the fit does not yield physically meaningful results because of the mutual dependence of the parameters $V_0$, $A$, and φ. We find, for instance, that the fit value of $V_0$ exhibits a dependence on $V_{exc}$, while it is evident from Equation 5 that $V_0$ should be a constant solely determined by system parameters. To yield the correct value $V_0^{lim}$, we plot the peak-to-peak amplitude $V_{pp}$ of the $V_{sig}$ fit curve (see Figure 3) as a function of $V_{exc}$, as shown in Figure 4. We find that $V_{pp}$ first rises with amplitude and then saturates at the amplitude limit $2V_0^{lim}$ (red arrow in Figure 4). A parameter that can reliably be deduced from the fit is $f_s$ as this is the characteristic fundamental frequency of the signal. In the second step of data evaluation, we perform a fit of the same fit function to the same experimental data, however, with a reduced number of fit parameters. In this fit, $V_0^{lim}$ and $f_s$ are taken over as fixed values from the first fit, while the other parameters are treated as free fit parameters. This two-step procedure allows us to determine all signal parameters with high accuracy.

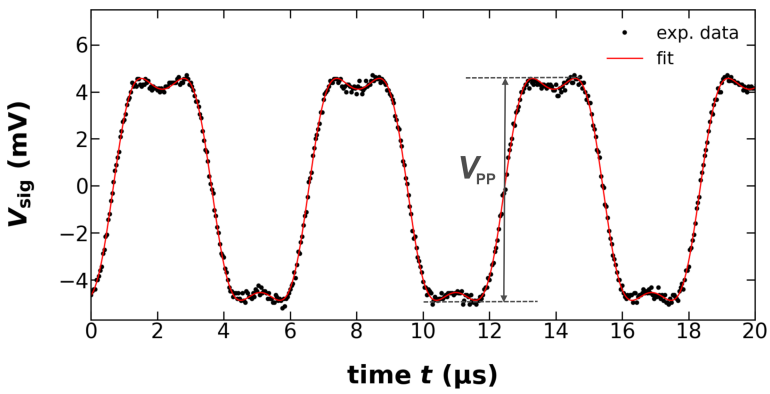


**Figure 3:** Fit of the model for the interferometer signal voltage $V_{sig}$ according to Equation 6 to experimental data. The cantilever excitation piezo voltage amplitude is $V_{exc}$ = 4.25 V corresponding to an amplitude $A$ = 86.61 nm.

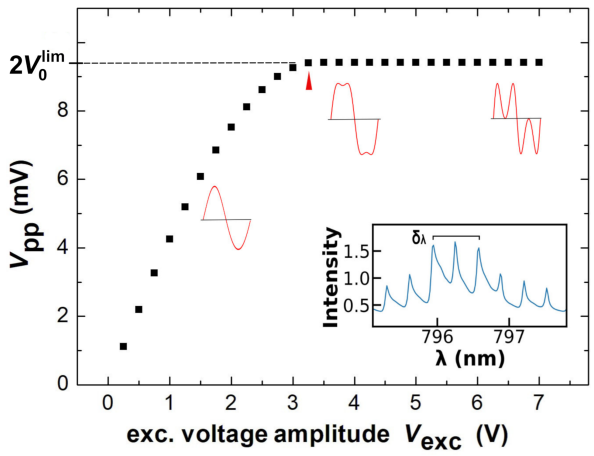


**Figure 4:** Peak-to-peak amplitude $V_{pp}$ of $V_{sig}$ (see Figure 3) as a function of the cantilever excitation voltage amplitude $V_{exc}$. The red arrow points to the onset of saturation. The insets show three typical waveforms for $I_M(t)$ ($V_{exc}$ = 1.75, 4, and 7 V) and the central part of the laser diode mode spectrum, with the wavelength representing the vacuum wavelength.

As the interferometric method is perfectly suited for the calibration of the cantilever oscillation amplitude, we exemplify the fit procedure and accuracy limits for the fit parameter $A$. Amplitude calibration means to relate the cantilever oscillation amplitude $A$ to the voltage $V_{exc}$ to yield the calibration factor $S = A/V_{exc}$ [18]. An accurate calibration is essential for quantitative NC-AFM; therefore, various methods have been suggested to determine the calibration factor $S$ [10,19-22]. There is a simple and rough, but commonly used, method of calibration of the cantilever displacement by an interferometer, which is based on the measurement shown in Figure 4. This method uses just the data point for the excitation amplitude $V_{exc}(A = \lambda/8)$, where saturation in $V_{pp}$ occurs (red arrow in Figure 4), indicating that the oscillation exactly covers one fringe with $-\lambda/8 \leq q \leq +\lambda/8$. For the experiment discussed here, such calibration yields $S$ = 20.38 nm/V. However, from Figure 4 it is clear that the precision of this value is limited as the λ/8 point is not well defined.

Figure 5 illustrates the enhancement in accuracy that can be achieved by applying the two-step fit procedure for data analysis. In this plot of $A(V_{exc})$, measurements taken at all amplitudes are included and fitted by a straight line. The green and blue curves represent measurements taken over two days, where the optical fiber has been re-adjusted slightly between the measurements. The curves (circle and triangle) represent data analyzed by a single fit, where the green curve represents the same data as those shown in Figure 4. Both measurements yield a linear behavior, however, with a somewhat different slope and, therefore, different calibration factors, which is due to the fiber re-adjustment. The residuals plotted in the lower part of the figure demonstrate that measurements are free of any significant noise [23]; however, we find a smooth undulation of the experimental values around zero, which stems from the residual mutual dependence of the fit parameters. The red curve (squares) represents the fit results for the data from the green curve treated with the two-step procedure. The analysis of the residuals reveals that the second step of data processing reduces, but cannot fully remove, the undulation.

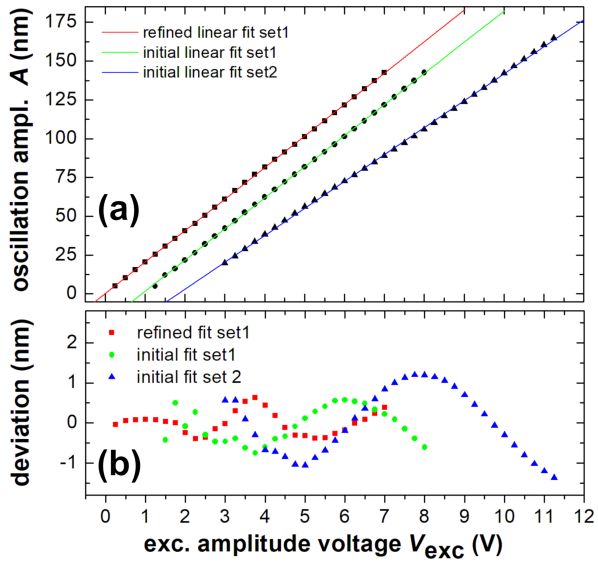


**Figure 5:** (a) The cantilever oscillation amplitude $A$ is derived from the linear fit of Equation 6 to experimental time traces $V_{sig}(t)$ as a function of the excitation voltage amplitude $V_{exc}$ (squares, circles, and triangles). Straight lines are linear fits of $A(V_{exc})$ data taken in two different measurement runs and one that underwent two different analysis procedures. (b) Residuals of the oscillation amplitudes with respect to the linear fit. Note, that the green and blue data are shifted by 1 V along the $V_{exc}$ axis for better visibility of the graphs.

At first sight, the undulation as a systematic error appears as the major limitation for the accuracy in determining the calibration factor $S$. An extended analysis of several sets of data covering a large range of amplitudes yields, however, that the effect of the undulation can be reduced to a negligible effect by a proper choice of the analyzed range of amplitudes. This is achieved by restricting the analysis to a range of amplitudes, where the undulating behavior yields a compensation of positive and negative deviations from the straight line. To obtain limits for the precision and accuracy of the result for the amplitude calibration factor, we consider four contributions to the error in $S$, which are expressed in the following formula of error propagation for the linear fit [24]:

$$\delta_S = S\sqrt{\left(\frac{\delta_{V_{exc}}}{V_{exc}}\right)^2 + \left(\frac{\delta_A}{A}\right)^2 + \left(\frac{\delta_\lambda}{\lambda}\right)^2 + \left(\frac{\delta_{l_c}}{l_c}\right)^2}, \qquad (7)$$

where $\delta_{V_{\mathrm{exc}}}/V_{\mathrm{exc}} = 0.010$ is the excitation voltage output uncertainty according to the HF2 specification. To take care of the systematic error due to the dependency in fit parameters, we determine $\delta_A/A = 0.0004$ as the mean of the residuals in $A$ divided by the mean value of $A$, determined as an oscillation amplitude error. The relative error in the wavelength measurement is $\delta_\lambda/\lambda = 0.00075$ as detailed below. The error in the adjustment of the light spot on the cantilever with length $l_c$ is the positioning error $\delta l_c = 5$ µm, which is the distance between the laser spot position and the tip position as illustrated in Figure 1. This error is estimated by visual inspection of a CCD camera image of the fiber–cantilever gap, and we find $\frac{\delta l_c}{l_c} = 0.022$. To estimate the wavelength error $\delta_\lambda$, we performed a careful measurement of the laser diode light wavelength λ with a spectrograph (Acton series SP-2500i-2556, Princeton Instruments, USA), which has been calibrated by 40 atomic lines distributed over the entire visible spectrum to yield an accurate value for the wavelength at a spectral resolution of 0.050 nm. As evident from the multimode spectrum of the laser diode light source shown in the inset of Figure 4, the spectrum is dominated by three modes with a center at the vacuum wavelength λ = 796.49 nm. Assuming that interference occurs in the optical fiber, we calculate the laser wavelength in the fiber with $n = 1.45$ as $\lambda_f = 549.3$ nm for oscillation amplitude calibration. We take the spectral distance of the two neighboring lines as a conservative estimate for the wavelength error $\delta_\lambda = 0.41$ nm. Note, that the errors $\delta_{V_{\mathrm{exc}}}$ and $\delta_A$ are not independent variables. We treat them separately as $\delta_{V_{\mathrm{exc}}}$ is a statistical error, while $\delta_A$ represents an additional systematic error due to the residuals in the linear fit of $A(V_{\mathrm{exc}})$. Taking these error margins into account, we obtain the final result for the amplitude calibration factor $S = (20.30 \pm 0.49)$ nm/V.

## Conclusion

In summary, we derived a model for the description of the time domain signal of a Michelson-type interferometer used to measure the displacement of a (quasi) harmonically oscillating microcantilever in an NC-AFM. The analysis demonstrates that the interferometer signal is a non-trivial function of the cantilever excitation, where increasing excitation amplitude is translated into increasing non-linearity and complexity of the response signal. A fit of the derived response function to experimental data yields excellent results for all system parameters. However, care has to be taken to minimize systematic errors resulting from the mutual dependence of fit parameters. The method specifically allows one to determine the cantilever oscillation amplitude calibration factor with a 2.4% relative error. This is way better than what can be achieved with a calibration based on the widely used γ-method [19]. We recently investigated the precision of the γ-method in detail and found that it is intrinsically prone to systematic error, where an error of 15% may result under realistic experimental conditions [25]. The strength of the interferometric calibration is the high precision that can be achieved as the calibration of the amplitude can be traced to the light wavelength, which can be measured most precisely and accurately. The error analysis shows that the weakest point relevant for NC-AFM measurements is the accurate positioning of the light beam at the position of the tip. In experiments, as introduced here, noise is not a limiting factor for the quantitative evaluation of the interferometric signal, and there is still room for improvement by optimising the experimental setup.

## Author Contributions

Knarik Khachatryan: conceptualization; data curation; formal analysis; investigation; methodology; resources; software; visualization; writing – original draft. Simon Anter: resources. Michael Reichling: conceptualization; formal analysis; project administration; supervision; writing – review & editing. Alexander von Schmidsfeld: conceptualization; writing – review & editing.

## ORCID® iDs

Knarik Khachatryan - https://orcid.org/0009-0006-8403-7274
Simon Anter - https://orcid.org/0009-0005-9649-6622
Michael Reichling - https://orcid.org/0000-0003-3186-9000

## Data Availability Statement

Data available upon request from the authors.

## Preprint

A non-peer-reviewed version of this article has been previously published as a preprint: https://doi.org/10.3762/bxiv.2024.29.v1

## References

1. Yang, S.; Zhang, G. *Meas. Sci. Technol.* **2018,** *29,* 102001. doi:10.1088/1361-6501/aad732
2. Bond, C.; Brown, D.; Freise, A.; Strain, K. A. *Living Rev. Relativ.* **2016,** *19,* 3. doi:10.1007/s41114-016-0002-8
3. Buikema, A., et al. *Phys. Rev. D* **2020,** *102,* 062003. doi:10.1103/physrevd.102.062003
4. Heinze, J.; Danzmann, K.; Willke, B.; Vahlbruch, H. *Phys. Rev. Lett.* **2022,** *129,* 031101. doi:10.1103/physrevlett.129.031101
5. Rugar, D.; Mamin, H. J.; Erlandsson, R.; Stern, J. E.; Terris, B. D. *Rev. Sci. Instrum.* **1988,** *59,* 2337–2340. doi:10.1063/1.1139958
6. Hoogenboom, B. W.; Frederix, P. L. T. M.; Yang, J. L.; Martin, S.; Pellmont, Y.; Steinacher, M.; Zäch, S.; Langenbach, E.; Heimbeck, H.-J.; Engel, A.; Hug, H. J. *Appl. Phys. Lett.* **2005,** *86,* 074101. doi:10.1063/1.1866229
7. Hoogenboom, B. W.; Frederix, P. L. T. M.; Fotiadis, D.; Hug, H. J.; Engel, A. *Nanotechnology* **2008,** *19,* 384019. doi:10.1088/0957-4484/19/38/384019
8. Morita, K.; Sugimoto, Y.; Sasagawa, Y.; Abe, M.; Morita, S. *Nanotechnology* **2010,** *21,* 305704. doi:10.1088/0957-4484/21/30/305704

9. Karci, O.; Dede, M.; Oral, A. *Rev. Sci. Instrum.* **2014,** *85,* 103705. doi:10.1063/1.4897147
10. Çelik, Ü.; Karcı, Ö.; Uysallı, Y.; Özer, H. Ö.; Oral, A. *Rev. Sci. Instrum.* **2017,** *88,* 013705. doi:10.1063/1.4973819
11. von Schmidsfeld, A.; Nörenberg, T.; Temmen, M.; Reichling, M. *Beilstein J. Nanotechnol.* **2016,** *7,* 841–851. doi:10.3762/bjnano.7.76
12. von Schmidsfeld, A.; Reichling, M. *Appl. Phys. Lett.* **2015,** *107,* 123111. doi:10.1063/1.4931702
13. Söngen, H.; Bechstein, R.; Kühnle, A. *J. Phys.: Condens. Matter* **2017,** *29,* 274001. doi:10.1088/1361-648x/aa6f8b
14. Tröger, L. *Aufbau eines Tieftemperatur-Rasterkraftmikroskopes;* Sierke Verlag, 2009. Thesis, Universität Osnabrück, Germany.
15. Lübbe, J.; Tröger, L.; Torbrügge, S.; Bechstein, R.; Richter, C.; Kühnle, A.; Reichling, M. *Meas. Sci. Technol.* **2010,** *21,* 125501. doi:10.1088/0957-0233/21/12/125501
16. Drevniok, B.; Paul, W. M. P.; Hairsine, K. R.; McLean, A. B. *Rev. Sci. Instrum.* **2012,** *83,* 033706. doi:10.1063/1.3694972
17. Moheiman, S. O. R. *Rev. Sci. Instrum.* **2008,** *79,* 071101. doi:10.1063/1.2957649
18. Rahe, P.; Heile, D.; Olbrich, R.; Reichling, M. *Beilstein J. Nanotechnol.* **2022,** *13,* 610–619. doi:10.3762/bjnano.13.53
19. Simon, G. H.; Heyde, M.; Rust, H.-P. *Nanotechnology* **2007,** *18,* 255503. doi:10.1088/0957-4484/18/25/255503
20. Sugimoto, Y.; Nakajima, Y.; Sawada, D.; Morita, K.-i.; Abe, M.; Morita, S. *Phys. Rev. B* **2010,** *81,* 245322. doi:10.1103/physrevb.81.245322
21. Martínez, J. F. G.; Nieto-Carvajal, I.; Colchero, J. *Nanotechnology* **2013,** *24,* 185701. doi:10.1088/0957-4484/24/18/185701
22. Dagdeviren, O. E.; Miyahara, Y.; Mascaro, A.; Grütter, P. *Rev. Sci. Instrum.* **2019,** *90,* 013703. doi:10.1063/1.5061831
23. Lübbe, J.; Temmen, M.; Rode, S.; Rahe, P.; Kühnle, A.; Reichling, M. *Beilstein J. Nanotechnol.* **2013,** *4,* 32–44. doi:10.3762/bjnano.4.4
24. Hughes, I. G.; Hase, T. P. A. *Measurements And Their Uncertainties;* Oxford University Press, 2009.
25. Heile, D.; Olbrich, R.; Reichling, M.; Rahe, P. *Phys. Rev. B* **2021,** *103,* 075409. doi:10.1103/physrevb.103.075409


## License and Terms

BEILSTEIN JOURNAL OF NANOTECHNOLOGY

# Local work function on graphene nanoribbons

Daniel Rothhardt[1,2,3], Amina Kimouche[*1], Tillmann Klamroth[4] and Regina Hoffmann-Vogel[*1]

Letter

Open Access

Address:
[1]Institute of Physics and Astronomy, University of Potsdam, Karl-Liebknecht-Str. 24–25, 14476 Potsdam-Golm, Germany, [2]current address: Swiss Federal Laboratories for Materials Science and Technology, CH-8600 Dübendorf, Switzerland, [3]current address: Department of Physics, University of Basel, CH-4056 Basel, Switzerland and [4]Institute of Chemistry, University of Potsdam, Karl-Liebknecht-Str. 24–25, 14476 Potsdam-Golm, Germany

Email:
Amina Kimouche[*] - Amina.Kimouche@uni-potsdam.de;
Regina Hoffmann-Vogel[*] - Regina.Hoffmann-Vogel@uni-potsdam.de

* Corresponding author

Keywords:
graphene nanoribbons; Kelvin probe force microscopy; local contact potential difference

*Beilstein J. Nanotechnol.* **2024,** *15,* 1125–1131.
https://doi.org/10.3762/bjnano.15.91

Received: 09 April 2024
Accepted: 30 July 2024
Published: 29 August 2024

This article is part of the thematic issue "Advanced atomic force microscopy techniques V".

Associate Editor: T. Glatzel



## Abstract

Graphene nanoribbons show exciting electronic properties related to the exotic nature of the charge carriers and to local confinement as well as atomic-scale structural details. The local work function provides evidence for such structural, electronic, and chemical variations at surfaces. Kelvin prove force microscopy can be used to measure the local contact potential difference (LCPD) between a probe tip and a surface, related to the work function. Here we use this technique to map the LCPD of graphene nanoribbons grown on a Au(111) substrate. The LCPD data shows charge transfer between the graphene nanoribbons and the gold substrate. Our results are corroborated with density functional theory calculations, which verify that the maps reflect the doping of the nanoribbons. Our results help to understand the relation between atomic structure and electronic properties both in high-resolution images and in the distance dependence of the LCPD.

## Introduction

Graphene's electronic properties are determined by its two-dimensionality as well as by its semimetallic gapless conical band structure [1]. Its electronic behavior depends strongly on the location of the Fermi level with respect to the Dirac point, the center of the Dirac cones [2]. The location of the Fermi level is a measure of the work function with respect to a different energy reference, the vacuum energy. This position can be tuned by gating [3] or by doping, for example, n-doping for graphene on SiC [4,5] and p-doping by Bi, Sb, and Au substrates [2]. Confining graphene to nanostructures [6,7], for example, to graphene nanoribbons (GNRs), that is, few nanometers wide stripes of graphene, opens additional possibilities of tuning the electronic properties by creating quantum-confined states [8] and opening a size-dependent energy gap [6,9]. As in graphene, the Fermi level of GNRs is also strongly influenced by charge transfer between the substrate and the GNR [10],

again related to differences in the work function. Here, we take the work function as a local property influenced by local charge, that is, by the local electrochemical potential. GNRs show strong electrostatic effects at their edges [11], where electrostatic forces occur that we expect to modulate the electrons' local electrochemical potential. Additionally, the chemical state of GNR edges allows one to substantially tune the bandgap [12], which is also related to the work function. GNRs can be synthesized with atomic precision in an ultrahigh-vacuum environment using on-surface synthesis [13]. This synthesis is well known on coinage metals, namely, Cu, Ag, and Au, which possess a high electron density.

To study these unique electronic properties, a suitable method to study the charge transfer, that is, the local work function, between a GNR and a metal substrate at the atomic scale is needed. In general, as detailed above, the local work function can provide evidence for structural, electronic, and chemical variations at surfaces, all related to charge differences; for a review, see [14]. Kelvin probe force microscopy (KPFM), a method derived from scanning force microscopy (SFM), allows one to study the local work function difference of a sample with great accuracy and with atomic resolution [15-20]. In KPFM, a voltage is applied to the tip in order to compensate electrostatic forces occurring between tip and sample. Such electrostatic forces arise from the different positions of the Fermi level in tip and sample, which give rise to charge transfer. In KPFM, the forces are measured by SFM during image acquisition [21,22]. In this way, an image of the local contact potential difference between tip and sample is obtained. This has been shown not only for general surfaces, for example, insulating surfaces, but also for molecules and molecular layers [18,23-25].

Here, we study the local work function difference of graphene nanoribbons fabricated by on-surface synthesis on Au(111). The GNRs can be clearly discerned from the substrate through their topography, but also through their contact potential difference. GNRs have a measured contact potential that is about 100 meV smaller than that of a Au. Variations in the measurement reveal local work function differences, which are ascribed to the Fermi level shift resulting from the charge transfer between the GNR and the Au substrate. Our results indicate that GNRs are positively charged compared to Au. This is confirmed by calculations and by distance-dependent measurements.

## Experimental

The experiments were conducted in an Omicron VT-SFM system (base pressure $2 \times 10^{-10}$ mbar). The Au(111) single crystal substrate (Mateck GmbH) was cleaned by repeated Ar ion sputtering–annealing cycles. The cleanliness of the samples was checked by SFM measurements. Then, 10,10′-dibromo-9,9′-bianthryl (DBBA) molecules were deposited by thermal evaporation (Kentax evaporator) onto the hot ($T_{\text{sample}}$ = 470 K) sample surface for 10 min. The deposition rate was kept constant using a quartz crystal microbalance. Annealing up to 670 K for 10 min after deposition induced cyclodehydrogenation and the formation of GNRs following [13,26]. The sample was introduced into our SFM attached to the same vacuum chamber, which was cooled down to 115 K using liquid nitrogen. Nanosensors Si tips (resonance frequency $f_0$ = 158 kHz and longitudinal force constant $c_L$ = 45 N/m) and PtIr-coated tips ($f_0$ = 292 kHz, $c_L$ = 41 N/m) were used for imaging in the frequency modulation (FM) mode operated by a Nanonis electronic system. The tips were cleaned by sputtering (Ar pressure $5 \times 10^{-3}$ Pa, energy 1 keV, 15 min) and annealing up to 375 K for 1–5 h (pressure below $1 \times 10^{-7}$ Pa) prior to measurement. KPFM imaging was performed in parallel to topographic imaging using an AC excitation voltage of $V_{AC}$ = 600–900 mV with $f_{AC}$ = 166–730 Hz measured by a lock-in amplifier. AC and DC biases were applied to the sample. In general, the polarity of the KPFM measurements depends on whether the voltage is applied to the tip or to the surface and on the polarity of the voltage applied. In order to ensure that the values and the polarity are compatible with previous results [20,27], the measured results were cross-checked on well-known surfaces, that is, Si(111) and Pb on Si(111). For the average taken over several measurements of the local potential difference (LCPD) shown below, we have mainly used PtIr tips and only a few Si tips since the results obtained in a previous work did not show any difference between metal-coated and non-coated Si-tips [27]. For this work, we assume that the non-coated Si-tips were covered by Au from the sample surface because of tip–sample interactions as we have observed a tip–sample contact prior to taking the data used here.

All calculations were done using the Vienna Ab initio Simulation Package [28,29] (vasp-5.4.4) with the PBE functional [30] and a projector-augmented plane-wave basis (PAW) [31,32]. Dispersion forces are included through Grimmes D3 method [33] with Becke–Jonson damping [34] (IVDW = 12). Further, we include non-spherical contributions from the gradient corrections inside the PAW spheres (LASPH = .TRUE.). For all slab calculations, the lowest gold layer was fixed using the optimized bulk lattice constant ($a_{Au}$ = 0.2897 nm). The initial positions for the geometry optimizations were chosen according to the structure reported in [35]. Section I of Supporting Information File 1 shows further details about the geometry of the calculations.

We calculate the local work function $\Phi(\underline{r})$ from the Hartree potential $V_{\text{eff}}(\underline{r})$ corrected by the Fermi energy, that is, $\Phi(\underline{r}) = V_{\text{eff}}(\underline{r}) - E_{\text{Fermi}}$ as done in [20]. We use different con-

stant values of $z$ for the LCPD maps. $\underline{z}$ is parallel to $\underline{c}$, $\underline{x}$ is parallel to $\underline{a}$, that is, the long axis of the GNR, and $\underline{y}$ is parallel to $\underline{b}$. The LCPD maps are derived from

$$\Phi^{(s)}(x,y) = \Phi(x,y,z_{\text{surf}} + s), \tag{1}$$

where $z_{\text{surf}}$ is given by the $z$ coordinate of the uppermost carbon atom of the GNR. $s$ is varied from 0.17 to 1.2 nm. Additional details about the density functional theory (DFT) calculations performed in this work are given in Supporting Information File 1.

## Results and Discussion

A topographic image of GNRs on the Au surface is shown in Figure 1a. While most GNRs are attached to gold step edges or to other ribbons, we additionally observe isolated individual ribbons. When the tip and the GNR are brought close together, electrostatic forces between tip and sample can be measured. Also, charges can equilibrate, the Fermi levels of tip and surface align, accompanied by an electron flow to the Au, and the GNR is charged, leading to additional electrostatic forces (Figure 1b). During imaging, a voltage is applied in order to compensate for these additional electrostatic forces at each point of the image, leading to a LCPD map.

In Figure 1c, $\Delta f(V)$ curves measured above a GNR and Au are shown. The maxima of the parabolae fitted to the measured data yield the difference of the LCPD values, $\Delta V$ = 120 mV. Since no impurities have been introduced, the LCPD indicates a charge transfer from the substrate (“p-type doping”), also seen in bulk graphene on a gold substrate [2,36-38].

Figure 2 shows a topographic image of GNRs on Au(111) surface and its associated LCPD map. In the LCPD map (Figure 2c), GNRs appear as blue stripes on the yellow Au(111) background. From the line profile taken across the ribbon indicated in Figure 2d, we deduce a contact potential difference of 145 mV between the GNR and the Au surface. In Figure 2c, some inhomogeneities of the LCPD along the GNR can be observed, with darker regions appearing along its length. Additionally, some irregularities such as kinks or defects at the edge are observed in the topography measurement. For example for the GNR where the cross section has been taken, marked by a black line, there is a kink associated with a darker region in the local work function, and in the topography image there are some small bright extensions at the side of the GNR also associated with darker regions of the LCPD of the GNR. The electronic states of kinks in GNRs have been studied on a narrower type of GNR in [39]. Only small modifications of their electronic structure have been found. Here, we show that small

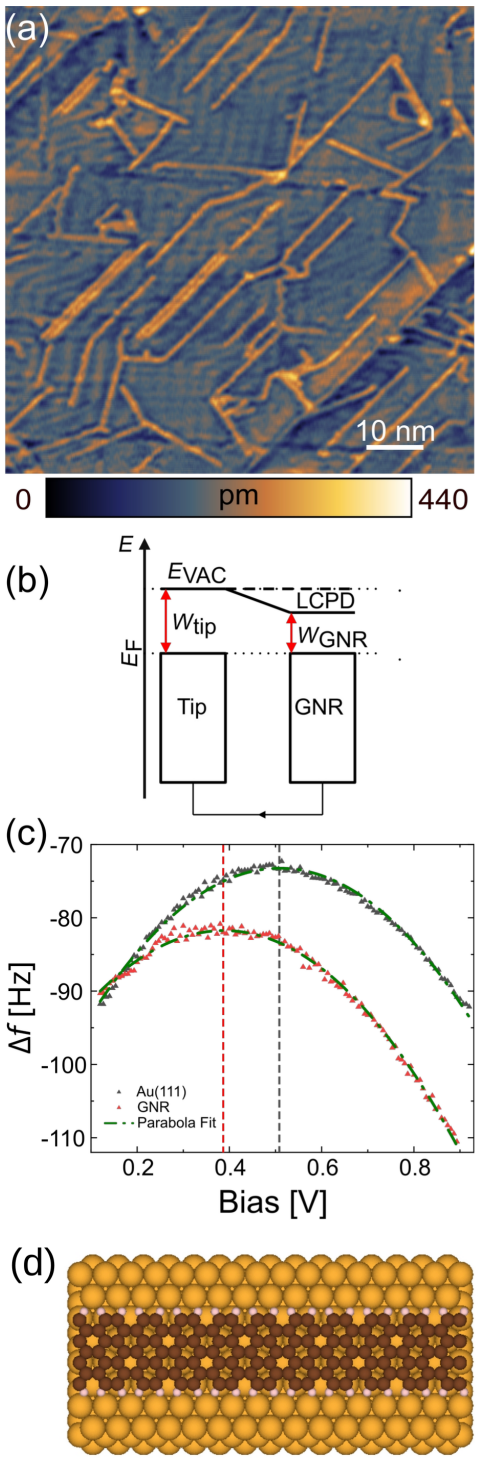


**Figure 1:** (a) Topography image of GNRs on Au, measured with a Si tip, $f_0$ = 170.91 kHz, $c_L$ = 40 N/m, $A$ = 1 nm, $Q$ = 20,000, and $\Delta f$ = –21 Hz. (b) In KPFM, local variations in contact potential (CPD) can be measured by applying a voltage between the sample and the AFM tip so that the electric field caused by the CPD is compensated. (c) $\Delta f(V)$ measurements using a PtIr-coated tip along with their second-order polynomial fit measured on GNR and Au. The dashed vertical lines indicate the respective values of the CPD. (d) Scheme of the GNR on Au.

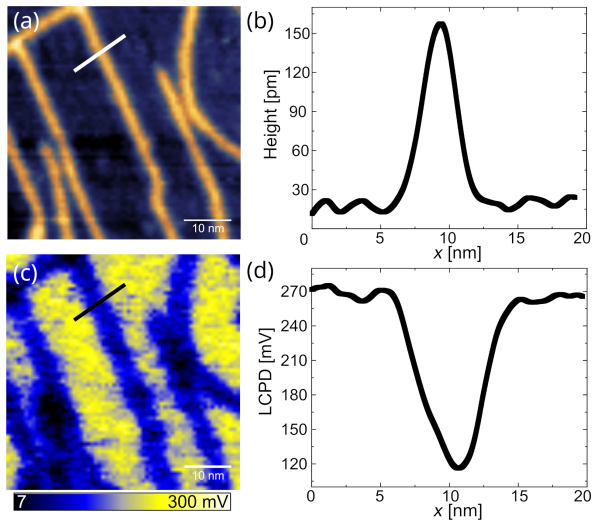


**Figure 2:** (a) Topography of GNR's and the Au(111) herringbone reconstruction, PtIr-coated tip, $f_0$ = 291.52 kHz, $c_L$ = 41 N/m, $A$ = 3 nm, $Q$ = 21 000, and $\Delta f$ = –45 Hz. (b) Line cut through the topographic image at the position indicated by the white line. (c) LCPD image recorded simultaneously with the topographic image, $f_{AC}$ = 730 Hz and $V_{AC}$ = 900 mV. (d) LCPD line profile taken across a ribbon (black).

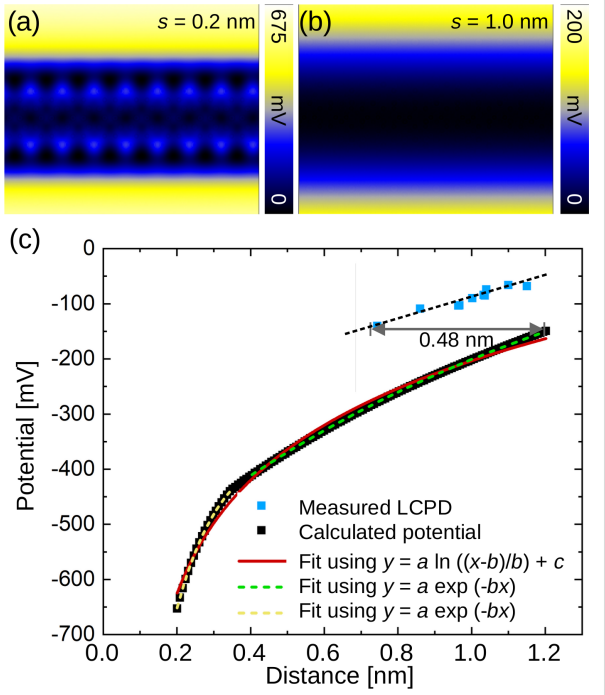


**Figure 3:** (a,b) Calculated LCPD maps at distances of $s$ = 0.2 and 1.0 nm from the GNR plane. (c) $\overline{\text{LCPD}}$ values on GNR/Au (blue squares) versus distance in comparison with calculated local potential values (black squares). The dashed black line serves as a guide to the eye, whereas the red, dashed green, and dashed yellow curves are fits to the data as described in the text.

structural modifications and the associated changes of the electronic states additionally cause a change in the local work function.

Figure 3a,b shows local work function difference maps calculated from the Hartree potential of GNR/Au(111). To match the calculated and the measured values, it is necessary to take the difference with respect to a point of reference, here, the Au surface. In the calculations we did not represent the Au herringbone reconstruction, because this is computationally very demanding [40]. At large distances (Figure 3b), the GNR appears as a featureless depression. When the surface is approached and the distance $s$ is reduced, the GNR submolecular structure is observed with increasing intensity (see Figure 3a,b and Supporting Information File 1, Figure S1d).

To obtain a more detailed understanding of the charge transfer and for comparison of the experimental results with calculations, we have performed measurements at different frequency shifts. We have then measured a force–distance curve to match each frequency shift to a distance to the sample surface (see Supporting Information File 1, Section II). We show the data in Figure 3c together with the calculated results. With this approach using an average over several measurements (over 257 LCPD line scans), the influence of the tip and sample microstructures on the resulting overall values is minimized. Additionally, $\overline{\text{LCPD}}$ is measured with respect to the reference LCPD recorded on the Au(111) surface to account for variations of the tip contact potential. Again the LCPD of the GNR is negative, and the predicted hole doping is confirmed. In Figure 3c, the $\overline{\text{LCPD}}$ values exhibit a slow decrease towards more negative values with decreasing tip–sample distance. Depending on the tip–sample distance, $\overline{\text{LCPD}}$ varies from 130 mV for 0.74 nm tip–sample distance to 70 mV for 1.18 nm. These features are consistent with previous results revealing a distance dependence of the LCPD or the electrostatic forces [41-44].

In general, we expect an exponential decay of the electrostatic field 2D Fourier components, where the decay constant λ is the lateral wavelength of the respective 2D Fourier component [45], that is,

$$\Phi(z) = A_0 \exp\left(-(z - z_0)/\lambda\right) + \Phi_0, \qquad (2)$$

where $A_0$ and $z_0$ are parameters to adjust the tip–sample distance, one of which is redundant, λ is the decay constant, and $\Phi_0$ is a parameter that allows one to adjust for a different choice of the zero level for voltages. This Fourier analysis could be done for any arrangement of charge and is often practical to find out the main distance dependence. Here, we expect a log-dependence of the electrostatic potential on distance because of

the shape of the nanoribbon. Both views are complementary as the logarithm arises from adding over a large number of Fourier components.

Previously, it has been shown that a line charge is a good approximation for electrostatic forces above graphene nanoribbons [41]. For a cylindrical charge with radius $R$, we expect an electrostatic potential that varies as

$$\Phi(z) = \frac{\rho}{2\pi\varepsilon_0} \ln\left(\frac{z-R}{R}\right) + \Phi_0, \quad (3)$$

where ρ is the charge per unit length [46]. We have fitted this function to the calculated data (black squares in Figure 3c) and obtained $\rho/2\pi\varepsilon_0$ = 203 mV, $R$ = 0.087 nm, and $\Phi_0$ = −680 mV, represented as a red line. The radius $R$ represents the height of the graphene nanoribbon. The charge is $\rho = Q/l$ = $1.13 \times 10^{-11}$ C/m and corresponds to 0.070 e/nm. The description of the data by the fitted function is good, but a slightly better choice is to describe the DFT-calculated curve by two exponential functions, one with decay length λ = 0.12 nm at close distance, arising from an intramolecular atomic-scale contrast, and a second one with a decay length of λ = 1.24 nm at far distance, resulting from the size of the graphene nanoribbon.

The experimental results (blue squares in Figure 3) generally follow the shape of the calculated curve with a shift. There are several possibilities to understand the origin of this shift. First, we discuss the possibility of a $z$ shift between experiment and calculated results. As shown in Figure 3c, a 0.48 nm shift in distance would be needed for experiment and calculations to match. This distance corresponds to the screening length of about one Fermi wavelength ($\lambda_F \approx 0.52$ nm) in Au, calculated from a Fermi energy of 5.53 eV and obtained by the assumption that each Au atom contributes one electron to the Fermi sea. In the calculations, the potential at a certain point in space is calculated, corresponding to a point-charge tip. In the experiment, the tip is either a Si tip or a metal-coated tip. For a perfect metallic layer on the tip, we expect that it adopts an image charge distribution that generates a similar electrostatic field as the charge located in the sample. The charge distribution in the sample in our own calculations is distributed over two atomic layers (Au–Au distance: 0.28 nm, see also Supporting Information File 1, Section III); hence, understanding the 0.48 nm shift as the apparent distance between the charge distribution in the tip and the tip apex is a reasonable assumption. In addition, we compare the shift to the value obtained in [41], 1.7 nm for the total distance, where the tip was composed of graphene nanoribbons with a longer screening length compared to Au. We conclude that the tip used in the experiments shown in this work is "sharp" concerning the electrical measurements in the sense that the charge distribution resides close to the tip apex.

A second way of understanding the shift between experiment and calculations is based on averaging effects [47]. Above, we have used a $z$ shift to describe the data, where the difference could be understood as a shift in the potential. The tip exposes its three-dimensional shape to the sample, and the forces result from the electrostatic field of the sample interacting with the tip at each point in space. The averaging effects depend on both the tip sharpness and the tip–surface distance. Here, we expect the relatively large tip radius of metal-coated tips (typically 20 nm) with respect to the width of the ribbons leading to averaging over a considerable part of the Au surface in addition to the GNR and to a reduction of the CPD values due to the long range nature of the electrostatic force.

## Conclusion

In summary, we have imaged graphene nanoribbons using KPFM. We confirm the p-type doping of the GNRs on the Au substrate. The measured LCPD values exhibit a slow decrease with tip–sample distance in qualitative agreement with calculations. Our results highlight the potential of Kelvin probe force microscopy to simultaneously study structural and electronic properties of GNRs and the capability of KPFM as a useful tool for observing the electronic properties in nanoelectronics.

## Supporting Information

### Supporting Information File 1

Additional information on the DFT calculations, on the force–distance data used for transforming frequency shift information into distance information, and on calculated charge differences.
[https://www.beilstein-journals.org/bjnano/content/supplementary/2190-4286-15-91-S1.pdf]

## Acknowledgements

We thank T. Beitz, P. P. Schmidt, and B. Weinschenk for help with the experiments.

## Funding

Funded by the Deutsche Forschungsgemeinschaft (DFG, German Research Foundation) – CRC/SFB 1636 – Project ID 510943930 - Project No. A07.

## Author Contributions

Daniel Rothhardt: data curation; formal analysis; investigation; visualization; writing – original draft. Amina Kimouche:

conceptualization; data curation; investigation; methodology; project administration; supervision; visualization; writing – original draft. Tillmann Klamroth: data curation; formal analysis; methodology; software; visualization; writing – original draft. Regina Hoffmann-Vogel: data curation; funding acquisition; investigation; methodology; project administration; resources; supervision; visualization; writing – original draft.

## ORCID® iDs

Daniel Rothhardt - https://orcid.org/0000-0002-7613-9047
Amina Kimouche - https://orcid.org/0000-0002-4223-0782
Tillmann Klamroth - https://orcid.org/0000-0001-5555-5490
Regina Hoffmann-Vogel - https://orcid.org/0000-0002-5771-7956

## Data Availability Statement

All data that supports the findings of this study is available in the published article and/or the supporting information to this article.

## Preprint

A non-peer-reviewed version of this article has been previously published as a preprint: https://doi.org/10.48550/arXiv.2203.06945

## References

1. Castro Neto, A. H.; Guinea, F.; Peres, N. M. R.; Novoselov, K. S.; Geim, A. K. *Rev. Mod. Phys.* **2009,** *81,* 109–162. doi:10.1103/revmodphys.81.109
2. Gierz, I.; Riedl, C.; Starke, U.; Ast, C. R.; Kern, K. *Nano Lett.* **2008,** *8,* 4603–4607. doi:10.1021/nl802996s
3. Koch, M.; Ample, F.; Joachim, C.; Grill, L. *Nat. Nanotechnol.* **2012,** *7,* 713–717. doi:10.1038/nnano.2012.169
4. Kedzierski, J.; Hsu, P.-L.; Healey, P.; Wyatt, P. W.; Keast, C. L.; Sprinkle, M.; Berger, C.; de Heer, W. A. *IEEE Trans. Electron Devices* **2008,** *55,* 2078–2085. doi:10.1109/ted.2008.926593
5. Gu, G.; Nie, S.; Feenstra, R. M.; Devaty, R. P.; Choyke, W. J.; Chan, W. K.; Kane, M. G. *Appl. Phys. Lett.* **2007,** *90,* 253507. doi:10.1063/1.2749839
6. Li, X.; Wang, X.; Zhang, L.; Lee, S.; Dai, H. *Science* **2008,** *319,* 1229–1232. doi:10.1126/science.1150878
7. Narita, A.; Wang, X.-Y.; Feng, X.; Müllen, K. *Chem. Soc. Rev.* **2015,** *44,* 6616–6643. doi:10.1039/c5cs00183h
8. Hämäläinen, S. K.; Sun, Z.; Boneschanscher, M. P.; Uppstu, A.; Ijäs, M.; Harju, A.; Vanmaekelbergh, D.; Liljeroth, P. *Phys. Rev. Lett.* **2011,** *107,* 236803. doi:10.1103/physrevlett.107.236803
9. Ritter, K. A.; Lyding, J. W. *Nat. Mater.* **2009,** *8,* 235–242. doi:10.1038/nmat2378
10. Vanin, M.; Mortensen, J. J.; Kelkkanen, A. K.; Garcia-Lastra, J. M.; Thygesen, K. S.; Jacobsen, K. W. *Phys. Rev. B* **2010,** *81,* 081408. doi:10.1103/physrevb.81.081408
11. Wang, Z.; Scharstein, R. W. *Chem. Phys. Lett.* **2010,** *489,* 229–236. doi:10.1016/j.cplett.2010.02.063
12. Wagner, P.; Ewels, C. P.; Adjizian, J.-J.; Magaud, L.; Pochet, P.; Roche, S.; Lopez-Bezanilla, A.; Ivanovskaya, V. V.; Yaya, A.; Rayson, M.; Briddon, P.; Humbert, B. *J. Phys. Chem. C* **2013,** *117,* 26790–26796. doi:10.1021/jp408695c
13. Cai, J.; Ruffieux, P.; Jaafar, R.; Bieri, M.; Braun, T.; Blankenburg, S.; Muoth, M.; Seitsonen, A. P.; Saleh, M.; Feng, X.; Müllen, K.; Fasel, R. *Nature* **2010,** *466,* 470–473. doi:10.1038/nature09211
14. Melitz, W.; Shen, J.; Kummel, A. C.; Lee, S. *Surf. Sci. Rep.* **2011,** *66,* 1–27. doi:10.1016/j.surfrep.2010.10.001
15. Nonnenmacher, M.; O'Boyle, M. P.; Wickramasinghe, H. K. *Appl. Phys. Lett.* **1991,** *58,* 2921–2923. doi:10.1063/1.105227
16. Kikukawa, A.; Hosaka, S.; Imura, R. *Rev. Sci. Instrum.* **1996,** *67,* 1463–1467. doi:10.1063/1.1146874
17. Jacobs, H. O.; Leuchtmann, P.; Homan, O. J.; Stemmer, A. *J. Appl. Phys.* **1998,** *84,* 1168–1173. doi:10.1063/1.368181
18. Barth, C.; Foster, A. S.; Henry, C. R.; Shluger, A. L. *Adv. Mater. (Weinheim, Ger.)* **2011,** *23,* 477–501. doi:10.1002/adma.201002270
19. Sadewasser, S.; Jelinek, P.; Fang, C.-K.; Custance, O.; Yamada, Y.; Sugimoto, Y.; Abe, M.; Morita, S. *Phys. Rev. Lett.* **2009,** *103,* 266103. doi:10.1103/physrevlett.103.266103
20. Pérez León, C.; Drees, H.; Wippermann, S. M.; Marz, M.; Hoffmann-Vogel, R. *J. Phys. Chem. Lett.* **2016,** *7,* 426–430. doi:10.1021/acs.jpclett.5b02650
21. Giessibl, F. J. *Rev. Mod. Phys.* **2003,** *75,* 949–983. doi:10.1103/revmodphys.75.949
22. García, R.; Pérez, R. *Surf. Sci. Rep.* **2002,** *47,* 197–301. doi:10.1016/s0167-5729(02)00077-8
23. Mohn, F.; Gross, L.; Moll, N.; Meyer, G. *Nat. Nanotechnol.* **2012,** *7,* 227–231. doi:10.1038/nnano.2012.20
24. Zerweck, U.; Loppacher, C.; Otto, T.; Grafström, S.; Eng, L. M. *Phys. Rev. B* **2005,** *71,* 125424. doi:10.1103/physrevb.71.125424
25. Neff, J. L.; Milde, P.; Pérez León, C.; Kundrat, M. D.; Eng, L. M.; Jacob, C. R.; Hoffmann-Vogel, R. *ACS Nano* **2014,** *8,* 3294–3301. doi:10.1021/nn404257v
26. Schneider, S. Herstellung von Graphenstreifen und ihre Untersuchung mit Rasterkraftmikroskopie. Ph.D. Thesis, Karlsruhe Institute of Technology, Germany, 2016.
27. Späth, T.; Popp, M.; Pérez León, C.; Marz, M.; Hoffmann-Vogel, R. *Nanoscale* **2017,** *9,* 7868–7874. doi:10.1039/c7nr01874f
28. Kresse, G.; Furthmüller, J. *Comput. Mater. Sci.* **1996,** *6,* 15–50. doi:10.1016/0927-0256(96)00008-0
29. Kresse, G.; Furthmüller, J. *Phys. Rev. B* **1996,** *54,* 11169–11186. doi:10.1103/physrevb.54.11169
30. Perdew, J. P.; Burke, K.; Ernzerhof, M. *Phys. Rev. Lett.* **1996,** *77,* 3865–3868. doi:10.1103/physrevlett.77.3865
31. Blöchl, P. E. *Phys. Rev. B* **1994,** *50,* 17953–17979. doi:10.1103/physrevb.50.17953
32. Kresse, G.; Joubert, D. *Phys. Rev. B* **1999,** *59,* 1758–1775. doi:10.1103/physrevb.59.1758
33. Grimme, S.; Antony, J.; Ehrlich, S.; Krieg, H. *J. Chem. Phys.* **2010,** *132,* 154104. doi:10.1063/1.3382344
34. Grimme, S.; Ehrlich, S.; Goerigk, L. *J. Comput. Chem.* **2011,** *32,* 1456–1465. doi:10.1002/jcc.21759
35. Liang, L.; Meunier, V. *Phys. Rev. B* **2012,** *86,* 195404. doi:10.1103/physrevb.86.195404
36. Giovannetti, G.; Khomyakov, P. A.; Brocks, G.; Karpan, V. M.; van den Brink, J.; Kelly, P. J. *Phys. Rev. Lett.* **2008,** *101,* 026803. doi:10.1103/physrevlett.101.026803
37. Wofford, J. M.; Starodub, E.; Walter, A. L.; Nie, S.; Bostwick, A.; Bartelt, N. C.; Thürmer, K.; Rotenberg, E.; McCarty, K. F.; Dubon, O. D. *New J. Phys.* **2012,** *14,* 053008. doi:10.1088/1367-2630/14/5/053008

38. Leicht, P.; Zielke, L.; Bouvron, S.; Moroni, R.; Voloshina, E.; Hammerschmidt, L.; Dedkov, Y. S.; Fonin, M. *ACS Nano* **2014,** *8,* 3735–3742. doi:10.1021/nn500396c
39. Kimouche, A.; Ervasti, M. M.; Drost, R.; Halonen, S.; Harju, A.; Joensuu, P. M.; Sainio, J.; Liljeroth, P. *Nat. Commun.* **2015,** *6,* 10177. doi:10.1038/ncomms10177
40. Hanke, F.; Björk, J. *Phys. Rev. B* **2013,** *87,* 235422. doi:10.1103/physrevb.87.235422
41. Schneider, S.; Hoffmann-Vogel, R. *Nanoscale* **2020,** *12,* 17895–17901. doi:10.1039/d0nr03348k
42. Kawai, S.; Glatzel, T.; Hug, H.-J.; Meyer, E. *Nanotechnology* **2010,** *21,* 245704. doi:10.1088/0957-4484/21/24/245704
43. Krok, F.; Sajewicz, K.; Konior, J.; Goryl, M.; Piatkowski, P.; Szymonski, M. *Phys. Rev. B* **2008,** *77,* 235427. doi:10.1103/physrevb.77.235427
44. Enevoldsen, G. H.; Glatzel, T.; Christensen, M. C.; Lauritsen, J. V.; Besenbacher, F. *Phys. Rev. Lett.* **2008,** *100,* 236104. doi:10.1103/physrevlett.100.236104
45. Feynman, R.; Leighton, R. B.; Sands, M. L. The electrostatic field of a grid. *The Feynman Lectures on Physics, Vol. II;* California Institute of Technology: Pasadena, CA, USA, 2013. https://www.feynmanlectures.caltech.edu/II_07.html
46. Kuchling, H.; Kuchling, T. *Taschenbuch der Physik;* Carl Hanser Verlag: Munich, Germany, 2022. doi:10.3139/9783446473645.fm
47. Glatzel, T.; Sadewasser, S.; Lux-Steiner, M. C. *Appl. Surf. Sci.* **2003,** *210,* 84–89. doi:10.1016/s0169-4332(02)01484-8

## License and Terms